EVALUATING THE EFFECTS OF PARTICLE-DELIVERED COMBINATION ADJUVANTS ON ANTIGEN-PRESENTING CELLS

A Dissertation
Presented to
The Academic Faculty

by

Alexandra Maria Atalis

In Partial Fulfillment
of the Requirements for the Degree
Doctor of Philosophy in the
Wallace H. Coulter Department of Biomedical Engineering

Georgia Institute of Technology and Emory University
May 2021

EVALUATING THE EFFECTS OF PARTICLE-DELIVERED COMBINATION ADJUVANTS ON ANTIGEN-PRESENTING CELLS

Approved by:

Dr. Krishnendu Roy, Advisor
School of Biomedical Engineering
Georgia Institute of Technology

Dr. Philip Santangelo
School of Biomedical Engineering
Georgia Institute of Technology

Dr. J. Brandon Dixon, Co-Advisor
School of Mechanical Engineering
Georgia Institute of Technology

Dr. Manmohan Singh
Senior VP, Pharmaceutical Sciences and Delivery Technologies
Beam Therapeutics

Dr. Susan Thomas
School of Mechanical Engineering
Georgia Institute of Technology

Date Approved: February 12, 2021

To my mom, Elaine Atalis, in loving memory

ACKNOWLEDGEMENTS

I would like to acknowledge all current and previous labmates who helped me throughout my Ph.D. journey. Dr. Jardin Leleux, Dr. Pallab Pradhan, Dr. Randall Toy, and Dr. Timothy Kassis taught me the basics of experimental design and foundational lab techniques and provided much-needed encouragement and motivation. Dr. Bhawana Pandey helped tremendously by preparing particle formulations for most experiments in Aim 2 and provided many chemistry-related experimental tips. When times were tough, she reminded me to stay positive. Cole Keenum and Alexander Beach were a big part of the COVID-19 research team. Alex collected BMDC cytokine and serological antibody titer data from ELISA and Luminex assays. Cole helped with preparing particle formulations, ELISA assays, and staining samples for flow cytometry. Paramita Chatterjee and Angela Jimenez performed RT-PCR experiments and data analysis. Paramita Chatterjee and Cole Keenum provided the single-cell mRNA and protein expression data analyzed in SEURAT. A big team worked on the COVID-19 intranasal vaccination study: Bhawana Pandey, Pallab Pradhan, Alexander Beach, Cole Keenum, Ritika Jain, Casey Vantucci, and Justin Hosten. Thank you to my advisors, Dr. Roy and Dr. Dixon, for all of their guidance and support, especially when I had to take a personal hiatus to spend time with family. To Dr. Dixon: I will never forget when attended the Lymphatics Gordon Research Conference in Italy with LLBB. Thank you for allowing me that opportunity. To Dr. Roy: it is hard to believe I have known you for over 10 years since I was a sophomore at UT Austin. I remember sitting in the lobby of the Biomedical Engineering Building wondering what I would do after college, and you encouraged me to apply to graduate school. Finally, thank you to my friends and family who have supported me through the

ups and downs. My roommate and friend, Dr. Roxanne Glazier, and I had many late-night talks about life and research that I will never forget. My close friend and confidante, Michelle Humphrey, was always a phone call away when times were tough (and thank you for the box of snacks to help me get through writing this dissertation). My godfather, Dr. John Pappadas has been my #1 fan since Day 1 of starting this program. He supported me through my anxiety and encouraged me to stick with it. Thank you to my brothers, Sam and John, and to cousins, aunts, uncles, and Yiayias who provided much love and prayer. Thank you to my Dad, Andy Atalis, who was always there to talk me through the tough moments and has encouraged me to be my best self. Thank you to my husband-to-be Nick Grivas, who is my rock. I look forward to our marriage and life together. Finally, I want to acknowledge my mother, Elaine Atalis, who passed away in 2017. Her strength continually inspires me to persevere through difficult moments. She is with me in spirit every step of the way.

TABLE OF CONTENTS

LIST OF TABLES

LIST OF FIGURES

LIST OF SYMBOLS AND ABBREVIATIONS

AF488	Alexa Fluor 488®
APC	Antigen-presenting cell
BAL	Bronchoalveolar lavage
BMDCs	Bone-marrow derived dendritic cells
CCL	Chemokine (C-C motif) ligand
CCR	Chemokine (C-C motif) receptor
CD	Cluster of differentiation
cDC	Conventional dendritic cell
COVID-19	Coronavirus disease 2019
CpG	5'—C—phosphate—G—3'
CTL	Cytotoxic T lymphocyte
DC	Dendritic cell
dLN	Draining lymph node
DNA	Deoxyribonucleic acid
FACS	Fluorescence-activated cell sorting
FLT3L	FMS-like tyrosine kinase 3 ligand
GM-CSF	Granulocyte macrophage colony stimulating factor
iDC	Inflammatory dendritic cell
IFN	Interferon
Ig	Immunoglobulin
IL	Interleukin
IR700	IRDye® 700
Iso-MLR	Isogeneic mixed lymphocyte reaction

LN	Lymph node
MDA5	Melanoma differentiation-associated protein 5
MHC	Major histocompatibility complex
Mo-DC	Monocyte-derived dendritic cell
MP	Microparticle
MPLA	Monophosphoryl Lipid A
mRNA	Messenger ribonucleic acid
NIR	Near-infrared
NP	Nanoparticle
ODN	Oligodeoxynucleotide
PAMP	Pathogen-associated molecular pattern
PBS	Phosphate-buffered saline
pDC	Plasmacytoid dendritic cell
PLGA	Poly(lactic-co-glycolic acid)
PLP	Pathogen-like particle
PRR	Pattern-recognition receptor
PUUC	PolyU/UC
RIG-I	Retinoic acid-inducible gene I
RLR	RIG-I-like receptor
RPMI	Roswell Park Memorial Institute
SARS-CoV-2	Severe acute respiratory syndrome coronavirus 2
Th	T helper cell
Tip-DC	TNF and iNOS-producing dendritic cell
TLR	Toll-like receptor
TNF	Tumor necrosis factor

SUMMARY

A strategy for modulating immunity during vaccination is to target specific professional antigen-presenting cells (APCs) and induce their maturation. Professional APCs effectively activate antigen-specific T cells, a requirement for induction of strong humoral and cellular responses. Mammalian cells, including APCs, possess pattern recognition receptors (PRRs) that bind to distinct molecules broadly expressed by different microorganisms, collectively known as pathogen associated molecular patterns (PAMPs), PAMPs differ in the types of PRRs they engage, the signaling pathways they trigger and the types of immune responses they generate. The nature of the immune response is also influenced by the stimulated APC subsets, which express different combinations of TLRs and other PRRs, resulting in cell and tissue-specific responses to microbes. To design combinatorial PRR-targeting adjuvant vaccines, it is essential to understand how different APC subsets interact with them and how that leads to specific immune outcomes. It is also essential to investigate how delivery vehicles influence cell responses to PAMPs, for example biomaterials-based particles. This thesis addresses the effects of combinatorial PRR-targeting adjuvant polylactic-co-glycolic acid (PLGA) particle vaccines on APC subsets at different stages of the immune response, including recruitment of innate immune cells, APC maturation and expression of costimulatory molecules, proinflammatory cytokine and interferon secretion, lymphatic migration, and activation of T cells.

CHAPTER 1: INTRODUCTION AND AIMS

1.1 Introduction

Vaccination is one of the earliest and most successful medical interventions in history and remains the standard method for global control of infectious diseases in the human population. The World Health Organization estimates vaccines save 2-3 million lives each year, and in developed countries, many fatal childhood diseases have been fully or nearly eradicated.[1] However, there is a need for improved understanding of the immunological mechanisms underlying vaccination to develop more effective vaccines against life-threatening infectious diseases. Current vaccine development challenges include targeting pathogens that are antigenically variable (e.g., HIV) or immune-evasive (e.g., Mycobacterium tuberculosis), tailoring immunogenicity for infants and aging populations (e.g., for RSV), designing single-dose vaccines for lifelong immunity (e.g., for influenza), and facilitating rapid formulation screening and development for curbing global outbreaks. Most recently, the coronavirus disease 2019 (COVID-19) pandemic caused by severe acute respiratory syndrome coronavirus 2 (SARS-CoV-2) has killed more than 3 million people worldwide, and the crisis elicited a global scientific effort to develop vaccines and therapies for the disease at an unprecedented speed. Phase I trials started as early as March 2020, and as of April 2021 there are more than 270 vaccines in various stages of development.[2] Three formulas from Pfizer-BioNTech, Moderna, and Johnson & Johnson (Janssen) have been authorized for emergency use in the United States and approved in several countries. However, much remains to be determined regarding immune correlates of protection against SARS-CoV-2 infection in various patient populations.

Vaccines utilize the ability of evolved human immune systems to engage and remember pathogenic antigens, components that stimulate the generation of antibodies and differentiation of cells that specifically recognize their biological structures. Traditional vaccines are composed of live-attenuated or inactivated pathogens, which contain endogenous adjuvants and antigens presented on particulate structures. To increase vaccine safety and effectiveness, emerging vaccines contain pathogen subunits, including recombinant proteins. Nucleic acid vaccines, like Moderna's mRNA vaccine for COVID-19, include mRNA or DNA that instructs a patient's cell to produce antigen on their own.

Many purified antigens in subunit vaccines are poorly immunogenic, so they are often formulated with adjuvants to increase the level and duration of adaptive immune responses following vaccination.[3] Aluminum-containing adjuvants have been included in vaccines to enhance immunogenicity since the 1930s, initially with diphtheria and tetanus vaccines. Aluminum salts continue to be added in vaccine formulations due to their historical success and low cost, and because the use of established adjuvants accelerates clinical development and regulatory approval pathways. However, most of the vaccines we use today were develop and tested empirically; as we gain a better understanding of protective immunity, the design strategy has shifted to a more rational approach, especially for fighting hard-to-target pathogens. For almost 60 years, it was accepted by the scientific community that aluminum salts were effective because they created a "depot effect," slowly releasing antigen from insoluble particles.[4] But research in the mechanisms of action of aluminum salts has reignited in the past two decades, and the exact relationship between the physiochemistry and immunoreactivity of aluminum salts remains elusive.[5] The lack of specificity makes them inadequate for a broad range of vaccines, specifically those that

require a cytotoxic, Th-1 skewed immune response. The goal of next generation vaccines is to assemble a structure where each component elicits a specific immunological pathway to tailor the resultant immune response.

A strategy for modulating immunity during vaccination is to target specific professional antigen-presenting cells (APCs) and induce their maturation. Professional APCs effectively activate antigen-specific T cells, a requirement for induction of strong humoral and cellular responses. Mammalian cells, including APCs, possess pattern recognition receptors (PRRs) at the cell surface, within endosomes and other intracellular organelles, as well as unbound in the cytosol. PRRs bind to distinct molecules broadly expressed by different microorganisms, collectively known as pathogen associated molecular patterns (PAMPs), including lipids, carbohydrates, peptides, and nucleic acid structures.[6] PAMP engagement with various PRRs trigger differential innate immune responses and are therefore being investigated as adjuvants to guide and strengthen protective immunity. Two classes of PRRs include toll-like receptors and RIG-I-like receptors (RLRs). RLRs, including RIG-I, MDA5, and LGP2, detect foreign RNA within the cytosol, including 5' triphosphate RNA, long double-stranded RNA, and sequences specific to viral genomes such as the poly-uridine region of Hepatitis C virus (i.e., polyU/UC or PUUC).[7,8] RLR pathways regulate transcription factors NFκB, IRF3, and IRF7, resulting in the production of interferons (IFNs) and pro-inflammatory cytokines, and can also limit viral replication by initiating cell death.[7]

Toll-like receptors (TLRs) are transmembrane glycoproteins that bind PAMPs at the plasma membrane, as well as in endosomes. Cell surface TLRs include TLR4, which primarily binds to lipopolysaccharides (LPS) in the outer membranes of Gram-negative

bacteria. Activation of TLR4 at the cell membrane signals through the MyD88 pathway and drives the production of proinflammatory cytokines (e.g., IL-12p70) through NFκB activation. A CD14-dependent pathway moves TLR4 from the plasma membrane into endosomes, where TLR4 signals via TRIF to induce type I IFN expression.[9] Monophosphoryl lipid A (MPLA) is extracted from LPS through hydrolysis and retains TLR4-stimulatory properties with reduced toxicity. It is available in FDA-approved clinical adjuvants, including Adjuvant System 04 (AS04), which combines MPLA with aluminum salts.[10] Nucleic acid-sensing TLRs are intracellular to detect nucleic acids liberated from bacteria or viral capsids in endo-lysosomal compartments, including ssRNA (TLRs 7/8) and unmethylated CpG DNA (TLR9). Ligand binding to nucleic acid-sensing TLRs activate MyD88-dependent pathways triggering the secretion of proinflammatory cytokines and type I interferons, particularly by plasmacytoid DCs (pDCs). There is an FDA-approved TLR9-targeted adjuvant, CpG 1018, that is used in a Hepatitis B vaccine.[11]

During an infection, it is likely that several ligands displayed by a pathogen activate multiple different PRRs, leading to increased innate and adaptive immune responses (Figure 1). For instance, the live-attenuated yellow fever vaccine activates TLR2, TLR7, TLR8, and TLR9 on different dendritic cell (DC) subsets.[12] Although pathogens present multiple PAMPs and antigens within a particulate structure, most research on PRR-targeting adjuvants involves delivering soluble antigens with single PRR agonists. Researchers have shifted their focus onto particulate vaccine delivery vehicles with combination adjuvants to mimic the composition of pathogens better and elicit more effective immune responses.

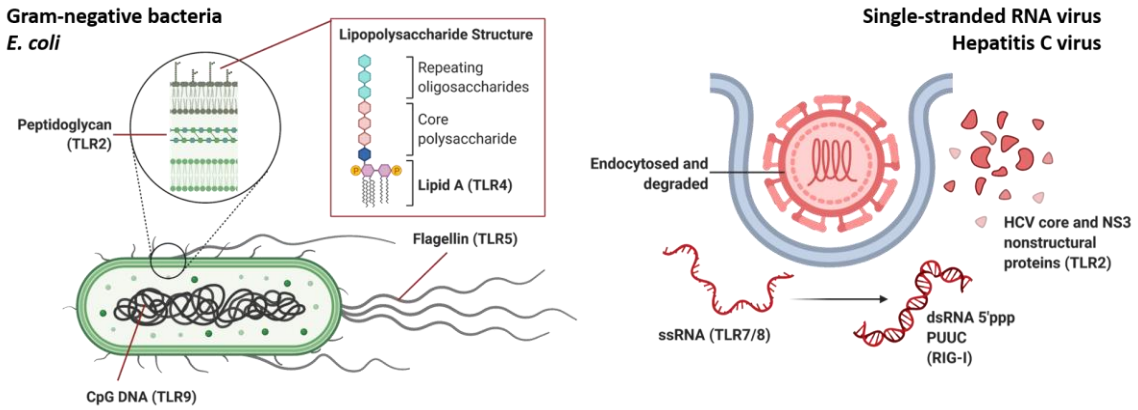

Figure 1: Pathogens endogenously express multiple PRR ligands. Gram-negative bacteria, such as *E. coli*, express TLR2, TLR4, TLR5, and TLR9 ligands. ssRNA viruses, such as Hepatitis C, contain ligands for TLR7/8, RIG-I, and TLR2. The coexpression of different PAMPs by pathogens supports the rationale for using combinations of purified PAMPs as vaccine adjuvants to stimulate the immune system. Figure created with ©BioRender, biorender.com

Studies have shown that combinations of agonists targeting various TLRs can result in synergistic, complementary, and antagonistic effects on innate and adaptive immunity. Stimulation of PRRs in different cellular compartments, which researchers have described as a "combinatorial security code," theoretically ensures invading pathogens will cause cells to generate robust immune responses.[13] In vitro, stimulation of mouse macrophages with both TLR3 and TLR9 ligands (poly(I:C) and CpG) upregulated production of TNF, IL-6, and IL-12p40, and combining TLR4 with TLR7/8 agonists induced 50-100-fold higher levels of IL-12 and IL-23 and more Th1 polarization compared to single agonists in human monocyte-derived DC culture.[13,14] In vivo, a combination of TL4 and TLR7-targeting adjuvants and recombinant hemagglutinin induced balanced Th1/Th2-type immunity against different influenza strains in mice, while HIV-1 glycoprotein gp140 co-delivered with TLR7/8 and TLR9 agonists elicited strong humoral immune responses in rhesus macaques.[15,16] Systemic analyses on the effects of combined TLR ligands have indicated the most significant synergies occur between stimuli that trigger different TLR-

mediated signaling pathways; for example, activation of both MyD88-dependent and TRIF-dependent pathways markedly increases IL-12p70 production.[17]

There is growing evidence that TLRs cooperate with other types of PRRs in the innate immune response to pathogens; however, researchers have not sufficiently investigated the immunological events occurring during the combined stimulation of RLRs and TLRs. A study revealed that poly(I:C), a synthetic analog of double-stranded RNA, can activate both TLR3 and MDA5, resulting in the production of different cytokines.[18] Interactions between poly(I:C) and TLR3 were primarily responsible for the induction of pro-inflammatory cytokines while activating MDA5 stimulated type I IFN responses. Clinical studies have shown that suppression of both RIG-I and TLR4-mediated signaling pathways is more common in children with an influenza-related critical illness, and increasing stimulation of both pathways may ameliorate antiviral and antibacterial responses.[19] Research on the collaboration of endosomal TLRs and RIG-I in primary human pDCs demonstrated pDCs upregulate RIG-I expression in a type I IFN-independent manner upon stimulation by TLR7 ligand R848 or TLR9 ligand type A CpG ODN.[20]

PAMPs differ in the types of PRRs they engage, the signaling pathways they trigger, and the types of immune responses they generate. The nature of the immune response is also influenced by the stimulated APC subsets, which express different combinations of TLRs and other PRRs, resulting in cell and tissue-specific responses to microbes. To design combinatorial PRR-targeting adjuvant vaccines, it is essential to understand how different APC subsets interact with them and how that leads to specific immune outcomes. It is also essential to investigate how delivery vehicles influence cell responses to PAMPs, for example biomaterials-based particles. Incorporating adjuvants into polymeric particles,

such as polylactic-co-glycolic acid (PLGA) particles, prevents rapid diffusion, which may reduce systemic toxicity and enable targeted delivery to immune cells. Another advantage of PLGA particles is they facilitate the co-delivery of chemically variable adjuvants, especially when combining hydrophobic molecules (e.g., MPLA or imiquimod, R848) with a highly hydrophilic molecule (e.g., CpG ODN or PUUC).

Therefore, this thesis addresses the effects of combinatorial PRR-targeting adjuvant PLGA particle vaccines on APC subsets at different stages of the immune response, including recruitment of innate immune cells, APC maturation and expression of costimulatory molecules, proinflammatory cytokine and interferon secretion, lymphatic migration, and activation of T cells.

1.2 Specific Aims

1.2.1 Hypothesis

Pathogens express multiple ligands recognized by various PRRs on APCs that together orchestrate APC maturation, migration, and activation of T cells. The central hypothesis of this thesis is combinations of two PRR-targeting adjuvants are more effective at stimulating APC-mediated innate and adaptive immune responses compared to single PRR-targeting adjuvants. The overall objective is to evaluate the immunogenicity of combination adjuvants by delivering TLR and RLR ligands on PLGA micro- and nanoparticles, otherwise known as pathogen-like-particles (PLPs), to stimulate APCs in vitro and in vivo. Aim 1 focuses on the effects of MPLA and CpG on APC migration toward lymphatics and particle delivery to lymph nodes, while Aim 2 investigates TLR-RLR adjuvant combinations for enhancing antigen-specific T cell responses to SARS-CoV-2.

1.2.2 Aim 1: Characterizing Immune Responses to Combined MPLA and CpG

The goal of this aim is to evaluate how single and combined TLR4 and TLR9 agonists MPLA and CpG ODN, both of which are expressed by gram-negative bacteria, regulate APC chemotaxis toward lymphatics and PLGA particle delivery to draining lymph nodes. The general hypothesis is that co-delivered MPLA and CpG enhance particle transport to lymph nodes by targeting migratory APC subsets in the muscle and inducing APC chemotaxis toward lymphatic chemokines. Aim 1 is divided into two sub-aims:

Aim 1.1: Evaluate how single and combined MPLA and CpG, delivered in soluble form or together on PLGA particles, modulate murine bone marrow-derived DC (BMDC) migration through collagen gel toward lymphatic chemokine gradients using a microfluidic platform. Cationic PLGA-polyethylenimine (PEI) microparticles encapsulating MPLA were fabricated using a double emulsion, solvent evaporation method and electrostatically loaded with Class B CpG ODN 1826. BMDCs were cultured with granulocyte macrophage colony-stimulating factor (GM-CSF) and interleukin-4 (IL-4) and characterized for CCR7 expression in response to soluble and PLP-loaded adjuvants. Within a microfluidic device, BMDCs were cultured in a 3D collagen matrix channel between two media reservoirs, only one of which containing CCL19 or CCL21, establishing a chemokine gradient stable for over 24 hours. Adjuvants were either diluted in media reservoirs or PLPs were incubated with BMDCs in the collagen matrix, and cell migration was imaged in real time with phase contrast microscopy. Finally, cell migration was quantified using high-throughput cell tracking software and analyzed using a logistic regression model and directional statistics.

Aim 1.2: Determine how single and co-loaded MPLA and CpG on PLGA nanoparticles (NPs) affect the recruitment and activation of muscle- and lymph node-resident APC subsets, as well as the kinetics of particle-adjuvant partitioning and delivery to different muscle-draining lymph nodes in mice. PLGA-PEI nanoparticles encapsulating synthetic MPLA (GLA) were functionalized with Alexa Fluor 488 and electrostatically loaded with IR700 Dye conjugated-CpG ODN or control ODN (GpC). The dual fluorescent label, dual adjuvant (or single adjuvant) PLPs were injected intramuscularly in mice, then anterior tibialis muscles and draining lymph nodes (dLN) were isolated after 24 and 48 hours. Popliteal, inguinal, and iliac dLN were imaged using near-infrared (NIR) microscopy to quantify fluorescence of lymphatically transported IR700-labeled PLPs. Cells from muscles and dLNs were analyzed via flow cytometry to characterize cell populations and determine which APC subsets internalized AF488-particles and/or IR700-ODN.

1.2.3 Aim 2: Characterizing Immune Responses to Combined RLR and TLR Agonists

Positive-strand RNA viruses, such as SARS-CoV-2, have been reported to trigger TLR4, TLR7/8, and RIG-I. The objective of this aim is to understand how combined TLR and RLR agonists on PLGA NPs with recombinant SARS-CoV-2 spike protein modulate innate and adaptive immune responses against SARS-CoV-2. The general hypothesis is delivering PUUC with a TLR ligand (MPLA, R848, or CpG) on PLGA NPs increases APC production of proinflammatory cytokines and interferons, resulting in enhanced T cell proliferation and anti-SARS-CoV-2 humoral and cellular immune responses. Aim 2 is divided into two sub-aims:

Aim 2.1: Identify PLP adjuvant combinations that enhance murine bone marrow-derived DC secretion of proinflammatory cytokines and interferons as well as T cell proliferation in an isogeneic mixed lymphocyte reaction (iso-MLR) with SARS-CoV-2 spike protein antigen. GM-CSF-dependent BMDCs (including $CD11b^{hi}$ APCs) and FLT3L-dependent BMDCs (including pDC and cDCs) were cultured for 24 hours with recombinant SARS-CoV-2 spike protein and PLPs loaded with one or two of the following ligands: Poly(I:C) (TLR3), GLA (TLR4), R848 (TLR7/8), CpG ODN 1826 (TLR9), or PUUC (RIG-I). Cell culture media was collected to quantify proinflammatory cytokine (e.g., IL-12p70 and TNF-α) and interferon secretion by BMDCs. T cells isolated from spleens and labeled with CFSE were mixed with activated BMDCs for 72 hours (iso-MLR culture). Media was collected from iso-MLR culture to quantify IFN-γ and IL-4, and T cells were analyzed via flow cytometry to quantify CD4+ and CD8+ T cell proliferation and predict which PLP formulations would stimulate Th1 and/or Th2 immune responses. Experiments were carried out with both female and male BMDCs and T cells to identify sex differences in immune responses.

Aim 2.2: Investigate how intranasally administered PLPs with various dual adjuvant formulations modulate innate immune cell populations and gene expression in the lung and tailor adaptive immune responses against SARS-CoV-2 in mice. PLGA NPs formulated with PUUC or PUUC and one TLR agonist (GLA, R848, CpG) were intranasally administered to mice. Lungs were collected at 4 and 24 hours to measure changes in inflammatory gene expression in response to PLPs. In a separate experiment, PUUC and MPLA-PUUC PLPs were delivered i.n. and lungs were collected again at 4 and 24 hours. Lung cell clusters were characterized based on protein and gene expression at the single-

cell level using CITE-Seq. Finally, mice were vaccinated i.n. with PLP formulations and soluble or PLGA NP-conjugated SARS-CoV-2 stabilized spike protein. Sera and bronchoalveolar lavage (BAL) fluid was collected before and after booster vaccinations to measure anti-spike antibody titers. Lungs were collected one week after booster shots, processed for single cell suspensions, and stimulated with SARS-CoV-2 spike peptide pools to measure Granzyme B, IFN-γ, and TNF-α responses in CD4+, CD8+, and CD69+CD103+ T cells.

CHAPTER 2: BACKGROUND

2.1 APCs: Linking Innate and Adaptive Immunity

As of 2020, the World Health Organization listed communicable diseases as three of the top 10 causes of death globally and *six* of the top ten in low-income countries, including neonatal conditions, lower respiratory infections, diarrheal diseases, malaria, tuberculosis, and HIV/AIDS.[21] Infectious diseases are caused by microorganisms called pathogens, each one responsible for a particular disease. The four major classes of pathogens are viruses, bacteria, fungi, and parasites. Pathogens must invade and colonize a host to survive and multiply. When pathogens breach the first lines of defense of the human immune system, including anatomical barriers (skin, mucosal surfaces), antimicrobial enzymes and peptides, and the complement system, the immune system's initial priority is to recognize and eliminate the pathogen. Pathogens are broadly and specifically recognized by the molecules they express (non-self) distinctly from host cell molecules (self). *Innate* immune cells possess **pattern recognition receptors** (PRRs) that bind to molecules common to most pathogens, known as **pathogen-associated molecular patterns** (PAMPs). This feature of innate immunity enables the host to nonspecifically target and clear pathogens immediately upon infection. *Adaptive* immune cells contain receptors specifically generated to recognize fine distinctions between closely related pathogenic molecules, called **antigens**. It takes about four days to generate an antigen-specific response to a new pathogen; however, if the host possesses immunological memory of a pathogen, then a strong and immediate antigen-specific response is mounted.[22] Professional **antigen-presenting cells** – mainly dendritic cells, macrophages, and B cells – bridge innate and adaptive immunity through their unique ability to recognize PAMPs and induce innate

responses, as well as present antigen to T cells and initiate adaptive responses.[23] This chapter introduces antigen-presenting cells (APCs), outlines APC subsets and their functions, reviews APC-targeted vaccine adjuvants, and delineates the roles of APCs and the lymphatic system in antigen and/or vaccine delivery to draining lymph nodes.

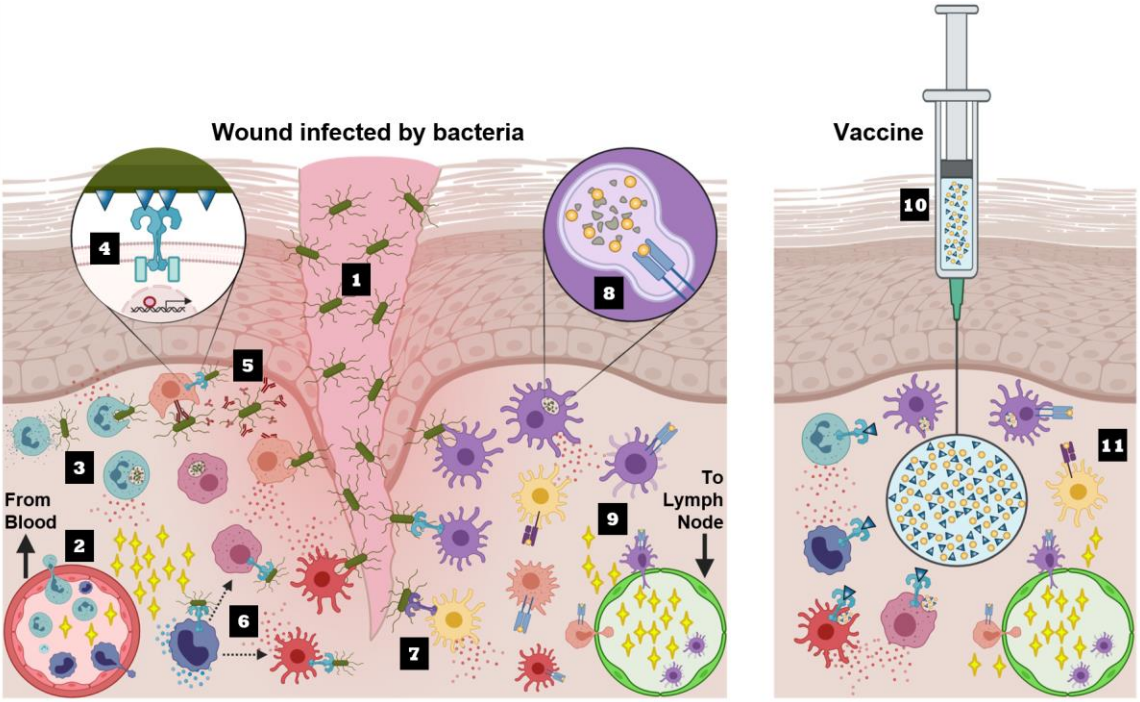

Figure 2: Innate immune response to infection and vaccination. 1) Bacteria enter tissue through a wound leading to inflammation and recruitment of immune cells at the site of infection. 2) Innate immune cells, such as neutrophils (light blue) and monocytes (dark blue), are recruited from the blood to tissue. 3) Neutrophils phagocytose and degrade bacteria, as well as kill bacteria through degranulation (release of anti-microbials) and release of neutrophil extracellular traps (NETs). 4) Innate immune cells express pattern recognition receptors (PRRs), which recognize and bind to pathogen-associated molecular patterns (PAMPs). 5) Immunoglobulins and complement factors specifically and non-specifically bind to pathogens (opsonization), enabling cells to target and phagocytose pathogens. 6) Monocytes express PRRs and secrete pro-inflammatory cytokines and have the potential to differentiate into DCs (dark red) and macrophages (light red) under inflammatory conditions. 7) Tissue-resident conventional DCs (derived from pre-DCs) recognize and endocytose bacteria. 8) Antigen-presenting cells (APCs), especially DCs, degrade pathogens and load antigens onto MHC-II molecules in endolysosomal compartments. 9) Mature APCs express MHC and costimulatory molecules and follow chemokine gradients through lymphatic vessels to lymph nodes where they activate T cells. cDC1 (yellow) have the ability to cross-present antigens on MHC-I molecules while cDC2 (purple) predominantly express MHC-II. 10) Subunit vaccines contain purified adjuvants

(e.g., PAMPs) and antigens to stimulate innate and adaptive immunity. 11) Immunization simulates infection by inducing inflammation and recruitment of innate immune cells to the injection site. APCs internalize soluble and particle-bound antigens and load them onto MHC molecules before migrating to lymph nodes. Figure created with ©BioRender, biorender.com.

Antigen-presenting cells are categorized for their proficiency in displaying antigens and **major histocompatibility complex** (MHC) molecules on their surface, which are specifically recognized by T cells. In combination with other molecular signals provided by APCs, antigen presentation is necessary to activate T cells and initiate effective adaptive immune responses. To display antigens, APCs must first recognize, internalize, and degrade pathogens to acquire antigens, then further process them into short fragments for loading onto MHC molecules. The mechanisms involved in acquiring antigen simultaneously trigger the release of molecular signals that control innate immune responses. In peripheral tissues, the largest population of APCs with the broadest range of combined antigen presentation and innate immune signaling are dendritic cells, followed by macrophages; therefore, this section will be primarily referring to these cell types.

Myeloid APCs develop in the bone marrow and migrate to peripheral tissues or continuously circulate through blood and lymphatic vessels to surveil for pathogens (Figure 2). Tissue-resident APCs engulf invading pathogens through phagocytosis and receptor-mediated endocytosis, regulated by the binding of microbial PAMPs to membrane-bound PRRs on APC surfaces. APCs can also capture pathogens through ingestion of large amounts of extracellular fluid, a process known as micropinocytosis. Once internalized, pathogens are degraded in endo-lysosomal compartments and release antigens as well as other PAMPs that bind to intracellular PRRs. Surface PRRs primarily bind to structural components of pathogens, such as bacterial cell wall lipopolysaccharides, viral envelope

proteins, and flagellin, while most intracellular PRRs bind to nucleic acids with pathogen-specific motifs, including single stranded RNA sequences with GU-rich sequences or DNA with unmethylated CpG islands.[7] Antigens from proteins degraded in endosomes are loaded onto MHC class II (MHC-II) molecules, while antigens from proteins degraded by the proteosome in the cytosol are loaded onto MHC class I (MHC-I) molecules. Antigen from endocytosed proteins require special processing for loading and "cross-presentation" to T cells on MHC-I molecules.[24]

The key outcome from PRR activation is the production and secretion of specific proteins called **cytokines**, which help promote and maintain inflammation. Cytokines can act in an autocrine, paracrine, or endocrine manner, to control behavior of the signaling cell, adjacent cells, or distant cells, respectively. The cytokines secreted by APCs are diverse and can be grouped into different families based on structure or function. Cytokine families include interleukins (IL), tumor necrosis factors (TNF), interferons (IFN), and colony stimulating factors (CSF); however, the nomenclature is continuously evolving as new cytokines are discovered. For example, the term interleukin was coined because ILs were first thought to be exclusively expressed by leukocytes (e.g., neutrophils), but were later found to be secreted by a wide range of immune cells.[25] The most important cytokines in the innate immune response include those in the IL-1 superfamily (IL-1α, IL-1β, and IL-18), hematopoietin superfamily (IL-6 and GM-CSF), TNF family (TNF-α) and type I interferons (IFN-α, IFN-β). Another class of chemoattractant cytokines, known as chemokines, are secreted during the innate immune response and direct migration of immune cells expressing the matching chemokine receptor. The combination of pro-inflammatory cytokines and chemokines induce the following events: vasodilation,

upregulation of adhesion molecules on endothelial cells, infiltration of immune cells from blood circulation into infected tissues, differentiation of myeloid progenitor cells into APCs, upregulation of MHC molecules, production of antiviral proteins, amplified fluid drainage to lymph nodes, and growth and differentiation of T and B cells.

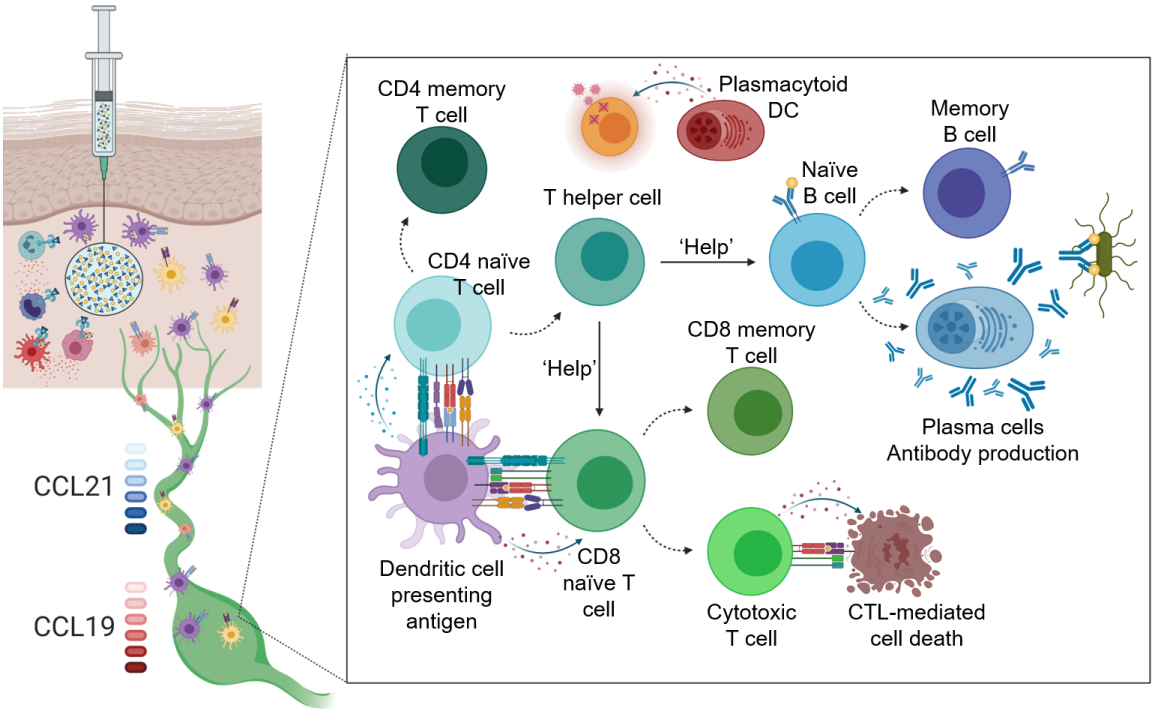

Figure 3: Adaptive immune response to vaccination. Migratory APCs follow gradients of chemokines CCL19 and CCL21 through lymphatic vessels to lymph nodes, where they encounter T cells. MHC-antigen complexes expressed by mature APCs engage with T cell receptors on $CD4^+$ and $CD8^+$ T cells. Activated $CD8^+$ T cells differentiate into memory and effector $CD8^+$ T cells, i.e., cytotoxic T cells. CTLs recognize and kill infected cells. Activated $CD4^+$ T cells differentiate into memory and effector $CD4^+$ T cells, i.e., T helper cells. T helper 1 cells assist differentiation of CTLs while T helper 2 cells assist differentiation of B cells into memory B cells and plasma cells. Plasmacytoid DCs primarily reside in lymphoid organs and are specialized in secreting interferons to prevent viral replication. Figure created with ©BioRender, biorender.com.

Many infections are cleared by innate immune responses and cause no disease; however, if infections are not quickly resolved, the innate immune system will attempt to contain the pathogen while triggering an adaptive immune response. Adaptive immune responses are

characterized by the production of antibodies against a particular pathogen-derived antigen. Most cases result in immunological memory, which confers protective immunity to reinfection with the same pathogens, and helps individuals adapt to their environments. The white blood cells that carry out adaptive responses are lymphocytes, mainly B cells and T cells, that primarily reside in lymphoid tissues. Lymphocytes that have not been activated are *naive* lymphocytes, and they require activation to differentiate into fully functional effector cells (Figure 3). Free antigen can bind to the B cell receptors (BCRs) on B cell surfaces, inducing proliferation and differentiation into plasma cells that secrete antigen-specific antibodies. Still, B cells require "help" from activated helper T cells for optimal immune responses.

T cells are activated through the binding of T cell receptors to specific peptide-MHC complexes on APCs. APCs must migrate from peripheral tissues, through lymphatic vessels, to deliver antigen to T cells in secondary lymphoid organs (e.g., lymph nodes, spleen). Even in the absence of infection, DCs continuously endocytose self-antigens or nonpathogenic environmental antigens and present them to T cells in dLNs to promote a tolerogenic response. To induce an optimal immunogenic response, APCs must undergo maturation, a process that is triggered by exposure to PAMPs and proinflammatory cytokines (Figure 4). During maturation, APCs upregulate MHC molecules and costimulatory molecules (CD80, CD86, CD40) and secrete more T cell-polarizing cytokines. Without all three signals, 1) antigen recognition, 2) costimulation, and 3) cytokine-mediated differentiation, T cells could become anergic or immunosuppressive. APCs present peptide-MHCI complexes to $CD8^+$ T cells, which differentiate into cytotoxic T cells, and present peptide-MHCII complexes to $CD4^+$ T cells, which differentiate into T

helper cells. T helper 1 (Th1) cells provide immunity against intracellular pathogens and require polarizing cytokine IL-12, while T helper 2 (Th2) cells provide immunity against parasites and helminths and require polarizing cytokine IL-4. There is also a third class of T helper cells, Th17, which protect against extracellular fungi and bacteria but are implicated in autoimmune diseases. APCs can also induce polarization of regulatory T cells through secretion of TGF-β and retinoic acid.

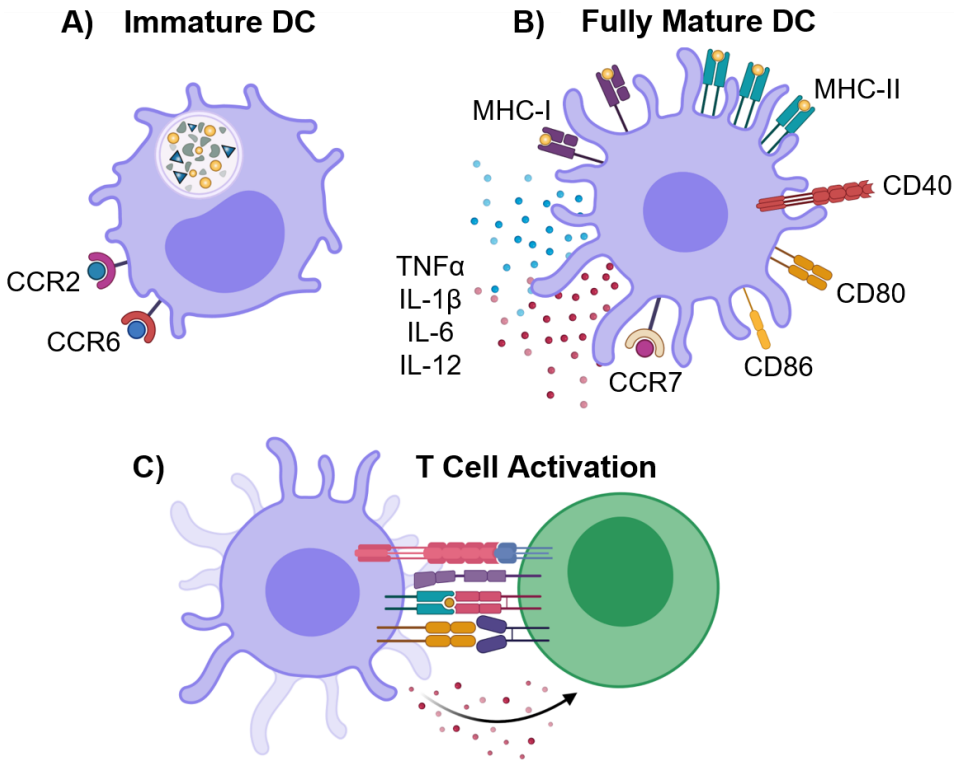

Figure 4: Mature dendritic cells express the necessary signals to activate T cells. Dendritic cell precursors and immature dendritic cells express CCR2 and CCR6 to enable recruitment from bone marrow and blood to peripheral tissues. Immature DCs have a high capacity for endocytosing and degrading pathogens, are morphologically round and smooth, and express low levels of MHC and costimulatory molecules. After engagement of PRRs and internalization of pathogens, DCs transition into a mature state, characterized by increased expression of MHC-I/MHC-II molecules, CD40 and CD80/CD86 costimulatory molecules, proinflammatory cytokines, and CCL19/CCL21 chemokine receptor CCR7. In lymph nodes, mature DCs present three signals to T cells for optimal activation: 1) MHC-antigen complex, 2) costimulatory molecules, and 3) secretion of T-cell differentiation cytokines, e.g., IL-12. Figure created with ©BioRender, biorender.com.

2.2 Pathogen Recognition Receptors

2.2.1 Toll-like Receptors

Toll-like receptors (TLRs) are a family of type I transmembrane PRRs named after the Toll proteins identified in *Drosophila melanogaster* and known for inducing antimicrobial responses when engaged.[22] There are ten functional TLRs in humans (TLRs 1-10) and twelve in mice (TLRs 1-9, 11-13), and each TLR has evolved to recognize different PAMPs and danger-associated molecular patterns (DAMPs). There are various combinations of TLRs expressed by immune cells, as well as other cell types including endothelial cells, epithelial cells, and fibroblasts; normally, pathogens will express more than one PAMP and trigger multiple TLRs on the same cell or different cells, eliciting diverse immune responses. TLRs that recognize the structural components of pathogens are expressed on the plasma membrane, and these include TLRs 1, 2, 4, 5, 6, and 10. The remaining TLRs 3, 7, 8 and 9 are expressed in the membranes of endosomes, and they recognize nucleic acids. There are some TLRs, such as TLR4, that can traffic from the plasma membrane to endosomes and signal different pathways depending on the location.

TLRs are comprised of a horseshoe-shaped N-terminal ligand binding domain, a transmembrane domain, and a C-terminal cytoplasmic signaling domain. The signaling domain of a TLR is known as the Toll IL-1 receptor (TIR) domain because of its similarity to the signaling domains of IL-1 cytokine receptors (IL-1Rs).[26] Upon ligand binding, TLRs form an "m"-shaped homodimer or heterodimer (e.g., TLR1/TLR2, TLR2/TLR6), and the TIR domains dimerize to initiate downstream signaling cascades.[27] TIR dimers recruit two different adaptor protein pairs: MyD88/MAL and TRIF/TRAM. Most TLRs signal through

the MyD88 pathway, which activates NFκB and induces the transcription of genes for pro-inflammatory cytokines including TNF-α, IL-1β, and IL-6. For TLRs 7-9, the MyD88 pathway also activates IRF7, which results in the production of IFN-α and IFN-β. TLRs that signal through the TRIF pathway (TLR3 and TLR4) activate IRF3, which induces expression of IFN-β.

TLR4 is one of the most studied TLRs and is expressed by several types of the immune cells including DCs and macrophages. TLR4 recognizes many microbial membrane components including mannans (e.g., on *C. albicans*), glycoinositol phospholipids (e.g., on *T. cruzi*), and viral envelope proteins (e.g., on RSV).[28–30] TLR4 also binds endogenous antigens released from damaged tissue including fibrinogen, heat shock proteins, and minimally modified low-density lipoproteins.[31] The most widely recognized ligand of TLR4 is lipopolysaccharide (LPS), a cell wall component of Gram-negative bacteria (e.g., *Salmonella minnesota R595*) (Figure 5). The composition of LPS varies between different bacteria, but the most conserved component is the lipid A moiety, an amphipathic lipid with a variable number of fatty-acid chains per molecule.[32] When Gram-negative bacteria enter the body they release LPS fragments from the cell wall as they grow or when they are destroyed. If LPS fragments enter the bloodstream, they activate cells via TLR4 throughout the body, causing systemic inflammation and inducing septic shock in humans. $TLR4^{-/-}$ mice are resistant to LPS-induced shock; however, they are not able to mount an adaptive immune response against bacteria.[22] TLR4 activation via LPS requires two accessory proteins – CD14, which acquires LPS from LPS-binding protein in the blood and extracellular fluid, and MD-2,which associates with the curved N-terminal domain and dimerizes TLR4.[33] The binding of TLR4 at the plasma membrane activates the MyD88

pathway and induces robust IL-12p70 production as well as enhances Th1 cellular and humoral responses.[34] CD14 mediates endocytosis of TLR4, which results in TRIF-dependent signaling from the endosome and activation of IRF3/7. CD14-dependent internalization of LPS can be bypassed by incorporating LPS into particles, which are taken up by phagocytosis.[9]

TLR2 recognizes many of the same structural PAMPs as TLR4 but instead forms heterodimers with other TLRs. For example, when binding to diacylated lipoproteins, such as lipoteichoic acid on Gram-positive bacteria, TLR2 complexes with TLR6.[35] When binding to triacylated lipoproteins (e.g., on *M. penumoniae*) TLR2 complexes with TLR1 which contains a hydrophobic channel capable of binding the third acetylated chain.[36] Both heterodimers lead to MyD88 and MAL-dependent activation of NFκB/AP-1 and secretion of proinflammatory cytokines. It is possible that TLR2 forms a homodimer but may not be functional because the TIR domains are too far apart to dimerize and initiate signaling.[37] TLR2 also complexes with CD14. Studies have shown when macrophages lack CD14, TLR2 signaling is greatly reduced.[38,39] TLR5 is a surface TLR that recognizes bacterial flagellin and is constitutively expressed in epithelial cells and immune cells, including monocytes and conventional DCs (cDC2 subset). TLR5 expression by intestinal epithelial cells is especially important for sensing gut microbiota that have breached mucosal barriers.[40] TLR10 has been shown to form a heterodimer with TLR2 but negatively regulates MyD88-dependent and independent TLR signaling.[41] Mouse TLR11 and TLR12 recognize profilin, while TLR13 recognizes bacterial 23S ribosomal RNA.[42,43]

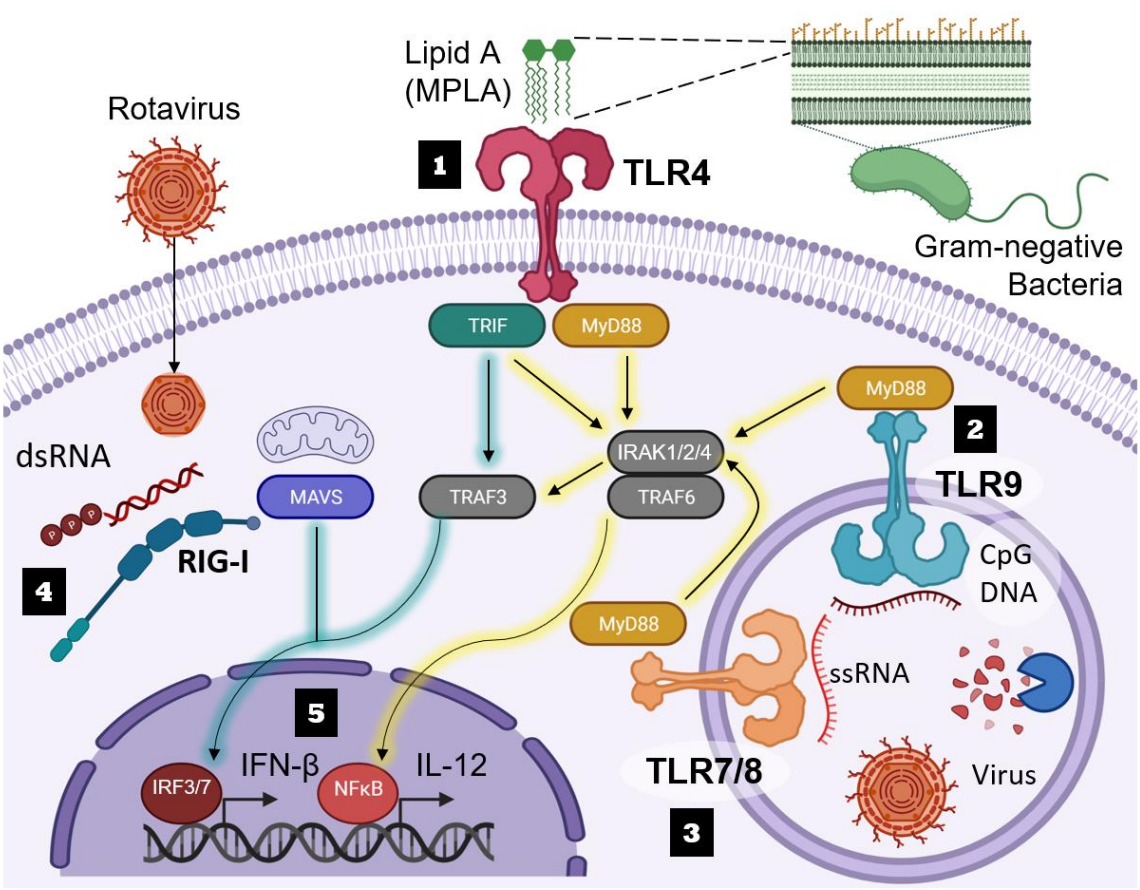

Figure 5: Toll-like and RIG-I-like receptor signaling. 1) Monophosphoryl lipid A, a moiety present in Gram-negative bacterial cell walls, binds to TLR4, which triggers the MyD88 pathway from the plasma membrane and TRIF pathway from endosomes. 2) TLR9 binds to CpG DNA released from bacteria and viruses in endosomes and signals the MyD88 pathway. 3) TLR7 and TLR8 bind to ssRNA in endosomes and triggers the MyD88 pathway. 4) RIG-I, a cytosolic receptor, recognizes dsRNA and activates adaptor protein MAVS on mitochondria or peroxisomes. 5) MyD88 signals IRAKs and TRAF6 (yellow arrows), while MyD88 and TRIF signal TRAF3 (green arrows), to activate transcription factors in the nucleus. IRF3/7 and NFκB regulate the transcription of genes associated with type I interferons and pro-inflammatory cytokines, respectively. MAVS signaling also activates IRF3 and IRF7. Figure created with ©BioRender, biorender.com.

Nucleic acid-sensing TLRs 3, 7, 8, and 9 strategically localize in endosomes to detect RNA and DNA liberated from degraded pathogens, and to limit activation by self-nucleic acids that are abundant in extracellular fluid.[34] TLR3 recognizes double-stranded RNA (e.g., from rotavirus), but may also be activated by messenger RNA released from dying host cells.[44] Polyinosinic:polycytidylic acid (Poly(I:C)) is a synthetic analog of dsRNA

commonly used to study TLR3 function. TLR3 is expressed by human DCs (cDC1) and intestinal epithelial cells, but is low or absent in monocytes, neutrophils, and lymphocytes.[45] TLRs 7 and 8 recognize single-stranded RNA (e.g., from flavivirus), particularly with poly-U or GU-rich sequences. They can be activated by synthetic imidazoquinolines including imiquimod (R837) and resiquimod (R848) as well as guanosine analogues (e.g., loxoribine). TLRs 7 and 8 are highly expressed in intestinal tissues, indicating they play a role in host defense against intestinal infections.[45] DCs and macrophages are the main cell types with TLR7/8, though human airway epithelial cells and cardiac cells have been shown to upregulate these receptors during infection.[46] TLR9 recognizes single-stranded DNA, and current dogma suggests that TLR9 discriminates self-DNA from non-self-DNA by recognizing unmethylated CpG motifs common to bacteria and viruses. However, contradictory results have shown that TLR9 senses natural, unmodified ssDNA in the endosome in a CpG-independent manner.[47] TLR9 is expressed constitutively in human B cells and pDCs, but is low or absent in monocytes/macrophages, T cells, NK cells, or cDCs.[45] In mice, TLR9 is expressed by myeloid DCs.[48]

Nucleic acid-sensing TLRs require interaction with transmembrane chaperone, UNC93B1, for exiting the endoplasmic reticulum. TLR9 is transported via UNC93B1 to the cell surface, then interacts with AP-2 to trigger endocytosis and trafficking to endosomes, where asparagine endopeptidase and cathepsins proteolytically cleave it to an active form.[49] TLR7 is not trafficked to the cell surface and instead associates with AP-4 in the Golgi complex, which delivers TLR7 directly to endosomes. Hijacking these trafficking pathways could enable recruitment of TLRs to distinct endosomes with unique signaling properties and tailor the immune response. For example, CpG Type A ODN signals TLR9

in early endosomes and recruits IRF7, leading to a type I IFN response. In contrast, CpG B ODN signals TLR9 in late endosomes and induces activation of NFκB and secretion of proinflammatory cytokines.[50] A method for tailoring endosomal delivery could be delivering TLR agonists on different sized polymeric particles. One study showed delivery of CpG ODNs on microparticles, which localize in early endosomes, stimulated IL-6 secretion, while CpG on nanoparticles, which localize in late endosomes, stimulated production of both IL-6 and IFN-α.[51]

2.2.2 RIG-I-like Receptors

Retinoic acid inducible gene (RIG)-I-like receptors (RLRs) are unbound intracellular receptors in the cytosol that recognize foreign nucleic acids. They are strategically located in the cytosol to survey for intracellular pathogens. RLRs recognize double-stranded RNA, a replication intermediate for RNA viruses, that exhibits viral motifs such as an uncapped 5' diphosphate or triphosphate end.[8] The best characterized RLRs are RIG-I and MDA5, which recognize different lengths of dsRNA: RIG-I selectively binds to short dsRNAs while MDA5 primarily recognizes long dsRNA.[52] The poly-uridine core of Hepatitis C Virus, poly-U/UC (PUUC), activates RIG-I and triggers potent anti-HCV responses.[53] Transfected poly(I:C) is also sensed by RIG-I/MDA-5, unlike naked poly(I:C) which is recognized by TLR3.[54] RIG-I and MDA5 contain N-terminal caspase activation and recruitment domains (CARDs) that relay signal to downstream signaling adaptor MAVS (mitochondrial antiviral-signaling protein).[55] MAVS signaling at the mitochondria activates IRF3 and induces type I IFN while signaling at peroxisomes activates IRF1/IRF3 and induces type III IFN and expression of interferon-stimulated genes (ISGs).[56,57] Signaling at both locations also triggers recruitment of TRAF2/TRAF6 which leads to

activation of NFκB.[55,58] The RLR signaling pathway can also limit viral replication by initiating a form of cell death called pyroptosis.[59]

2.3 APC Subsets and their Functions

In the late 19th century, Ilya Metchnikoff discovered the phagocyte system, comprised of cells he termed macrophages (Greek for "large eaters") and microphages ("small eaters"), now known as polymorphonuclear leukocytes (i.e., neutrophils, eosinophils, and basophils).[60] Later, a specialized macrophage with long finger-like membrane protrusions (i.e., dendrites) was discovered and thought to be pivotal in the production of antibodies. In the 1970s, Ralph Steinman and colleagues performed studies with the “dendritic macrophages,” now distinctly classified as dendritic cells, and found they expressed high levels of MHC molecules and were potent inducers of T cell activation in mixed leukocyte reaction (MLR) assays.[61] Currently there are several different subsets of dendritic cells, as well as other members of the mononuclear phagocyte system (i.e., monocytes and macrophages), that have been defined by their lineage, morphology, surface marker expression, and function.

Dendritic cells originate from hematopoietic stem cells (HSCs) in the bone marrow. The downstream progeny of HSCs includes common myeloid progenitors (CMPs) and common lymphoid progenitors (CLPs).[62] Adoptive transfer of CLPs and CMPs into irradiated mice (radiation ablates host bone marrow cells) produces DCs in mice, and similarly human CLPs and CMPs differentiate into DCs in vitro.[63] However, the contribution of CLPs to DC populations remain unclear while CMPs are more widely studied.[64] CMPs give rise to granulocyte-macrophage progenitors (GMPs), which differentiate into macrophage-

dendritic progenitors (MDPs), which develop into common monocyte progenitors (CMoP) and common dendritic cell progenitors (CDPs). CDPs have lost monocyte and macrophage-differentiation potential and give rise only to cells in the DC lineage. It is from here that CDP branch into different lineages resulting in two main functional DC types: conventional DCs (cDCs) and plasmacytoid DCs (pDCs). In this section we will discuss cDCs and pDCs as well as other APCs integral to the adaptive immune response: monocyte-derived DCs, macrophages, and B cells.

2.3.1 Conventional DCs

In the bone marrow, CSF-1R$^+$ CDPs give rise to pre-DCs, which circulate through the blood to reside in lymphoid organs (e.g., spleen, lymph nodes) and non-lymphoid tissues (e.g., skin, lung, liver, kidney, intestines).[65–67] In these tissues, pre-DCs differentiate further into conventional DCs, with the superior potential to process and present antigen, migrate to lymph nodes in steady and inflamed states, and prime naïve T cell responses. Traditionally, expression of MHCII and integrin alpha X chain (i.e., CD11c) have been used to define cDCs. However, with the advent of multiparameter flow cytometry, CyTOF technology and RNA sequencing, it has become evident that these markers alone are not sufficient for precisely identifying cDCs, as the molecules are shared by multiple macrophage subsets.[64] Conventional DCs have been grouped into two main subsets, cDC1 and cDC2, which can be further subdivided based on additional surface markers and the tissues in which they reside.

In all tissues, the cDC1 subset is highly proficient at cross-presenting exogenous peptides on MHC-I molecules to activate CD8$^+$ T cells and induce cytotoxic immune responses.

cDC1 in the spleen and dermis also are a critical source of IL-12, which is required for differentiation of $CD4^+$ T cells into Th1 cells.[68,69] Transcription factors Batf3, ID2, Nfil3, and Irf8 are all involved in cDC1 development and survival. Short-term development of cDC1 was observed in the absence of ID2, Nfil3, and Batf3, suggesting that Irf8 is the master regulator of cDC1 lineage development.[70] Even so, $Baft3^{-/-}$ mice are deficient in cDC1 and show no changes in cDC2 populations.[71] Due to cDC1 deficiencies in the dermis and secondary lymphoid tissues, $Baft3^{-/-}$ mice are unable to mount CD8+ T cell responses against influenza virus and West Nile virus, and fail to generate adequate Th1 responses against *Toxoplasma gondii* and *Candida albicans*.[68,69,72,73] In mice, all cDC1 tissue subsets express Clec9A, CD24, DEC-205, and XCR1. Several studies have shown that TLR3 is preferentially expressed in cDC1 and promotes cross-presentation.[74] In the skin, lung, and intestine, cDC1 express CD103 and are $CD11b^{-/lo}$, while lymphoid cDC1 are $CD8\alpha^+$ and $CD103^{+/-}$. $CD103^+CD8\alpha^+$ lymphoid cDC1 are not well characterized but have been found in the marginal zone of lymph nodes as well as in intestinal draining lymph nodes (i.e., mesenteric LNs).[75–78] The human homolog to mouse cDC1 are $CD141^+$BDCA-3^+ DCs.[79]

In contrast with cDC1, cDC2 subsets excel at activating $CD4^+$ T cells and inducing Th2 and Th17 responses due to increased expression of proteins involved in MHC-II processing.[79,80] Studies have shown cDC2 were required for Th2 responses against *Schistosoma mansoni* and dust mite allergens as well as Th17 responses against *Aspergillus fumigatus* infection in the lung.[81–83] Dermal cDC2 produce the vitamin A metabolite retinoic acid, which promotes the generation of $Foxp3^+$ regulatory T cells.[84] Activation of lymphoid $CD4^+$ cDC2 with TLR7 agonists can induce secretion of type I associated cytokines, and antigen targeting via DCIR2 in combination with TLR3 agonist poly(I:C)

elicits protective $CD8^+$ T cell responses against tumors.[85,86] cDC2 are the most abundant type of DC in the skin and share many phenotypical characteristics with macrophages and monocyte-derived DCs, especially in a state of inflammation.[87] cDC2 are distinguished from other APCs based on their expression of IRF4, CD11b, and CD172a (SIRPα). Irf4-deficient mice completely lack cDC2 in some tissues, while in other tissues cDC2 are short-lived and cannot migrate to draining lymph nodes.[64,88] According to one study, a group of migratory cDC2 known as $CD301b^+$ DCs were required for transporting antigen injected subcutaneously with Th2-type adjuvants.[89] Depletion of $CD301b^+$ DCs led to decreased expression of CD69 by $CD4^+$ T cells in lymph nodes, dampened IL-4 production by OVA-specific OT-II transgenic $CD4^+$ T cells, and impaired Th2 cell development upon infection with *Nippostrongylus brasiliensis.* Surprisingly, depletion of $CD301b^+$ has also enhanced the development of T follicular helper (Tfh) cells, germinal center B cells, and antibody responses against protein antigens. CD301b+ also express high levels of programmed death ligands PD-L1 and PD-L2, and blocking these ligands also suppressed Tfh cells.[90]

2.3.2 Monocyte-derived DCs

Unlike cDCs which arise from pre-DCs, monocyte-derived DCs (mo-DCs) differentiate from $Ly6C^{hi}$ monocytes recruited to tissues in response to inflammation; therefore, they are also referred to as inflammatory DCs. During differentiation, mo-DCs gradually lose Ly6C expression while acquiring MHC-II expression, and are difficult to distinguish from macrophages because they share the receptors F4/80, CD64, CD11b, and CD206.[91] The function of mo-DCs in regulating adaptive immunity is not clear-cut. Research has shown that mo-DC are inferior to cDC2 in migrating to lymph nodes and activating T cells after stimulation with the hapten dinitrofluorobenzene, yet mo-DCs are required for the

activation of CD8+ tissue resident memory (Trm) cells after HSV-1 infection.[87,92] One study found after subcutaneous immunization with fungal antigens, Ly6C$^+$ Mo-DCs were the first antigen-bearing cells to reach lymph nodes, but failed to prime T cells. It was proposed that migrating mo-DCs transfer antigen to lymph node-resident cDCs, which subsequently induce T cell proliferation.[93] In some inflammatory settings, mo-DCs become TNF- and iNOS-producing DCs (i.e., Tip-DCs) with potent antimicrobial effector functions. Tip-DCs were found to be essential for clearing bacterial infection but not for T cell priming.[94] A recent work has suggested that Ly6C$^+$ monocytes can enter steady-state non-lymphoid tissues, upregulate MHC-II expression, and migrate to lymph nodes without differentiation to macrophages or DCs.[95]

2.3.3 Plasmacytoid DCs

Plasmacytoid DCs are a rare, long-lasting population of immune cells that make up 0.3-0.5% of human PBMCs. They are the primary producers of type I interferon (IFN-α, IFN-β) during a viral infection and secrete up to 1000x more IFN compared to other cell types. pDCs also secrete TNF-α and IL-12. pDCs effectively couple viral recognition by TLRs (TLR7, TLR9) and RLRs to the production of interferon, which is generated by infected pDCs or uninfected pDCs detecting virus from neighboring cells. IFN-α secretion in response to TLR9 ligand CpG is mediated exclusively by pDCs. The most documented phenotype of pDCs is a high expression of B220, low to moderate expression of MHC-II, and low to negative expression of CD11c. Humans pDCs express ILT7, IL3Rα, BDCA-4, and inhibitory receptor BDCA-2. Mouse pDCs express receptors Siglec-H (inhibitory), Bst2 (i.e., CD317/PDCA-1), and Ly49Q, as well as signaling protein IRF7 and transcription factor Runx2. Receptor Ly49Q was found to be required for optimal IFN

production in pDCs, while Bst2 is an IFN-inducible membrane protein that direct inhibits viral replication. pDCs are directly recruited from blood to lymph nodes through expression of CXCR3, which is a chemokine receptor for T cell-produced chemokines CXCL9, CXCL19, and CXCL11.

pDCs are known to present antigen to T cells and upregulate costimulatory molecules in the presence of viral PAMPs and antigens. It is hypothesized that pDC IFN secretion and pDC maturation may be separate fates of pDCs, and pDCs differentiate into $CD8\alpha^+$ cDCs in the lymph node upon viral activation. During pDC activation, E2-2 expression is downregulated, while Id2, a transcription factor of cDC1, is upregulated. Mature pDCs prime $CD8^+$ T cells as well as $CD4^+$ T cells and induce Th1 polarization. pDC activity in humans has been most studied in cases of HIV and Hepatitis C infection. pDCs respond to HCV hepatocytes through TLR7 and RIG-I signaling. In the case of HIV, the virus infects pDCs and drives IFN secretion, which may cause T cell hyperactivation and depletion and contribute to immunodeficiency. It is also hypothesized that HIV infects and depletes pDCs or infected pDCs pass on virus to T cells, leading to poor cellular immune responses. In a mouse model of lung RSV, pDC depletion leads to increases in viral titers and exacerbated tissue pathology, and while in a model for hepatitis virus, pDC depletion nearly abolishes IFN response to MHV, which requires TLR7 signaling and type I interferon for viral clearance.

2.3.4 Macrophages

Macrophages are highly phagocytic cells that primarily reside in tissues. Different inflammatory stimuli cause macrophages to modify their metabolic function and polarize

toward a M1 or M2 phenotype.[96] M1 macrophages are key effector cells for eliminating pathogens, infected cells, and cancer cells. M1 macrophages produce toxic molecules (e.g., ROS and NO), proinflammatory cytokines (e.g., IL-1β, TNF-α, and IL-6), as well as Th1/Th17-polarizing cytokines (e.g., IL-12, IL-23). M2 macrophages maintain tissue integrity by eliminating or repairing damaged cells and tissue matrices. M2 macrophages produce ornithine, which promotes cell proliferation and tissue repair through polyamine and collagen synthesis, or fibrosis. There are distinct macrophage populations that load extracellular antigen onto MHC-II, upregulate costimulatory molecules CD80/CD86, and prime $CD4^+$ T cells toward a Th1/Th2 phenotype.[97] DCs may be more efficient at activating T cells because they have limited lysosomal proteolysis compared to macrophages, preventing internalized antigens from being degraded prior to encountering T cells in the lymph node.[98]

Tissue macrophages have a dual origin involving both embryonic and adult hematopoiesis. Some macrophages, including liver Kupffer cells and brain microglia are established prior to birth and self-renew without adult hematopoiesis. Other macrophages, particularly those in the lamina propria of intestines or red pulp of the spleen, continuously derive from circulating $Ly6C^{hi}$ monocytes. Due to their overlapping phenotypes, it is difficult to distinguish macrophages from cDC2 and mo-DCs within most tissues and evaluate their exact contribution to immune responses. Markers used to differentiate macrophages include CD11b, CD14, CD68, CD64, CD115, EMR-1 (human), F4/80 (mice), and CD206 (M2 Mφ). Macrophages also express low to intermediate levels of CD11c and MHCII.

There are many tissue-specific macrophage subsets with unique functions. The lymph node sinus is lined with $CD169^+CD11b^+CD11c^{lo}$ macrophages that prevent systemic

dissemination of pathogens by clearing microbes entering the afferent lymph. They have low endocytic potential, and therefore retain antigen on their surface and promote antigen presentation of viral antigens to B cells.[99] Medullary macrophages efficiently phagocytose and degrade opsonized antigens and particulates from the lymph. Alveolar macrophages, previously thought to be restricted to the alveoli, have been discovered transporting antigen from the lung to draining lymph nodes immediately following exposure to Streptococcus pneumonia.[100]

2.3.5 B Cells

B cells develop in the bone marrow and continuously circulate through secondary lymphoid organs. They enter lymph nodes through HEVs and localize within the cortical region near the subcapsular sinus. Though many antigens do not enter the body as soluble molecules during an infection, there are some natural immunogens that do, including: insect toxins, anti-coagulants, snake venoms, and many allergens.[22] B cells are uniquely adapted to bind to specific soluble molecules through their cell-surface immunoglobulin (Ig). There is also evidence they can pick up antigen from other APCs in the lymph node, including subcapsular sinus macrophages and follicular dendritic cells.[99,101] B cells are able to internalize molecules and form peptide:MHCII complexes, which they constitutively express, allowing them to be targeted by antigen-specific $CD4^+$ T cells. They also can upregulate costimulatory molecules in the presence of microbial stimuli. Dendritic cells play a larger role than B cells in priming naïve T cells because they have a greater capacity for endocytosing, degrading, and processing whole pathogens for acquiring peptide antigens. DCs also have a broader range of MHC molecules and antigen specificity and therefore are more likely to be recognized by a wide range of T cells. After T cells have

been activated and undergone clonal expansion, the chances of encountering a matching antigen-specific B cell greatly increase.

2.3.6 In Vitro Models of APCs

In 1992, Inaba et al. published a novel method for generating DCs from murine bone marrow cultures with GM-CSF.[102] Shortly thereafter, Sallusto et al. reported that a combination of GM-CSF and IL-4 was most efficient at differentiating human peripheral blood monocytes into DCs with high expression of CD1, MHC-II, and costimulatory molecules.[103] Ever since there has been speculation on whether IL-4 is necessary to induce DC maturation in murine bone marrow cultures, and numerous studies on DC behavior *in vitro* have been completed with BMDCs generated with GM-CSF alone or with IL-4.[104,105] There was a recent study demonstrating both GM-CSF and GM-CSF+IL-4 cultures contain not only conventional DCs, but monocyte-derived macrophages as well.[106] In 2000, Brasel et al. developed a FLT3L-dependent bone marrow culture system that generated cells sharing morphological characteristics with a more diverse range of DC subsets, including pDCs and lymphoid tissue-resident cDCs.[107]

2.4 PRR Agonists as Vaccine Adjuvants

Many pathogens can be eliminated by host immunity but there are some dedicated pathogens that have developed highly specialized mechanisms for evading immune responses, as well as eliciting host responses that contribute to their survival and replication. Therefore, they require help from treatments specially designed to prevent infection, primarily vaccines. Today there are several different types of vaccines, including those with live-attenuated pathogens, inactivated/killed pathogens, or inactivated toxins.

Comprised of recombinant proteins or synthetic peptides, subunit vaccines offer advantages over live-attenuated and inactivated vaccines in terms of safety, ease of manufacture, and precise immune targeting. However, the purified protein-based antigens in subunit vaccines require additional material that trigger the nonspecific innate immune signaling pathways that precede antigen-specific immune responses. The immunogenic supplement is termed an adjuvant, from the Latin word *adjuvare* meaning 'to help,' because it enhances the response to an antigen.

In the 1920s the first adjuvant included in a human vaccine was aluminum salt (i.e., alum), which remains the most popular adjuvant in use today. Alum mainly stimulates Th2 immune responses, potentiating IgG1 and IgE antibody production, which does not confer the best protection for viral infections, including HCV and HIV.[55] Other well-established adjuvant are AS03 and MF59®, squalene-based oil-in-water emulsions that trigger balanced Th1/Th2 responses and are currently used in influenza vaccines.[108] The precise modes of action of alum and emulsion-based adjuvants remain unclear, but the most widely accepted theory is they form a "depot effect" and retain antigen at the injection site to prolong immune responses. Another hypothesis is alum activates the Nalp3 inflammasome pathway to promote Th2 immunity.[109] The current challenge is to develop adjuvants with well-defined mechanisms of action that induce strong Th1 and CTL-mediated immune responses, which is important for developing vaccines to protect against cancer and infectious diseases such as HIV or dengue.[110–112] PRR activation triggers production of pro-inflammatory cytokines and type I interferons that coordinate the elimination of pathogens and infected cells; therefore, natural and synthetic PRR ligands have the

potential to be effective vaccine adjuvants. A number of these agonists are approved for use, in clinical trials and in late preclinical stages of development.

2.4.1 Monophosphoryl Lipid A (TLR4)

The intact molecule of TLR4 ligand, LPS, is toxic and not suitable for use as a vaccine adjuvant.[34] MPLA is derived from the bacterial cell wall of *Salmonella Minnesota* and detoxified by mild hydrolytic treatment. It was the first defined TLR ligand to be used in licensed vaccines and achieve clinical and regulatory success. It is a component in two approved adjuvant systems developed by GlaxoSmithKline: 1) AS01, a liposome-based adjuvant containing 3-O-desacyl-4'-MPLA and saponin QS-21, and used in the malaria vaccine, RTS,S (Mosquirix) and 2) AS04, an adjuvant combining MPLA with aluminum salt, and currently used in vaccines against HPV (Cervarix) and HBV (Fendrix).[10,113,114] Preclinical and clinical studies have shown MPLA improves Th1 immunity and induces production of IgG2a antibodies.[115] Fendrix with AS04 induced higher seroprotection rates and antibody titers compared to licensed, alum-based HBV vaccine Engerix-B® in clinical trials and required one less shot; it is now approved in Europe.[34] Cervarix with AS04 induced significantly higher anti-HPV16 and anti-HPV18 L1 antibody responses compared to the same vaccine with alum.[116] MPLA has also been evaluated in clinical trials as a vaccine adjuvant against many types of cancers, including melanoma (Melacine™), colorectal carcinoma, and prostate cancer (OncoVax-P).[117]

2.4.2 Imiquimod and Resiquimod (TLR7/8)

Imidazoquinolines imiquimod (R837, TLR7 agonist) and resiquimod (R848, TLR7/8 agonist) have primarily been investigated for use as topical agents to treat skin conditions

and cancer. Imiquimod (brand name Aldara™, 3M) is currently licensed for topical use to treat anogenital warts, superficial basal cell carcinoma and precancerous growths (actinic keratoses).[118] Imiquimod has been tested in Phase I/II clinical trials with cancer vaccines against chronic myeloid leukemia, vulval cancer, and prostate cancer.[119–121] Skin biopsies in a clinical trial for an intradermal melanoma NY-ESO-1 subunit vaccine showed imiquimod significantly enhanced infiltration of T cells, APCs, and NK cells.[34,122] Resiquimod was also evaluated as topical adjuvant for NY-ESO-1 protein vaccines and induced strong $CD4^+$ T cell responses in the majority of patients, as well as $CD8^+$ T cell responses in some patients.[123] Generally, topical administration of imidazoquinolines is well tolerated, but severe side effects arise with oral or systemic use in humans. In a clinical study of oral resiquimod for treating chronic HCV infection, subjects receiving 0.2 mg/kg of resiquimod reported adverse events including fever, headache, shivering and lymphopenia. This was due to the high secretion of IFN-α, which correlated with decreases in viral titer as well as lymphocyte counts, and increases in neutrophil counts.[124] Repeated application of imiquimod can also lead to psoriasis-like skin inflammation, propagated by cDC2 and double-negative DCs that secrete IL-23 and γδ T cells secreting IL-17.[125] If imidazoquinolines are to be administered non-topically, delivery will have to be optimized to prevent systemic toxicity and adverse effects.

2.4.3 CpG Oligodeoxynucleotides (TLR9)

CpG ODNs are short synthetic single-stranded DNA molecules containing unmethylated CpG motifs. They are composed of phosphorothioate nucleotides, which are more resistant to nucleases than natural phosphodiester nucleotides found in genomic bacterial DNA.[34] There are three types of CpG ODN, including Class A (Type D), Class B (Type K) and

Class C. CpG-A ODNs possess a mixed phosphodiester/phosphothioate backbone and contain a single CpG motif flanked by palindromic sequences and 3' poly-G string. They trigger high production of IFN-α by pDCs but are weak stimulators of TLR9-dependent NF-κB signaling and proinflammatory cytokine production. CpG-B ODNs contain one or more CpG dinucleotides on a phosphorothioate backbone. They efficiently stimulate B cells to produce IgM and IL-6, and trigger pDC to produce TNF-α but weakly stimulate IFN-α secretion. CpG-C ODNs also contain a complete phosphorotioate backbone like CpG-B ODNs and palindromic CpG motif like CpG-A ODNs. They induce strong IFN-α production by pDCs and stimulate B cells. CpG ODN-driven activation of $CD8^+$ T Cells is stronger in mice compared to humans, which may be because TLR9 expression in humans is restricted to pDCs and B cells while in mice, TLR9 is also expressed on cross-priming cDCs.[126] Clinical trials examining TLR9-based adjuvants have focused on CpG-B ODN, including vaccine trials for malaria, influenza, and anthrax.[127–130] In 2017, Heplisav-B, a vaccine that contains CpG 1018, was approved by the FDA for the prevention of Hepatitis B in people 18 years and older.[11]

2.4.4 RIG-I-Like Receptor Ligands

RLR agonists trigger antiviral immunity and have the potential to be used as pan-antivirals, vaccine adjuvants and antitumor agents. SB9200 is a nucleotide-based RLR ligand that has been tested in clinical trials for treating chronic Hepatitis B and Hepatitis C. Used in combination with Entecavir, SB2900 reduced viremia and delayed recrudenscence of viral replication in woodchucks infected with woodchuck hepatitis virus (WHV).[131] 5'pppRNA confers protection again vesicular stomatitis virus, vaccinia virus, and dengue virus in lung epithelial cell culture (A549), and treating mice with 5'pppRNA prior to influenza virus

challenge reduces incidence of pneumonia.[132] 5'pppRNA with a uridine-rich sequence and 99-nucleotide hairpin (M8) specifically activates RIG-I and was used in conjunction with virus-like particles expressing H5N1 hemagglutinin and neuraminidase proteins.[133] Vaccination with M8 increased the survival rate of H5N1-challenged mice, simulated Th1 immunity, and generated higher antibody titers than other adjuvants, including alum, AddaVax, and Poly(I:C).[134]

2.4.5 Combination Adjuvants

There are a few FDA-approved combination adjuvants containing PRR ligands - for example, AS01 and AS02 contain MPL and QS-21 while AS04 is MPL adsorbed onto aluminum salts.[135] Live-attenuated tuberculosis vaccines BCG and CADI-05 target TLR2/TLR4 and TLR2/NOD2, respectively; however, live-attenuated vaccines have a lower safety profile for patients and manufacturers.[136,137] To date there are no approved combination adjuvants with two or more non-endogenously expressed PRR ligands that could be used with subunit or nucleic acid-based vaccines.

There have been multiple preclinical studies with combinations of PRR agonists. Early in vitro studies conducted by Napolitani et al. revealed stimulation of human mo-DCs TLR4 and TLR7 agonists enhanced proinflammatory cytokine production compared to stimulation with single TLR agonists.[13] Another study showed IL-12p70 production by human PBMCs required combined stimulation of TLR7/8 with TLR4 or TLR3.[138] The stimulation of GM-CSF/IL-4 BMDCs on TLR3 and TLR7/8 agonists enables induction of CTL-mediated responses against colon tumor cells in mice, while stimulation of TLR2 plus TLR3 on FLT3L BMDCs enhances CD4+ and CD8+ T cell immunity against tumor

challenge.[17,139] CD8+ T cell responses are enhanced by targeting DNA-encoded antigen HIV-1 Gag to DEC205 on APCs with CpG and Poly(I:C), and simultaneous administration of TLR2, TLR3, and TLR9 ligands increased CD8+ T cell responses and conferred protection against HIV challenge in mice.[140,141] Combination adjuvants also improve humoral responses. Carter et al. observed the highest diversity of antibody responses against *Plasmodium vivax* antigen PvRII was observed in animals immunized with vaccines containing both TLR4 and TLR7/8 agonists.[142]

2.5 Vaccine Delivery to Lymph Nodes

2.5.1 Particle-Based Vaccine Delivery

There are major deficiencies associated with using soluble antigens and adjuvants for immunization including their vulnerability to extracellular protease degradation, rapid lymphatic clearance, and high levels of systemic exposure and toxicity.[143,144] Delivering soluble adjuvants limits their effective dosages and ratios in formulation, preventing optimal stimulation of immune cells at the site of injection.[145] To synergize innate immune cell activation with antigen uptake, adjuvants and antigens are strategically co-delivered in the same vector.

Poly(lactic-co-glycolic acid) (PLGA) particles are popular vaccine delivery vehicles because they allow for both encapsulation and surface loading of antigens and adjuvants. PLGA is biodegradable, so contents are slowly released over time at the site of injection to sustain immunity over a longer period.[146] Scaling the size of particles to mimic pathogens is an approach to trigger endocytosis by specific APC subsets and downstream immune signaling pathways. For example, Leleux et al. studied how PLGA particle size influenced

DC subset migration to dLNs using 250 nm-sized particles to mimic the size of large viruses (200-300 nm) and 1 μm-sized particles to mimic bacteria (1-2 μm). They observed nanoparticles preferentially activated $CD103^+$ cDC1, a hallmark of viral infection.[147]

There is a significant amount of literature on how size affects particle trafficking to dLNs through passive drainage or immune cell-mediated transport.[148–150] After subcutaneous or intradermal injection, particle vaccines in the 20 to 100 nm size range preferentially drain to lymph nodes while smaller molecules disseminate to systemic circulation and larger particles stay in the tissue.[146] Particles 20-50 nm are less hindered by convection through the ECM due to its mean mesh size of 50 nm.[151] This concept was recently challenged by published work showing rapid lymphatic drainage (seconds to minutes) of 1 μm-diameter microspheres. They attributed the phenomena to breaches of peripheral skin that occur during common microbial infections and are independent of injection-induced hydrodynamic fluxes.[148]

2.5.2 Dendritic Cell Migration Through Lymphatic Vessels

Lymphatic endothelial cells (LECs) secrete chemokines CCL19 and CCL21 and express adhesion molecules (e.g., ICAM-1 and E-selectin) to guide DC migration from lymphatic capillaries to dLNs. CCL19 and CCL21-Ser are secreted by LECs and stromal cells in the thymus and secondary lymphoid organs, while CCL21-Leu is secreted by LECs in peripheral tissues. CCL19 is also secreted by mature DCs during autocrine signaling.[152,153] These chemokines bind to DCs through receptor CCR7, which has been implicated in a diverse set of immune signaling pathways including: the survival of mature DCs, the polarization of Th17 cells by splenic DCs, the activation of endocytosis and migration of

mature DCs, and the proliferation and increased antigen presentation by BMDCs.[154] Structurally, CCL21 differs from CCL19 because it has an extra 32 amino acid C-terminus of basic amino acids and the CCR7 pathway is reported to be differentially regulated by the two ligands. For example, CCL19 inducing a higher PIK3R1 and AKT1 activation in mature DCs compared to CCL21.[155]

A study by Johnson et al. observed that DC migration in steady state is predominantly controlled through chemotactic gradients, while in an inflammatory state DC migration is β2-integrin dependent. During inflammation, TNF-α is secreted in the periphery and stimulates a rapid burst of CCL21 released by LECs, as well as upregulation of ICAM-1 and VCAM-1. They hypothesize CCR7 signaling enhances the affinity of LFA-1 on DCs for ICAM-1, suggesting a synergistic mechanism to facilitate DC homing to dLNs during inflammation.[156] Vaahtomeri et al. observed physical contact between DCs and the lymphatic endothelium is necessary to trigger calcium signaling and release of CCL21 from intracellular vesicles from LECs. This enriches CCL21 at endothelial cell-cell junctions and creates a positive feedback loop recruiting more DCs toward lymphatic vessels.[157]

2.6 Adjuvants in SARS-CoV-2 Vaccines

Coronaviruses are enveloped positive-sense single-stranded RNA viruses. SARS-CoV-2 is a novel coronavirus that is highly transmissible and causes coronavirus disease 2019 (COVID-19), which manifests as mild symptoms to severe respiratory illness in humans.[158] The club-like spike (S) protein of SARS-CoV-2 recognizes and binds to host cell receptor angiotensin-converting enzyme 2 (ACE-2). The S protein is composed of two subunits, S1

and S2. The S1 subunit contains a receptor-binding domain (RBD) that binds to ACE-2 while S2 mediates membrane fusion and entry into the host cell.[159] The S protein is the most common antigen included in SARS-CoV-2 vaccine candidates, and most neutralizing antibodies developed against the virus react to the RBD of the S protein. The nucleocapsid (N) protein is also highly conserved and has been shown to induce cytotoxic T lymphocytes; however, the N protein also triggers pro-inflammatory cytokine production (cytokine storm) and leads to severe lung pathology.[160]

There are currently approved SARS-CoV-2 vaccines that induce potent immunological responses without additional adjuvants. For example, the adenovirus vector vaccine by Johnson & Johnson endogenously expresses viral proteins that stimulate PRRs, while the nucleic acids in the Moderna and Pfizer mRNA vaccines intrinsically engage innate immune receptors. A few adjuvants have been formulated for subunit or inactivated antigens including aluminum salts, emulsions, and TLR agonists.[161] PiCoVacc, an inactivated SARS-CoV-2 virus vaccine, was administered with alum in rhesus macaques and was successful in producing anti-S protein, anti-RBD, and anti-N protein IgG titers; however, CD4+ and CD8+ T cell activation and expansion did not occur up to 29 days after vaccination.[162] Inactivated vaccine candidate, BBIBP-CorV, delivered with alum was successful at producing neutralizing antibody titers and protection against SARS-CoV-2 in macaques but also failed to induce T cell responses.[163] Alum has also been combined with S protein subunit vaccines and plays a role in dose-sparing. In mice, an alum-adjuvanted 5-μg S protein subunit vaccine produced twice as many neutralizing antibodies as the non-adjuvanted 50-μg S protein subunit vaccine.[164] Emulsion adjuvants, including MF49 and

AS03, elicited both humoral and cellular immune responses to MERS-CoV inactivated and subunit vaccines.[165,166]

Positive-sense single-stranded RNA viruses interact with TLR7 and TLR8, and produce dsRNA replication intermediates that are recognized by RIG-I and TLR3.[167–170] TLR2 (dimerized with TLR1 or TLR6) and TLR4 have also exhibited potential to recognize viral proteins; in fact, SARS-CoV-2 S protein reportedly induces TLR4 signaling.[171–173] Zhao et al. evaluated the immune responses of peptide-specific CD8+ T cells induced by HLA-A*0201-restricted SARS-CoV S epitopes combined with TLR-targeted adjuvants CpG ODN, Poly(I:C), and R848 in mice.[174] Results showed that the frequency of SARS-CoV S peptide-specific IFN-γ^+ CD8+ T cells, which showed a memory phenotype ($CD45RB^+CD62L^-$), was the highest in response to S peptides plus CpG ODN. CpG also enhances IgG production in animals immunized with inactivated SARS-CoV vaccine.[175] Langellotto et al. reported single-shot biomaterials-based subunit vaccines consisting of GM-CSF, MPLA, and SARS-CoV-2 antigens in mesoporous silica rods rapidly generated antibodies against SARS-CoV-2 S1, S2, and N proteins with neutralizing activity.[176] Research on PRR-targeted combination adjuvants with SARS-CoV-2 antigens is limited. Liu et al. recently reported lipid nanoparticle-based subunit vaccines co-delivering S1 protein antigen, MPLA, and CpG elicited stronger CD4+ and CD8+ T cell responses in mice than unformulated S1, MPLA, plus CpG, or unformulated S1 plus alum.[177] The objective of Aim 2 in this thesis is to investigate PRR-targeting combination adjuvants delivered with S1 or S protein, specifically including the RIG-I ligand PUUC.

CHAPTER 3: AIM 1.1. INVESTIGATING HOW SOLUBLE AND PARTICLE-BASED DELIVERY OF MPLA AND CPG DIFFERENTIALLY MODULATE 3D CHEMOTAXIS OF BONE MARROW-DERIVED DENDRITIC CELLS

To rationally design a vaccine that enhances DC-mediated delivery to the lymph node, there is a need for more research into how adjuvants and other vaccine components (e.g., vaccine delivery carriers) influence DC migration. For example, there have been reports showing Th2 immunization (OVA with papain) promotes the migration of CD301b+ DCs while Th1 immunization (OVA plus LPS and poly(I:C)) promotes the migration of CD103+ dermal DCs.[178,179] The combination of TLR agonists MPLA (TLR4 ligand) and CpG DNA (TLR9 ligand), both expressed on gram-negative bacteria, have been reported to synergistically enhance DC maturation and humoral responses.[13,145,180,181] Here we assessed whether MPLA and/or CpG, delivered unformulated (herein referred to as "soluble" adjuvant) or on PLGA MPs, stimulates mouse BMDC 3D migration toward CCL19 and CCL21 in a device that maintains a stable gradient for up to 24 hours. We developed a logistic regression model to filter high volumes of cell tracking data and identify migratory cell tracks, and then applied circular statistical methods to compare the directionality of cell migration toward CCL19 and CCL21 gradients under different adjuvant conditions. Ever since the BMDC differentiation method with GM-CSF was published, there has been speculation on whether IL-4 is necessary to induce DC maturation.[102] Therefore, we sought to confirm whether IL-4 is essential for induction of CCR7 expression and migration of GM-CSF-cultured cells. Additionally, we characterized monocyte, macrophage, and DC populations in BMDC culture and their relative CCR7 expression in response to MPLA and CpG.

3.1 Materials and Methods

3.1.1 Bone marrow-derived cells (BMDCs)

All animal experiments were conducted in accordance with protocols approved by the Institutional Animal Care and Use Committee (IACUC) at Georgia Institute of Technology (Protocol reference #A100207). Bone marrow was collected from femurs and tibiae of female C57BL/6J mice 5 to 10 weeks old (Jackson Laboratory). Red blood cells were lysed with RBC Lysis Buffer (Invitrogen), and remaining cells were plated at 1 million cells/mL in 12 mL RPMI complete medium (Gibco) in a 100-mm tissue culture-treated petri dish (Corning). RPMI complete medium contained characterized fetal bovine serum (10% v/v) (HyClone), penicillin-streptomycin (1% v/v) (HyClone), sodium pyruvate (1 mM) (Gibco), MEM non-essential amino acids (1X) (Gibco), 2-mercaptoethanol (55 µM) (Gibco), GM-CSF (20 ng mL^{-1}) (Peprotech), and IL-4 (10 ng mL^{-1}) (Peprotech). GM-CSF-only BMDCs were prepared identically except without IL-4 in the media. Cells were cultured in a humidified incubator at 37°C with 5% CO_2. Half of the media (6 mL) was removed and replaced with fresh media on days 2 and 4. Half of the media volume (6 mL) was added on day 6 (for total of 18 mL) with cytokine concentrations maintained. Loosely adherent cells were collected by vigorous pipetting on days 6-7 for migration and flow cytometry experiments.

3.1.2 Synthesis of PLGA Microparticles

PLGA microparticles (PLGA – Resomer 502H, Sigma Aldrich) were synthesized using a water-oil-water double emulsion, solvent evaporation method previously published.[182–184] MPLA (Lipid A Purified/Detoxified from Salmonella minnesota R595, Avanti) was encapsulated in particles (1 µg MPLA per mg PLGA). Particles were modified with 70,000 MW, 30% w/v branched polyethylenimine (PEI, VWR) to create cationic particles, followed by electrostatic adsorption of Class B CpG ODN 1826 (Invivogen) (10 µg CpG per mg PLGA MP). To characterize PLGA MPs, size and zeta potential were measured with dynamic light scattering (Malvern Zetasizer Nano) (Figure S1).

3.1.3 Flow Cytometry Experiments

Loosely adherent BMDCs cultured for 6-7 days as described above were collected from petri dishes and replated in 12-well plates with fresh RPMI complete media (1 million cells mL^{-1}, 1 to 1.5 million cells per well) containing adjuvants either in soluble form or loaded onto PLGA MPs. Soluble (unformulated) MPLA was pre-diluted in DMSO and added to media at a final concentration of 50 ng mL^{-1} and/or soluble CpG DNA was pre-diluted in DNAse-free water and added to media at a final concentration of 500 ng mL^{-1}. PLGA MPs were concentrated in media (50 µg mL^{-1}) with particulate adjuvant doses equivalent to soluble adjuvant doses. BMDCs were incubated with soluble or PLGA MP-loaded adjuvant overnight at 37°C and 5% CO_2, and then collected for flow cytometry analysis using a cell scraper to remove adherent BMDCs.

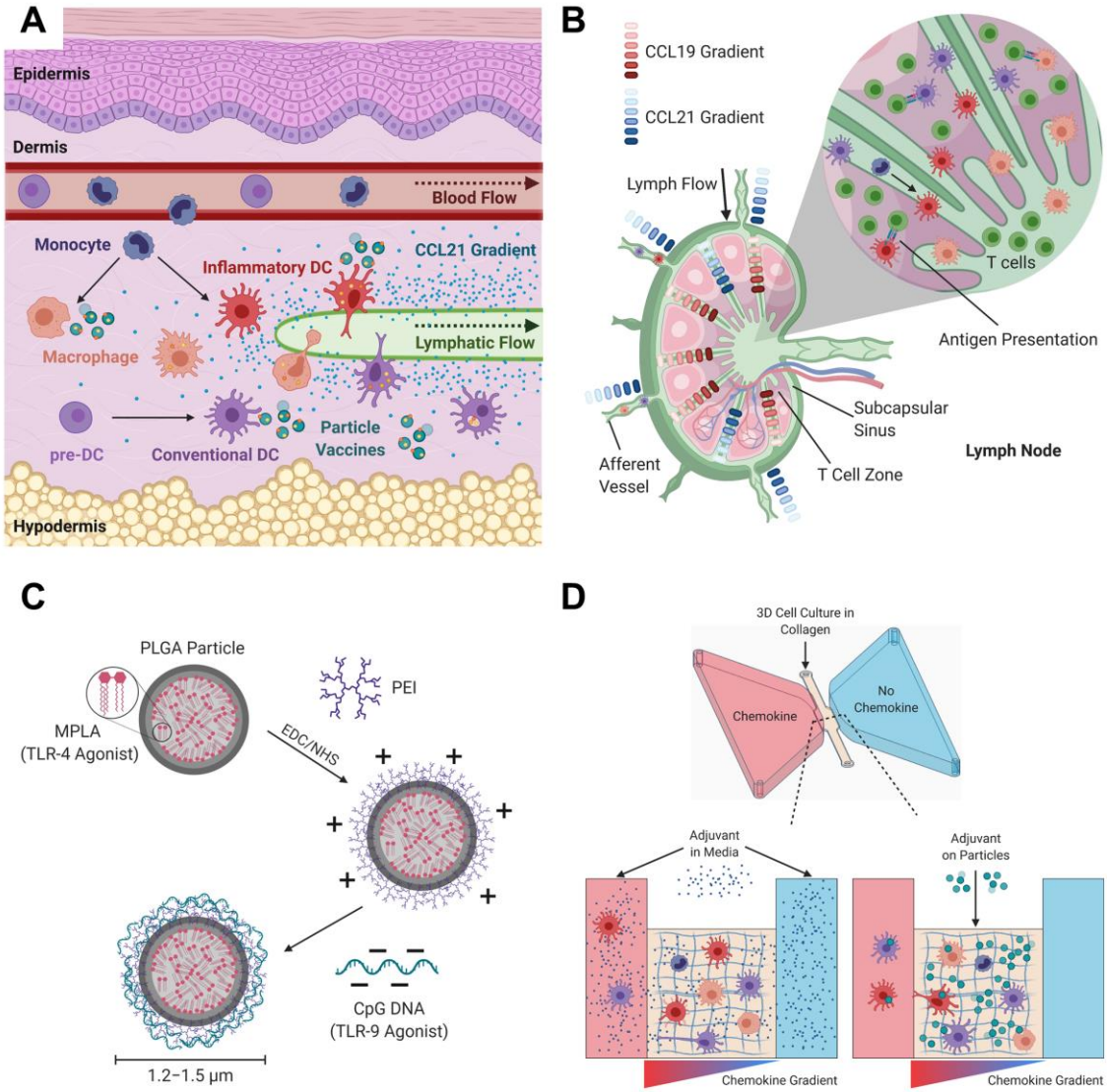

Figure 6: Antigen-presenting cell migration toward lymphatic chemokine gradients in vivo and in vitro in response to soluble and particulate adjuvants. A) Schematic of antigen-presenting cells (APCs) endocytosing particulate vaccines, causing them to activate and follow a CCL21 gradient toward lymphatic vessels in the dermis. Arrows represent differentiation. B) Depiction of lymph node chemokine gradients and antigen presentation by APCs in the T cell zone. CCL21 (blue gradient) is secreted by LECs in afferent vessels and CCL21 and CCL19 (red gradient) are secreted by LECs and stromal cells in the node. APCs follow gradients through the subcapsular sinus to the paracortex (T cell zone), where they present antigen to T cells. Monocytes are shown differentiating to inflammatory DCs in both the dermis and the lymph node. C) Adjuvant loading scheme on PLGA MPs. MPLA is encapsulated during PLGA MP synthesis. PEI is conjugated to the surface through a sulfo-NHS plus EDC crosslinking reaction. Positively charged PEI enables electrostatic loading of CpG DNA to the particle. D) Setup of microfluidic device for study of BMDC migration in response to adjuvant. DCs are loaded in a central collagen matrix channel

while chemokine is diluted in media in the left-hand chamber. Soluble adjuvant is diluted in media in both chambers and diffuses through the collagen matrix, while adjuvanted PLGA MPs are mixed with cells in the collagen matrix. A-D) Created with ©BioRender - biorender.com.

Cells were collected in flow tubes or V-well plates (for HTS) and washed with PBS, centrifuged at 500xg for 5 minutes, then resuspended in Zombie Green (Biolegend, 20 minutes RT, 1:1000 dilution in PBS) for labeling of dead cells. Cells were washed with FACS buffer (1% BSA, 0.1% sodium azide, 0.5 mM EDTA in PBS) and blocked with FcBlock (TruStain FcX anti-mouse anti-CD16/CD32, Biolegend, 1:100 dilution) for 30 minutes at 4°C prior to adding the fluorescent antibody cocktail: anti-Ly6C (clone HK1.4, Brilliant Violet 711, 0.125 µg per 100 µL, Biolegend), anti-CD11c (clone N418, Brilliant Violet 421, 0.25 µg per 100 µL, Biolegend), anti-CD11b (clone M1/70, BUV395, 0.25 µg per 100 µL, Biolegend), anti-CCR7 (clone 4B12, allophycocyanin, 1 µg per 100 µL, Biolegend) anti-MHCII (clone M5/114.15.2, allophycocyanin-Cy7, 0.125 µg per 100 µL, Biolegend or PE, 0.02 µg per 100 µL, eBioscience), anti-CD40 (clone 3/23, 0.25 µg per 100 µL, PE-CF594, BD), anti-F4/80 (clone BM8, PE/Cy7, 0.125 µg per 100 µL, Biolegend). Cells were incubated with antibody cocktail for 30 minutes at 37°C, as suggested by Biolegend for labeling with anti-CCR7 antibody. Cells were washed with FACS buffer and centrifuged at 500 xg for 5 minutes, and then finally resuspended in FACS buffer for flow cytometric analysis with the BD LSRFortessa. Flow cytometry data analysis was done with FlowJo (BD). Doublets were excluded by gating singlets on SSC-A vs. SSC-H. Debris was excluded by gating cells on FSC-A vs. SSC-A. Dead cells exhibiting high Zombie Green fluorescence were also excluded (FITC vs. SSC-A). Gating

for monocytes, macrophages, and DCs depicted in Figure 7. tSNE plots were created in FlowJo.

3.1.4 Microfluidic Device Setup

Chemotaxis devices (ibidi GmbH) have a central channel (2 mm L x 1 mm W x 0.07 mm H) between two 65-µL reservoirs. The collagen gel mixture was prepared according to manufacturer's instructions (Gibco) by mixing collagen (Rat Tail Collagen I, Gibco) with 10X PBS (Quality Biological), 1N NaOH (Sigma-Aldrich, sterile filtered and suitable for cell culture), and cells suspended in RPMI complete medium (described above). The first three ingredients were mixed to obtain a pH of 7 and then cells were added to obtain concentrations of 1.5 mg collagen and 3 million cells per mL of gel mixture. If PLGA MPs were included, they were first suspended with cells at 50 µg MPs (50 ng MPLA and/or 500 ng CpG) per 3 million cells prior to adding the rest of the gel mixture. Around 20,000 cells (6-7µL gel mixture) were loaded into the central channel, and collagen gel polymerized 30 to 45 min at 37°C. Soluble adjuvants and chemokines were diluted in RPMI complete medium prior to filling reservoirs. Soluble CpG and MPLA were first diluted in DNAse-free water and DMSO, respectively, and then added to media at concentrations of 50 ng mL^{-1} (MPLA) and/or 500 ng mL^{-1} (CpG). Chemokines CCL19 (9.4 kDa, R&D Systems) and CCL21 (12 kDa, R&D Systems) were concentrated in media at 1 µg mL^{-1} and added to the left reservoir (Figure 6D). The filling ports of the left reservoir were plugged while filling the right and vice versa, to avoid disturbances in gradients prior to imaging. Gradients were established within 1 hour and maintained over a period of 24 hours, validated by measuring the gradient of 10,000 MW FITC Dextran (Sigma Aldrich) at 10-minute increments over 24 hours and plotting the fluorescence vs. the position over the

width of the channel (Figure S2). Chemokine gradients were also validated with AF488-fluorescent CCL19 and CCL21 (AFA488 NHS ester, Lumiprobe), which were stable with and without the presence of MPLA and CpG in media reservoirs for at least 18 hours (Figure S7). Twelve devices were imaged simultaneously with phase contrast microscopy using a 4X objective in a humidified chamber at 37°C every 3 minutes for 12-24 hours (Lionheart, Biotek). The depth of field for the 4X objective is 50 μm, which is about 72% the height of the 3D DC culture channel (70 μm). A Z stack of central gel channel was imaged with a confocal microscope to confirm 3D culture (Figure S8).

3.1.5 Cell Tracking

Phase contrast images of cells within the central channel were combined into stacks and corrected for movement due to stage drift with an ImageJ plugin (Template_Matching.jar).[185,186] Image sequences were uploaded into Volocity Quantitation Software (PerkinElmer), a high-throughput automated cell tracking software. Cells were identified by an 8-bit intensity threshold (lower limit 70, upper limit 255). The model selected in the software to identify the most likely position for each cell at each time point is the Trajectory Variation model with the sensitivity of the algorithm set to "Erratic." The measurements derived from each cell track include distance, displacement, velocity, meandering index (displacement divided by distance) and bearing angle (the angle of displacement from the origin) (Figure 8A).

3.1.6 Statistical Analysis

To estimate regression coefficients for Equation 2, distances, velocities, displacements, meandering indices, and bearing angles (cosine values) from one thousand cell tracks

observationally categorized as migratory and sedentary were input into MATLAB (function mnrfit). To include only migratory cells in analyses evaluating the chemotactic response to adjuvants (Figures 9-11), the distance, velocity, displacement, MI, and cos(BA) values were input into Equation 2. If the odds ratio was less than 1, the cell was predicted to be migratory and included in polar plots (Figure 9C-D, Figure 10A-D, Figure 11A-D) and violin plots (Figure 10E-F, Figure 10E-F). For each treatment group (e.g., GM-CSF/IL-4 BMDCs with CpG MP and CCL19), migratory cell track data from three ibidi chemotaxis devices (n=3) was combined into a single polar plot or violin plot. Polar plots of bearing angle data (function polarhistogram) and violin plots of meandering index data (function violin) derived from migratory cell tracks were generated using MATLAB (The MathWorks, Inc.).[187] Mean directions and resultant lengths (indicative of variance, as length approaches 1, the variance of directions approaches 0) in Figures 10C-D and 11C-D were calculated with equations defined by Mardia & Jupp.[188] The Cox test was used to assess whether directional data followed a von Mises distribution, comparable to a normal distribution of linear data.[188–190] For all cases where the data did not fit a von Mises distribution, mean directions were compared using the nonparametric multi-sample method for circular data, the Mardia-Watson-Wheeler Uniform Scores Test.[188] Post-hoc analysis was performed according to methods proposed by Tasdan and Yeniay.[191] Statistics on circular data are explained further in the Supporting Information section. The two-sample Kolmogorov Smirnov test estimated equality between meandering index distributions. For Figure 9A-B, data was compiled from two separate flow experiments, each with three technical replicates (n=6 for each group). Data was confirmed as normally distributed with the D'Agostino and Pearson test and analyzed using Two-way repeated measures ANOVA

and Tukey's post-hoc test. For Figure 10G (BMDC subset CCR7 expression in response to soluble adjuvants), data was derived from four different trials, with three technical samples in each trial (n=12 each group). For normal data, One-way ANOVA with Tukey post-hoc test was performed to assess statistical significance (Macrophages, iDCs, cDCs) and for non-normal data Kruskal-Wallis with Dunn's post-hoc test was performed (Monocytes). For Figure 11G (CCR7 expression in response to particle adjuvants), data was derived from two separate trials (one with 3 and another with 6 technical replicates) for a sample size of 9 for each group. Significance was estimated with One-way ANOVA and Tukey post-hoc test. Statistical analyses were performed and plotted for cell migration data using MATLAB and for BMDC subset and CCR7 expression data using Graphpad Prism software.

3.2 **Results**

3.2.1 Synthesis of PLGA Microparticles for Dual Adjuvant Delivery

The design of MPLA- and CpG-loaded PLGA MPs is outlined in Figure 6C. PLGA MPs were synthesized using a water-oil-water double emulsion, solvent evaporation method previously published.[182–184]To encapsulate MPLA into the particles, MPLA was included with PLGA in dichloromethane for the first emulsion (1 µg MPLA per mg PLGA). Particles were covalently modified with 70,000 MW 30% w/v branched polyethylenimine (PEI) to create cationic particles for electrostatic adsorption of Class B CpG ODN 1826 (10 µg per mg PLGA MP). To characterize PLGA MPs, size and zeta potential were measured with dynamic light scattering. The average diameters for Blank and MPLA PLGA-PEI MPs are around 1.5 and 1.2 µm, respectively (Figure S1 A-B). The average

surface charges for Blank and MPLA PLGA-PEI MPs are 35 and 29 mV, respectively (Figure S1 C-D).

3.2.2 Generation of Heterogenous Cell Populations in BMDC Culture

To generate BMDCs, bone marrow was collected from femurs and tibiae of female C57BL/6J mice 5 to 10 weeks old. Red blood cells were lysed, and cells were plated in RPMI complete medium containing fetal bovine serum, penicillin-streptomycin, sodium pyruvate, non-essential amino acids, 2-mercaptoethanol, and 20 ng mL^{-1} granulocyte macrophage colony stimulating factor (GM-CSF) with or without 10 ng mL^{-1} interleukin-4 (IL-4). Loosely adherent BMDCs were collected by vigorous pipetting after 6-7 days of culture for flow cytometric and microfluidic chemotaxis experiments.

BMDC flow samples (gated for singlets and excluding debris and dead cells) were concatenated in FlowJo and gated on relative surface expression of Ly6C and CD11c, and CD11b, resulting in four main populations. Figure 7A shows concatenated samples from GM-CSF and GM-CSF-IL-4 cultures, as well as inactivated (no adjuvant) to activated cells (with adjuvant) to best visualize all possible cell populations. $Ly6C^{hi}CD11b^{+}CD11c^{-}$ cells were categorized as classical monocytes,[192–194] $Ly6C^{hi}CD11b^{hi}CD11c^{int/hi}$ cells as macrophages,[106,195,196] $Ly6C^{lo/int}CD11b^{hi}CD11c^{hi}$ cells as inflammatory DCs (iDCs), [91,197] and $Ly6C^{lo/int}CD11b^{int}CD11c^{hi}$ cells as conventional DCs (cDCs).[65,106,196,197] T-distributed stochastic neighbor embedding (tSNE) plots in FlowJo were calculated and displayed to visualize relative concentrations of BMDC subpopulations (Figure 7B). Gated populations were overlaid on tSNE plots, and heatmaps of CD11b, CD11c, Ly6C, F4/80, MHC-II, and CCR7 expression were generated to characterize the tSNE clusters (Figure 7B-C). The

monocyte, macrophage and DC populations were further validated by comparing the relative median fluorescence intensities (MFI) of F4/80, MHC-II, CD40 and CCR7. DCs exhibited high MFI of MHC-II, CD40, and CCR7, macrophages expressed high MFI of F4/80 and intermediate MFI of MHC-II, CD40, and CCR7, and monocytes exhibited low MFI of these markers (Figure 7D).[106]

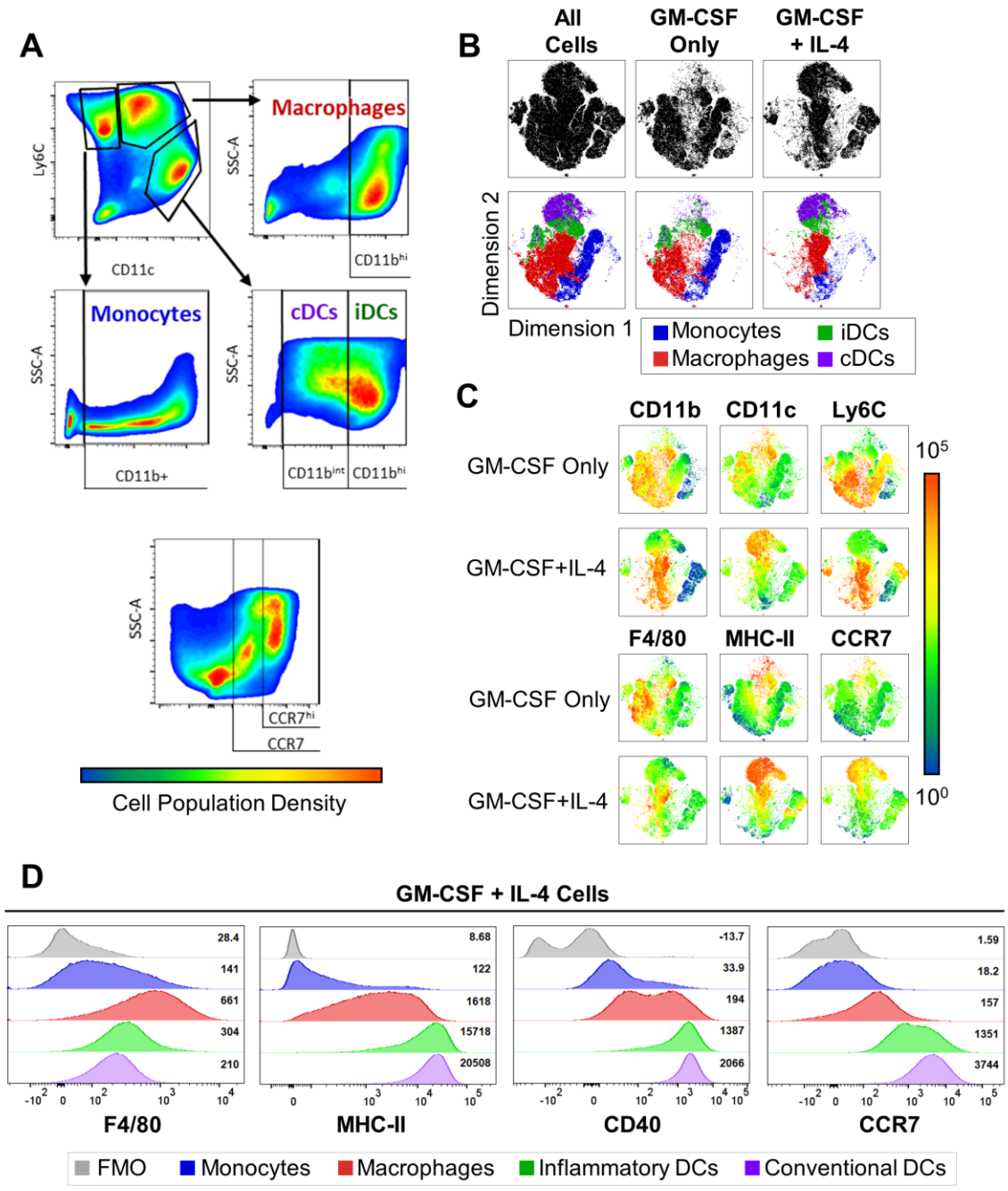

Figure 7: GM-CSF and GM-CSF-IL-4 derived BMDC cultures contain different proportions of monocytes, macrophages, and dendritic cells. A) Gating strategy for monocyte, macrophage, iDC and cDC subpopulations based on Ly6C, CD11c, CD11b surface expression, as well as gating strategy for CCR7+ and CCR7-hi BMDCs. B) Combined and separated tSNE plots of GM-CSF-only BMDCs and GM-CSF-IL-4 BMDCs with overlaid BMDC monocyte (blue), macrophage (red), iDC (green), and cDC (purple) subpopulations. C) Heatmaps of tSNE plots depicting relative fluorescence intensity of BMDC markers. D) Comparing relative fluorescence intensity of APC markers on

monocytes, macrophages, iDCs, and cDCs. Fluorescence minus one (FMO) controls included (grey). Median Fluorescence intensity values displayed by each histogram.

3.2.3 Logistic Regression Model Filters Data for Migratory Cell Tracks

The experimental setup of culturing cells with adjuvant in chemotaxis devices (ibidi GmbH) is outlined in Figure 6D and detailed in Experimental Methods. Devices are composed of a central channel (2 mm L x 1 mm W x 0.07 mm H) for 3D cell culture between two reservoirs. To generate a gradient, the left reservoir contains CCL19 or CCL21 (1 μg mL^{-1}) in RPMI complete media, while the right reservoir contains media without chemokine. Gradients are established within 1 hour and maintained over a period of 24 hours, validated by measuring the gradient of 10,000 MW FITC Dextran at 10-minute increments over 24 hours and plotting the fluorescence vs. the position over the width of the channel (Figure S2). Cells in the central channel are suspended in 1.5 mg mL^{-1} rat tail collagen I gel, to mimic tissue matrix. Soluble adjuvants are added to media in both reservoirs at concentrations of 50 ng mL^{-1} for MPLA and 500 ng mL^{-1} for CpG DNA and diffuse through the collagen matrix. PLGA MPs are included in the collagen matrix, and concentration of particles is adjusted to maintain adjuvant concentrations of 50 ng mL^{-1} for MPLA and 500 ng mL^{-1} for CpG (50 μg PLGA MPs mL^{-1}). Twelve devices were imaged simultaneously with phase contrast microscopy using a 4X objective in a humidified chamber at 37°C every 3 minutes for 12-24 hours (Lionheart, Biotek).

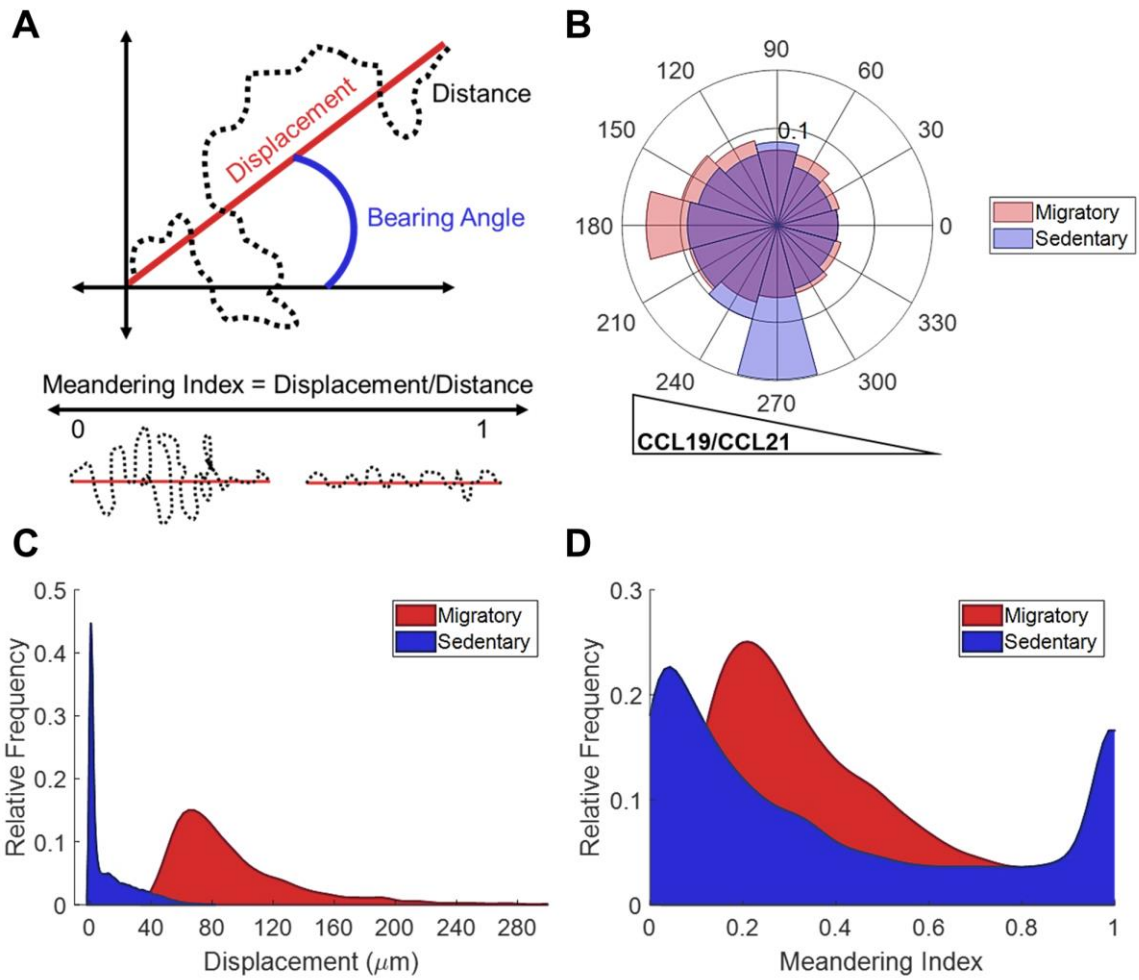

Figure 8: Multinomial Logistic Regression Model-Informed Separation of Sedentary and Migratory Cell Tracks. Example data set with cell tracks categorized as migratory and sedentary using the logistic regression model includes all cell tracks from the soluble adjuvant chemotaxis experiments. A) Visualization of displacement, bearing angle, and distance derived from tracked cells. Meandering index (MI) is the ratio between displacement and distance, and the migration follows a straighter line as MI approaches 1. B) Polar histograms of cell track bearing angles (BA) for migratory and sedentary cells, categorized based on odds ratio (OR) calculation from logistic regression model (OR>1 sedentary, OR<1 migratory). Chemokine gradient directs cells toward the left (BA ~180°). C) Displacement distributions and D) meandering index distributions of migratory and sedentary cells. Any cell track with a displacement of 0 was removed from distributions in B-D.

Image sequences were uploaded into Volocity Quantitation Software (PerkinElmer), a high-throughput automated cell tracking software. The measurements derived from each cell track include distance, displacement, velocity, meandering index (displacement

divided by distance) and bearing angle (the angle of displacement from the origin) (Figure 8A). To prevent mistakenly tracked cells in Volocity from adding noise to data analysis of cell chemotaxis, and avoid individually reviewing thousands of cell tracks, a logistic regression model was calculated to separate migratory cells from sedentary cells. These sedentary cells included dead or immobile cells that were tracked due to stage drift that could not be entirely corrected with the ImageJ algorithm and DCs with appendages that were mistakenly tracked as objects moving separately from the cell body. To estimate the regression coefficients, the model **(Equation 1)** was fit to a data set containing 1,000 cell tracks observationally categorized as sedentary or migratory (*dist* is distance, *vel* is velocity, *disp* is displacement, *MI* is meandering index, *BA* is bearing angle).

$$\ln(\mathrm{Y}) = \ln\left(\frac{P(Outcome\ 1)}{P(Outcome\ 2)}\right) = \beta_0 + \beta_1 X_1 + \cdots + \beta_i X_i \quad (\mathbf{1})$$

$$\ln\left(\frac{P(Sedentary)}{P(Migratory)}\right) = 0.87 + 0.0013X_{dist} + 6.7X_{vel} - 0.033X_{disp} + 0.84X_{MI} + 0.21X_{\cos(BA)} \quad (\mathbf{2})$$

When any distance, velocity, displacement, meandering index, and cosine of bearing angle values from a cell track were input into **Equation 2**, if the odds ratio (Y, Equation 1) was greater than 1, the cell was estimated to be sedentary. If less than 1, the cell was estimated to be migratory. Polar histograms of bearing angles confirmed that chemotactic cells, moving toward the gradient in the left chamber, were predicted as migratory and immobile cells that were mistakenly tracked in the direction of the stage drift (toward 270°) were predicted as sedentary (Figure 8B).

The distributions of displacement values (Figure 8C) confirmed most migratory cells were moving at least 40 μm away from the point of origin, while most sedentary cells were

barely moving above 0 μm. The distributions of meandering indices (Figure 8D) showed migratory cells had a MI peak of about 0.21, while sedentary cells peaked around 0.04 and then around 1. Because sedentary cells could be DCs with appendages counted as separate objects migrating around a center of origin (the cell body), the distance will appear large while the displacement is very small, explaining the peak around 0.04. Also, sometimes two immobile cells were accidentally connected as a single cell directly moving from point A to point B, explaining the MI peak of 1 (displacement equaling distance). For each adjuvant and chemokine condition, three devices with cells were imaged, three separate experiments. The cell tracks were pooled together, and migratory cell tracks were identified using the logistic regression model for subsequent data analysis.

3.2.4 Addition of IL-4 to BMDC Culture Increases CCR7 Expression and Chemotaxis

There is speculation on whether IL-4 is necessary to stimulate DC maturation in murine bone marrow cultures,[106] and numerous studies on DC behavior in vitro have been completed using BMDCs generated with GM-CSF alone or combined with IL-4.[104,105] CCR7 expression and migration data were obtained for cells cultured under both conditions to confirm whether IL-4 is essential to enable chemotaxis of BMDCs. BMDCs treated with only GM-CSF prominently contains monocytes, macrophages and $CD11b^{hi}$ DCs (iDCs) while monocyte concentration decreases and $CD11b^{int}$ DC (cDC) concentration increases drastically with addition of IL-4 (Figure 9A). CCR7 expression is significantly increased across all populations in GM-CSF/IL-4 BMDC culture compared to GM-CSF BMDCs (Figure 9B), with GM-CSF/IL-4 DCs expressing the highest CCR7 mean fluorescence intensity (Figure 7C-D).

For all polar plots in this study, migratory cells exhibiting chemotaxis toward CCL19 or CCL21 have a mean bearing angle (MBA) to the left between 150° and 210° (exhibited in Figure 9C toward CCL21) and the variance of cell directions decreases as the resultant length (RL) of the MBA approaches 1 on a unit circle (exhibited in Figure 9D toward CCL21). Without adjuvant, GM-CSF/IL-4 BMDCs exhibited a baseline level of chemotaxis while inactivated GM-CSF BMDCs did not exhibit any chemotaxis toward CCL21. The addition of MPLA and CpG did stimulate some chemotaxis of GM-CSF BMDCs but more significantly induced GM-CSF/IL-4 BMDC chemotaxis (Figure 9C). BMDCs generated with only GM-CSF did not exhibit any chemotaxis when activated with adjuvant-loaded PLGA MP (Figure S3). Because IL-4 induced expression of CCR7 (Figure 9B) and exhibited baseline chemotaxis (similar to steady state in vivo),[198] as well as increased chemotaxis with addition of adjuvant in solution or on particles, GM-CSF/IL-4 BMDC cultures were used for the migration experiments.

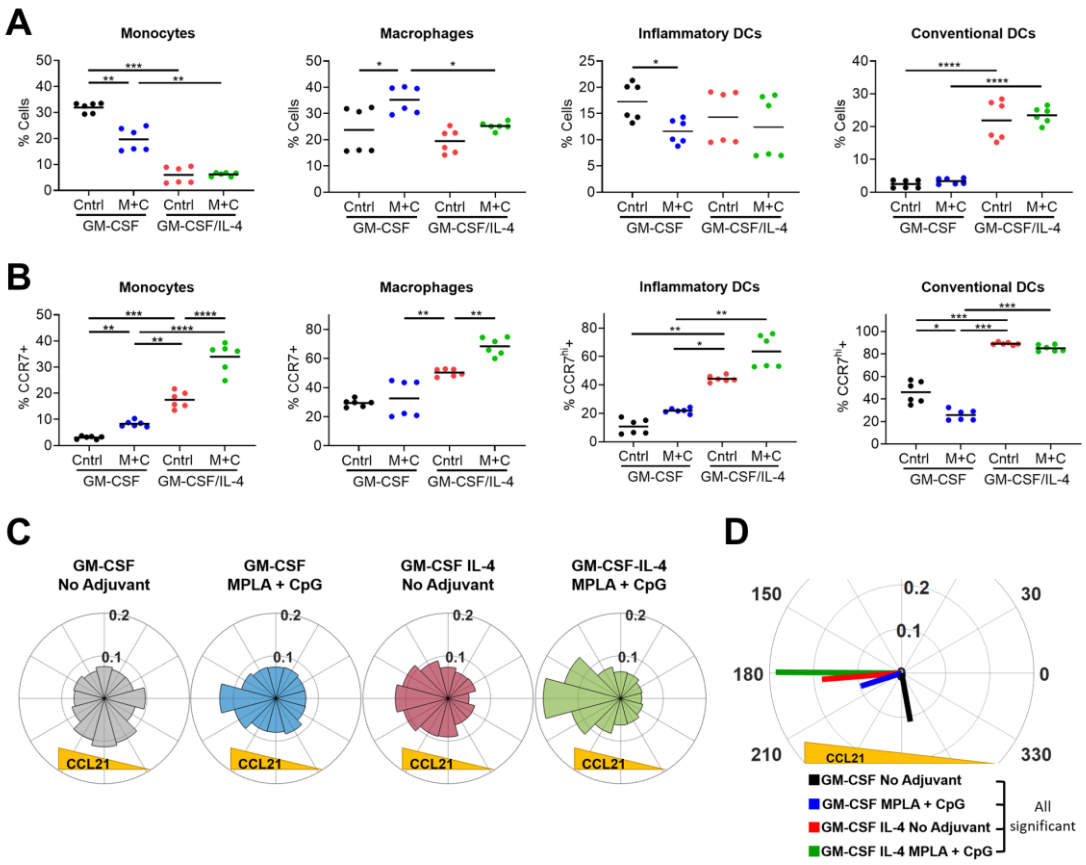

Figure 9: IL-4 increases CCR7 expression and BMDC chemotaxis toward CCL21. A-B) Percentage (out of total BMDC population) of monocyte, macrophage, inflammatory DC (iDC), and conventional DC (cDC) subpopulations in GM-CSF BMDC versus GM-CSF-IL-4 BMDC culture with and without adjuvant (soluble MPLA+CpG). Percentage of each subpopulation expressing CCR7 in response to soluble MPLA+CpG in GM-CSF-only or GM-CSF-IL-4 BMDC culture. *p<0.05, **p<0.01, ***p<0.001 ****p<0.0001 Two-way repeated measures ANOVA and Tukey's post-hoc test. Data combined from two separate flow experiments, each with 3 technical replicates, therefore n=6 for each group. C) Polar histograms of cell track mean bearing angles (BA) normalized to cell number. Cells from three devices (each device from a separate experiment) combined into each polar plot. Yellow triangle indicates direction of CCL21 gradient (from left-hand chamber, toward 180° on polar plot). D) Mean directions and resultant lengths of each polar histogram, where length of line is inversely proportional to directional variance (as length approaches 1, more cells moving in the same direction). All mean directions significant (p<0.01) according to Mardia Watson Wheeler Uniform Scores Test and Tasdan-Yeniay post hoc test.

3.2.5 Soluble MPLA Increases While Soluble CpG Decreases Chemotaxis

As seen with CCL21, GM-CSF-IL-4 BMDCs also exhibited a baseline level of chemotaxis toward CCL19 without stimulation by an adjuvant (Figure 10A). Compared to the control (no adjuvant), soluble CpG DNA did not increase chemotaxis toward CCL19 or CCL21. Conversely, MPLA induced the most directed migration toward CCL19 and CCL21 (Figure 10C-D). Increasing the CpG DNA concentration from 50 to 5000 ng mL^{-1} did not affect chemotaxis, while increasing the MPLA concentration steadily increased chemotaxis toward CCL21 (Figure S4). There was no benefit of combining soluble CpG with MPLA to induce chemotaxis toward either chemokine. Cells exhibited no significant difference in chemotaxis toward either chemokine when exposed to soluble MPLA-CpG compared to MPLA alone (Figure 10C-D). MPLA-induced chemotaxis toward CCL19 and CCL21 and CpG-driven decrease in chemotaxis toward CCL19 was also evident by the significant differences in meandering index distributions (Figure 10E). A MI distribution skewed toward 1 indicates more cells move along a straight path whereas a MI toward 0 indicates more cells deviate from a straight path. There was an opposite effect on velocity of cells exposed to CCL19 gradients – CpG DNA increased while MPLA decreased cell velocity (Figure 10F). CCR7 expression on GM-CSF-IL-4 monocyte and macrophage subpopulations (Figure 10G) followed a similar trend to soluble adjuvant-stimulated cell chemotaxis, but not on DC subpopulations. MPLA was the strongest inducer of CCR7 expression on monocytes and macrophages, while CpG most effectively stimulated CCR7 expression on iDC and cDC subpopulations. Because ~100% of DCs expressed an intermediate to high level of CCR7, $CCR7^{hi}$ expression was compared between adjuvant groups (Figure 7A depicts gating).

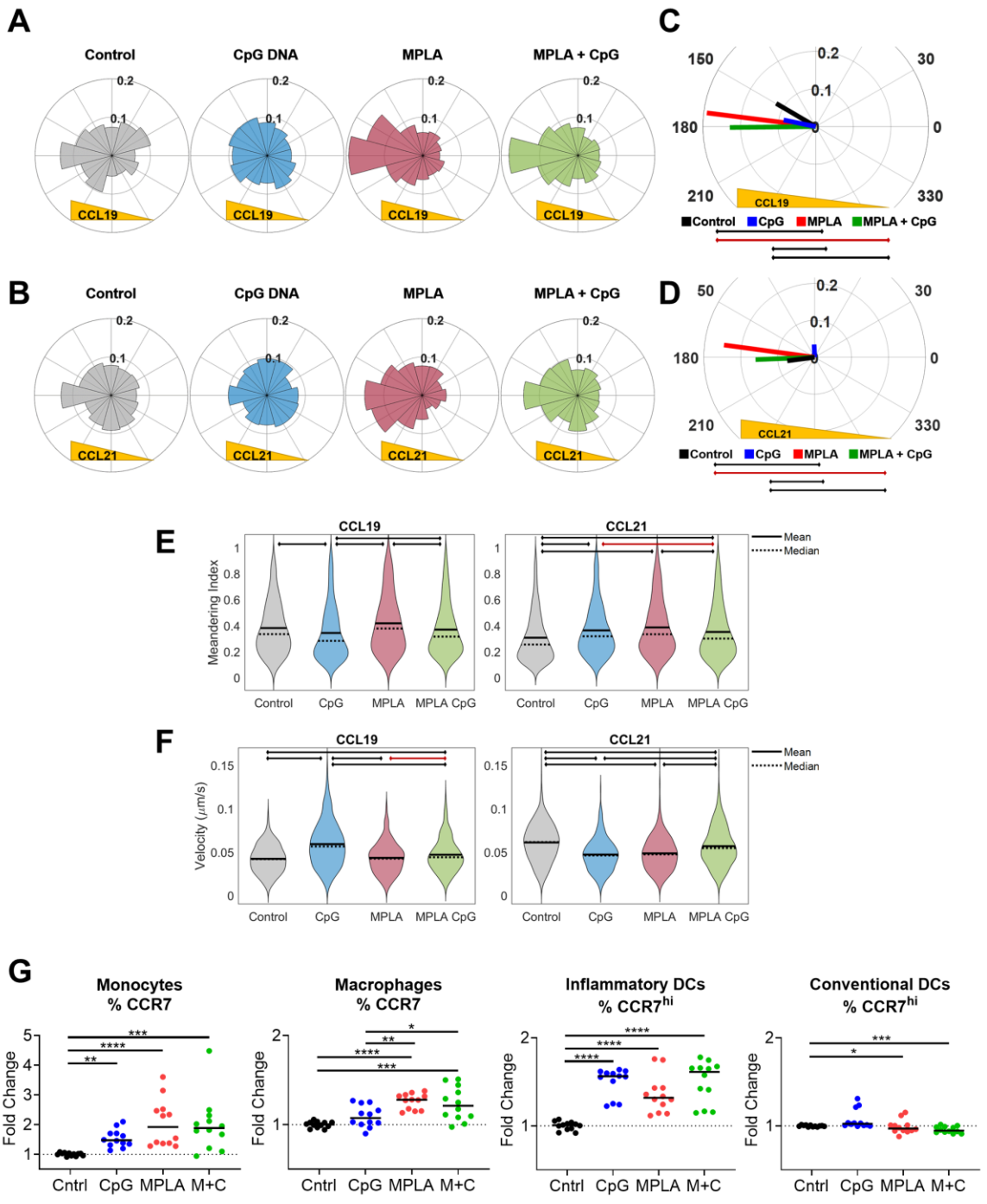

Figure 10: Soluble MPLA increases BMDC chemotaxis while soluble CpG does not induce BMDC chemotaxis toward CCL19 and CCL21. A-B) Normalized polar histograms depicting cell orientation bias toward CCL19 and CCL21 when cultured with adjuvants. Control is no adjuvant. Yellow triangles indicate direction of CCL19 and CCL21 gradients (from left-hand chamber, toward 180° on polar plot). C-D) Mean directions and resultant lengths for each group. Black lines under legend indicate statistical significance ($p<0.01$) between mean directions according to Mardia Watson Wheeler Uniform Scores Test and

Tasdan-Yeniay post hoc test. Red lines indicate $p<0.05$. Migratory cell track data from three devices (ranges from 432 to 1000 cell tracks for adjuvant and control groups, data normalized to cell number) combined into each polar histogram. E--F) Violin plots of meandering index and velocity distributions with mean (black solid) and median (black dashed). Black lines at the top of the graph indicate significance according to Kolmogorov Smirnov two sample test ($p<0.01$) and red lines indicate $p<0.05$. G) CCR7 expression on various BMDC subpopulations in response to soluble adjuvants, normalized to control mean from each experimental run. Data from four different trials combined, three technical samples each. ~100% of iDCs and cDCs expressed CCR7, so CCR7-hi expression was compared. *$p<0.05$, **$p<0.01$ ***$p<0.001$ ****$p<0.0001$ One Way ANOVA with Tukey Test for Macrophages, iDCs, and cDCs; Kruskal-Wallis with Dunn's test for Monocytes. M+C is MPLA and CpG combined.

3.2.6 CpG Delivered on PLGA MP Increases Cell Chemotaxis

CpG delivered on PLGA MP (CpG MP) induced more directed migration toward CCL19 and CCL21 compared to particles without adjuvant (Blank MP) and MPLA encapsulated in MP (MPLA MP) (Figure 11C-D). MPLA and CpG co-delivered on PLGA MP did not significantly increase BMDC chemotaxis compared to CpG MP (Figure 11C-D). The meandering index distribution of cells migrating toward CCL21 was skewed more toward 1 with MPLA-CpG MP compared to Blank MP, whereas MPLA MP significantly decreased meandering index of cells migrating toward CCL19 (Figure 11E). Like cells stimulated with soluble CpG, cells mixed with MPLA MP migrated faster in the presence of CCL19 than when mixed with other particles (Figure 11F). Single and dual adjuvant PLGA MP did not change CCR7 expression on monocyte, macrophage and cDC subsets, but CpG MP and MPLA-CpG MP did increase percentages of $CCR7^{hi}$ iDCs (Figure 11G).

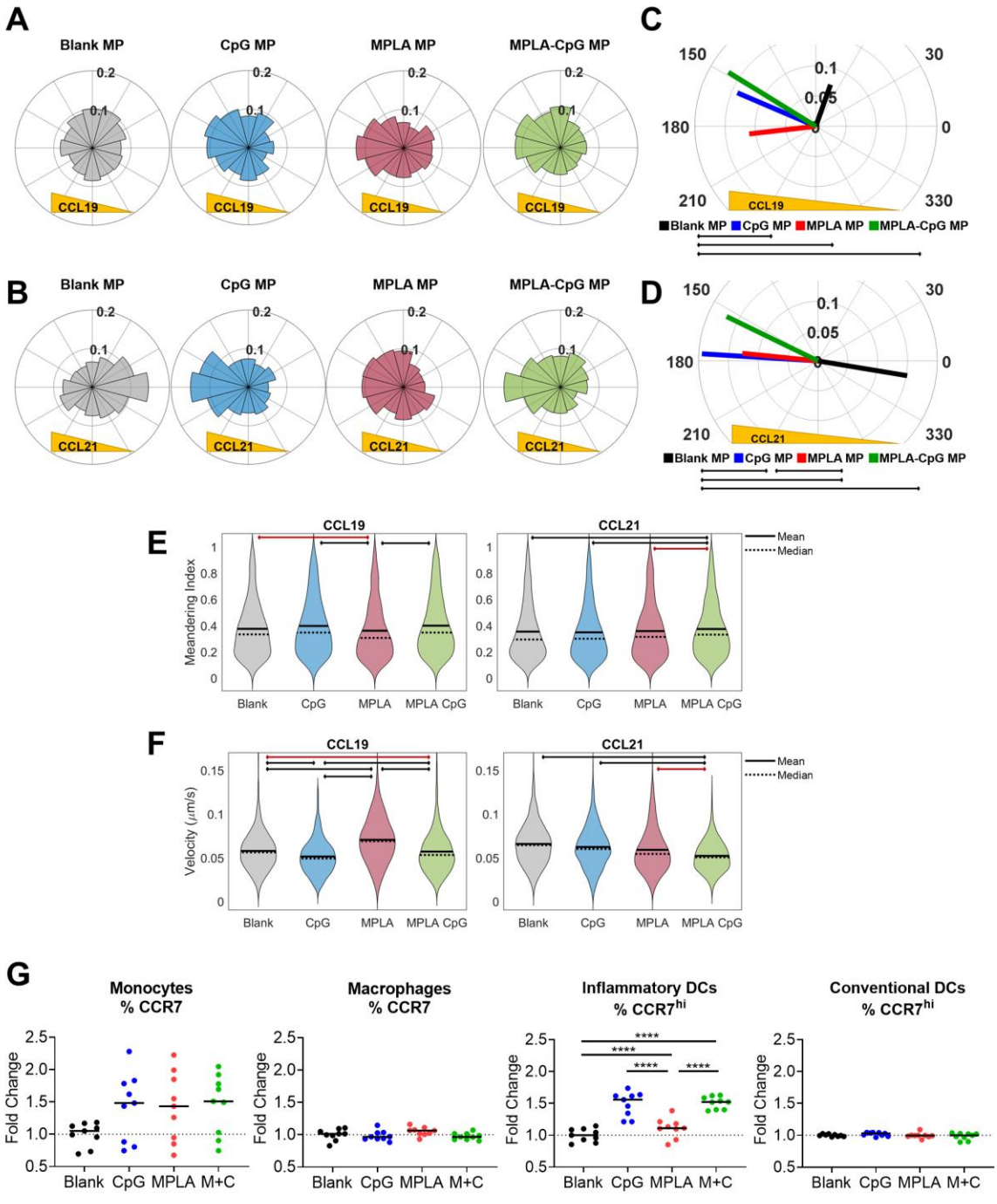

Figure 11: CpG delivered on PLGA MP increases BMDC chemotaxis toward CCL19 and CCL21. A-B) Normalized polar histograms depicting cell orientation bias toward CCL19 and CCL21 when cultured with particle-loaded adjuvants. Blank PLGA MP have no adjuvant. M+C is MPLA and CpG combined. Yellow triangles indicate direction of CCL19 and CCL21 gradients (from left-hand chamber, toward 180° on polar plot). C-D) Mean directions and resultant lengths for each group. Black lines under legend indicate statistical significance ($p<0.01$) between mean directions according to Mardia Watson Wheeler

Uniform Scores Test and Tasdan-Yeniay post hoc test. Migratory cell track data from three devices for CCL21 and four devices for CCL19 combined into each polar histogram. E-F) Violin plots of meandering index and velocity distributions with mean (black solid) and median (black dashed). Black lines at the top of the graph indicate significance according to Kolmogorov Smirnov two sample test ($p<0.01$) and red lines $p<0.05$. G) CCR7 expression on various BMDC subsets in response to PLGA NP groups, normalized to control mean from each experimental run. Data from two different experiments combined, one with n=3 technical replicates and one with n=6, for a total of n=9 shown here for each group. ~100% of iDCs and cDCs expressed CCR7, so CCR7-hi expression was compared. *$p<0.05$, **$p<0.01$ ***$p<0.001$ ****$p<0.0001$ One Way ANOVA with Tukey Test. M+C is MPLA and CpG combined on PLGA MP.

3.3 Discussion

We investigated the singular and combinatorial effects of adjuvants MPLA and CpG, delivered in soluble form or on synthetic biomaterial-based particulate carriers (PLGA MPs), on the chemotaxis of GM-CSF/IL-4 BMDCs toward lymphatic chemokines CCL19 and CCL21. Our data suggests the BMDC chemotactic response to MPLA and CpG is context dependent on the method of delivery (soluble vs. PLGA MP). Soluble MPLA and CpG PLGA MP were most effective at inducing BMDC chemotaxis, possibly due to the bioavailability of these agonists to their respective TLRs. TLR4 signaling recruits MyD88 at the plasma membrane where it most likely to encounter lipopolysaccharide (LPS), a component of Gram-negative bacterial membranes from which MPLA is derived.[199] TLR4 also translocates to endosomes and activates TRIF-dependent signaling, and it has been reported that signaling both TRIF and MyD88 pathways optimizes DC maturation.[200,201] Encapsulating MPLA in PLGA particles as a slow-release formulation reduces its bioavailability to surface-bound TLR4 compared to soluble MPLA of the same dose. TLR9 is localized on the endoplasmic reticulum and trafficked to lysosomes containing CpG DNA from disintegrated bacteria.[202,203] Soluble CpG DNA is taken up by cells through fluid phase and receptor-mediated endocytosis.[204] When soluble CpG enters a cell via

receptor-mediated endocytosis it is contained in early and late endosomes and lysosomes that bud off the plasma membrane or Golgi apparatus. Particle-loaded CpG DNA enters into phagosomes that directly fuse with the ER,[204] which could provide more direct access to TLR9. The direct exposure to surface TLR4 by soluble MPLA and ER-localized TLR9 by particle-loaded CpG DNA could explain the enhanced chemotactic response to those adjuvants. Surface-bound TLR4 and TLR9 both signal MyD88, which has been reported to be required for migration of DCs to dLNs.[205–207]

Interestingly, we did not observe a synergistic chemotactic response to MPLA and CpG in our devices. Previous work has shown combinations of TLR agonists delivered in soluble form and on biomaterials have elicited inflammatory cytokine responses in vitro and enhanced vaccine responses in vivo.[13,145,180,181,208] For example, co-delivered MPLA and CpG stimulate stronger IFN-β and IL-12p70 responses from GM-CSF BMDCs.[13,145,180] Though this does not correlate with an enhanced migratory response in vitro, there is still strong potential for combination adjuvants to induce strong immune responses in vivo. Additionally, other biophysical parameters with PLGA particles can be adjusted in future experiments to enhance the synergistic chemotactic response, including adjuvant density, particle size, and surface charge.

A common divergence in BMDC culture method is the inclusion or exclusion of IL-4. We demonstrated that supplementing GM-CSF with IL-4 enhances BMDC chemotaxis and expression of CCR7. GM-CSF/IL-4 BMDC culture is a heterogeneous mixture of cells, majority of which phenotypically resemble monocytes, macrophages, or dendritic cells.[105,106] Purifying subpopulations would help identify which cells are migrating in response to adjuvants and chemokines. However, studies have shown that fluorescence-

activated cell sorting potentially activates stress pathways, including p38 MAPK which is also involved in chemotaxis regulation.[209–211] Antibody binding may activate signaling pathways that alter functional changes of the purified cell population, and high pressures during cell sorting may stimulate aberrant dendritic cell maturation.[212–215] In addition to GM-CSF and IL-4, there are cytokines differentially secreted by subpopulations that contribute to the overall phenotype and function of BMDCs. For example, in GM-CSF BMDC culture, macrophages secrete higher levels of TNF-α while DCs secrete more IL-12.[180,216]

It is generally accepted that while undergoing maturation, DCs downregulate chemokine receptors that facilitate DC entry to inflamed peripheral tissues (e.g., CCR2 and CCR6) while upregulating CCR7, which increases responsiveness to CCL19 and CCL21 and migration to dLNs.[217,218] There are a few atypical chemokine receptors reported to interact with CCL19 and CCL21, including ACKR5 (CCRL2), which is upregulated by LPS, TNF-α, and other inflammatory stimuli; however, whether stimulation of CCRL2 induces cell migration is under debate.[219,220] Though we observed upregulation of CCR7 on DCs in response to soluble CpG, there was no increase in BMDC chemotaxis (Figure 10). Scandella et al. concluded upregulation of CCR7 was not sufficient for migration, and lipid mediator prostaglandin E2 (PGE2) is required to facilitate chemokine receptor signaling in human monocyte derived DCs.[221] It has been shown in mice that DC chemotaxis toward CCL19 is regulated by cysteinyl leukotrienes LTC_4 and LTD_4 and ADP-ribosyl cyclase CD38 controls migration of DCs from peripheral sites to lymph nodes.[222,223] A preliminary study has shown soluble CpG decreases genetic expression of CD38, prostaglandin E synthase (which catalyzes conversion of PGH2 to PGE2), CCR7, CCL19, and other

migration signaling proteins while soluble MPLA maintains and combined MPLA-CpG increases their expression (Figure S5). Therefore, it is likely the delivery of soluble CpG to BMDCs must be supplemented with other molecular signals to sensitize CCR7 to CCL19 and CCL21. For example, Tayalia et al. included PGE2 with delivery of soluble CpG to induce DC chemotaxis out of a 3D photopolymerized scaffold toward chemokine in collagen gel.[224]

The phenotype and function of DCs is reportedly influenced by 2D versus 3D culture conditions and substrate stiffness.[225,226] A study by Mennens et al. demonstrated culturing human PBMCs on low (2 kPa) and high (50 kPa) stiffness substrates increased CCR7 expression and cell migration toward CCL21 compared to medium (12 kPa) stiffness substrates.[226] Sapudom et al. reported culturing human monocytic THP-1 cells in 2D and transferring to 3D 1 mg mL^{-1} collagen gels (~47 Pa) slightly increased CCR7 and CD11c expression. Our data reveals culturing GM-CSF/IL-4 BMDCs (removed from 2D culture after 6 days) in 1.5 mg mL^{-1} collagen gel for 24 hours does not affect CCR7 expression and increases CD11c expression on live cells while lowering CD11b and Ly6C expression (Figure S6). Collagen gels were digested using Collagenase D (2 mg mL^{-1} media), which does have effects on cell viability and could downregulate the density of surface markers cells express in 3D.[227]

Surprisingly, there were minimal differences in cell orientation bias (Fig 5A-B, Fig 6A-B) between CCL19 and CCL21 gradients in response to adjuvants. Haessler et al. reported when BMDCs were exposed to two opposing gradients off CCL19 and CCL21 in a microfluidic device, BMDCs migrated preferentially toward CCL21.[228] However, we examined the gradients separately, and future work would be to investigate if adjuvants

change the preference of chemokines when exposed to opposing gradients. CCL21 is capable of binding to sulfated proteoglycans (e.g., heparan sulfate) and forming a fixed gradient. There were no proteoglycans directly added to the collagen gel mixture; however, a component of the growth medium, fetal bovine serum, does contain glycosaminoglycans (GAGs) that could have bound to type I collagen and CCL21.[229,230] Schumann et al. demonstrated matrix bound CCL21 triggered integrin-mediated adhesion of DCs and random movement along CCL21-presenting surfaces. DCs would truncate anchoring residues when directly engaging with CCL21, creating soluble CCL21 gradients. Once soluble, CCL21 along with CCL19, which lacks the C-terminus mediating glycosaminoclycan binding,[231] stimulated directed migration toward chemokines but did not induce adhesion.[232] Furthermore, our results show that where CCL19 did not induce directed migration of BMDCs with soluble CpG and MPLA MP, there was an increase in cell velocity (Fig 5D, Fig 6D). It has been reported that there are independent signaling pathways controlling CCR7-dependent chemotaxis and migratory speed.[211] The MAPK pathway involving ERK1/2, JNK, and p38 regulates chemotaxis, while the Rho/Pyk2/cofilin pathway regulates speed; therefore, different combinations of adjuvants with CCL19 and CCL21 could selectively tune the directionality and motility of DCs.

In summary, we built a framework to measure and analyze BMDC chemotaxis in 3D to screen for soluble and particulate adjuvants that enhance CCL19/21 mediated chemotaxis, and with our analyses discovered soluble MPLA and particulate CpG were the most effective in this regard. Our framework included a logistic regression model to isolate migratory cells based on cell track measurements (e.g., MI, displacement), and there is potential for the model to differentiate BMDC subpopulations based on parameters such as

morphology or migration dynamics (e.g., extension-retraction cycles). Isolation of cells based on sorting or fluorescent labeling methods (e.g., using reporter mice) would need to be optimized to assign a subpopulation category to each cell and inform the model. We observed CCR7 expression and chemotaxis of BMDCs are enhanced by supplementing culture media with IL-4, which gives rise to a heterogeneous population of monocytes, macrophages, and dendritic cells that collectively, differentially respond to MPLA and CpG DNA. The delivery method of MPLA and CpG were important to induce chemotaxis, most likely due to the bioavailability of the adjuvants and the cellular location of the TLRs. While soluble CpG did increase CCR7 expression on DCs, there was no increase in chemotaxis, possibly due to the absence of essential CCR7-signaling mediators such as PGE2 and CD38. Most prominently under CCL19 gradients, formulations that increased directed migration also decreased cell velocity, aspects of migration controlled by different signaling pathways. The delivery of MPLA and CpG together in soluble form or on particles did not significantly increase BMDC chemotaxis over delivery of each adjuvant alone. It is possible there are synergistic migratory responses to alternative adjuvant combinations, such as such as R848 (TLR7/8) and PolyU/UC (RIG-I), which could be investigated.[233] Along with synergy of combination adjuvants, biophysical parameters of adjuvant delivery vehicles such as particle size, charge, and adjuvant density could impact DC chemotaxis.[234] Furthermore, the effects of particulate adjuvant formulations on DC chemotaxis should be studied in vivo using intravital imaging methods demonstrated by Halin et al. and Sixt et al.[235,236]

Our results show that 3D migration of DCs toward lymphatic chemokines CCL19 and CCL21 can be influenced by both adjuvant type and the delivery method. These findings

uncover new directions for rationally designing formulations that drive DC migration and cell-mediated antigen delivery to the lymph node and tailor the immune response, a major goal in vaccine development.

CHAPTER 4: AIM 1.2. ASSESSING HOW MPLA AND CPG REGULATE IMMUNE CELL POPULATIONS AND PARTICLE TRANSPORT TO DRAINING LYMPH NODES IN VIVO

4.1 Materials and Methods

4.1.1 Synthesis of Fluorescent Nanoparticles

Polylactic-co-glycolic acid (PLGA) nanoparticles were synthesized using a water-oil-water double emulsion, solvent evaporation method as described in previous protocols.[147,180,233] 200 mg of PLGA (Resomer® RG 502H, Sigma Aldrich) was dissolved in 4 mL of dichloromethane and 1 mL of endotoxin-free water in a 50 mL polypropylene centrifuge tube. For MPLA particles, 1.2 mg of MPLA-PHAD® (Avanti) was added to this solution. The primary emulsion was sonicated over ice for 2 minutes using a 130W Ultrasonic Processor with titanium probe at 65% power. The primary emulsion was added to 16 mL of 5% w/v polyvinyl alcohol solution and sonicated for 5 minutes over ice to form a secondary emulsion. To remove dichloromethane by evaporation, the secondary emulsion was added to a beaker with magnetic stirring in the fume hood for three hours. The PLGA-PVA solution was transferred to a 50 mL centrifuge tube and centrifuged at 3,500 x g for 20 minutes to remove PLGA microparticles. The nanoparticles were subsequently pelleted using ultracentrifugation at 22,000 x g for 20 minutes at 4°C and washed with di H_2O. The washed particles were resuspended in 5 mL di H_2O and left to dry on a lyophilizer for 2 days. Polyethylenimine (PEI) was added to nanoparticles with an EDC/NHS reaction. 168 mg EDC (Pierce, Thermo Fisher) and 104 mg Sulfo-NHS (Pierce, Thermo Fisher) were added to 160 mg PLGA NPs in 5 mL 0.1M MES buffer (pH 5.5). The solution was vortexed and rotated for 2 hours at room temperature. After 2 hours, the PLGA/EDC/NHS solution

was added to 24 mL branched PEI (MW 70,000 30% w/v aq. soln., Polysciences), 48 mL of 0.2 M MES buffer (pH 6.5), and 3 mL HCl in a beaker on magnetic stirrer for 2 hours at room temperature. PLGA-PEI nanoparticles were pelleted using ultracentrifugation (80,000 x g for 20 minutes), washed with NaCl solution, washed with di H_2O, and resuspended in 5 mL RNase/DNase free water (Boston BioProducts). PLGA-PEI nanoparticles were lyophilized for 2 days and stored at -20°C.

To fluorescently label particles (Figure 12A), 50 μg of AlexaFluor 488 NHS ester (Lumiprobe) was added to 10 mg of PLGA-PEI nanoparticles in 1 mL sodium bicarbonate (pH 8) and rotated overnight at 4°C. AF488 PLGA PEI NPs were centrifuged at 10,000 x g for 20 minutes, washed with di H_2O, resuspended in 200 μL RNase/DNase free water, and lyophilized overnight. The zeta potential of AF488-conjugated particles was quantified as 19 mV using a Malvern Zetasizer. IRDye700-conjugated oligodeoxynucleotides (ODNs) were custom-made from Integrated DNA Technologies (IA). IRDye700-CpG ODN sequence is /5IRD700/TC CAT GAC GTT CCT GAC GTT. The control ODN, IRDye700-GpC ODN Is /5IRD700/TC CAT GAT ATT CCT GAT ATT. For electrostatically loading ODN, 36 μg IR700-CpG ODN or IR700-control ODN was added to 1 mg AF488-PLGA-PEI nanoparticles in 400 μL sodium phosphate buffer (pH 6.5) and rotated overnight at 4°C. IR700-ODN-AF488-PLGA PEI nanoparticles were washed with RNAse/DNAse free H_2O prior to resuspension in saline and intramuscular injections. To calculate CpG or control ODN loading, ssDNA levels were measured using the Nucleic Acid Quantification feature on the BioTek plate reader. The maximum IR700-ODN loading per mg of AF488-conjugated particles was quantified as 38.24 ± 2 μg.

4.1.2 Intramuscular Injections

Female Balb/cJ mice (9-10 wks old) were placed under anesthesia (5% isoflurane). To prepare particles for intramuscular injections, 6 mg of IR700-AF488 PLGA NP were resuspended in 225 μL of physiological saline solution (0.9% NaCl). A dose of 30 μg ODN (CpG or control) with or without 5 μg MPLA in 0.8 mg of PLGA NP (30 μL total) was injected into the right anterior tibialis muscle of each anesthetized mouse with a 29G 0.3 mL insulin syringe. Mice were euthanized 24 or 48 hours post-injection. Right anterior tibialis muscles, as well as popliteal, inguinal, and iliac lymph nodes (Figure 12B) were collected from each mouse and placed in 1X phosphate buffered saline (PBS) without calcium or magnesium (Corning).

4.1.3 NIR Imaging of Lymph Nodes

Popliteal, inguinal, and iliac lymph nodes were individually added to each well of a solid black 96-well polystyrene microplate, in 200 μL 1X PBS each well. Nodes were imaged using a near-infrared system consisting of a cooled EMCCD camera (Evolve eXcelon, Photometrics) attached to a stereomicroscope (MVX10, Olympus) with adjustable zoom, xenon arc light source (Lambda LS, Sutter Instrument Company), and manual filter wheel with standard Cy5.5 filter cube (Chroma Technology). Images were acquired with a 200 ms exposure time, executed using Micro-Manager microscopy software. Node images were uploaded into ImageJ, “regions of interest” (ROIs) were drawn around the perimeter of the nodes using the Wand Tool, and the raw integrated density of the ROI (summation of pixels), area of the ROI, and median pixel gray value of the ROI were quantified.

4.1.4 Tissue Preparation and Staining for Flow Cytometry

Muscles were enzymatically and mechanically dissociated into viable single cell suspensions with the Skeletal Muscle Dissociation Kit and gentleMACS Octo Dissociator (Miltenyi Biotec). Dissociated tissue was strained through a 40 μm cell strainer into a 50 mL polypropylene tube. Cells were pelleted through centrifugation at 500 x g for 5 minutes. Red blood cells were lysed using 1X RBS Lysis buffer with ammonium chloride (eBioscience™). Cells from each muscle were resuspended in 5 mL RBC lysis buffer and incubated for 10 minutes at room temperature. The reaction was stopped by adding 20-30 mL of fluorescence activated-cell sorting (FACS) buffer, which consists of 0.1% sodium azide, 1 mM EDTA, and 5% v/v FBS in PBS. Lymph nodes were dissociated in 40 μg/mL DNAse I and 1 mg/mL Collagenase D in RPMI 1640 medium through a 40 μm cell strainer using a 1mL-syringe plunger. The strainer was the top of a 5 mL Falcon™ Round-Bottom Polystyrene test tube.

Muscle and lymph node cell suspensions were centrifuged at 500 x g for 5 minutes. Each muscle and lymph node sample were resuspended in 200 μL FACS buffer and transferred to a well of a V-bottom 96 well plate. Plates were centrifuged at 500 x g for 5 minutes, samples were washed with PBS, and resuspended in 1:1000 Zombie Aqua™ Fixable Viability dye in PBS (Biolegend). Cells were incubated in Zombie Aqua for 30 minutes at room temperature, and then washed with FACS buffer. Cells were subsequently stained with fluorophore-conjugated antibodies in FACS buffer (200 μL antibody cocktail per muscle and 100 μL antibody cocktail per lymph node, estimated about 1 million cells/mL). The dendritic cell marker panel consisted of the following (for muscles and lymph nodes): BUV395 Rat anti-mouse CD11b (clone M1/70, BD), Brilliant Violet 421™ hamster anti-

mouse CD11c (clone N418, Biolegend), Brilliant Violet 785™ rat anti-mouse CD86 (clone GL-1, Biolegend), PE rat anti-mouse MHC class II (I-A/I-E, clone M5/114.15.2, Thermo Fisher), PE/Dazzle™ 594 hamster anti-mouse CD103 (clone 2E7, Biolegend), PE/Cyanine7 rat anti-mouse CD301b (clone URA-1, Biolegend), and allophycocyanin anti-mouse/human CD45R/B220 (clone RA3-6B2, Biolegend). For muscles, PE/Cyanine5 rat anti-mouse CD40 (clone 3/23, Biolegend) was added and for lymph nodes, PE/Cyanine5 rat anti-mouse CD8a (clone 53-6.7, Biolegend) was added. The macrophage and monocyte marker panel consisted of the following (for muscles only): BUV395 anti-CD11b, Brilliant Violet 421™ anti-CD11c, Brilliant Violet 785™ rat anti-mouse Ly-6G, PE mouse anti-mouse CD64 (FcγRI, clone X54-5/7.1, Biolegend), PE/Dazzle™ 594 rat anti-mouse Ly-6C (clone HK1.4, Biolegend), PE/Cyanine5 rat anti-mouse F4/80 (clone BM8, Biolegend), PE/Cyanine7 rat anti-mouse CD206 (MMR, clone C068C2, Biolegend), and allophycocyanin rat anti-mouse CD197 (CCR7, clone 4B12, Biolegend). Fluorescence-minus one (FMO) and single-stain controls for each laser/filter channel were included to optimize flow gating and compensation. Cells were washed with PBS and fixed with FluoroFix™ buffer (Biolegend) containing paraformaldehyde, optimized to stabilize tandem dyes. Cells were kept at 4°C overnight and imaged via multicolor flow cytometry (BD LSRFortessa™). Flow Cytometry Standard (FCS) files were uploaded into FlowJo (FlowJo, LLC, BD) for analysis. Prior to gating for APC markers, singlets were isolated using FSC-A vs. FSC-H and SSC-A vs. SSC-H scatter plots, debris removed from FSC-A vs. SSC-A scatter plots, and live cells gated on low BV510 (Zombie Aqua) fluorescence, optimized with the BV510 FMO. Cells were confirmed positive for APC markers using FMO controls. tSNE plots were generated by concatenating 5,625 of live cells from all

Blank NP, CpG NP, MPLA NP, and MPLA-CpG NP flow samples (total 180,000 cells) and running the tSNE feature.

4.1.5 Statistical Analysis

Cell percentages and median fluorescence intensity (CD86, BV786 channel) were calculated using FlowJo and exported as tables, which were uploaded into GraphPad for creating bar graphs and conducting statistical analysis. Statistical significance was calculated between treatment (adjuvant/particle) groups and time points using Two-Way ANOVA and Sidak's or Tukey's multiple comparisons test.

4.2 Results

4.2.1 Fluorescence of IR700-Conjugated CpG and Control ODN Loaded on PLGA PEI NP Peaks at 24 Hours and Decreases at 48 Hours in Muscle-Draining Lymph Nodes

Fluorescent images of lymph nodes using a standard Cy5.5 filter on a near-infrared microscope system were acquired with a 200 ms exposure time (example Figure 12C). The *mean fluorescence intensity* (sum of pixel gray values normalized by the area of the ROI) was plotted for each popliteal, iliac, and inguinal lymph node collected at 24- and 48-hours post-injection from mice injected with IR700-Control (GpC) ODN PLGA-PEI NP (**Blank NP**), IR700-CpG ODN PLGA-PEI NP (**CpG NP**), IR700-Control (GpC) ODN PLGA-PEI MPLA NP (**MPLA NP**), and IR700-CpG ODN PLGA-PEI MPLA NP (**MPLA-CpG NP**). The mean fluorescence intensity of averaged lymph nodes was calculated by averaging the means of the iliac, inguinal, and popliteal nodes from each mouse subject. Two separate

studies were conducted each with a sample size of 4 mice for each treatment (adjuvant/particle) group at 24 and 48 hours; therefore, for each treatment group at each time point the sample size was 8 mice (except for MPLA NP at 48 hours, which had 7 mice). Background (autofluorescent) signal was calculated by averaging the mean fluorescence intensity of 17 nodes from saline mice. The background signal was subtracted from combined-node and single-node mean fluorescence intensities from each mouse subject within each treatment group (Figure 12D-G). It is important to note that the ODNs were covalently labeled with NIR dye IR700 while the particles were covalently labeled with AF488, which is not detectable with NIR microscopy. For simplicity, the treatment groups herein are referred to as Blank NP, CpG NP, MPLA NP, and MPLA-CpG NP while understanding that the NIR signal could be from CpG and GpC ODNs separated from or electrostatically loaded on PLGA NPs.

NIR imaging data reveals IR700-GpC and IR700-CpG ODNs drained to lymph nodes within 24 hours of intramuscular injection on PLGA NPs (Figure 12D). For each treatment group, the mean fluorescence intensity (averaged between iliac, inguinal, and popliteal nodes for each mouse subject) significantly decreased by 48 hours (Figure 12D). When 24- and 48-hour data is combined for each treatment group, the mean fluorescence intensity of CpG NPs for averaged nodes is significantly higher than the mean fluorescence intensity of Blank NPs (Figure 12D). The differences between treatment groups when analyzing the fluorescence between single draining lymph nodes were not as apparent. For example, there were no statistical differences in fluorescence of iliac lymph nodes between treatment groups and time points (Figure 12E). The fluorescence of inguinal nodes was significantly higher for MPLA-CpG NP-injected mice compared to MPLA NP-injected mice, and the

inguinal node fluorescence decreased for most treatment groups by 48 hours (Figure 12F). The fluorescence of popliteal nodes was significantly higher for CpG NP-injected mice compared to Blank NP- and MPLA-CpG-injected mice, and the popliteal node fluorescence decreased for the Blank NP and CpG NP groups by 48 hours (Figure 12G).

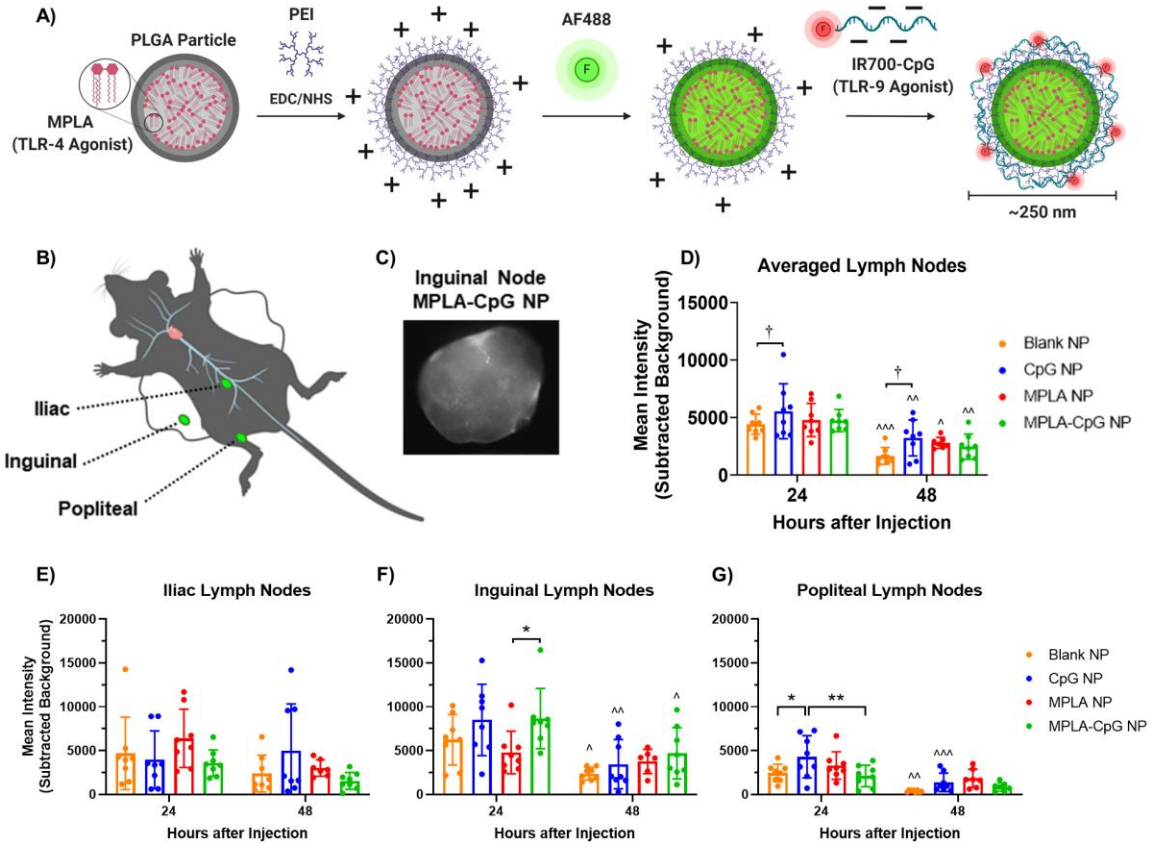

Figure 12: IR700-ODN Loaded on PLGA NP Appears in Muscle-Draining Lymph Nodes by 24 Hours. A) Scheme for loading PEI, AF488, and IR700-ODN on PLGA nanoparticles. B) Locations of iliac, inguinal, and popliteal lymph nodes in the mouse. Iliac nodes are located at the terminal segment of the abdominal aorta and origin of the common iliac artery. Inguinal (i.e., subiliac) nodes are located near the groin in a fat pad accessible by pulling away skin from the mouse. Popliteal nodes are in the popliteal fossa between the biceps femoris muscle and semitendinosus muscle. C) Near-infrared image of an inguinal lymph node 48 hours after injection of mouse with MPLA-CpG NP. D) Mean fluorescence intensities (sum of brightness normalized by ROI area) averaged between the iliac, inguinal, and popliteal lymph nodes of each mouse subject in each particle and time group. Background fluorescence (average mean fluorescence intensity of 17 saline mice nodes) subtracted from each data point. E-G) Mean fluorescence intensities of individual nodes (iliac, inguinal, and popliteal) of each mouse with background fluorescence subtracted.

**p<0.01 *p<0.05 significance between treatment groups within the same time group. ^^^p<0.001, ^^p<0.01, ^p<0.05 significance between 24 and 48 hours within same treatment group. Significance determined with Two-Way ANOVA and Sidak's multiple comparisons test. †p<0.05 between treatment groups when 24- and 48-hour data combined (main column effect). Significance for † calculated with Tukey's post-hoc test.

Data collected via flow cytometry reveals $AF488^{+}IR700^{+}$ events in the muscle, as well as $AF488^{lo}IR700^{+}$ events, indicating the IR700 ODN is dissociating from the AF488 PLGA PEI NP (Figure 13A). The $AF488^{lo}IR700^{+}$ signal diminishes between 24 and 48 hours. There are also three separate signals, $AF488^{+}IR700^{+}$, $AF488^{lo}IR700^{+}$, and $IR700^{lo}AF488^{+}$ in the draining lymph nodes. The three signals are more apparent at 48 hours (Figure 13B).

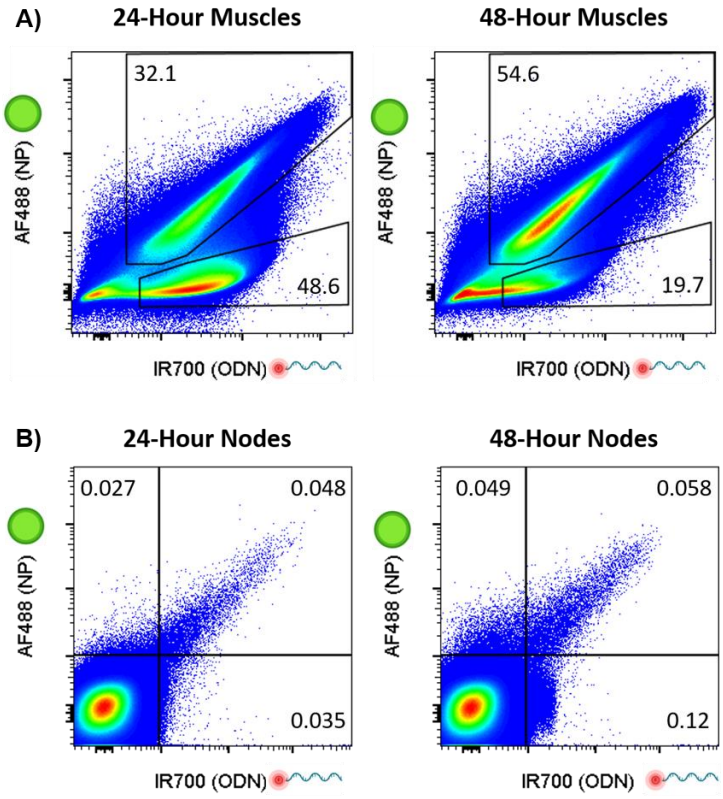

Figure 13: Scatter plots of AF488 vs. IR700 events reveal ODN dissociation from PLGA NP in the muscle and draining lymph nodes. A) Concatenated events from all muscles injected with fluorescent particles collected at 24 (left) and 48 (right) hours after injection. X axis is fluorescence in the Alexa Fluor 700 channel and Y axis is fluorescence in FITC channel; both axes are on a log-10 scale. Gates are drawn around double positive AF488-I700 events and IR700-only events. Numbers reveal percentages of events in both gates.

B) Concatenated events from draining lymph nodes of mice injected with fluorescent particles, collected at 24 (left) and 48 (right) hours post-injection. X and Y axes are the same as described in Fig. 2A. Numbers are percentage of total events in each gate.

4.2.2 Particle-Delivered MPLA and CpG ODN Differentially Regulate Innate Immune Cell Populations and Maturation in the Muscle

Muscle cell suspensions were split into two groups, each group stained with a different antibody cocktail: one targeting monocyte, macrophage, and neutrophil (MMN Panel) markers and one targeting dendritic cell markers (DC Panel). A tSNE plot based on concatenated muscle samples (from Blank, CpG, MPLA, and MPLA-CpG NP groups) was generated for each panel (Figure 14A, Figure 15A). There was a clear neutrophil cluster (purple) in the MMN Panel tSNE plot that was $Ly6G^{hi}Ly6C^{int}CD11b^{hi}$ (Figure 14B). All particles induced neutrophil infiltration into the muscle, with dual-adjuvant MPLA-CpG NP inducing the most significant increase in neutrophils (Figure 14C). The percentage of neutrophils significantly decreased between 24 and 48 hours.

There were also closely-related clusters co-expressing CD11b, CD64 (FCγRI), and F4/80, indicating populations of monocytes, macrophages, and mo-DCs. These clusters differentially expressed Ly6C – monocytes are $Ly6C^{hi}$, while macrophages and mo-DCs are $Ly6C^{int}$. The percentage of M2 macrophages, characterized by expression of CD206, were highest in the saline and Blank NP groups at 48 hours, while the CpG, MPLA, and MPLA-CpG NPs significantly decreased or prevented differentiation of this population (Figure 14E). The percentage of monocytes increased most significantly with the Blank NP and CpG NP groups compared to MPLA and MPLA-CpG NP groups (Figure 14F), while the percentage of macrophages and mo-DCs increased with MPLA NP at 24 hours

(Figure 14F). The percentage of $CD64^{+}F4/80^{+}$ cells expressing CCR7 slightly increased in the MPLA-CpG NP group at 24 hours (Figure 14G).

In the DC marker tSNE plot, there was a clear $CD11b^{lo}CD11c^{hi}$ cluster, most likely the neutrophils and monocytes distinguished in the MMN panel (Figure 15A-B). However, the $CD11c^{+}MHCII^{+}$ population, traditionally recognized as DCs, was much smaller compared to the population of $CD64^{+}F4/80^{+}$ cells. The $CD11c^{+}MHCII^{+}$ population statistically increased from 24 to 48 hours post-injection, and most prominently with Blank NP and MPLA NP groups (Figure 15C). It could be that CpG ODN prevents the increase of $CD11c^{+}MHCII^{+}$ cells, or the control (GpC) ODN promotes their expansion. This trend remained the same for $CD11c^{+}MHCII^{+}CD11b^{hi}$ cells (cDC2) as well as $CD11c^{+}MHCII^{+}CD103^{+}$ cells (cDC1). MPLA NP and MPLA-CpG NP groups most significantly increased CD40 expression by cDC2 and cDC1, while simultaneously decreasing CD86 expression (Figure 15E-F, 15H-I). CD40 expression increased significantly for MPLA and MPLA-CpG NP groups between 24 and 48 hours, while CD86 expression decreased significantly for CpG NP mice between 24 and 48 hours. Expression of CD301b was low but overlapped with $CD11c^{+}MHCII^{+}$ cells and $CD301b^{+}$ cells shared the same trends as cDC2 (data not shown). B220 expression was barely detectable, indicating low presence of pDCs or B cells in the muscle (Figure 15B).

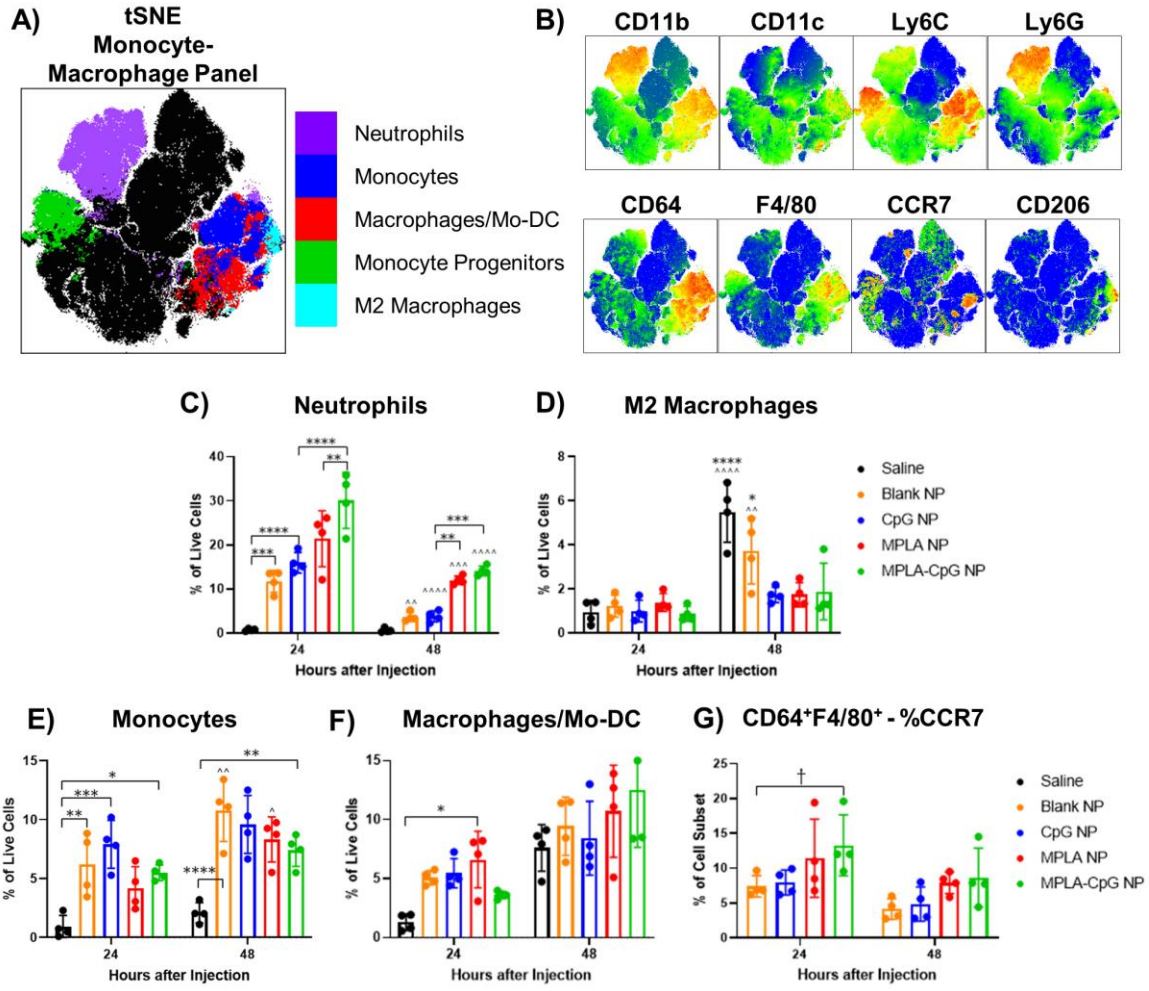

Figure 14: PLGA PEI NP with MPLA and/or CpG differentially regulate monocyte, macrophage, and neutrophil populations in the muscle. A) tSNE clusters overlaid with neutrophil, monocyte and macrophage populations and B) corresponding heatmaps of each marker included in the panel. C) Percentage of live cells expressing neutrophil phenotype ($Ly6G^{hi}Ly6C^{int}$). D) Percentage of live cells expressing monocyte/macrophage phenotype ($CD64^{+}F4/80^{+}$). E) Percentage of live cells expressing CD64, F4/80, and CD206 (M2 macrophages). F) Percentage of live cells that are $Ly6C^{hi}$, $CD64^{+}$, $F4/80^{+}$ (circulating monocytes) and G) Percentage of live cells that are $Ly6C^{int}$, $CD64^{+}$, $F4/80^{+}$ (differentiating monocytes). H) Percentage of $CD64^{+}F4/80^{+}$ cells that are expressing CCR7. Saline group was dropped from this graph because allophycocyanin and Alexa Fluor 700 channels had strong spectral overlap and saline groups did not have any particles. With the high fluorescence of particles at the muscle, compensation in the allophycocyanin channel will be much different between saline and particle groups. ****$p<0.0001$, ***$p<0.001$ **$p<0.01$ *$p<0.05$ significance comparing all groups within the same time point according to Two-Way ANOVA and Tukey test. ^^^^$p<0.0001$, ^^^$p<0.001$, ^^$p<0.01$, ^$p<0.05$ significance comparing 24 and 48 hours within same particle group according to Two-Way ANOVA and Sidak's multiple comparison test. †$p<0.05$ significance between two groups according to T-test, not significant in a Two-Way ANOVA.

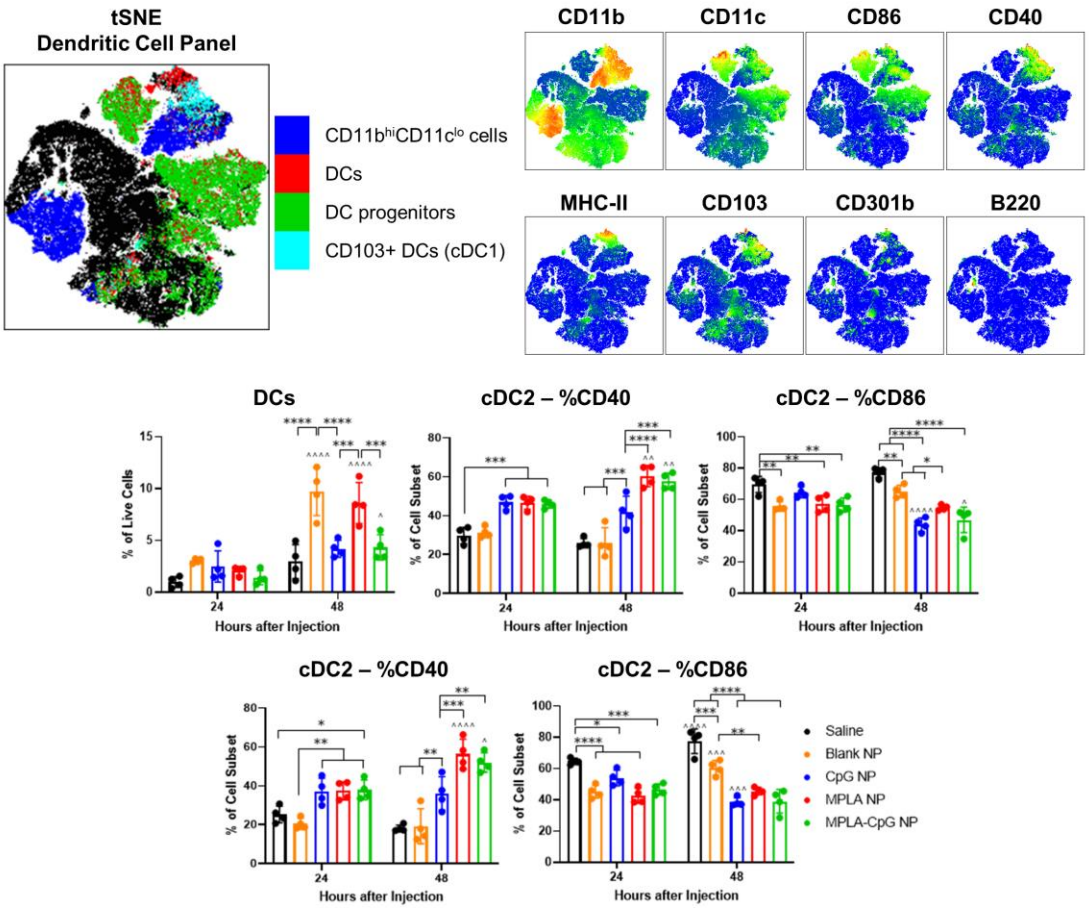

Figure 15: PLGA PEI NP with MPLA and/or CpG differentially regulate DC populations and their expression of costimulatory molecules, CD40 and CD86, in the muscle. A) tSNE clusters overlaid with DC populations and B) corresponding heatmaps of each maker included in the panel. C) Percentage of live cells expressing DC phenotype ($CD11c^{+}MHCII^{+}$). D) Percentage of live cells expressing cDC2 phenotype ($CD11c^{+}MHCII^{+}CD11b^{hi}$). E-F) Percentage of cDC2 expressing CD40 and CD86. G) Percentage of live cells expressing cDC1 phenotype ($CD11c^{+}MHCII^{+}CD103^{+}$). H-I) Percentage of cDC1 expressing CD40 and CD86. ****$p<0.0001$, ***$p<0.001$ **$p<0.01$ *$p<0.05$ significance comparing all groups within the same time point according to Two-Way ANOVA and Tukey test. ^^^^$p<0.0001$, ^^^$p<0.001$, ^^$p<0.01$, ^$p<0.05$ significance comparing 24 and 48 hours within same particle group according to Two-Way ANOVA and Sidak's multiple comparison test.

4.2.3 MPLA and CpG ODN Loaded on PLGA PEI NP Differentially Regulate APC Populations and CD86 Expression in Muscle-Draining Lymph Nodes

In iliac (IL), inguinal (IG), and popliteal (PO) lymph nodes, CpG NP and MPLA-CpG NP groups increased percentages of B cells at 48 hours (Figure 16A), while CpG NP significantly increased populations of pDCs at 48 hours (Figure S9B). Increases in CD86 expression on B cells were more prominent at 24 hours (Figure S9C). At this time point, CD86 expression increased with MPLA and MPLA-CpG NP in iliac lymph nodes, Blank NP and CpG NP in inguinal lymph nodes, and MPLA-CpG NP in popliteal lymph nodes, highlighting how the isolation of different draining lymph nodes can shape conclusions on immune response (Figure S9C). CpG NP continued to upregulate CD86 on B cells, compared to controls, in the iliac and inguinal nodes at 48 hours (Figure S9C). Higher percentages of pDCs expressed CD86, and statistical trends resembled B cells in lymph nodes at the 24-hour time point (Figure S9D). CD86 expression did not decrease at 48 hours (as seen with B cells) and was upregulated by different particle groups at this time point depending on the lymph node: all particle groups upregulated pDC-CD86 expression in the iliac node, only Blank, CpG, and MPLA-CpG NP did so in the inguinal node, and only CpG NP and MPLA NP groups increased pDC-CD86 expression in the popliteal nodes (Figure S9D).

There were no major changes in populations of cDC1 and cDC2 in lymph nodes in response to particles, except CpG NP statistically increased all types in the popliteal node at 48 hours (Figure S10). cDC1 and cDC2 are expressed in the peripheral and lymphoid tissues, although CD103 is only expressed on rare populations of lymphoid cDC1 in the marginal zone of lymph nodes or in intestinal draining lymph nodes (including the iliac nodes).

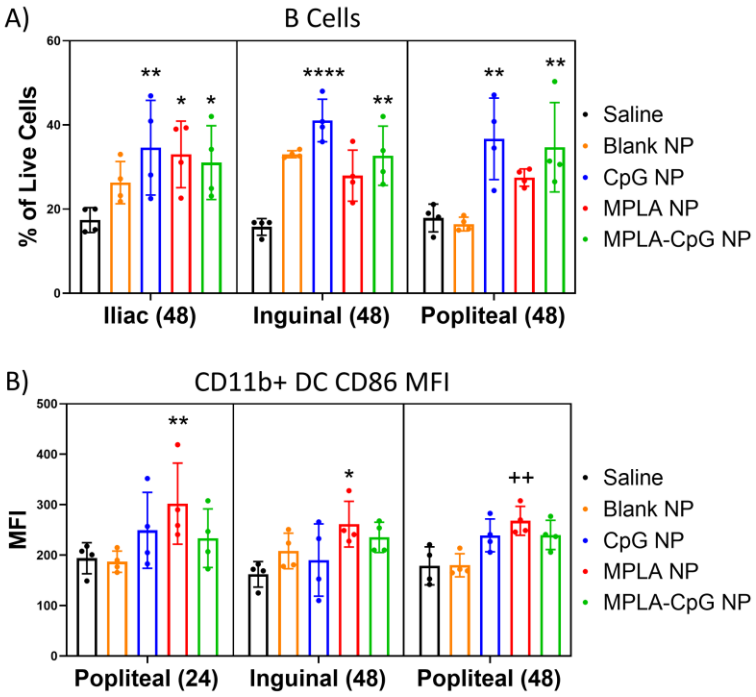

Figure 16: CpG and MPLA-CpG NPs increase B cell populations while MPLA NPs increase CD86 expression on $CD11b^+$ DCs in muscle-draining lymph nodes 24 to 48 hours after intramuscular injection. A) Percentage of B cells ($B220^+MHCII^+CD11c^-$) out of live cells in the iliac, inguinal, and popliteal lymph nodes at 48 hours. B) Median fluorescence intensity of CD86 on viable $CD11b^+CD11c^+MHCII^+$ DCs in the popliteal nodes at 24 hours, and inguinal and popliteal nodes at 48 hours. *p<0.05, **P<0.01, ****p<0.0001 from Two Way ANOVA with Tukey multiple comparison test and $^{++}$p<0.01 with One Way ANOVA (Popliteal-48hr group alone) and Tukey test.

Adjuvant groups differentially upregulated CD86 expression on cDC subsets in lymph nodes (Figure 16B, Figure S10). cDCs in the lymph node express higher percentages of CD86 compared to B cells and pDCs, therefore median fluorescence intensity of CD86 was compared with statistical analysis to detect more nuanced changes in expression. CD86 on cDC2 was statistically increased by MPLA NP in the popliteal node at 24 hours, and in inguinal and popliteal nodes at 48 hours (Figure 16B). Patterns of CD86 expression by cDC1 followed B cells and pDCs. cDC1 upregulated CD86 at 24 hours in response to MPLA and MPLA-CpG NP in iliac nodes, and Blank NP and CpG NP in inguinal nodes (Figure S10).

CHAPTER 5: AIM 2.1. EVALUATING HOW RLR- AND TLR-TARTETING PLGA NANOPARTICLES DIRECT BONE MARROW-DERIVED DC CYTOKINE SECRETION AND T CELL ACTIVATION IN VITRO

4.3 Motivation

The goal of this sub-aim is to identify particulate adjuvant combinations that enhance APC and T cell responses in isogeneic mixed lymphocyte reaction (iso-MLR) assays in vitro. Single and combination adjuvants, including TLR agonists MPLA (TLR4), CpG (TLR9), R848 (TLR7), and RIG-I ligand PUUC, on PLGA-PEI NP were screened to elucidate which adjuvants have the potential to enhance the immune response to SARS-CoV-2 subunit vaccines.

4.4 Materials and Methods

4.4.1 Synthesis of PUUC RNA

HCV-mimicking poly-U/UC (PUUC) RNA was transcribed from synthetic DNA ODN templates (Integrated DNA Technologies, PAGE-purified Ultramer Oligos) using the MEGAshortscript™ T7 Transcription Kit (Ambion, Thermo Fisher). The custom DNA templates were as follows: 5'-TAA TAC GAC TCA CTA TAG GCC ATC CTG TTT TTT TCC CTT TTT TTT TTT CTT TTT TTT TTT TTT TTT TTT TTT TTT TTT TTT TTC TCC TTT TTT TTT CCT CTT TTT TTC CTT TTC TTT CCT TT-3' and 5'-AAA GGA AAG AAA AGG AAA AAA AGAG GAA AAA AAA AGG AGA AAA AAA AAA AAA AAA AAA AAA AAA AAA AAA AAA AAA GAA AAA AAA AAA GGG AAA AAA ACA GGA TGG CCT ATA GTG AGT CGT ATT A-3’. RNA was purified through alcohol

precipitation and measured using the Nucleic Acid Quantification feature on the plate reader (Biotek). PUUC was resuspended in RNAse/DNAse free H_2O (Boston BioProducts) at 1 mg/mL and frozen at -80°C for long-term storage.

4.4.2 Preparation of PLGA-PEI Nanoparticles and Loading of Adjuvants

PLGA-PEI nanoparticles were prepared as described in Chapter 4 (Aim 1.2). For preparing high-density MPLA NP, MPLA-PHAD® (Avanti), also known as GLA, was added to the primary PLGA emulsion (6 µg MPLA-PHAD per mg of NP).[180] For R848 NP, non-water-soluble R848 (STEMCELL Technologies) was added to the primary emulsion (5 µg per mg of NP). R848 encapsulation was quantified by dissolving PLGA PEI NP in DMSO and measuring absorbance at 324 nm on a plate reader (BioTek).[233] R848 encapsulation efficiency ranged from 60% to 96%. PLGA NP concentration was always adjusted to match the desired dose of R848. CpG ODN (InvivoGen), Poly(I:C) (InvivoGen) and PUUC were loaded onto PLGA-PEI NP in sodium phosphate buffer (pH 6.5, 5 mg NP per mL) in RNAse-DNAse free low-adhesion 2 mL polypropylene tubes, vortexed for 30 seconds, and rotated overnight at 4°C. PLGA PEI NP were centrifuged at 10,000 x g for 10-20 minutes, and ssRNA (PUUC), dsRNA (Poly(I:C), ssDNA (CpG ODN) loading was indirectly calculated by measuring the A_{260}/A_{280} ratio with the Nucleic Acid Quantification feature on the BioTek plate reader. Adjuvant-loaded PLGA-PEI nanoparticles will be referred to in this section as PLPs.

4.4.3 Bone-marrow derived Dendritic Cell (BMDC) Culture

GM-CSF-BMDC cultures were prepared using similar methods to Aim 1.2. However, the BMDC density was altered to match consistency with research conducted by Pradhan et al.[180] Instead of 12 mL per petri dish, 20 mL of BMDCs in RPMI complete medium was added to each dish at 1 million cells/mL. For GM-CSF-BMDCs the medium only contained GM-CSF (20 ng/mL) and no IL-4. For FLT3-derived BMDCs, bone marrow cells were cultured with human FLT3L (PeproTech) concentrated at 200 ng per mL complete RPMI medium. The cells were plated at 2 million cells/mL of medium for 9 days in a 6-well plate, 10 million cells per well. There was no change in medium. Loosely adherent GM-CSF-BMDC and FLT3L-BMDCs were harvested at days 7 and 9 of culture, respectively, with vigorous pipetting and plated in fresh medium for further experiments. All bone marrow cells were collected from 5- to 10-week old female or male Balb/cJ mice tibiae and femurs.

4.4.4 Characterizing APC Subsets in BMDC Culture with Flow Cytometry

FLT3L and GM-CSF BMDCs were washed with PBS and stained with 1:1000 Zombie Green Fixable Viability Dye (Biolegend). BMDCs were blocked with TruStain™ FcX (anti-mouse CD16/CD32, Biolegend) in FACS buffer (0.1% sodium azide, 1 mM EDTA, and 5% v/v FBS in PBS) at 4°C for 30 minutes. The fluorescent antibody cocktail included anti-mouse CD11b (BUV395, BD), CD11c (BV421, Biolegend), B220 (allophycocyanin, Biolegend), Ly6C (BV711, Biolegend), Ly6G (BV786, Biolegend), CD64 (PE, Biolegend), F4/80 (PE/Cyanine5, Biolegend), and MHC-II (allophycocyanin/Cyanine7, Biolegend). Cells were analyzed using the BD LSRFortessa and FlowJo software.

4.4.5 Iso-Mixed Lymphocyte Reaction

PLPs and the S1 subunit of the SARS-CoV-2 spike protein (Biotechne) (100 ng/500,000 BMDCs/mL media) were added to GM-CSF or FLT3L-cultured BMDCs in a U-bottom 96 well plate. Each well contained 100,000 BMDCs and PLP concentrations were adjusted according to Table 1. The cells were incubated with PLPs for 24 hours. To isolate T cells, spleens from male and female Balb/cJ mice were dissociated in 2 mg/mL Collagenase D in OptiMEM (Gibco) and filtered through a 40 µm cell strainer. T cells were magnetically separated from other splenocytes using the Mouse Pan-T Cell Isolation Kit II (Miltenyi Biotec), labeled with CellTrace™ CFSE (Thermo Fisher), and resuspended in complete RPMI medium at 1 million cells/mL. BMDC-PLP U-bottom plates were centrifuged at 500 x g for 5 minutes, and supernatants were collected to quantify BMDC pro-inflammatory cytokine and interferon secretion using ELISA and Luminex kits. 200,000 T cells were added to each well containing BMDCs and PLPs. After 72 hours, cells were centrifuged, and supernatants collected for future IFN-γ and IL-4 ELISAs. T cells were stained with Zombie UV to exclude dead cells, and stained with anti-mouse CD3 (BV786, Biolegend), anti-mouse CD4 (allophycocyanin, Biolegend) and anti-mouse CD8a (PE, Biolegend) to identify $CD4^+$ and $CD8^+$ T cells. A well containing only CSFE-stained T cells was included as a non-proliferative control. Percentages of proliferating T cells were calculated by gating on the reduced FITC signal. The signal of CFSE decreases as T cells divide.

Table 1: Single and combination adjuvant loading on PLGA NP and doses for BMDC culture.

Particulate Adjuvants	PAMP combinations	Loading level (ug/mg NP)	Dose for BMDCs (ng/1 million cells)
PLGA-MPLA +CpG	MPLA	6 ug/mg	50 ng/mL
	CpG	60 ug/mg	500 ng/mL
PLGA-R848+PUUC	PUUC	5 ug/mg	100 ng/mL
	R848	4.8 ug/mg	100 ng/mL
PLGA-MPLA+PUUC	PUUC	6 ug/mg	100 ng/mL
	MPLA	6 ug/mg	100 ng/mL
PLGA-CpG+PUUC	PUUC	6 ug/mg	100 ng/mL
	CpG	30 ug/mg	500 ng/mL
PLGA-Poly(I:C)+PUUC	PUUC	6 ug/mg	100 ng/mL
	Poly(I:C)	6 ug/mg	100 ng/mL
PLGA-MPLA	MPLA	6 ug/mg	100 ng/mL
PLGA-PUUC	PUUC	6 ug/mg	100 ng/mL
PLGA-CpG	CpG	60 ug/mg	500 ng/mL
PLGA-Poly(I:C)	Poly(I:C)	6 ug/mg	100 ng/mL

4.4.6 Analysis of BMDC Cytokine Secretion

Supernatants from FLT3L and GM-CSF BMDC culture after 24-hr incubation with PLGA NP formulations and SARS-CoV-2 S1 Spike-S1 protein were frozen at -20°C. Supernatants were analyzed for IFN-β and IFNλ3 using DuoSet ELISA kits from R&D Systems. IFN-γ, TNF-α, IL-12p70, IL-1β, IL-6, IL-10, and IL-27 concentrations were measured using a customized Luminex® kit (R&D Systems). Supernatants were diluted 4-fold for all cytokines except for IL-1β and IL-6, in which case they were diluted 8-fold. Supernatants were analyzed in triplicate for each experimental condition. All cytokine concentration values were calculated from standard curves. Cytokine concentrations were averaged for each treatment and BMDC group, and input into JMP Pro 16 (SAS). For optimal visualization of all groups, z-scores were calculated for each individual cytokine

across all groups, by using the "Standardize" feature in JMP. For example, in Figure 18, z-scores were calculated across each row to view relative increases and decreases in cytokine concentration between PLP treatment groups. Z-scores were displayed in a heatmap with 3-part colorbar using Graphpad software.

4.5 Results

4.5.1 FLT3L and GM-CSF Bone Marrow-Derived Dendritic Cell Cultures are Comprised of Different APC Subsets

FLT3L and GM-CSF differentially express monocyte, macrophage, and dendritic cell markers (Figure 17). FLT3L BMDCs are predominantly comprised of plasmacytoid DCs ($B220^{+}Ly6C^{+}CD11c^{+}MHCII^{lo}Ly6G^{lo}$) and conventional DCs ($CD11c^{+}MHCII^{hi}CD64^{lo/-}F4/80^{lo/-}$). GM-CSF BMDCs are mainly monocytes ($Ly6C^{hi}CD11c^{-}$), monocyte-derived macrophages ($CD64^{+}F4/80^{+}$) and monocyte-derived DCs ($CD64^{+}F4/80^{+}$), which are also referred to as inflammatory DCs (see Background and Aim 1.1). There is some macrophage survival in FLT3L culture, and neutrophil survival in GM-CSF culture.[237,238]

4.5.2 GM-CSF and FLT3L BMDC Secrete Distinct Cytokine Patterns in Response to Combination Adjuvants

PLGA-PEI nanoparticles with different combinations of PRR agonists, including TLR ligands CpG, MPLA, and R848, as well as RLR ligand, PUUC, were incubated with GM-CSF and FLT3L BMDCs for 24 hours. SARS-CoV-2 Spike S1 protein was also included at a dose of 100 ng per 100,000 BMDCs. Supernatants were collected to measure concentrations of interferons, IFN-β, IFN-λ3, and IFN-γ, as well as cytokines TNF-α, IL-

12p70, IL-1β, IL-6, IL-10, and IL-27. Overall, GM-CSF BMDCs secreted more IFN-β, TNF-α, and IL-6 compared to FLT3L BMDCs (Figure 18). With GM-CSF BMDCs, MPLA-CpG NPs increased IL-12p70 and IL-10 secretion (Figure S14), MPLA-PUUC NPs increased IL-1β and IL-27 secretion, and R848-PUUC NPs increased IL-12p70 and IL-27 secretion compared to single-adjuvant particles (Figure 19).

Overall, FLT3L BMDC secreted more IL-10, IFN-γ, and IFN-λ3 compared to GM-CSF BMDCs, and CpG was a strong inducer of innate immune cytokines in FLT3L BMDC culture (Figure 18). MPLA-CpG NPs promoted stronger IFN-γ and TNF-α responses in FLT3L BMDC culture compared to single adjuvants (Figure S14). CpG-PUUC produced synergistic and antagonistic effects depending on the BMDC culture type (Figure 20). With GM-CSF BMDCs, CpG-PUUC NPs synergistically increased IFN-β secretion, while in FLT3L BMDC culture, CpG-PUUC NPs decreased IFN-λ3 levels compared to single-adjuvant particles. Across multiple trials, female BMDCs produced more IFN-β and IFN-λ3 compared to male BMDCs in response to adjuvanted particles, particularly MPLA-PUUC and R848-PUUC NPs (Figure 21).

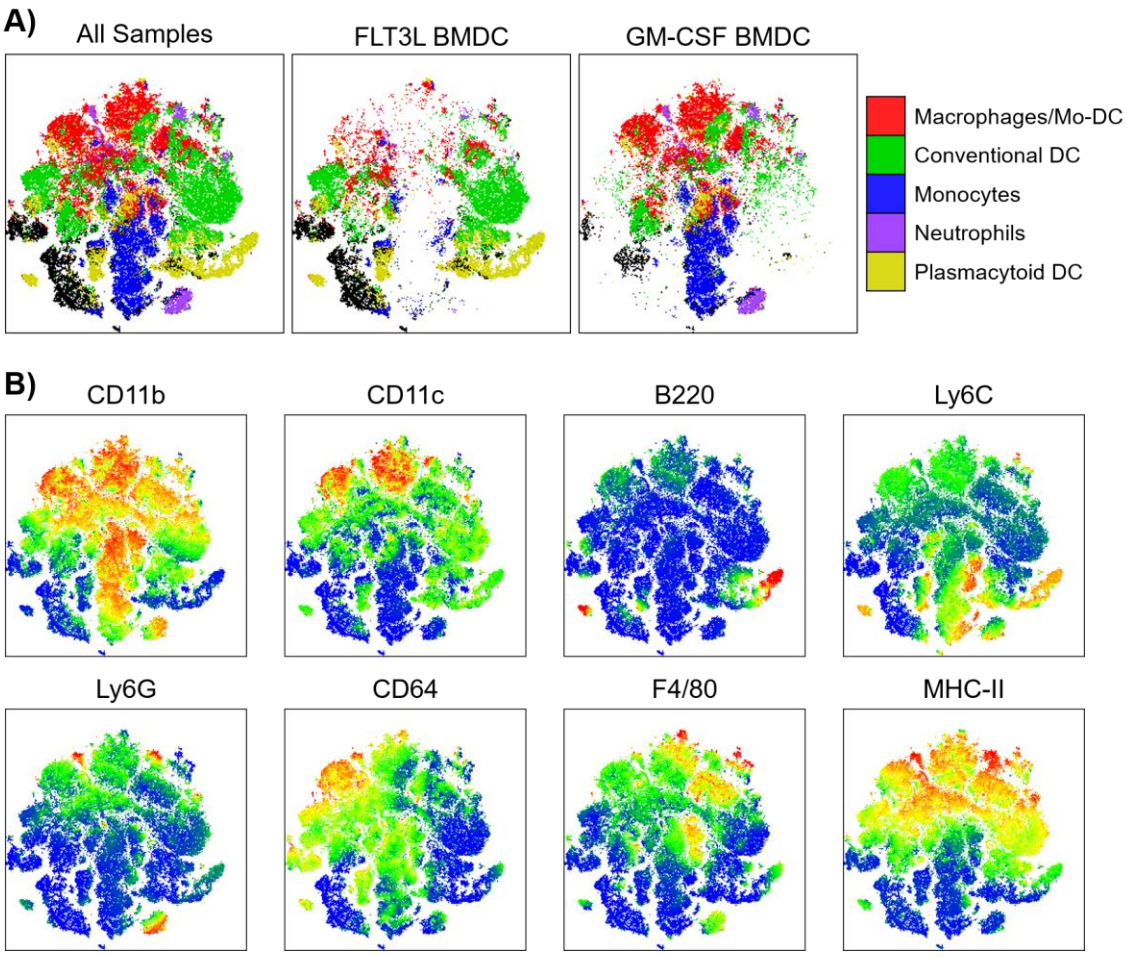

Figure 17: FLT3L and GM-BMDCs are comprised of different APC subsets. A) tSNE plots of FLT3L and GM-CSF BMDCs with overlaid clusters of APC subsets. Neutrophils are $Ly6G^{hi}Ly6C^{+}$, Monocytes are $Ly6C^{hi}CD11c^{-}$, Macrophages/Mo-DCs are $CD64^{+}F4/80^{-}$, cDCs are $CD11c^{+}MHCII^{+}CD64^{lo}F4/80^{lo}$, pDCs are $B220^{+}Ly6C^{+}CD11c^{+}MHCII^{lo}$. B) Heatmaps of innate immune cell marker expression.

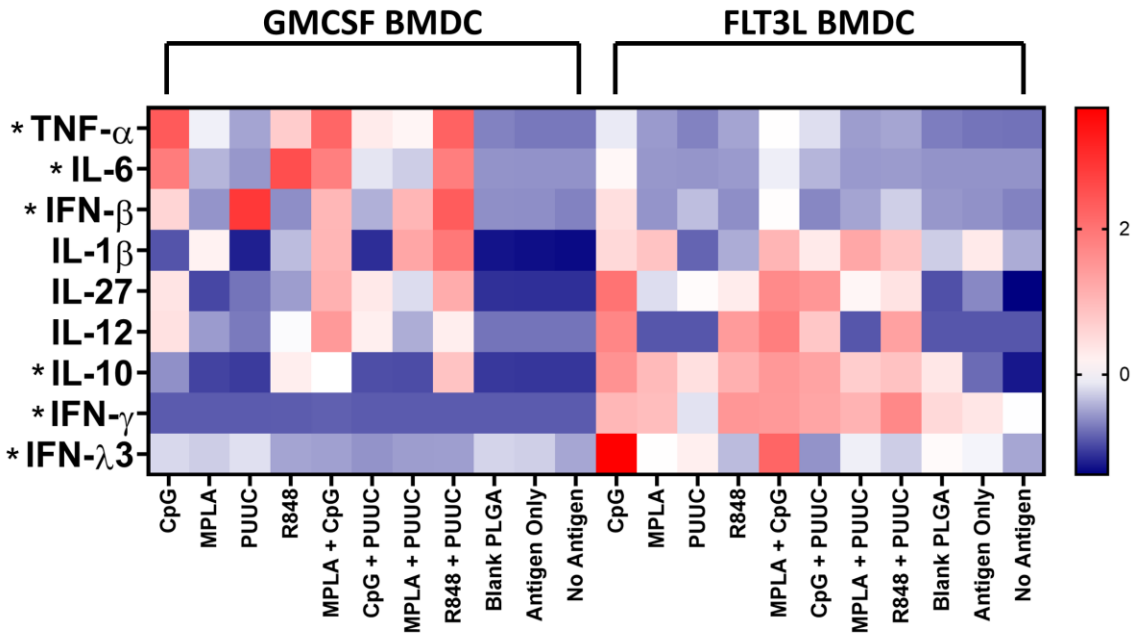

Figure 18: FLT3L and GM-CSF BMDCs differentially secrete cytokines in response to adjuvanted particles. Cytokine concentrations (pg/mL) standardized across each row. Scale bar for standardization score, also known as z-score, located to the right of the heatmap. Higher z scores depicted with red color while lower z scores depicted with blue. *$p<0.05$ between GM-CSF and FLT3L BMDC cytokine secretion calculated with multiple t tests (one unpaired t test per row). Sample size for each square is 3 replicates.

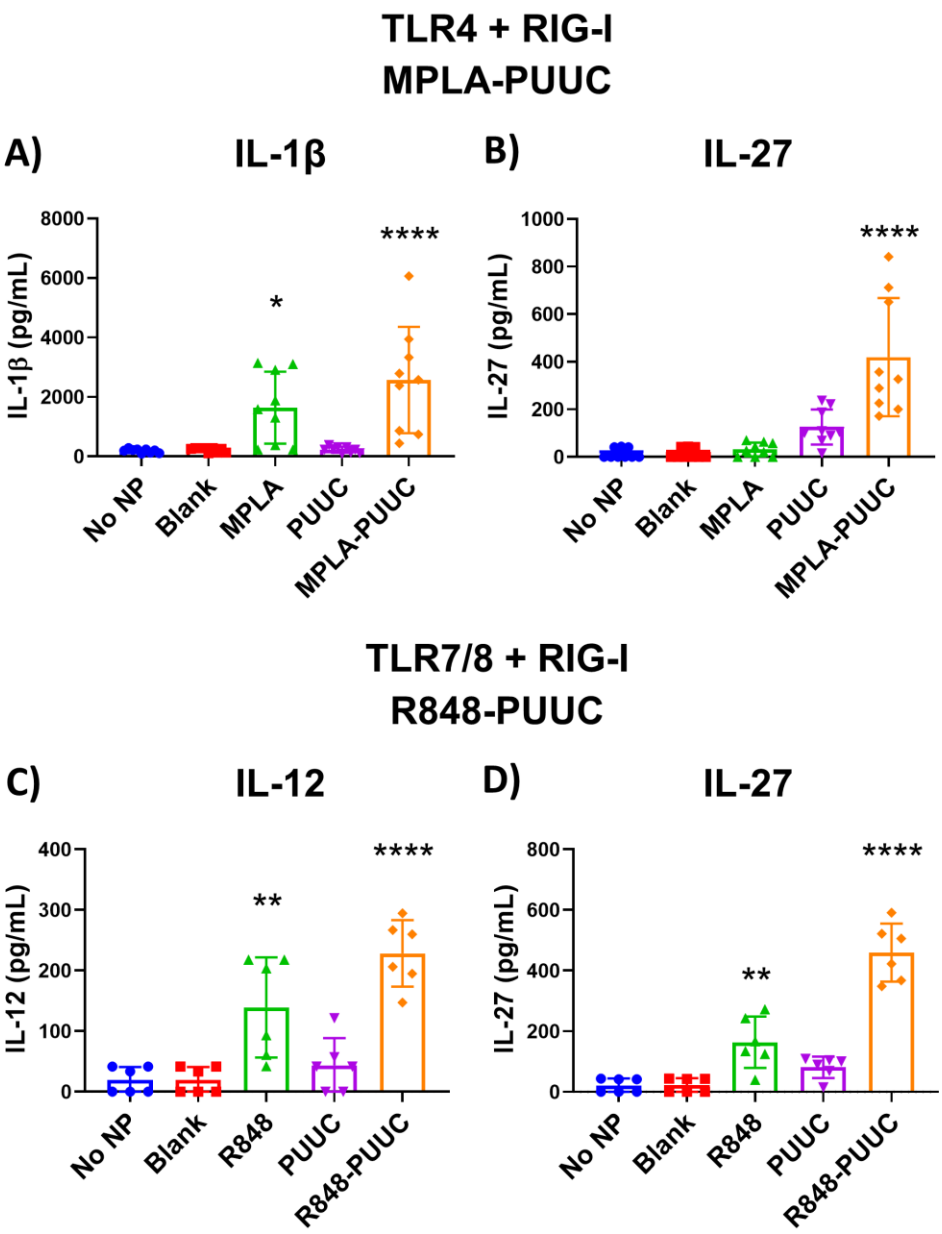

Figure 19: MPLA-PUUC and R848-PUUC increase proinflammatory cytokine secretion by GM-CSF BMDCs. A-B) IL-1β and IL-27 secretion by GM-CSF BMDCs in response to 24-hr incubation with MPLA-PUUC NPs. C-D) IL-12p70 and IL-27 secretion by GM-CSF BMDCs in response to 24-hr incubation with R848-PUUC NPs. *p<0.05, **p<0.01, ****p<0.0001 calculated with One-way ANOVA and Tukey multiple comparisons test.

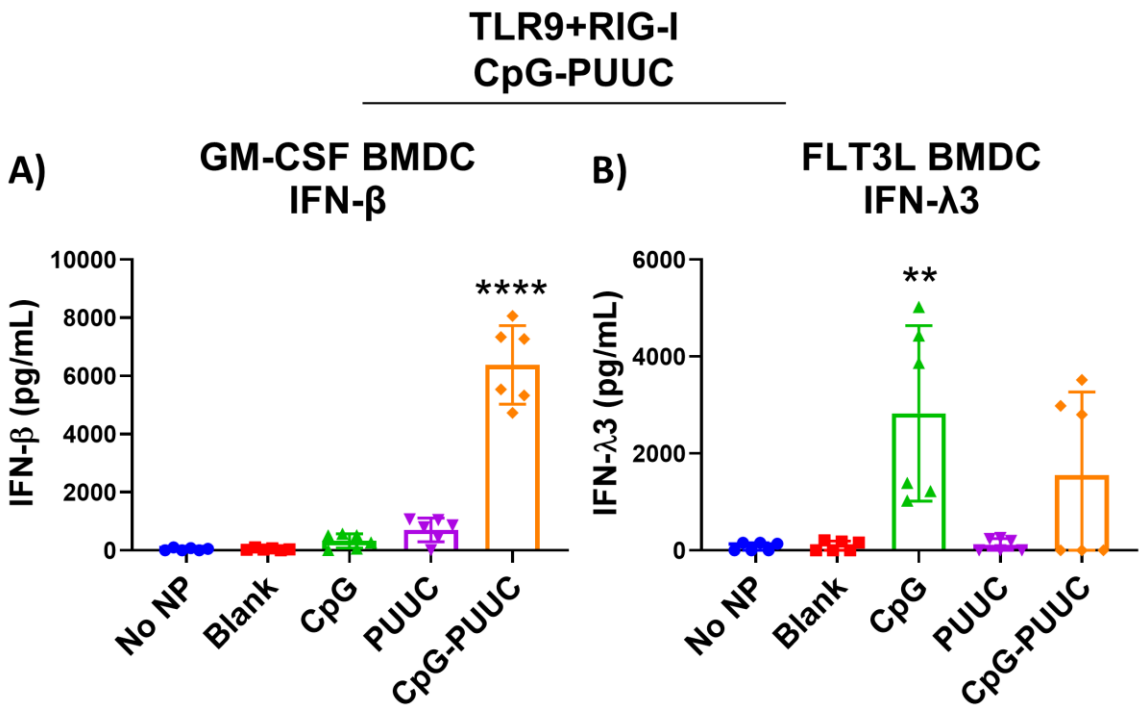

Figure 20: CpG-PUUC impacts interferon production in GM-CSF and FLT3L BMDCs. A) CpG-PUUC NPs synergistically increase IFN-β secretion by GM-CSF BMDCs after 24-hr incubation. B) CpG-PUUC NPs antagonistically decrease IFN-λ3 secretion by FLT3L BMDCs after 24-hr incubation. **p<0.01, ****p<0.0001 calculated with One-way ANOVA and Tukey multiple comparisons test.

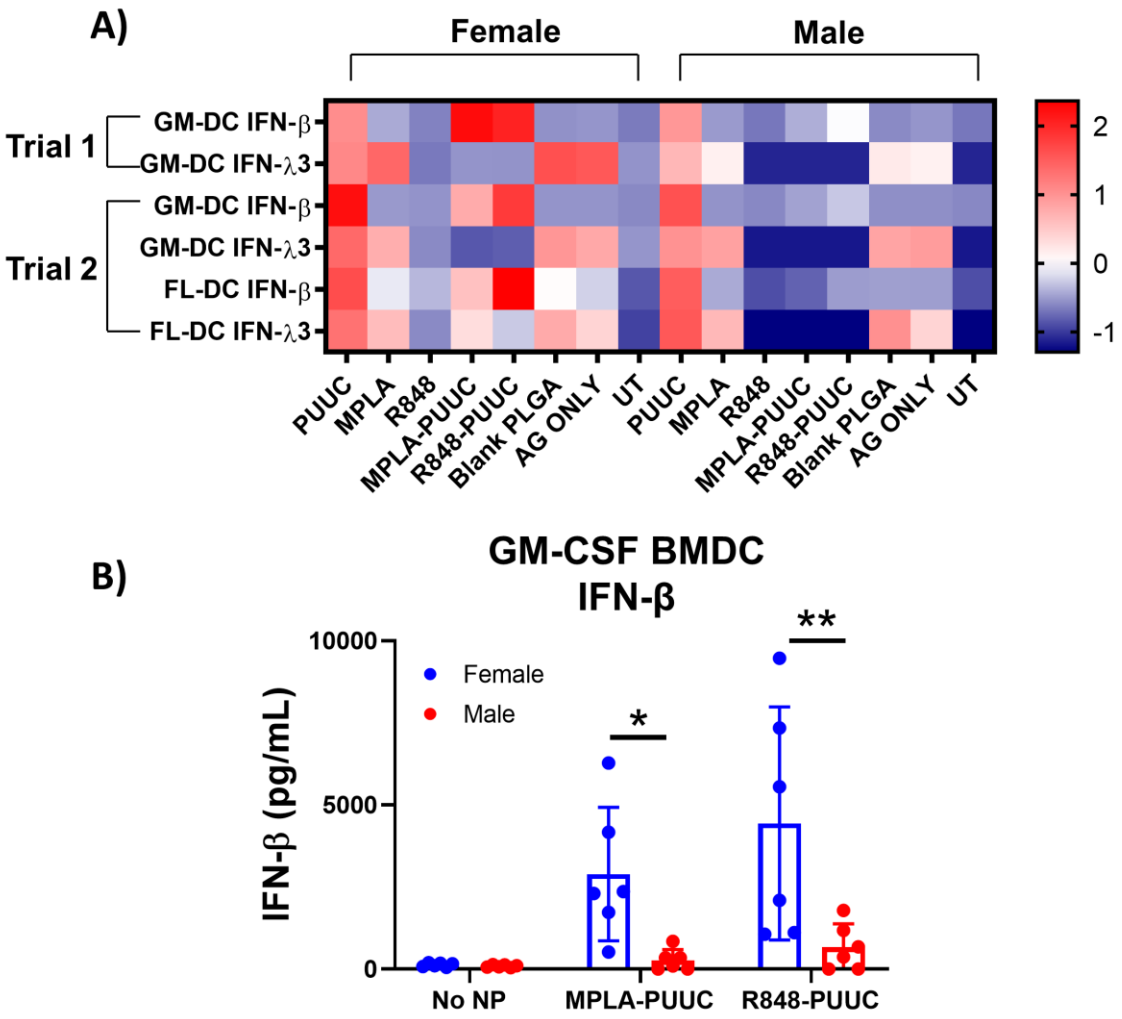

Figure 21: Female and male BMDCs differentially secrete IFN-β and IFN-λ3 in response to combination adjuvants. A) Heatmap of z-scores (mean cytokine concentration in pg/mL standardized across each row) with red color indicating higher relative z-score and blue depicting lower relative z-score. Sample size for each square is three replicates. B) MPLA-PUUC and R848-PUUC NPs induce more IFN-β secretion by female GM-CSF BMDCs compared to male GM-CSF BMDCs. **p<0.01 Two-way ANOVA with Tukey multiple comparisons test.

4.5.3 GM-CSF and FLT3L BMDCs Selectively Respond to PRR-Targeted Adjuvants to Induce CD8$^+$ T Cell Proliferation and T Cell Death in Iso-MLR Assay

After BMDCs were incubated with PLGA NP adjuvant formulations for 24 hours, supernatants were removed, and T cells were added in a 2:1 ratio to BMDCs. T cells and BMDCs were cultured together for 72 hours, supernatants were collected to measure IFN-γ and IL-4, while T cells were stained to measure proliferation by flow cytometry. GM-CSF BMDC statistically increased CD8$^+$ T cell proliferation in the presence of MPLA PLGA NP, while other adjuvants, including combination adjuvants significantly decreased proliferative CD4$^+$ and CD8$^+$ T cells (Figure 22A-B). All combination adjuvants statistically increased T cell death compared to controls and single adjuvant formulations (Figure 22C). FLT3L BMDCs strongly induced CD8$^+$ T Cell proliferation when cultured with CpG PLGA NP, and even more so with MPLA-CpG NP and CpG-PUUC NP (Figure 23B). Culturing FLT3L BMDCs with all PLGA NP formulations induced T Cell Death, most strongly with MPLA-CpG NP (Figure 23C).

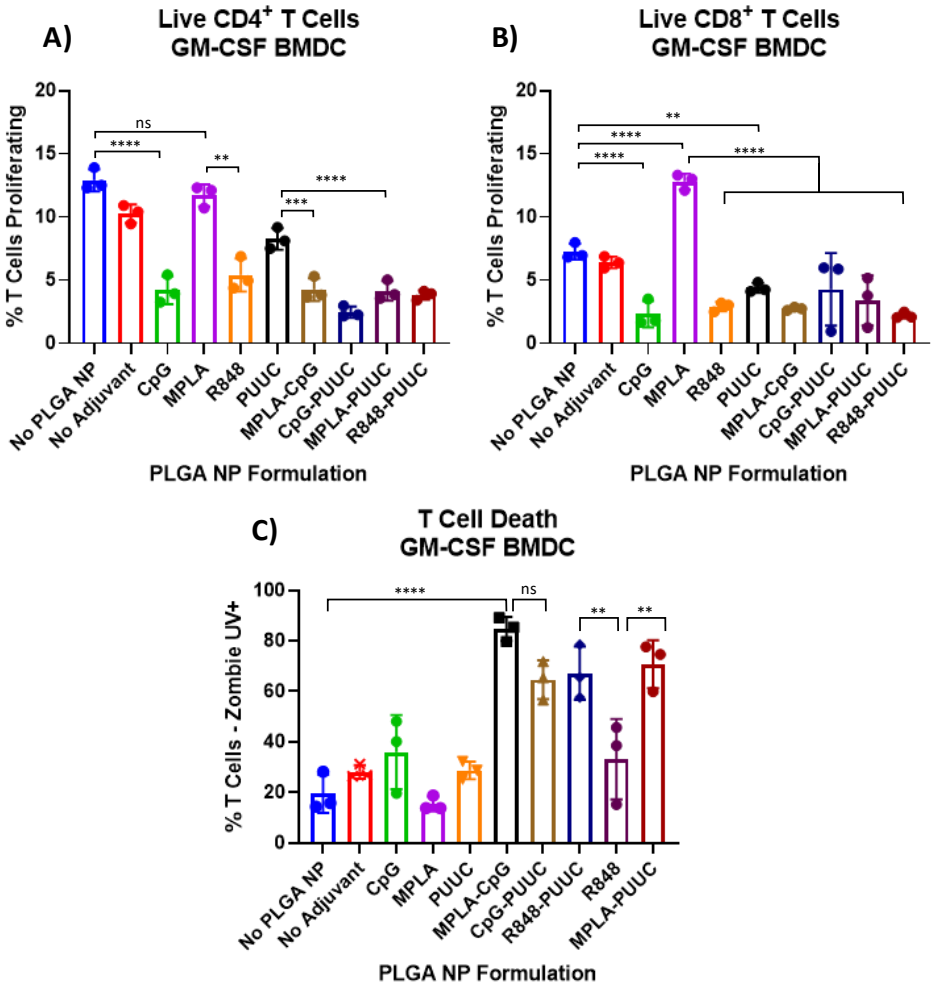

Figure 22: GM-CSF BMDCs Promote $CD8^+$ T Cell Proliferation in Response to MPLA PLGA NP and Combination Adjuvants Induce T Cell Death. A) Percentage of live $CD3^+CD4^+$ T cells proliferating in presence of GM-CSF BMDC, gated on diminished CFSE signal (see Supplementary section for example). B) Percentage of live $CD3^+CD8^+$ T cells proliferating in presence of GM-CSF BMDCs. C) Percentage of $CD3^+$ Cells expressing Zombie UV (dead cells). *p<0.05. **p<0.01, **p<0.001, ****p<0.0001 One-Way ANOVA and Tukey Test for multiple comparison

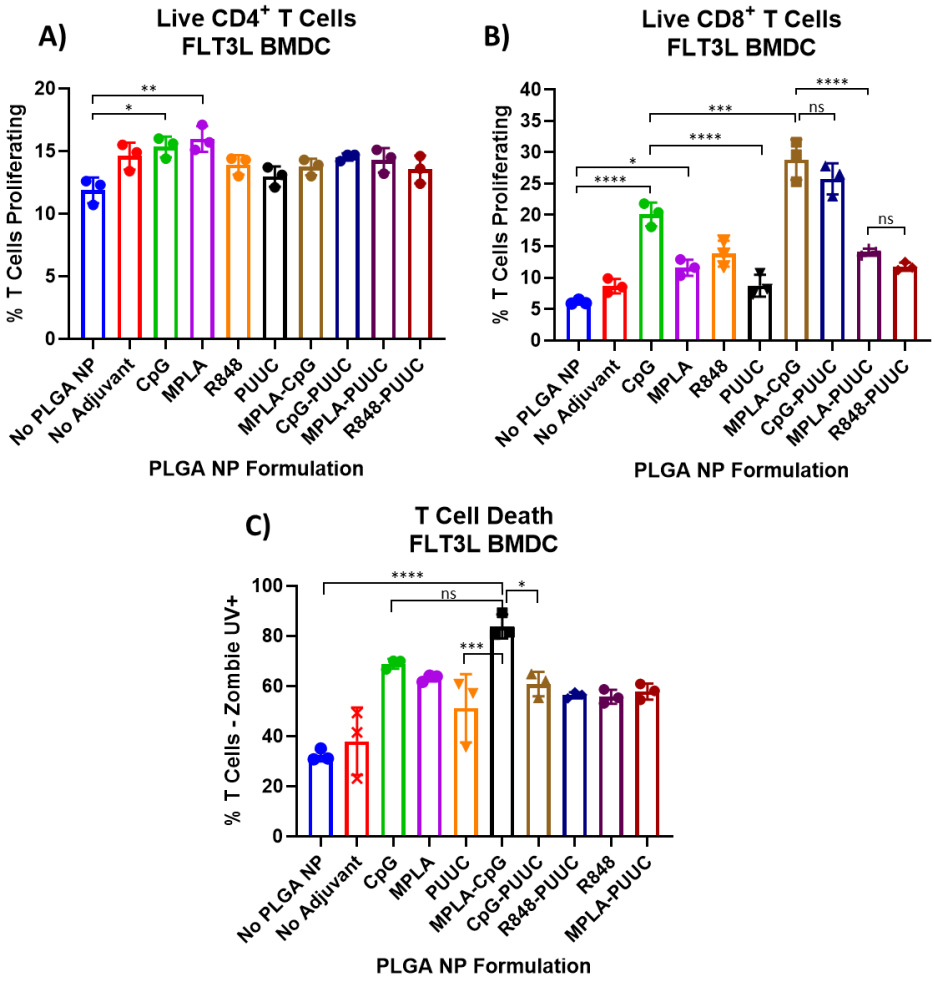

Figure 23: FLT3L BMDCs Promote $CD8^+$ T Cell Proliferation in Response to Single and Combination Adjuvants with CpG. A) Percentage of live $CD3^+CD4^+$ T cells proliferating in presence of FLT3L BMDC, gated on diminished CFSE signal (see Supplementary section for example). B) Percentage of live $CD3^+CD8^+$ T cells proliferating in presence of FLT3L BMDCs. C) Percentage of $CD3^+$ Cells expressing Zombie UV (dead cells). *p<0.05. **p<0.01, **p<0.001, ****p<0.0001 One-Way ANOVA and Tukey Test for multiple comparison

CHAPTER 6: AIM 2.2. CHARACTERIZING INNATE AND ADAPTIVE IMMUNE RESPONSES TO INTRANASAL VACCINATION WITH CO-DELIVERED RLR AND TLR AGONISTS ON PLGA NANOPARTICLES

5.1 Materials and Methods

5.1.1 Intranasal Administration of PLPs

PLPs were formulated with adjuvants using methods outlined in Chapters 4 and 5 (Aim 1.2 and Aim 2.1). Female Balb/cJ mice, 9-10 weeks old, were anesthetized using 5% isoflurane. Adjuvant-PLP doses were resuspended in 60 µL (total volume) of physiological saline (0.9% NaCl), administered dropwise to both mouse nostrils. IVIS imaging confirmed fluorescent PLPs are present in the trachea and all mouse lung lobes 24 hours after intranasal administration (Figure 24).

5.1.2 Lung Gene Expression Analysis with RT-PCR

For this experiment, three mice were included in each treatment group, at each time point: PUUC (20 µg dose), CpG-PUUC (20 µg CpG and 20 µg PUUC), MPLA-PUUC (24 µg MPLA and 20 µg PUUC), and R848-PUUC (20 µg R848 and 20 µg PUUC). For each mouse ~4 mg of PLGA NP were delivered intranasally. A control group of mice with only saline administered was also included. Mice were euthanized at 4 and 24 hours after intranasal administration of PLPs. Lungs were collected in 1 mL TRIzol™ Reagent (Invitrogen) in a tube with 1.4 mm ceramic beads. Tubes were placed on a tissue homogenizer (MP Bio FastPrep-24) for 3 1-minute increments. 200 µL of chloroform was added to the tissue homogenate, and the samples were centrifuged for 15 minutes at 12,000

x g at 4°C. The mixture separated into a lower red phenol-chloroform phase, interphase, and clear upper aqueous phase. The upper aqueous phase was mixed at a 1:1 ratio with ethanol and added to RNeasy spin columns (Qiagen) to purify the RNA. The RNA binds to the silica membrane of the spin column and contaminants are washed away. DNAse is also added to remove residual DNA. Pure RNA is eluted with RNAse/DNAse free water, RNA is quantified with Nanodrop spectrophotometer (Thermo Fisher), and frozen at -80°C. cDNA was synthesized from RNA using the SuperScript® III First-Strand Synthesis System (Thermo Fisher) and purified cDNA was kept at -80°C. For each treatment group, at each time point, cDNA from three mice was pooled (e.g., pooled cDNA for PUUC 4 hr group, pooled cDNA for PUUC 24 hr group). About 8 ng cDNA combined with SYBR Green Mastermix (Qiagen) was aliquoted to each well of a 384-well RT^2 Profiler PCR Array with genes specific to **Mouse Inflammatory Response & Autoimmunity** (Qiagen). One plate was prepared for each treatment group, at each time point (e.g., one plate PUUC 4 hr group, one plate PUUC 24 hr group). Plates were run in the Applied Biosystems QuantStudio Flex 6 rtPCR instrument, and data was analyzed using resources from Qiagen's GeneGlobe Data Analysis Center. Gene expression for the control and treatment groups was first normalized to reference genes (Actb, B2m, Gapdh) and then the treatment groups were normalized to the control group. All genes with at least one treatment group expressing a normalized fold change greater than 2 was included in the heatmap in Figure 25.

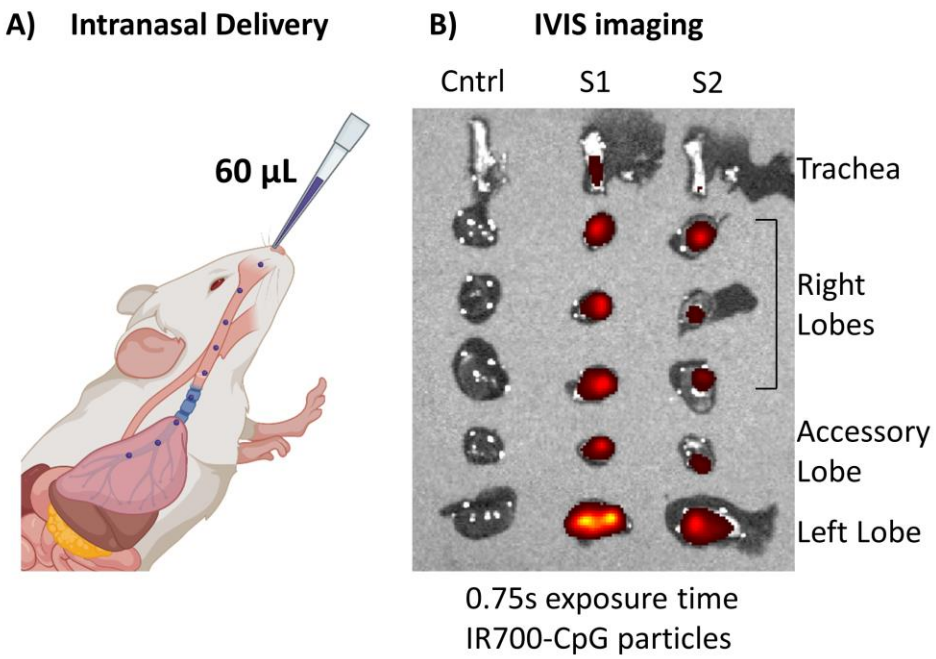

Figure 24: Intranasal administration of fluorescent PLPs and IVIS imaging of mouse lungs. A) Schematic of intranasal delivery of PLPs in 60 µL saline. B) Fluorescent image of NIR-dye labeled PLPs in mouse trachea and lungs taken 24 hours after i.n. administration. Image generated with IVIS and 0.75s exposure time.

5.1.3 Single-Cell Gene and Protein Expression Analysis with CITE-Seq

For this experiment, three mice were included in each treatment group, at each time point: PUUC (20 µg dose) and MPLA-PUUC (24 µg MPLA and 20 µg PUUC). For each mouse ~4 mg of PLGA NP were delivered intranasally. The control group for this experiment included naïve mice. A saline group was not included, as the previous RT-PCR experiment revealed there were some genetic differences between the saline groups at 4 and 24 hours, and we could only include one control for the CITE-Seq experiment. Mice were euthanized at 4 and 24 hours after intranasal administration of PLPs. Lungs were collected in 1X PBS in a 6-well plate, transferred to gentleMACS C tubes with enzyme solutions from the Lung Dissociation Kit (Miltenyi Biotec), and mechanically dissociated with the gentleMACS™ Octo Dissociator. Red blood cells were removed with 1X RBC Lysis Buffer (eBioscience).

Lungs cell suspensions from three animals were pooled for each treatment group (and naïve group) at each time point. Live cells were enriched using the Dead Cell Removal Kit (Miltenyi Biotec). CITE-Seq samples were prepared according to protocols available on the Biolegend and 10X Genomics websites, also outlined in published work.[239] Cells were blocked with TruStain FcX™ Fc Blocking reagent for 5-10 minutes at 4°C and TotalSeq™ -A antibody cocktail was added to each cell sample for an additional 30 minutes. Cells were washed, resuspended in PBS, and barcoded using the Genomics Single Cell 3' v3 Reagent Kit. cDNA was amplified, ADT-derived cDNAs and mRNA-derived cDNAs were separated, and libraries were sequenced. CITE-Seq data was analyzed using Seurat 4.0, an R toolkit for single cell genomics.[240] The CITE-Seq data included in this chapter is lung cell clustering based on relative mRNA expression using tSNE. Clustering based on mRNA and protein expression is included in future work.

5.1.4 SARS-CoV-2 Vaccination Groups

For this experiment, there were six mice per treatment and control group for a total of 78 mice in thirteen groups: **(A)** Seven vaccine groups included 1 µg of unformulated SARS-CoV-2 spike protein delivered with adjuvanted PLPs: MPLA (24 µg), CpG (20 µg), PUUC (17 µg), CpG-PUUC (20 µg, 17 µg), MPLA-PUUC (20 µg, 17 µg), R848-PUUC (20 µg, 20 µg), and MPLA-CpG (24 µg, 20 µg). **(B)** Two vaccine groups included 1 µg of PLGA NP-conjugated SARS-CoV-2 spike protein delivered with adjuvanted PLPs: PUUC (17 µg) and MPLA-PUUC (20 µg, 17 µg). **(C)** There were three controls included: saline, unformulated SARS-CoV-2 spike only (1 µg) and PLGA NP-conjugated SARS-CoV-2 spike only (1 µg). **(D)** One vaccine group included 2 µg of unformulated stabilized SARS-CoV-2 spike protein delivered with MPLA-PUUC PLPs (20 µg, 17 µg). The following

spike protein was delivered unformulated: SARS-CoV-2 Spike (Active Trimer), with C-terminal Histidine, recombinant from HEK293 cells, obtained from R&D Systems. The following spike protein was conjugated to PLGA NP: Spike Glycoprotein (Stabilized) from SARS-CoV-2, Wuhan-Hu-1 with C-terminal Histidine and Avi Tags, Recombinant from HEK293F cells obtained from BEI Resources, NIAID, NIH.

5.1.5 Preparation of Spike Protein-Conjugated PLGA PEI NPs

For conjugation of spike to PLGA-PEI NP, 5 mL of 2 mg/mL PLGA NP in non-amine buffer (0.1 M phosphate buffer, pH 8, 0.15 M NaCl, 2 mM EDTA) was mixed with excess Traut reagent (150 mM). The mixture was left at room temperature for overnight rotation. Thiolated PLGA-PEI-NP (PLGA-PEI-SH) were purified using centrifugation and washing two times. Particles were lyophilized overnight. The remaining number of amine groups on thiolated particles were determined using a fluorescamine assay with lysine as the standard. According to the assay, particles were 60-70% thiolated. Thiolated patricles were stored at -20°C prior to loading spike protein.

A stock solution of PEG-SPDP (100 mg) was prepared by dissolving NHS-PEG-SPDP in 50 µL of DMSO. 5 mg of PLGA-PEI-SH NP was sonicated in 1 mL of PBS with 2 mM EDTA (pH 7.6), and then mixed with excess NHS-PEG-SPDP (200 µg in 0.1 µL) and 50 µg of Avi Tag- spike protein. The mixture was left at room temperature for six hours on a rotator. Particles were centrifuged n at 21,000 x g for 10 minutes, twice, and supernatant was pooled. The supernatant was filtered through a 100,000 MW Ultra-4 Amicon filter tube to retain unconjugated protein and remove NHS-PEG-SPDP. The remaining spike protein concentration was measured using a micro-BCA assay (Boster Bio). The protein

conjugation efficiency ranged from 84% to 92%, so the final concentration of spike on PLGA PEI NP ranged from 8.4 to 9.2 µg per mg PLGA PEI NP and the particle dose per mouse ranged from 119 µg to 108 µg to deliver 1 µg of spike protein (small compared to the ~4 mg dose of adjuvanted PLPs).

5.1.6 Vaccination Timeline and Tissue Collection

Vaccinations with particle-conjugated or unformulated SARS-CoV-2 spike protein and PLPs were administered intranasally in 10-week-old female Balb/cJ mice. Three mice out of the six in each treatment and control group were sacrificed at Day 27 to collect blood and bronchoalveolar lavage fluid for anti-spike IgG and IgA ELISA assays. A booster intranasal vaccination was administered to the remaining mice on Day 28. A week later (Day 35), mice were euthanized, and lungs were collected for ex vivo stimulation assays with spike protein. Blood and BAL fluid were also collected to assess post-booster antibody responses. To collect serum, blood samples were left at room temperature for 1 hour to clot, and then were centrifuged at 3000 rpm, for 10 minutes at 4°C. Serum (supernatants) was transferred to a 2 mL low-adhesion tube and heat-inactivated for 30 minutes at 56°C. Serum was aliquoted into low adhesion stubes at stored at -80°C until use. BAL fluid samples were also centrifuged at 3000 rpm for 10 minutes at 4°C and were aliquoted and stored at -80°C.

5.1.7 IgG and IgA ELISA Assays

Nunc Maxisorp™ flat-bottom 96-well plates were coated with 1 mg/mL stabilized SARS-CoV-2 spike protein in carbonate-bicarbonate buffer (pH 9.6), 100 µL per well, and incubated overnight at 4°C. Plates were washed three times with PBS-Tween20 buffer

(0.05% TWEEN®20, pH 7.4, PBST buffer). Plates were blocked with PBST buffer containing 1% BSA and 0.02% sodium azide (PBSTBA buffer), 300 µL per well, and incubated overnight at 4°C. Serum samples were serially diluted in PBSTBA, 100 µL of diluted serum was added per well and incubated at 4°C overnight. Plates were washed three times with PBST Buffer, and 100 µL of 1:5,000 biotinylated anti-mouse IgG or IgA (Southern Biotech) in PBSTBA was added. After incubating 1 hour at RT, plates were washed three times with PBST buffer and 100 µL of 1:2,500 Strep-HRP (Thermo Fisher) in PBSTBA was added. After another hour at RT, plates were washed six times and 100 µL 1-Step Ultra TMB Substrate solution (Thermo Fisher) was added to each well. After 30 minutes, 2N Sulfuric Acid stop solution was added to each well and within 2 minutes the absorbance of plates at 450 and 630 nm was quantified with a plate reader. Final absorbance values for serum titers were calculated by subtracting the absorbance at 630 nm from the absorbance at 450 nm. Absorbance values were plotted in GraphPad, and statistical significance between treatment groups was determined with Two-Way ANOVA and Tukey test.

5.1.8 Ex Vivo Lung Cell Stimulation Assays

Lungs from vaccinated mice were dissociated into single cell suspensions as previously described. After RBC lysis, lung cells were resuspended in RPMI complete medium (10% FBS, 1% Penicillin-streptomycin, 1 mM Sodium Pyruvate, and 55 µM beta-mercaptoethanol) at 10 million cells/mL. 2.4 million cells were added to each well of a U-bottom cell-culture treated 96-well plate and left overnight in a cell culture incubator at 37°C and 5% CO_2. After 6 hours, cells were centrifuged at 500 x g for 5 minutes, the supernatant was discarded, and cells were resuspended in complete RPMI medium with 20

µL of PeptTivator® SARS-CoV-2 Prot_S (Miltenyi Biotec) and 5 µg of Brefeldin A (Biolegend) per mL of media. The PepTivator® peptide pools contain peptides of 15-mer sequences with 11 amino acid overlap, covering the immunodominant sequence domains of the surface glycoprotein of SARS-CoV-2. This includes sequence domains aa 304-338, 421-475, 492-519, 683-707, 741-770, 785-802, and 885-1273. The final concentration of each peptide was about 1 µg per mL of medium, therefore about 1 µg of peptide per 10 million lung cells.

5.1.9 Intracellular Cytokine Staining

After 6 hours, lung cells were centrifuged, resuspended in PBS and transferred to a V-bottom well plate for flow staining. Cells were stained for viability with Zombie Green Fixable Viability Dye (Biolegend) (30 min RT) and blocked with TruStain FcX and True-Stain Monocyte Blocker™ solutions (Biolegend) (30 minutes 4°C). The surface staining antibody cocktail contained the following: anti-mouse CD45 (BUV395, BD), CD44 (BV711, Biolegend), CD69 (BV785, Biolegend), CD103 (PE-Dazzle 594, Biolegend), CD8a (PE/Cyanine5, Biolegend), and CD4 (allophycocyanin-fluorophore, Biolegend) (30 minutes 4°C). Stained cells were fixed and permeabilized with the Foxp3/Transcription Factor Staining Buffer Set (eBiosciences), and intracellular staining cocktail included the following antibodies: anti-mouse IFN-γ (PE, Biolegend), Granzyme B (Pacific Blue, Biolegend), and TNF-α (PE/Cyanine7, Biolegend). Flow cytometry of samples was performed on the BD LSRFortessa and analysis done with FlowJo software (BD). Graphs were produced and statistical analysis conducted using GraphPad software. Statistical significance of T cell population percentages and cytokine expression between treatment groups was determined with a One-Way ANOVA and Tukey test for multiple comparison.

5.2 Results

5.2.1 PUUC-TLR Agonist Combinations Differentially Regulate Inflammatory Gene Expression in Mouse Lungs after Intranasal Administration

High-throughput screening of genes associated with inflammation and autoimmunity was performed with mouse lung tissue after intranasal administration of PUUC NP, CpG-PUUC NP, MPLA-PUUC NP, and R848-PUUC NP (Figure 25). Combination adjuvants upregulated inflammatory genes at 4 hours, while PUUC upregulated more genes, particularly chemokine-related, at 24 hours. MPLA-PUUC strongly increased expression of proinflammatory cytokine-related genes, particularly IL-1β and IL-6, compared to other adjuvants (Figure 26A). MPLA-PUUC also strongly upregulated the lymphotoxin alpha gene, Lta, which encodes a protein produced by activated Th1 and $CD8^+$ T cells as well as NK cells. It is of note that MPLA-PUUC simultaneously increases expression of IL6, IL23a, and IL17a, all genes for Th17-associated cytokines. IL17a expression is also maintained by MPLA-PUUC at 24 hours. Not surprisingly, MPLA also induced expression of CD14 and peptidoglycan protein recognition protein (PGLYRP1). CD14, IL1β, IL6, and IL23a are all associated with immune responses to Mycobacterium tuberculosis and Bordetella pertussis (Gram-negative bacteria). At 24 hours MPLA-PUUC upregulates the gene for Tollip, an adaptor protein that inhibits TLR4 signaling and reduces inflammation, and conversely has been implicated in propagating low-grade inflammation.[241]

At 4 hours, CpG-PUUC upregulated a cluster of genes associated with the JAK/STAT signaling pathways, including: Ifna4, Ifne, IL10, IL13, IL19, Il20ra, and IL24 (Figure 26B). While MPLA-PUUC and R848-PUUC induced higher expression Ifnb1, CpG-

PUUC stimulated the highest expression of Ifna and Ifne. Ifne (encoding novel type I IFNε) is expressed in mucosal tissues, including the lungs, small intestine, and female reproductive tract, particularly by epithelial cells.[242,243]

R848-PUUC uniquely induced expression of multiple genes associated with T cells: at 4 hours, CCL1, CCL8, CXCL11, and IL9, and at 24 hours, IL2. CCL1 and CCL8 are produced by monocytes and bind to chemokine receptor CCR8, expressed by monocytes, macrophages, $CD301b^+$ DCs, Th2 cells, and regulatory T cells (Figure 26C).[178,244] CXCL11 recruits activated T cells and its gene expression is stimulated by IFN-γ and IFN-β.[245] Therefore, the upregulation of CXCL11 is consistent with R848-PUUC-induced Ifnb1 expression. IL-9 is secreted by $CD4^+$ T cells, particularly Th9 cells, a subset that is associated with allergy and asthma, cancer, helminth infection, and autoimmune diseases; however, their exact role is poorly understood.[246] IL-2 promotes T cell survival, proliferation, and differentiation into effector cells.[247] In steady-state conditions, IL-2 is mainly produced by $CD4^+$ T cells, and to a lesser extent, $CD8^+$ T cells, NK cells, and NKT cells. R848-PUUC also upregulated inflammatory gene MMP25, which is mostly expressed by granulocytes and secondarily NK cells, and involved in NF-κB activation.[248] Between 4 and 24 hours R848-PUUC maintained expression of REG3A, CCL8, and Nodal. REG3A is an antimicrobial protein homologous to a C-type lectin that controls bacterial infection and may influence tissue regeneration.[249] Is mostly expressed in the human intestine and pancreas, not in human lung, but it has been detected in mouse lung tissue. R848-PUUC also upregulated Prg3 at 4 hours, which is associated with eosinophil function.

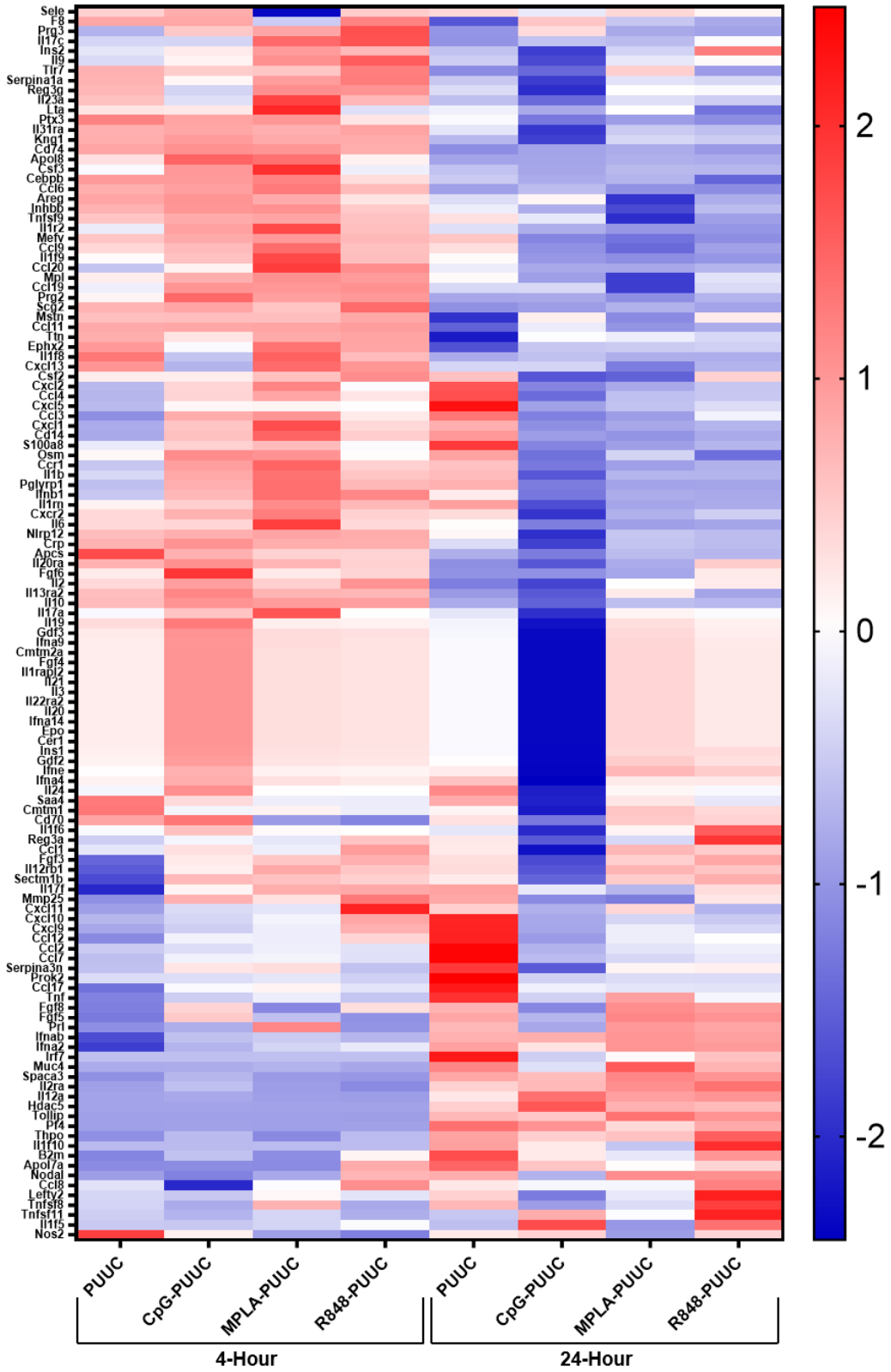

Figure 25: Expression of Inflammatory Genes in the Mouse Lung after Intranasal Injection of PUUC with CpG, MPLA, and R848 on PLGA NP. Heatmap correlates with z-scores of

expressions of inflammatory genes; z-scores were calculated for each gene type (i.e., standardized across rows) to show relative upregulation and downregulation of genes between groups. All treatment group fold regulation was first normalized to reference genes and control group (saline) before z-scores were calculated.

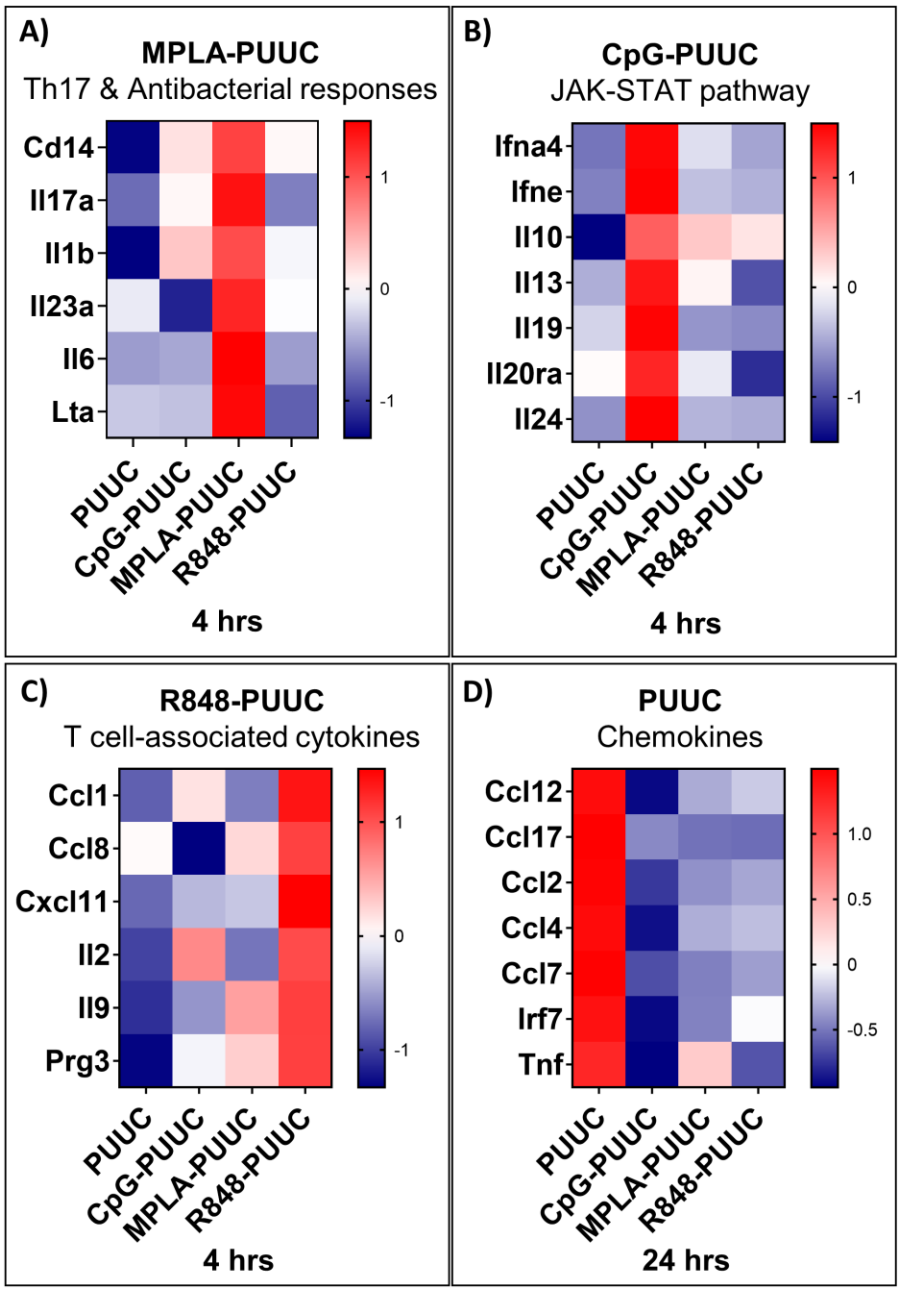

Figure 26: MPLA-PUUC, CpG-PUUC, R848-PUUC, and PUUC PLPs differentially induce inflammatory gene expression in mouse lungs 4 and 24 hours after intranasal administration. Heatmaps correlate with z-scores of gene fold regulation, standardized across rows. Fold regulation values calculated by normalizing to reference genes and control group (saline) prior to standardization.

PUUC NPs distinctly upregulate chemokine gene expression in the lung at 24 hours; an effect that is diminished with the addition of TLR agonists (Figure 26D). These chemokines, including CCL12, CCL17, CCL2, CCL4, and CCL7, are involved in neutrophil and monocyte recruitment. PUUC NPs induce the highest genetic expression of IRF7, a signaling protein involved in type I interferon production, while also upregulating IFN-α genes. PUUC NPs also upregulated TNF expression at 24 hours and Nos2 expression at 4 hours, which suggests Tip-DCs and macrophages were activated.

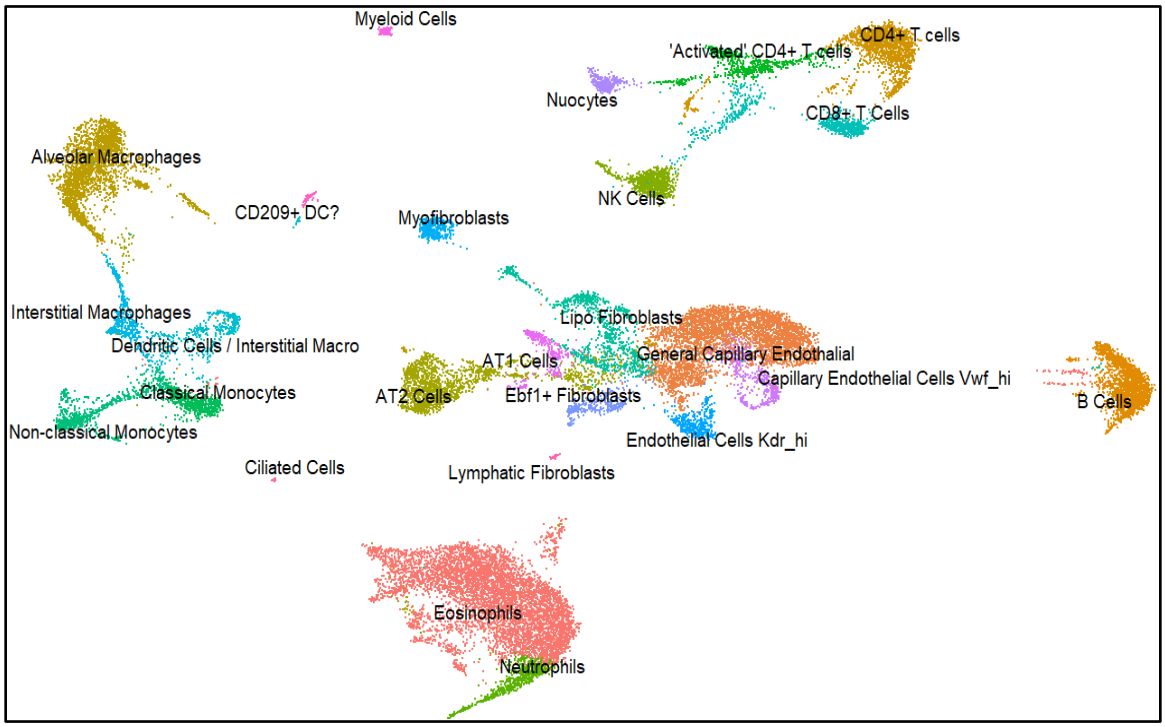

Figure 27: UMAP of Cell Subsets in the Mouse Lung Clustered based on mRNA and protein expression. CITE-Seq analysis incorporated both the barcoding of cells to measure mRNA expression as well as the antibody-tagging of cells to measure protein expression. Data was input into SEURAT to compute a UMAP of lung cell clusters based on mRNA and protein expression. This UMAP incorporates all groups into one map.

5.2.2 CITE-Seq Analysis Reveals Changes in Lung Cell Populations and Genetic Expression in Response to PUUC and MPLA-PUUC PLGA NPs

Lung cells were collected from mice intranasally treated with PUUC NP and MPLA-PUUC NP, and analyzed with CITE-Seq to elucidate cell-specific immune responses to PAMPs and inform vaccine design. MPLA-PUUC NP was selected as the combination adjuvant due to its strong induction of proinflammatory and Th17-polarizing cytokines and maintenance of immune response- and inflammation-related genes between 4 and 24 hours. MPLA-PUUC is also a TLR-RLR combination that is not naturally co-expressed and could direct a unique immune response. For cost purposes, the analysis was restricted to five samples, and RT-PCR revealed differences in PUUC and MPLA-PUUC signaling at 4 and 24 hours; therefore, both treatment groups and time points were included in the experiment. Naïve mice were selected as a control because saline injections caused variable gene expression at 4- and 24-hours post-injection and six samples could not be included in the CITE-Seq analysis. Cells were clustered based on mRNA and protein expression.

By 4 hours post-administration of PLPs, PUUC NP and MPLA-PUUC NP induced infiltration and differentiation of $CD4^+$ and $CD8^+$ T cells, NK cells, B cells, monocytes, alveolar macrophages, eosinophils, and neutrophils (Figure 27, Figure 28). PUUC NP and MPLA-PUUC NP also increased the number of AT2 cells, which often regenerate from stem cells during lung injury.[250] At 24 hours, there was a clear increase in interstitial macrophage and dendritic cell populations, suggesting inflammation-driven monocyte differentiation into APCs. Neutrophils and eosinophils continued to be recruited to the lung at 24 hours, more so in response to MPLA-PUUC. There is an apparent decrease in endothelial cell, epithelial cell (AT1/AT2), fibroblast, and lymphocyte populations by 24

hours. Live cells were enriched for CITE-Seq analysis so the reduction in clusters could be a result of cell death. There are a few variables in CITE-Seq analysis that influence the clustering of cells types, including the proportion of mitochondrial DNA (mtDNA), which is used as a threshold to filter out low-quality and dying cells. Changing this threshold adjusts the inclusion of cells based on mtDNA expression, which can be misleading; for example, activated T cells increase expression of mtDNA. Also, UMAPs show the relative differences of cell populations between clusters. Because there is significant infiltration of granulocytes in the presence of adjuvant at 24 hours, this could change the proportion of other cell subsets in the lung. More analysis needs to be conducted to verify these results.

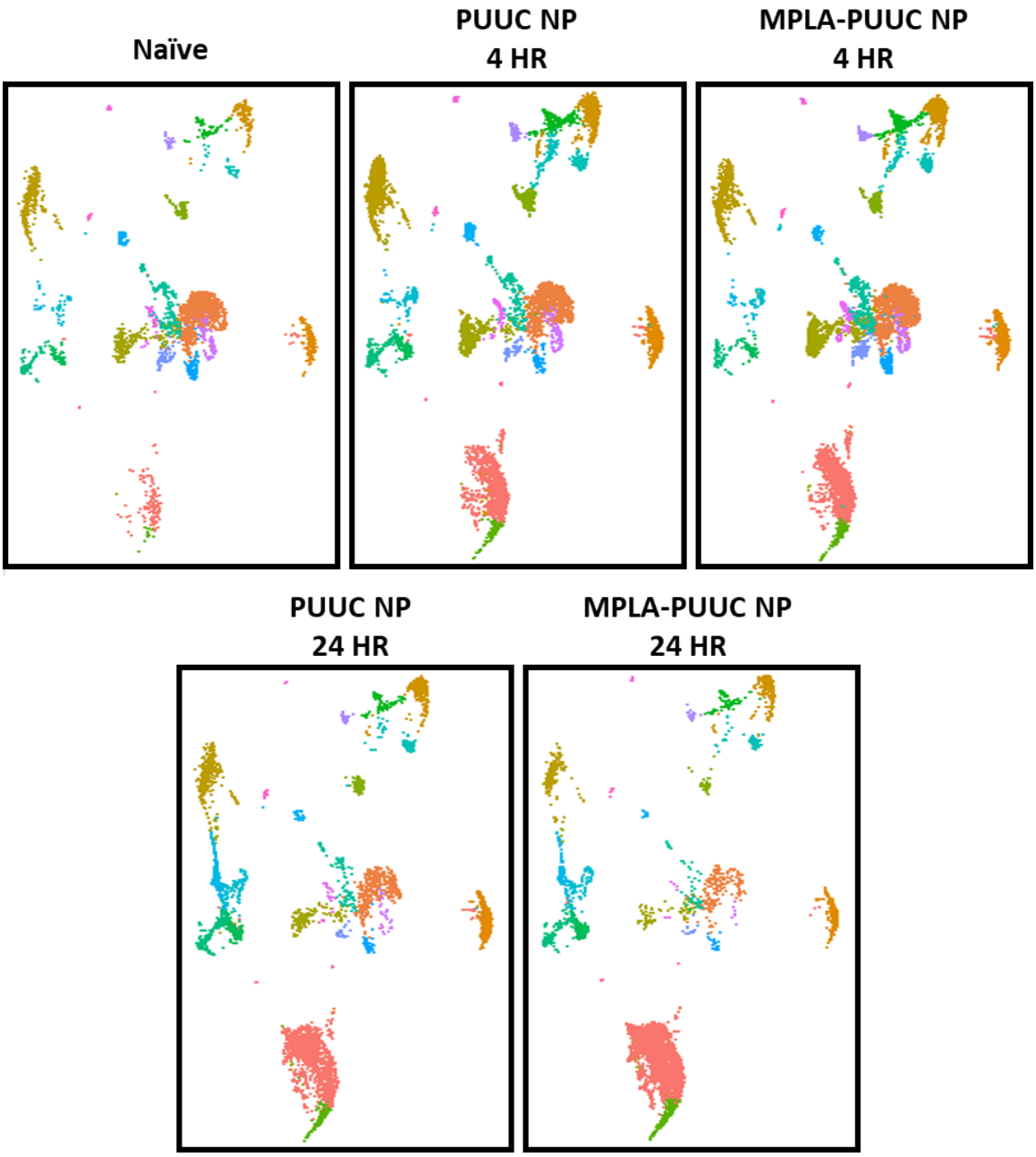

Figure 28: Relative distribution of UMAP clusters between naive, PUUC, and MPLA-PUUC treatment groups. UMAP from Figure 27 is separated by group to see relative difference in immune cell populations between treatment groups and 24/48 hours.

5.2.3 MPLA-PUUC NP Increase $CD4^+$ and $CD103^+CD69^+$ T Cell Responses to Restimulation with SARS-CoV-2 Spike Peptide Pools

Combinations of PUUC and TLR agonists, CpG, R848, and MPLA were screened as adjuvants for intranasal subunit vaccines against SARS-CoV-2. The primary formulations inducing humoral and cellular immune responses were PUUC NP and MPLA-PUUC NP; therefore, for simplicity, only the single and dual adjuvant groups containing MPLA and/or PUUC are included in the figures of this section. Aim 2.2 Supplementary Information contains graphs with all adjuvant groups.

Two different methods of antigen delivery were screened with combination adjuvants: unformulated ("soluble") stabilized SARS-CoV-2 spike protein, and PLGA-NP-conjugated stabilized SARS-CoV-2 spike protein (with Avi Tag for conjugation). The reasoning for delivery of antigen on particles is similar to that of adjuvants – the immune system has evolved to recognize the particulate state of microbes, and endocytosis of particulate microbes stimulates intracellular processing of antigens.[146,251] Studies have shown that delivering antigens and adjuvants in separate PLGA particles can improve or attain the same immune responses compared to co-delivered antigens and adjuvants.[252,253] Therefore, we opted to deliver antigen and adjuvant separately for this study.

Sera and BAL fluid collected from mice 27 days (without booster) and 35 days (one week post-booster) after intranasal vaccination were tested for presence of anti-SARS-CoV-2-spike IgG and IgA. Only the PUUC NPs with soluble spike protein produced anti-spike IgG detectable in serum, without booster (Figure 29). This result was not replicated in mouse sera collected one week later, post-booster. Mice immunized with MPLA NP

produced moderate levels of anti-spike IgG post-booster, with high variability. One MPLA NP-immunized mouse with high serum anti-spike IgG also possessed high BAL fluid anti-spike IgA. None of the other BAL fluid samples contained detectable levels of anti-spike IgA pre- or post-booster.

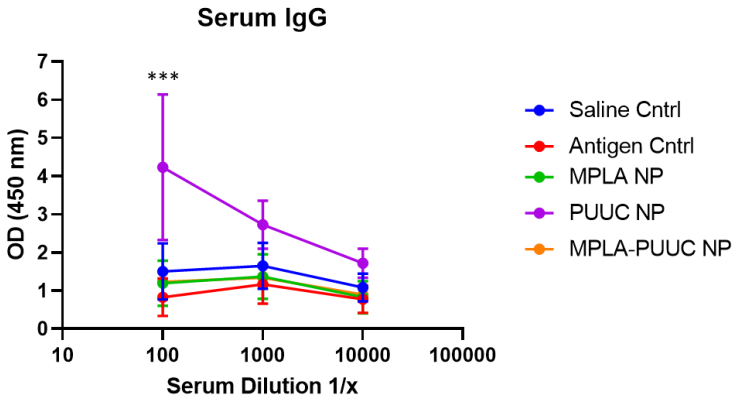

Figure 29: Serum Anti-Spike IgG Titer in Mice 28 days after intranasal administration of adjuvanted PLGA NP and soluble spike protein (no booster). Results from ELISA assay measuring anti-spike IgG in serially diluted mouse sera. Groups contain 3 biological replicates, each with 2 technical duplicates. Technical duplicates averaged first, and curves represented here contain the mean and standard deviation from the 3 biological replicates. ***p<0.001 with Two-Way ANOVA and Tukey Test.

Lung cells from mice that received the prime and booster vaccines were restimulated with overlapping spike peptide pools for six hours *ex vivo* and intracellularly stained for flow cytometry. Restimulated lung cells from mice immunized with MPLA-PUUC NP and particle-conjugated spike protein contained the highest percentages of IFN-γ- and TNF-α-secreting $CD4^+CD44^+$ T cells (Figure 30). CD44 is a cell-surface protein commonly expressed by effector and central memory T cells.[254] MPLA-PUUC NP with soluble spike led to the highest percentages of $CD69^+CD103^+$ T cells, known as tissue-resident memory cells, in restimulated lungs (Figure 31). These cells exhibit a double negative $CD4^-CD8^-$ phenotype, suggesting these cells are γδ T cells, a subset of T cells enriched in epithelial

and mucosal tissues that are activated in an MHC-independent manner (Figure S23).[255] Adjuvants with soluble spike protein, and more so adjuvants with NP-conjugated spike protein, decreased percentages of TNF-α-producing $CD8^+CD44^+$ and $CD69^+CD103^+$ T cells. There were no significant changes in overall $CD8^+$ effector and central memory T cell percentages, or percentages of Granzyme-B- and IFN-γ-secreting $CD8^+$ T cells.

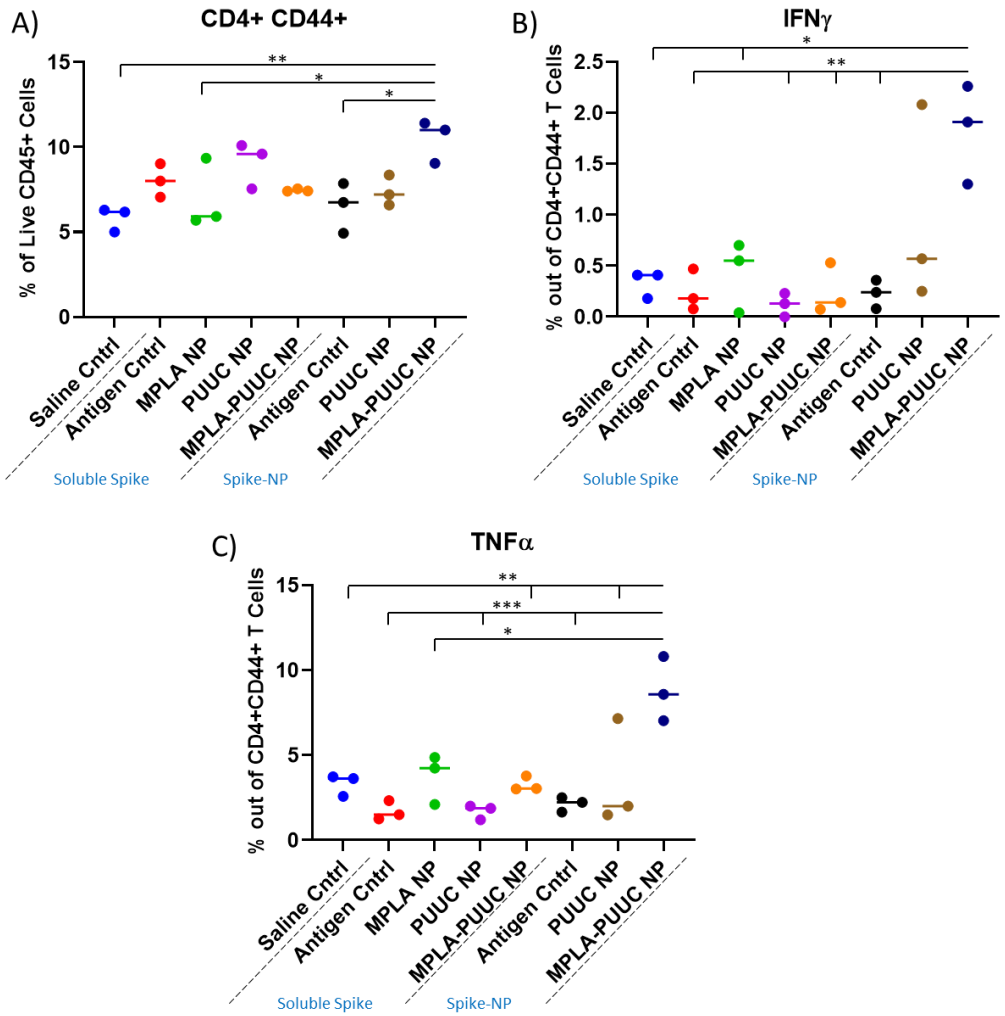

Figure 30: CD4+ CD44+ T Cell IFN-γ and TNF-α secretion in isolated lung cell culture from Vaccinated Mice (prime and booster) after Restimulation with Spike Peptide Pool. A) Percent of CD45+ lung cells expressing CD4 and CD44 (effector and central memory CD4 T Cells). B) Percent of CD4+CD44+ T cells expressing IFN-γ. C) Percent of CD4+CD44+ T cells expressing TNFa. Each group has three biological replicates. *p<0.05, **p<0.01, ***p<0.001 One-Way ANOVA and Tukey Test

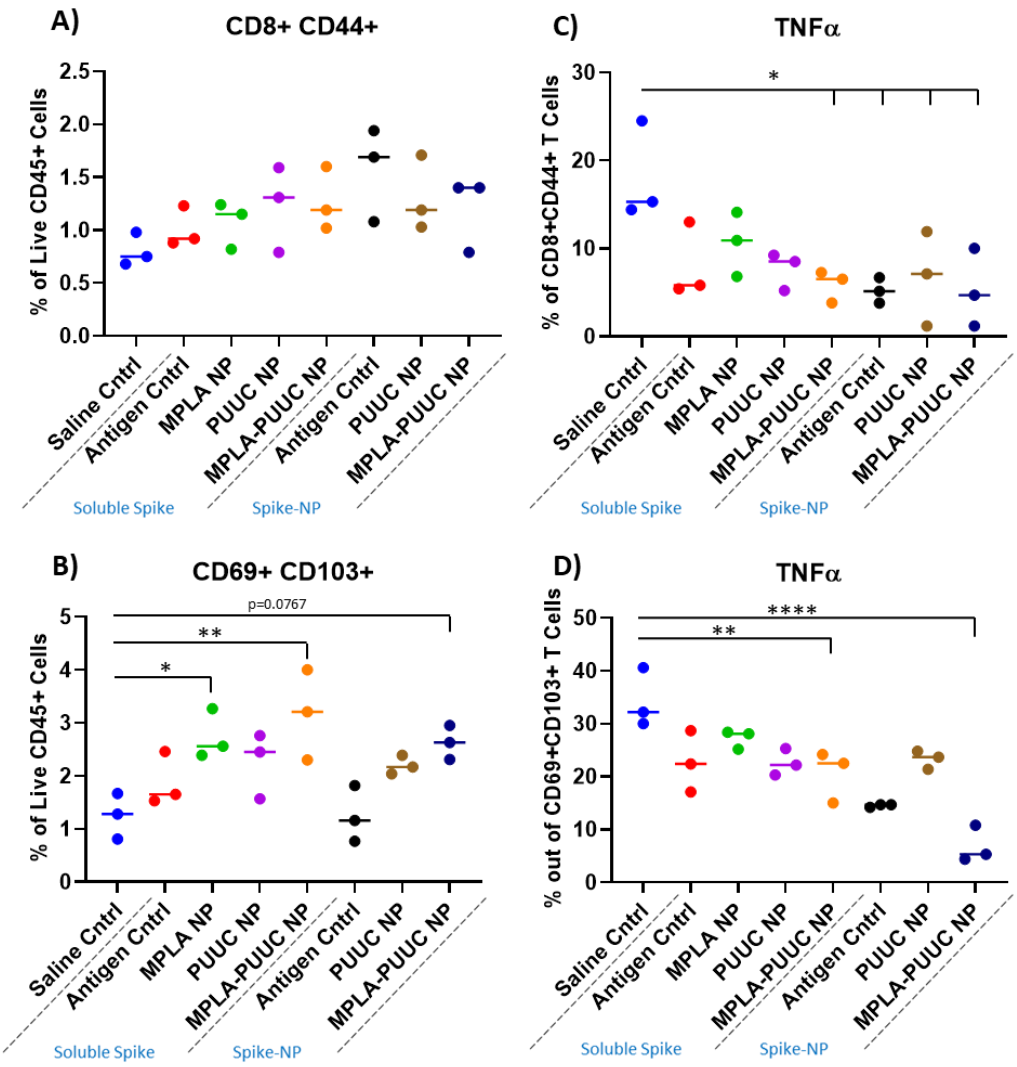

Figure 31: CD8+ CD44+ T Cell and CD69+CD103+ T Cell Populations and TNF-α secretion in isolated lung cell culture from Vaccinated Mice (prime and booster) after Restimulation with Spike Peptide Pool. A) Percent of CD45+ lung cells expressing CD8 and CD44 (effector and central memory CD8 T Cells). B) A) Percent of CD45+ lung cells expressing CD69 and CD103 (tissue resident memory T cells). C) Percent of CD8+CD44+ T cells expressing TNFa. D) Percent of CD69+ CD103+ cells expressing TNFa. Each group has three biological replicates. *p<0.05. **p<0.01, ****p<0.0001 One-Way ANOVA and Tukey Test

CHAPTER 7: CONCLUSIONS AND FUTURE WORK

6.1 Conclusions

6.1.1 APC-Mediated Immune Responses to Combination Adjuvants In Vitro are Dependent on the Type of APC Culture

The three most common in vitro models of antigen-presenting cells are based on hematopoietic stem cell culture with GM-CSF, GM-CSF and IL-4, or FLT3L.[102,106,107,237,256] Consistent with previous studies, this work demonstrates that GM-CSF BMDCs are a heterogenous mixture of neutrophils, monocytes, macrophages and monocyte-derived DCs (also known as inflammatory DCs), and the addition of IL-4 induces cDC phenotypes characterized by higher expression of CCR7, CD40, and MHC-II and decreased expression of F4/80 (Figure 7). The differentiation of cDCs in vitro with IL-4 is supported by the fact that IL-4 strongly induces IRF4, which is highly expressed by cDC2 in vivo.[64,88] FLT3L BMDCs are mainly made up of cDCs and pDCs, though FLT3L also promotes the survival of some macrophages in culture (Figure 17).[237]

Studies in Aim 1.1 and Aim 2.1 showed that APC response to single and combination adjuvants were dependent on the cytokines used in BMDC culture. In Aim 1.1, GM-CSF BMDCs did not exhibit as strong of CCR7 upregulation and chemotaxis toward CCL21 as BMDCs cultured with GM-CSF and IL-4 (Figure 9). Gating on APC subsets within GM-CSF/IL-4 BMDC culture also revealed differential expression of CCR7 in response to MPLA and CpG (Figure 10). In Aim 2.1, GM-CSF BMDCs secreted more IFN-β, TNF-α, IL-1β, and IL-6 in response to PUUC and TLR agonists while FLT3L secreted more IFN-

γ and IFN-λ3. GM-CSF BMDC culture is useful for assessing the proinflammatory cytokine response to adjuvants, while experiments with FLT3L BMDC culture may be more predictive of IFN response in vivo. Combination adjuvants also differentially stimulated both types of BMDC culture. Additive or synergistic cytokine responses to combination adjuvants, particularly MPLA-PUUC and R848-PUUC, were induced more in GM-CSF culture (Figure 19). This highlights the important role of monocytes, macrophages, and mo-DCs in the innate immune response to co-expressed PAMPs on pathogens.

BMDC activation of T cells activation in response to combination adjuvants, specifically MPLA-CpG and CpG-PUUC, was more significant with FLT3L culture (Figure 23). Strong T cell activation with FLT3L culture is supported by data showing cDCs are more present in FLT3L culture, and according to literature cDCs are more proficient at antigen presentation compared to mo-DCs, macrophages and monocytes.[22,257] The correlation of T cell death with T cell activation was also dependent on BMDC culture type. Increased $CD8^+$ T cell proliferation with GM-CSF BMDC culture correlated with lower T cell death but with FLT3L culture, $CD8^+$ T cell proliferation correlated with higher T cell death, as well as reduced IL-4 secretion. FLT3L BMDCs could potentially overstimulate T cells with antigen, leading to T cell exhaustion.[258]

6.1.2 APC-mediated Immune Responses to Combination Adjuvants and Antigens are Dependent on Vaccine Delivery Systems

APCs in vitro and in vivo differentially responded to soluble vs. particle-delivered antigens and adjuvants. In Aim 1.1, BMDC chemotaxis toward CCL19 and CCL21 was more strongly induced by unformulated ("soluble") MPLA compared to MPLA PLGA MP, and by CpG MP compared to soluble CpG. The conclusion was that microparticles limited the bioavailability of MPLA to the cell surface, where MPLA triggers the MyD88 pathway. CpG delivery on PLGA MP stimulates phagocytosis by APCs, and phagosomes directly fuse with the ER, therefore providing more direct access to TLR9, which also signals MyD88.[202,203] Induction of chemotaxis with soluble MPLA and CpG MP, triggering surface TLR4 and endosomal TLR9, respectively, is consistent with studies showing that MyD88 signaling regulates migration of DCs to draining lymph nodes.[205,207,259]

Induction of Th1 immunity, characterized increased IFN-γ and TNF-α secretion by effector $CD4^+$ T cells, was more apparent in SARS-CoV-2 spike peptide-restimulated lung cells collected from mice immunized with MPLA-PUUC and spike protein delivered on separate PLGA particles (Aim 2.2). Contrarily, increases in $CD103^+CD69^+$ T cell percentages, which may be γδ T cells due to the lack of CD4 and CD8 expression, were observed with lung cells from mice immunized with MPLA-PUUC NP and unformulated spike protein. In Aim 1.1, MPLA-PUUC NP induced higher cytokine secretion of IL-1β and IL-27 in GM-CSF BMDC culture, which contains high percentages of macrophages, proficient phagocytes. Activation of macrophages through MPLA-PUUC and stimulation of IL-1β and IL-27 along with phagocytosis of NP-conjugated antigen, may all culminate in effective priming of $CD4^+$ T cells and induction of Th1 immunity. IL-1β, shown to be

upregulated in vivo by MPLA-PUUC (Figure 25), also enhances the polarization of M1 macrophages, which are capable of promoting Th1 polarization of $CD4^+$ T cells.[260,261] Activation of monocytes, macrophages, and mo-DC with particle MPLA-PUUC NP and unformulated spike protein may be sufficient to stimulate inflammation but not antigen presentation; hence, MHC-independent γδ T cells, which function as innate immune cells, are activated.[262]

In Aim 1.2, IRDye700-conjugated CpG and control (GpC) ODN dissociated from AF488-conjugated PLGA NP in the muscle by 24 hours, and the $IR700^+AF488^{lo/-}$ signal diminished from 24 to 48 hours (Figure 13). NIR images of lymph nodes also exhibited higher fluorescence at 24 hours compared to 48 hours (Figure 12). Soluble ODN triggered CD86 expression by B cells, pDCs, and cDC1 in the lymph node by 24 hours, and while CpG ODN specifically triggered B cell proliferation by 48 hours (Figures S9, S10). Meanwhile, PLGA NP were retained in the muscle at 48 hours and increased CD40 expression by DCs (Figure 15) as well as differentiation of macrophages (Figure 14). This work suggests that differential timing of delivery by co-administered adjuvants could amplify the immune response; in the case of MPLA-CpG NP, dissociated CpG could directly target and activate B cells in draining lymph nodes while MPLA NP retained in tissues enhances monocyte, macrophage, and cDC activation (Figure S9, Figure 15).

6.1.3 Route of Administration Determines Success for Combination Adjuvants

Combination adjuvants including MPLA-CpG, MPLA-PUUC, CpG-PUUC, and R848-PUUC differentially upregulate expression of profinflammatory cytokines and interferons that control immune cell populations at the site of administration (Figure 18, Figure 25).

MPLA, co-delivered with either CpG or PUUC, strongly increases infiltration of neutrophils within 24 hours after delivery into the muscle and lungs (Figure 14, Figure 28) and produces high levels of proinflammatory cytokines (Figure S14, Figures 18-19, Figure 25). Cytokine storm and recruitment of polymorphonuclear cells to the lung is observed in the immune response to SARS-CoV-2 and neutrophilia has been associated with severe respiratory symptoms and poor outcomes for COVID-19 patients.[263,264] Neutrophils have a short lifespan, and after exhaustion and apoptosis are removed by phagocytes under normal conditions. However, if apoptotic neutrophils are not removed in time, they progress toward secondary necrosis, which contributes to chronic inflammation and development of diseases such as chronic obstructive pulmonary disease.[265,266] MPLA-PUUC, MPLA-CpG, and R848-PUUC also induce more IFN-β production by BMDCs and lung cells compared to single adjuvants (Figure 18, Figure 25).[267] Patients with severe and critical cases of COVID-19 have highly impaired type I interferon responses, characterized by the absence of IFN-β and low IFN-α production.[268] Inhaled IFN-beta has been identified as a potential therapeutic for COVID-19 patients in combination with other treatments such as lopinavir, ritonavir, ribavirin, and remdesivir.[269–272]

CpG with and without MPLA induces high expression of IFN-λ3 (Figure 18), which has intrinsic antiviral effects and signals IFNLR in the airway epithelium and is therefore being investigated as another potential IFN-related treatment.[273] However, studies have shown that IFN-λ produced by mice in response to influenza increases susceptibility to pneumonia, and higher amounts of IFN-λ mRNA in BAL fluid and naso-oropharyngeal samples from SARS-CoV-2-positive patients correlated with disease morbidity.[274,275] In response to poly(I:C), which can signal through both TLR3 and MDA5 (an RLR), dendritic

cells in the lung produced strong levels of IFN-λ that caused damage to the lung epithelium (in contrast, R848 caused upregulation of proinflammatory cytokines but did not correlate with barrier function decrease).[275] Major et al. found that IFN-λ hampered lung repair by inducing the p53 pathway and impairing differentiation of alveolar epithelial progenitor cells into secretory and multiciliated cell types.[276] Overproduction of type III IFN could explain the decrease in epithelial cell population 24 hours after intranasal administration of PUUC NP and MPLA-PUUC NP in mice (Figure 27, Figure 28); however analysis of differentially expressed genes in cell clusters must be completed to confirm this theory. In other tissues, inhibition of cell division and death of infected cells would be an appropriate antiviral response and more well-tolerated, highlighting the benefits of intramuscular or intradermal injections for SARS-CoV-2 immunization.[273]

The route of administration also influences which lymph nodes (and how many) receive vaccine cargo from migratory APCs and flow of lymph from the injection site. In turn, this determines where APCs activate T cells, generating effector, central memory, and tissue-resident memory T cells, and promote localized antigen-specific immune responses to infection. For example, Takamura et al. found that intranasally primed memory $CD8^+$ T cells were superior to intraperitoneally primed $CD8^+$ T cells in their ability to be reactivated by antigen in the mediastinal lymph nodes in mouse models of influenza and parainfluenza virus infection.[277] In Aim 1.2, fluorescent particles injected into the muscle draining to multiple lymph nodes, including the popliteal, inguinal and iliac nodes, which exhibited different APC responses to adjuvants (Figure 12). In addition to intramuscular injections, intradermal and footpad injections drain to these lymph nodes, and studies have shown that tail injections drain to inguinal nodes and the colon and spine drains to iliac lymph

nodes.[278–280] More defined lymph node mapping and specific targeting of lymph nodes in humans could mediate localized immune responses to sites of infection.

6.2 Future Work

There are several more parameters of vaccine design to be investigated in the screening of combination adjuvants. In the context of biomaterials-based particle delivery systems, factors include particle size, surface charge, surface modifications, and polymer composition.[281,282] Each of these factors influence the loading capacity, encapsulation efficiency, release kinetics, and targeted delivery of antigens and adjuvants to shape immune responses.[282] There are also non-polymeric particles to evaluate for delivery of combination adjuvants, including inorganic particles (e.g., gold nanoparticles/nanorods, carbon nanotubes, silica-based particles), liposomes, and virus-like particles.[283] The SARS-CoV-2 antigen used in the intranasal subunit vaccine formulation was the spike protein that is encoded by mRNA in current COVID-19 vaccines.[284] There are many other types of SARS-CoV-2 antigens, including envelope, membrane, and nucleocapsid proteins, as well as other pathogen-derived antigens to be tested with RLR/TLR combination adjuvants.[285]

More physiologically relevant in vitro models are necessary for high-throughput screening of combination adjuvant formulations and predicting immune responses in vivo. Work in Aim 1.1 optimized an in vitro model of BMDC chemotaxis in response to adjuvants to predict migration of APCs and cell-mediated antigen transport to draining lymph nodes during vaccination. There are more biological, chemical, and physical parameters to change or add for improvement of this model, including (a) the application of flow and

pressure mimicking interstitial fluid dynamics during vaccination, (b) the addition of extracellular matrix proteins that regulate cell migration and chemokines (e.g., CCL21) gradients, and (c) the inclusion of lymphatic endothelial cells as the source of chemokine. There are also new BMDC culture methods effective at generating distinct APC subsets that can be utilized to elucidate APC-subset-specific responses to combination adjuvants. For example, a BMDC culture method with FLT3L and GM-CSF generates functional Baft3-dependent $CD103^+$ cDC1.[286]

Studies in Aim 1.2 measured how co-delivery with MPLA influenced lymphatic transport of CpG ODN. Presence of IRDye700-conjugated ODN in lymph nodes, as well as changes in APC populations in the muscle and draining lymph nodes are indirect measurements of APC migration. More complex in vivo models must be utilized to measure direct migration of APCs; for example, Kaede transgenic mice. Kaede is a photoconvertible fluorescent protein that converts from green to red upon exposure to UV light. When lymph nodes are imaged or processed for flow cytometry, the cells fluorescing red are presumably those that have migrated from the site of UV exposure.[287] To better predict partitioning of cargo from PLGA particles using NIR microscopy, particles will be conjugated to IR dye emitting around 800 nm and measured in a separate filter from IRDye700-conjugated cargo. Also, the colocalization of particles and cells in the lymph node can be quantified based on fluorescent immunohistochemistry and confocal microscopy of lymph nodes.

Vaccines with combination adjuvants for SARS-CoV-2 are still under investigation. A second round of vaccinations with PUUC and MPLA-PUUC NP mixed with unformulated or particle-conjugated spike protein is underway; for this round, particles were injected intramuscularly, and spleen will be collected for restimulation with spike peptide pools.

Though priming of T cells in mediastinal lymph nodes has been shown to induce more potent cell-mediated immunity upon reinfection in the lungs, particle-based formulations must be optimized to ensure efficient delivery into the lungs. The controlled release of combination adjuvants and proper dosing is also important to control inflammatory responses and prevent cytokine storm. There is more analysis to be done with the CITE-Seq data, including differential gene expression analysis between different lung cell clusters and treatment groups.

Through the presentation of multiple PAMPs on micro- and nano-sized delivery vehicles, particle-based combination adjuvants have the potential to elicit more tailored humoral and cell-mediated responses to confer protective immunity against infectious pathogens. This work has shown the differential effects of combination adjuvants on a) APC expression of CCR7 and migration toward lymphatic chemokines, b) recruitment, differentiation, and maturation of immune cell populations at injection sites and draining lymph nodes, c) APC cytokine secretome and activation of T cells, and d) adaptive immune responses to SARS-CoV-2 spike protein. More detailed characterization of immune responses must be carried out in vitro and in vivo to better understand specific combination adjuvant-APC subset interactions and optimize APC targeting for modulation of immunity.

APPENDIX A: SUPPLEMENTARY FIGURES AND METHODS

8.1 Aim 1.1 Supporting Information

8.1.1 Supplemental Experimental Methods

8.1.1.1 Measuring phenotype of BMDCs in 2D vs. 3D culture

GM-CSF/IL-4 BMDCs were cultured for six days in RPMI complete medium as described in the main paper. Loosely adherent cells were removed and cultured in 48-well plates at a density of 1.5 million cells mL^{-1} in media or collagen gels (1.5 mg mL^{-1} collagen). For 3D culture replicates, 100 µL of BMDCs in collagen gel mixture was added to each well and polymerized for 1 hour at 37°C. For the 2D replicates, 100 µL of BMDCs in media was added per well. After 1 hour, 200 µL of media with unformulated (soluble) MPLA was added per well with a final adjuvant concentration of 50 ng mL^{-1}. After 24 hours, cells were collected from 2D wells using a cell scraper and 3D wells by digesting gels with Collagenase D (2 mg mL^{-1} media) for 10 minutes. Cells were analyzed by flow cytometry as described in the main paper. Results shown in Figure S6.

8.1.1.2 Validating CCL19 and CCL21 gradient stability and 3D culture in devices

9-kDa CCL19 and 12-kDa CCL21 were incubated with AF488 NHS ester in sodium bicarbonate buffer for 3 hours (Lumiprobe). Buffer was exchanged for PBS and fluorescent chemokines were concentrated using Amicon 3 kDa Ultra-2 Centrifugal Filters (Millipore Sigma). AF488-fluorescent chemokines diluted in media (1 µg mL^{-1}) were added to the left reservoir of microfluidic devices. Media without chemokines was added to the right reservoir. Collagen gel channels were imaged with the Lionheart Biotek fluorescent

microscope using the 4X objective for 18 hours, with images taken every 10 minutes. The fluorescence intensity across the channel was measured using the "Plot Profile" function of ImageJ and graphed with MATLAB (Figure S7). To validate 3D culture of BMDCs in the collagen gel, live cells were labeled with Biotracker 555 Orange Cytoplasmic Membrane Dye (Sigma-Aldrich) and NucBlue™ Live ReadyProbes™ Reagent (Invitrogen) before suspended in the collagen gel channel (left to polymerize for 1 hour at 37°C). Media reservoirs were filled with Live Cell Imaging Solution (Gibco). A 40 μm Z stack was taken (20 slices) using a ZEISS confocal microscope. The image was projected in 3D using ImageJ. The xy and zy planes are shown in Figure S8.

8.1.2 Circular Statistical Methods

8.1.2.1 Calculation of Mean Direction and Resultant Length

For the analysis in this paper, cell displacements are assumed to be unit vectors (sample size=*n*) with corresponding bearing angles. These vectors are arranged so the beginning of the first vector is at the origin. The mean bearing angle of cell migration is the direction of the resultant vector and of the center of mass [1].[188] The Cartesian coordinates of the center of mass are:

$$\bar{C} = \frac{1}{n}\sum_{i=1}^{n}\cos\theta_i \quad \bar{S} = \frac{1}{n}\sum_{i=1}^{n}\sin\theta_i \quad i = 1, \dots, n \qquad (\boldsymbol{S1})$$

The mean resultant length is given by:

$$\bar{R} = \sqrt{(\bar{C}^2 + \bar{S}^2)} \quad 0 \le \bar{R} \le 1 \qquad (\boldsymbol{S2})$$

When the mean resultant length is greater than 0, the mean direction (bearing angle) is:

$$\bar{\theta} = \begin{cases} \tan^{-1}\left(\frac{\bar{S}}{\bar{C}}\right), & \bar{S} > 0, \bar{C} > 0 \\ \tan^{-1}\left(\frac{\bar{S}}{\bar{C}}\right) + \pi, & \bar{C} < 0 \\ \tan^{-1}\left(\frac{\bar{S}}{\bar{C}}\right) + 2\pi, & \bar{S} < 0, \bar{C} > 0 \\ \frac{\pi}{2} & S > 0, C = 0 \\ -\frac{\pi}{2} & S < 0, C = 0 \end{cases} \quad (\boldsymbol{S3})$$

If cell bearing angles are more concentrated toward a single direction, the mean resultant length will be closer to 1. If the bearing angles are dispersed, then the mean resultant length will be closer to 0. Another measure of dispersion is the circular variance, which is defined as:

$$V = 1 - \bar{R} \quad (\boldsymbol{S4})$$

Therefore, as the mean resultant length approaches 1, the variance decreases.

8.1.2.2 Cox Test

Prior to conducting a multi-sample statistical test, it is important to assess whether the distribution of cell directions follows a von Mises distribution. The von Mises distribution for points on a circle is comparable to a normal distribution of points on a line.[189] The Cox test is a goodness-of-fit test where the null hypothesis of a von Mises distribution is rejected for large values of S.[190] Under the null hypothesis, the sampling distribution of S is a chi-squared distribution with two degrees of freedom. The function $I_v(\kappa)$ is the modified Bessel function of the first kind and order *v*.

$$S = \frac{s_c^2}{v_c(\hat{\kappa})} + \frac{s_s^2}{v_s(\hat{\kappa})} \quad (\boldsymbol{S5})$$

$$s_c = \sum_{i=1}^{n} \cos 2(\theta_i - \bar{\theta}) - n\,\bar{R} \qquad s_s = \sum_{i=1}^{n} \sin 2(\theta_i - \bar{\theta}) \tag{S6}$$

$$v_c(\kappa) = \frac{I_0(\kappa)^2 + I_0(\kappa)I_4(\kappa) - 2I_2(\kappa)^2}{2I_0(\kappa)^2} - \frac{\left(I_0(\kappa)I_3(\kappa) + I_0(\kappa)I_1(\kappa) - 2I_1(\kappa)I_2(\kappa)\right)^2}{2I_0(\kappa)^2\left(I_0(\kappa)^2 + I_0(\kappa)I_1(\kappa) - 2I_1(\kappa)^2\right)} \tag{S7}$$

$$v_s(\kappa) = \frac{\left(I_0(\kappa) - I_4(\kappa)\right)\left(I_0(\kappa) - I_2(\kappa)\right) - \left(I_0(\kappa) - I_3(\kappa)\right)^2}{2I_0(\kappa)\left(I_0(\kappa) - I_2(\kappa)\right)} \tag{S8}$$

Assuming the sample size is greater than 15, the value of the concentration parameter of a von Mises distribution, κ, would be equal to the following:

$$\hat{\kappa} \simeq \begin{cases} 2\bar{R} + \bar{R}^3 + \frac{5\bar{R}^5}{6}, & \bar{R} < 0.53 \\ -0.4 + 1.39\bar{R} + \frac{0.43}{V}, & 0.53 \le \bar{R} < 0.85 \\ \frac{1}{2V - V^2 - V^3}, & \bar{R} \ge 0.85 \end{cases} \tag{S9}$$

Further details can be found in Mardia & Jupp (2000) as well as Fisher (1993).[188,288]

If each cell migration data set fits a von Mises distribution, next step is a circular statistical equivalent to the one-way ANOVA, known as the Watson-Williams High Concentration F Test. Given the more likely scenario all the data sets do not fit a von Mises distribution, mean directions would be compared using the non-parametric multi-sample method, a Mardia-Watson-Wheeler Uniform Scores Test.

8.1.2.3 Mardia-Watson-Wheeler Uniform Scores Test

Suppose you have q populations. In this paper, each population is a condition cells are tested under (for example, cells activated with a particular adjuvant, migrating toward a particular chemokine). The null hypothesis is

$$H_0: F_1 = \cdots = F_q$$

where F_q is the continuous distribution function of q population. The alternative hypothesis is that the distribution functions are not all the same. Each population has a sample size of

n_i. All the populations are combined into a single data set with a combined sample size of $n=n_1+\ldots+n_q$.

Within the combined data set, the angles are ranked with 0° being the lowest ranking. If there are ties between angles, then the rankings are randomly assigned. For example, if there are two cells with bearing angles of 20°, instead of both being assigned a ranking of 15, they will be randomly assigned 15 and 16. The ranking is denoted by symbol *r*. The values of the bearing angles are replaced with their uniform scores, denoted by β:

$$\beta_{ij} = \frac{2\pi r_{ij}}{n} \qquad j = 1, \ldots, n_i \qquad i = 1, \ldots, q \qquad n = \sum_{i=1}^{q} n_i \tag{$\boldsymbol{S10}$}$$

For this test, the null hypothesis is rejected for larger values of W, where

$$W = 2\sum_{i=1}^{q} \frac{R_i^2}{n_i} \tag{$\boldsymbol{S11}$}$$

The variable R_i is the resultant length of the uniform scores in the *i*th sample, and according to Equation S2 would be

$$R_i^2 = \left(\sum_{j=1}^{n_i} \cos\beta_{ij}\right)^2 + \left(\sum_{j=1}^{n_i} \sin\beta_{ij}\right)^2 \tag{$\boldsymbol{S12}$}$$

If there are two data sets, for example, then W would be calculated as

$$W = 2\left(\frac{R_1^2}{n_1} + \frac{R_2^2}{n_2}\right) \tag{$\boldsymbol{S13}$}$$

If each population has a sample size greater than 10, then the distribution of W is comparable to a chi-square distribution with 2(g-1) degrees of freedom.[289]

8.1.2.4 Post-Hoc Test

There are two post-hoc tests proposed by Tasdan and Yeniay to identify means that are significantly different from each other after performing the Watson-Williams and Mardia-Watson-Wheeler tests.[191] The first post-hoc test uses the classical Bonferroni procedure while the second test uses Holm's improved Bonferroni procedure for testing pairwise

hypotheses. Watson Williams or Mardia-Watson Wheeler tests can be used for pairwise comparisons. The p-value from each pairwise comparison is ranked in order from smallest (P_1) to largest (P_m).

$$H_0 = \{H_1, H_2, \dots H_m\} \quad (\boldsymbol{S14})$$

Post-Hoc Test 1: Reject the null hypothesis (H_i) if

$$P_i \leq \frac{\alpha}{m} \qquad i = 1, 2, \dots, m \quad (\boldsymbol{S15})$$

Post-Hoc Test 2: Reject the null hypothesis if

$$P_i \leq \frac{\alpha}{m-j+1} \qquad i = 1, 2, \dots, m \qquad j = 1, 2, \dots, i \quad (\boldsymbol{S16})$$

and H_0 is always rejected if any H_i is rejected.

8.1.3 Supplemental Figures

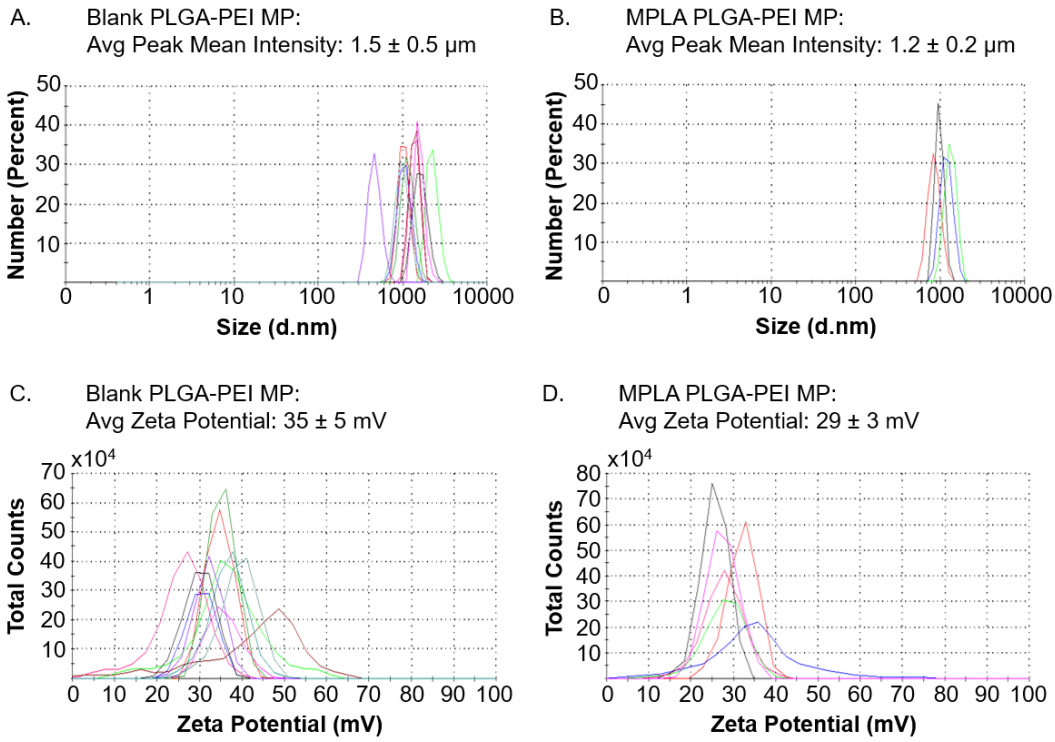

Figure S1: Size and charge characterization of PLGA MP. The size and charge (zeta potential) of Blank and MPLA-encapsulated PLGA-PEI MP were measured using dynamic light scattering (Malvern Panalytical Zetasizer Nano ZS). Each colored line represents a different batch of Blank or MPLA-PLGA-PEI microparticles. A) Average peak mean intensity (d.nm) for Blank PLGA-PEI MP and graph of size distribution by number. 10 batches represented. B) Average peak mean intensity (d.nm) for MPLA PLGA-PEI MP and graph of size distribution by number. 4 batches represented. C) Average surface zeta potential of Blank PLGA-PEI and graph of zeta potential distribution. 11 batches represented. D) Average surface zeta potential of MPLA-PLGA-PEI and graph of zeta potential distribution. 6 batches represented.

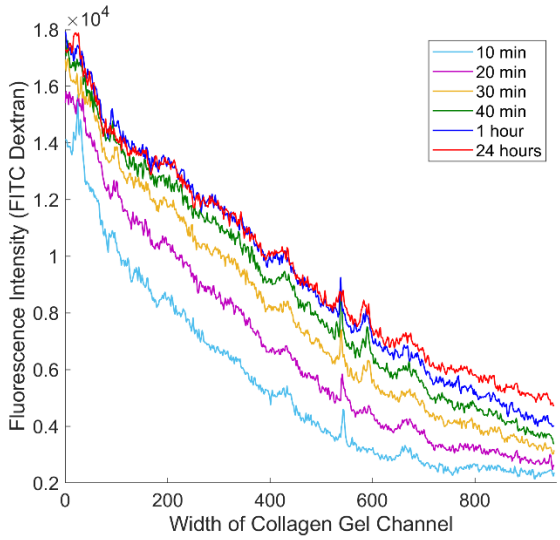

Figure S2: FITC dextran gradient through collagen matrix is stable for 24 hours in microfluidic device. The fluorescence intensity of 10,000 MW FITC-Dextran plotted across the width of the collagen matrix channel (μm). At 0 μm is the left reservoir with chemokine media, and at 1000 μm is the right reservoir without chemokine. After 1 hour, the gradient is established and is stable up to 24 hours. Intensity measurements calculated with ImageJ.

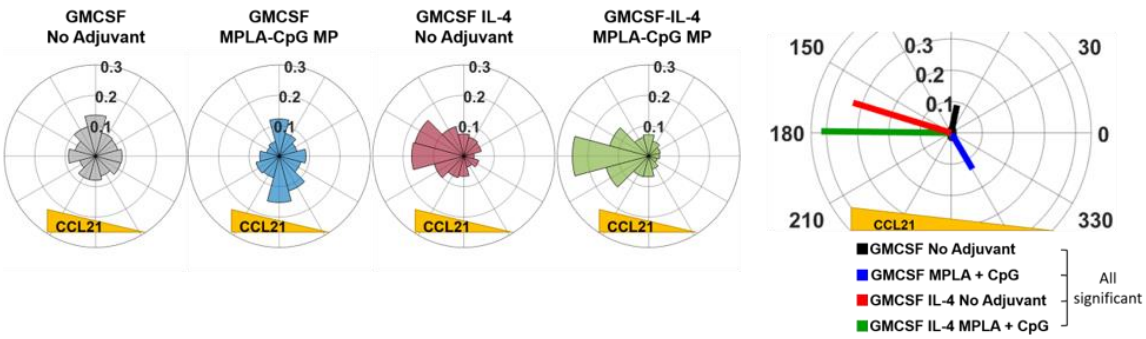

Figure S3: GM-CSF-only BMDCs do not exhibit chemotaxis in response to MPLA-CpG MP. Polar histograms of GM-CSF and GM-CSF+IL-4 cell orientation toward CCL21 gradients (yellow triangles represent gradient direction toward left reservoir, 180° on polar plot) after activation with MPLA-CpG MP (No Adjuvant indicates no MP present). Far right: polar plot comparing mean directions and resultant lengths (inversely proportional to directional variance). Black brackets next to legend indicates statistical significance between mean directions ($p<0.01$) with Mardia-Watson-Williams Uniform Scores Test and Tasdan-Yeniay post-hoc test.

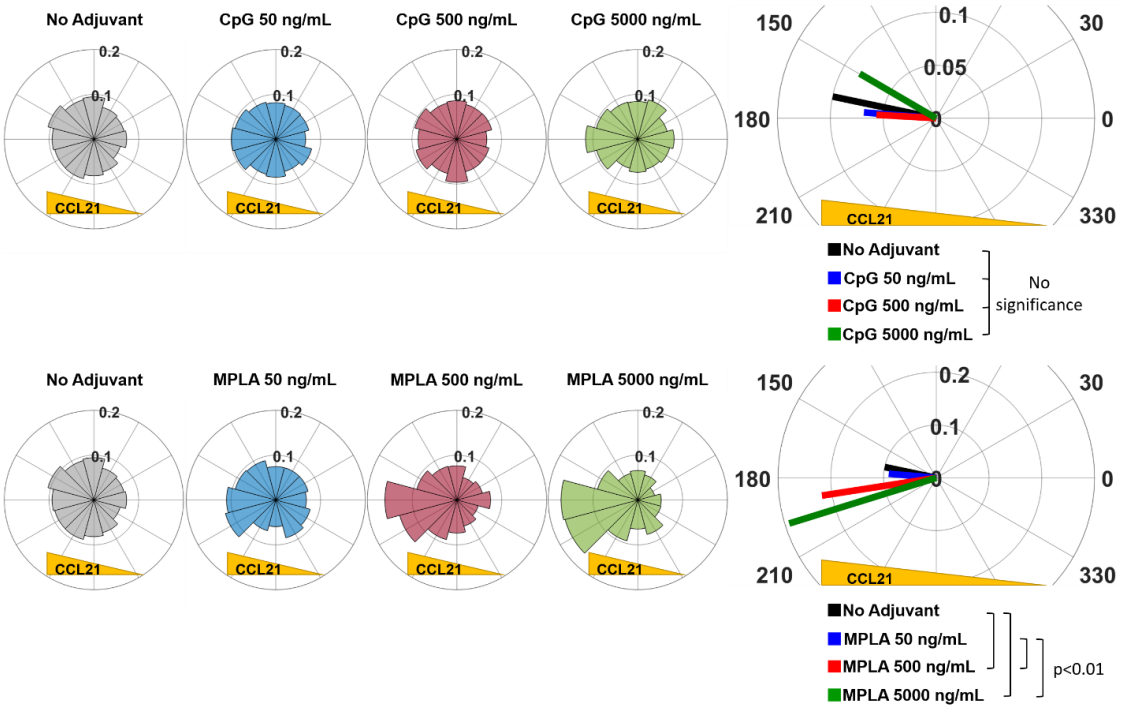

Figure S4: Increasing concentrations of soluble MPLA correlates with increased BMDC chemotactic response, while increasing concentrations of soluble CpG do not stimulate chemotaxis. Normalized histograms of BMDC orientation toward CCL21 gradients (250 ng/mL, different from rest of experiments with 1 ug/mL chemokine) in response to A) increasing concentrations of CpG DNA or B) increasing concentrations of MPLA. Yellow triangles represent gradient direction toward left reservoir, 180° on polar plot. Control is no adjuvant. Far right polar plots compare mean directions and resultant lengths (inversely proportional to directional variance). Black brackets next to legend indicates statistical significance between mean directions ($p<0.01$) with Mardia-Watson-Williams Uniform Scores Test and Tasdan-Yeniay post-hoc test.

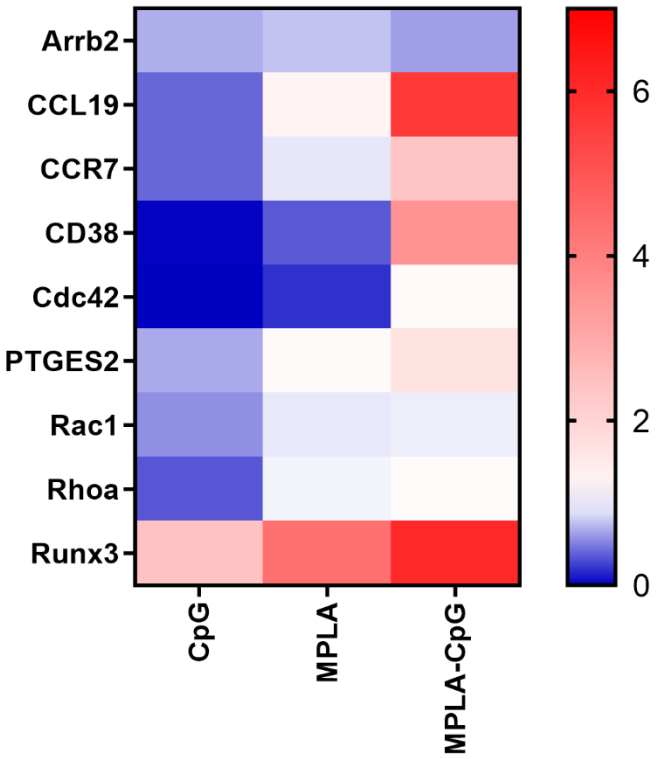

Figure S5: Soluble CpG decreases expression of CCR7 signaling mediators while MPLA maintains and MPLA-CpG increases expression. BMDCs were cultured with soluble MPLA and CpG as described in Methods section for 12 hours, then homogenized to collect RNA for PCR analysis. Blue on the color scale depicts decreased expression (negative fold change) of genetic markers compared to the control (BMDCs without adjuvant) while red depicts increased expression (positive fold change) compared to the control. Data normalized to Hprt housekeeping gene. Markers were selected for the following reasons: (1) Arrb2, internalization of CCR7;[290] (2) CCL19, autocrine chemotaxis signaling;[153,217,291] (3) CCR7, chemokine receptor; (4) CD38, reported mediator of CCR7 signaling;[223] (5) Cdc42, controls CCR7-dependent endocytosis and change in cytoarchitecture;[155] (6) PTGES2, catalyzes conversion of PGH2 to PGE2 to enhance CCR7 signaling;[221,292] (7) Rac1, controls CCR7-dependent endocytosis and change in cytoarchitecture;[155] (8) Rhoa, controls CCR7-dependent migratory speed;[155] (9) Runx3, reportedly regulates TGFβ-mediated attenuation of CCR7 expression.[293]

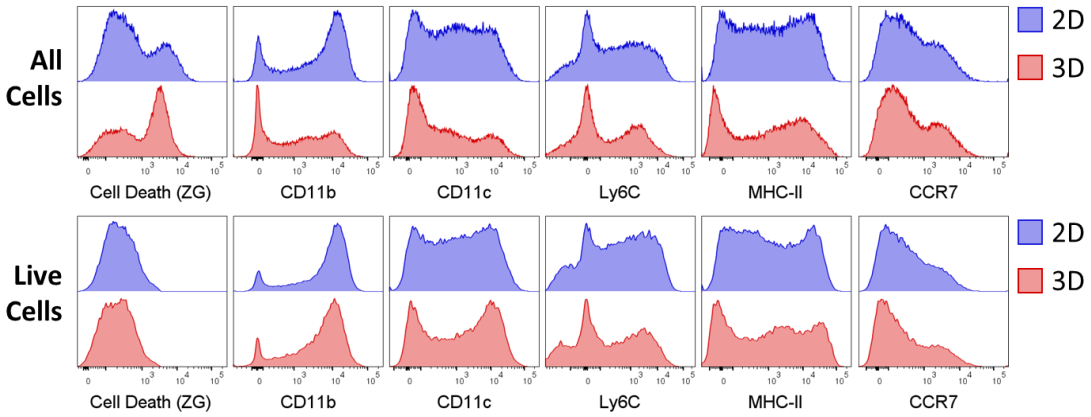

Figure S6. Phenotype of GMCSF/IL-4 BMDCs activated by MPLA in 2D vs. 3D. Representative histograms of cells cultured for 24 hours in 2D (suspended in media) or 3D (suspended in collagen gel with media above the gel) and activated by MPLA. Top panel shows histograms of marker fluorescence for all cells and the bottom panel shows marker fluorescence for live cells, which have a low Zombie Green (ZG, fixable viability dye) signal.

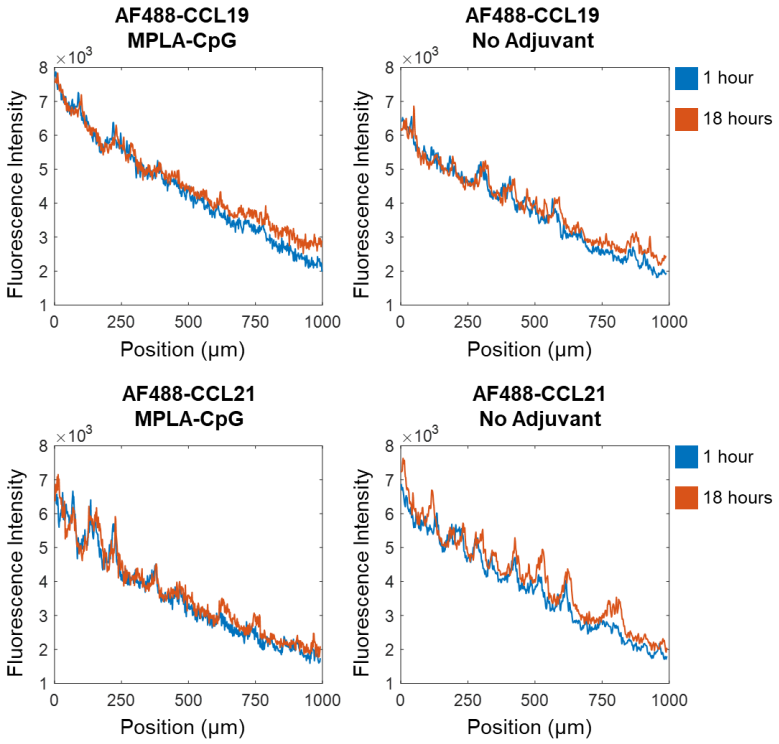

Figure S7: Stability of AF488-fluorescent CCL19 and CCL21 gradients with addition of soluble adjuvants. Top panel: CCL19 fluorescence intensity across collagen gel (width 1 mm) with and without MPLA and CpG in media. Bottom panel: CCL21 fluorescence intensity across collagen gel with and without MPLA and CpG in media reservoirs. Blue plot is gradient at 1 hour and red plot is gradient at 18 hours.

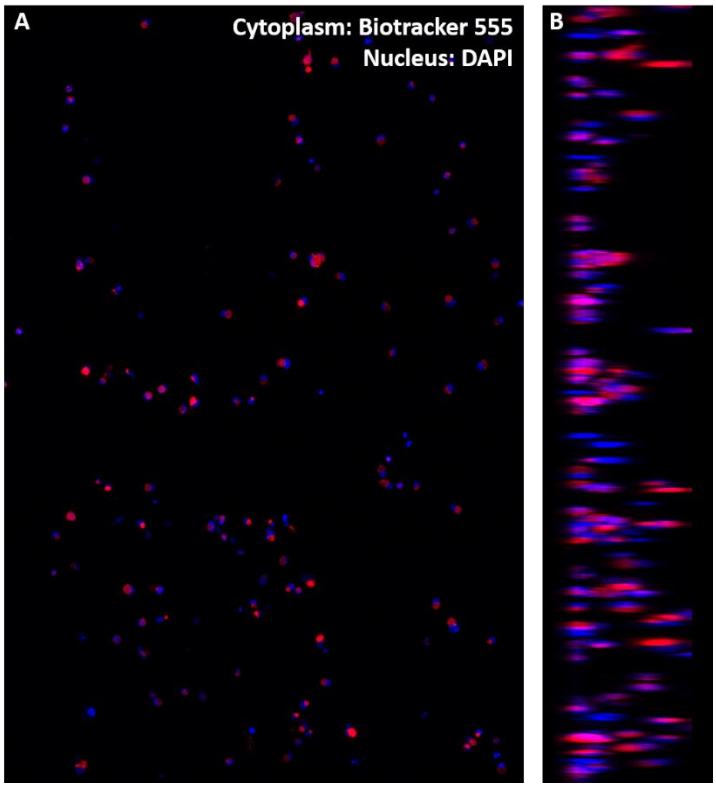

Figure S8: 3D BMDC culture in collagen gel channel of microfluidic device. A) Center of collagen gel channel in x-y plane imaged with a 20X objective. Cytoplasm was labeled with Biotracker 555 and nucleus labeled with DAPI. B) Collagen channel in z-y plane. Z stack was imaged over a distance of 40 µm.

8.2 Aim 1.2 Supporting Information

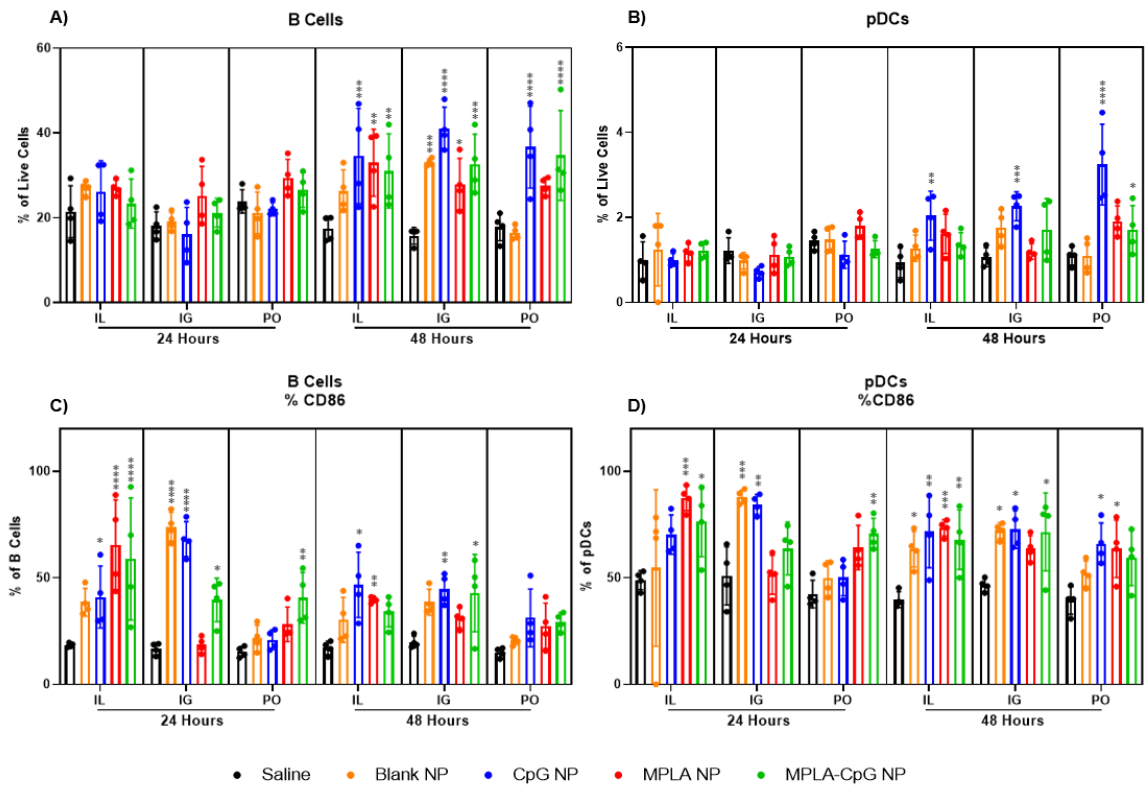

Figure S9: PLGA PEI NP with MPLA and/or CpG differentially regulate B cell and pDC populations and their expression of CD86 in draining lymph nodes. A) Percentages of B cells out of live cells ($B220^{+}MHCII^{+}CD11c^{-}$) in iliac (IL), inguinal (IG), and popliteal (PO) at 24 and 48 hours. B) Percentages of pDCs ($B220^{+}MHCII^{+}CD11c^{+}$) out of live cells. C) Percentages of B cells expressing CD86. D) Percentages of B cells expressing CD86. ****p<0.0001, ***p<0.001, **p<0.01, *p<0.05 significance for particle groups compared to saline within each lymph node group according to Two-Way ANOVA and Tukey test for multiple comparison.

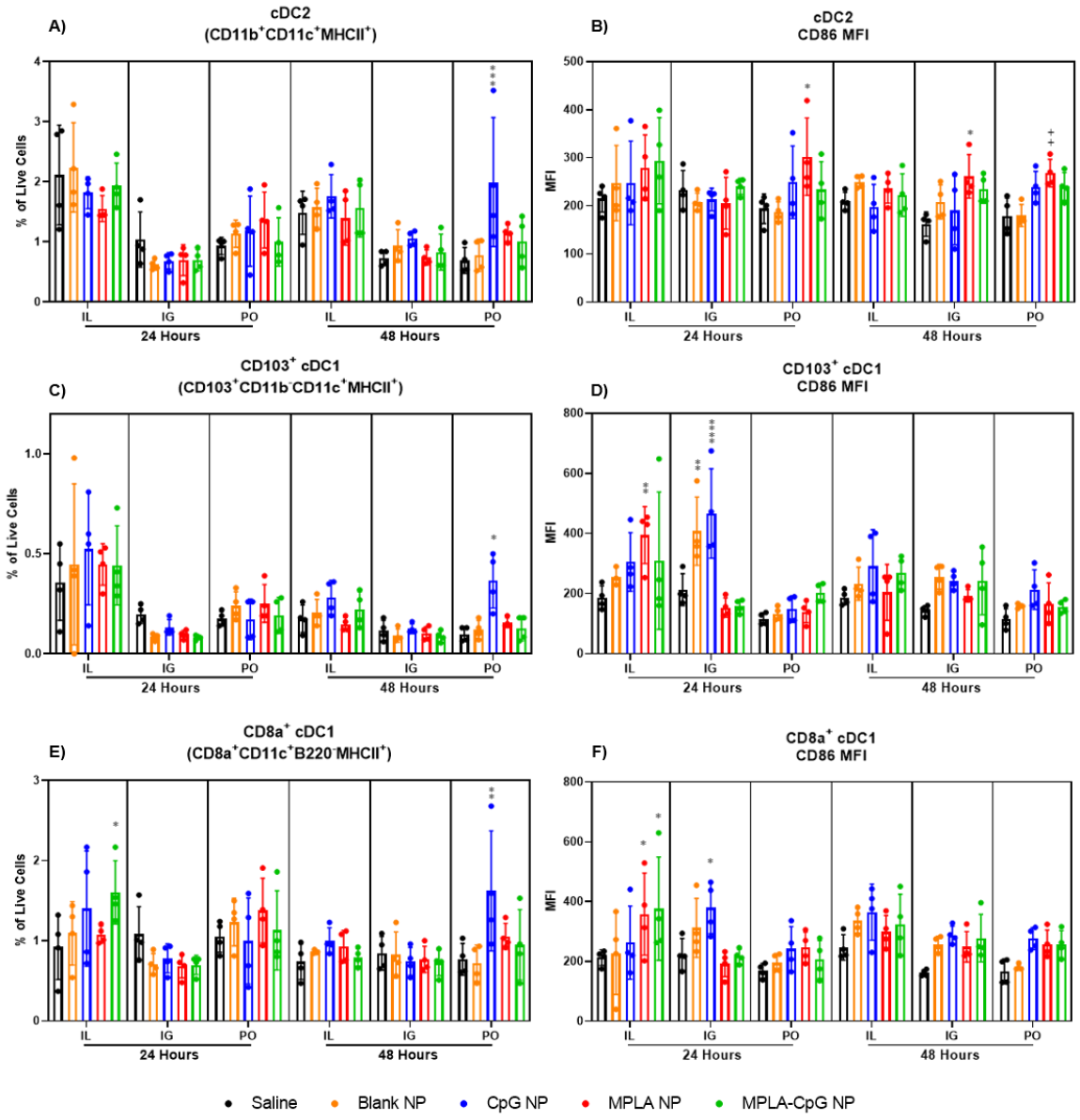

Figure S10: PLGA PEI NP with MPLA and/or CpG differentially regulate cDC populations and their expression of CD86 in draining lymph nodes. All cDC populations are negative for B220 to exclude B cells and pDCs. A-B) Changes in cDC2 ($CD11c^+MHCII^+CD11b^+$) percentages out of live cells and CD86 expression (BV786 median fluorescence intensity). C-D) Changes in $CD103^+$ cDC1 ($CD11c^+MHCII^+CD11b^{lo/-}CD103^+$) percentages out of live cells and CD86 expression (BV786 MFI). E-F) Changes in $CD8a^+$ cDC1 ($CD11c^+MHCII^+CD8a^+$) percentages out of live cells and CD86 expression. ****p<0.0001, ***p<0.001, **p<0.01, *p<0.05 significance for particle groups compared to saline within each lymph node group according to Two-Way ANOVA and Tukey test for multiple comparison. $^{++}$p<0.01 according to One-Way ANOVA and Tukey test, but not Two-Way ANOVA.

8.3 Aim 2.1 Supporting Information

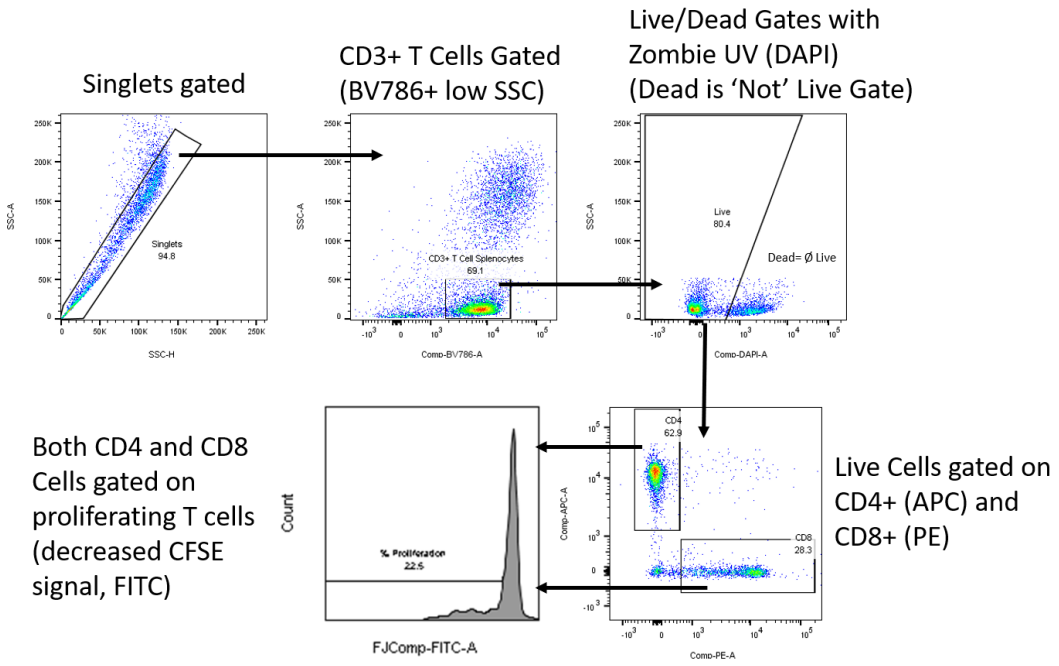

Figure S11: Flow gating scheme for measuring T cell proliferation in iso-MLR assay.

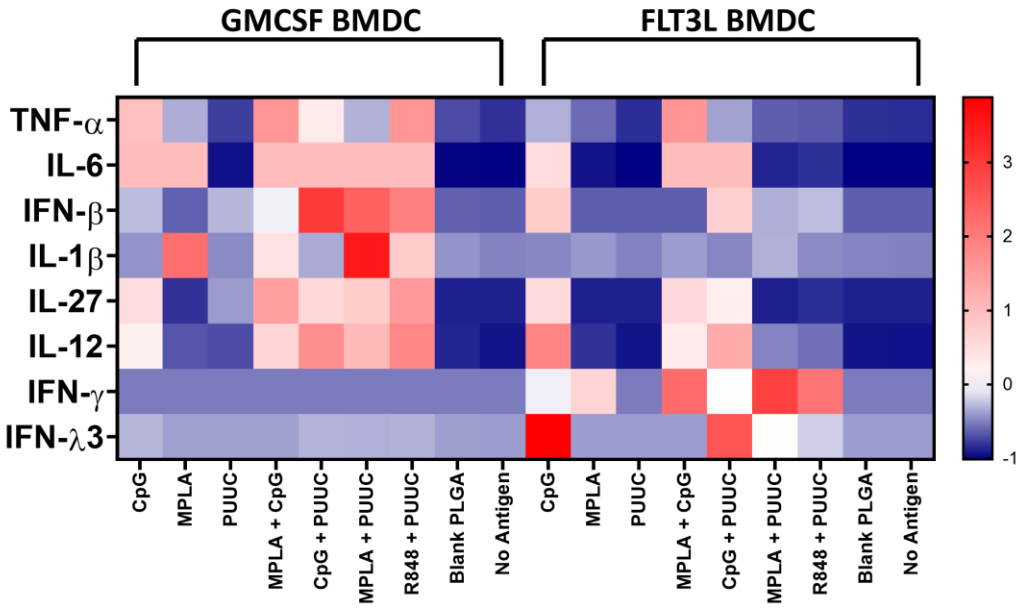

Figure S12: Heatmap of cytokine levels produced by GM-CSF and FLT3L BMDCs after 24 hours of incubation with PLPs from iso-MLR Trial #3 with female BALB/cJ mice. Color scale corresponds with z-scores, calculated by standardizing mean cytokine concentration values (pg/mL) across rows. Each square is a z-score calculated from a cytokine concentration value averaged from three technical replicates.

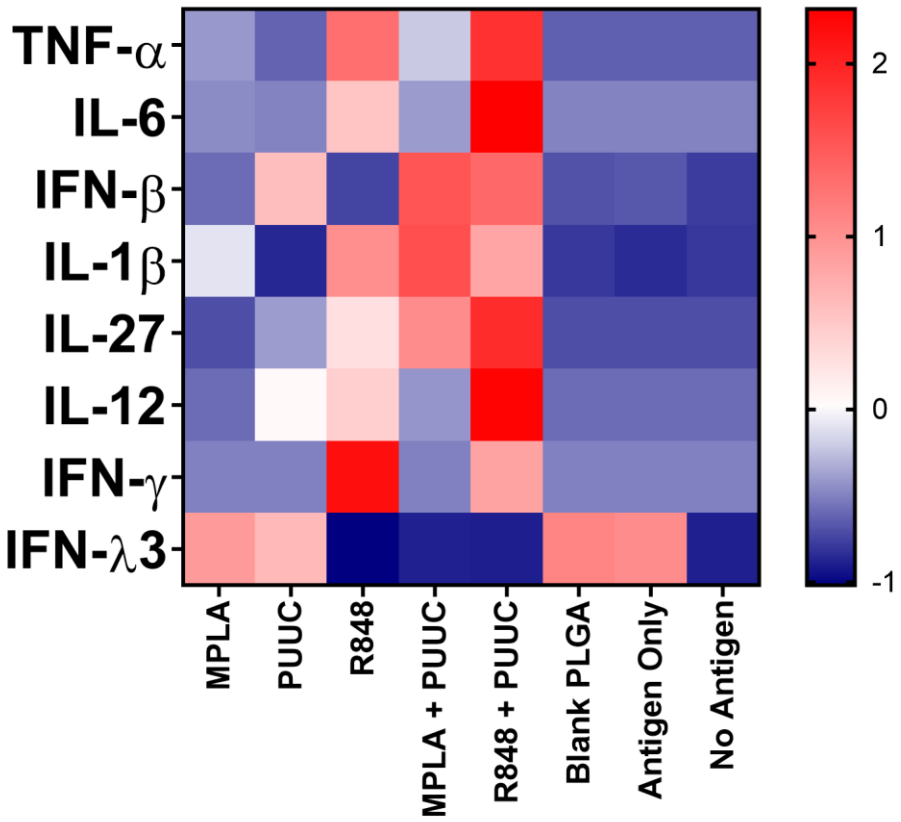

Figure S13: Heatmap of cytokine levels produced by GM-CSF BMDCs after 24 hours of incubation with PLPs from iso-MLR Trial #6 with female BALB/cJ mice. Color scale corresponds with z-scores, calculated by standardizing mean cytokine concentration values (pg/mL) across rows. Each square is a z-score calculated from a cytokine concentration value averaged from three technical replicates.

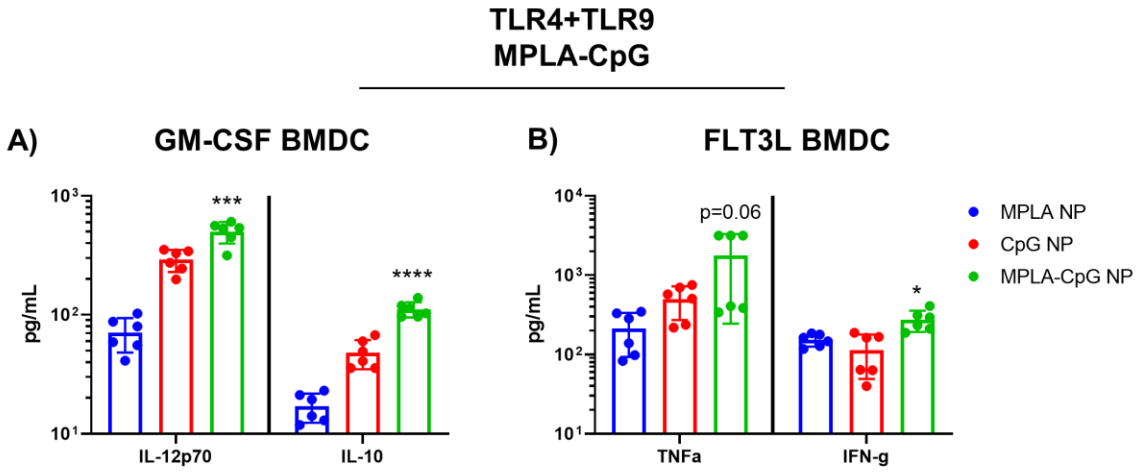

Figure S14: MPLA-CpG NPs enhance pro-inflammatory cytokine and interferon production by GM-CSF and FLT3L BMDCs after 24 hours of incubation. A) IL-12 and IL-10 secretion by GM-CSF BMDCs after 24-hr incubation with MPLA NPs, CpG NPs, and MPLA-CpG NPs. Sample size is 6, with 3 technical replicates from two separate trials. For IL-12 data set, all BMDCs were from female BALB/cJ mice. For IL-10 data set, one trial was with female BMDCs and one with male BMDCs. *$p<0.05$, ***$p<0.001$, ****$p<0.0001$ from One-Way ANOVA with Tukey multiple comparisons test.

8.4 Aim 2.2 Supporting Information

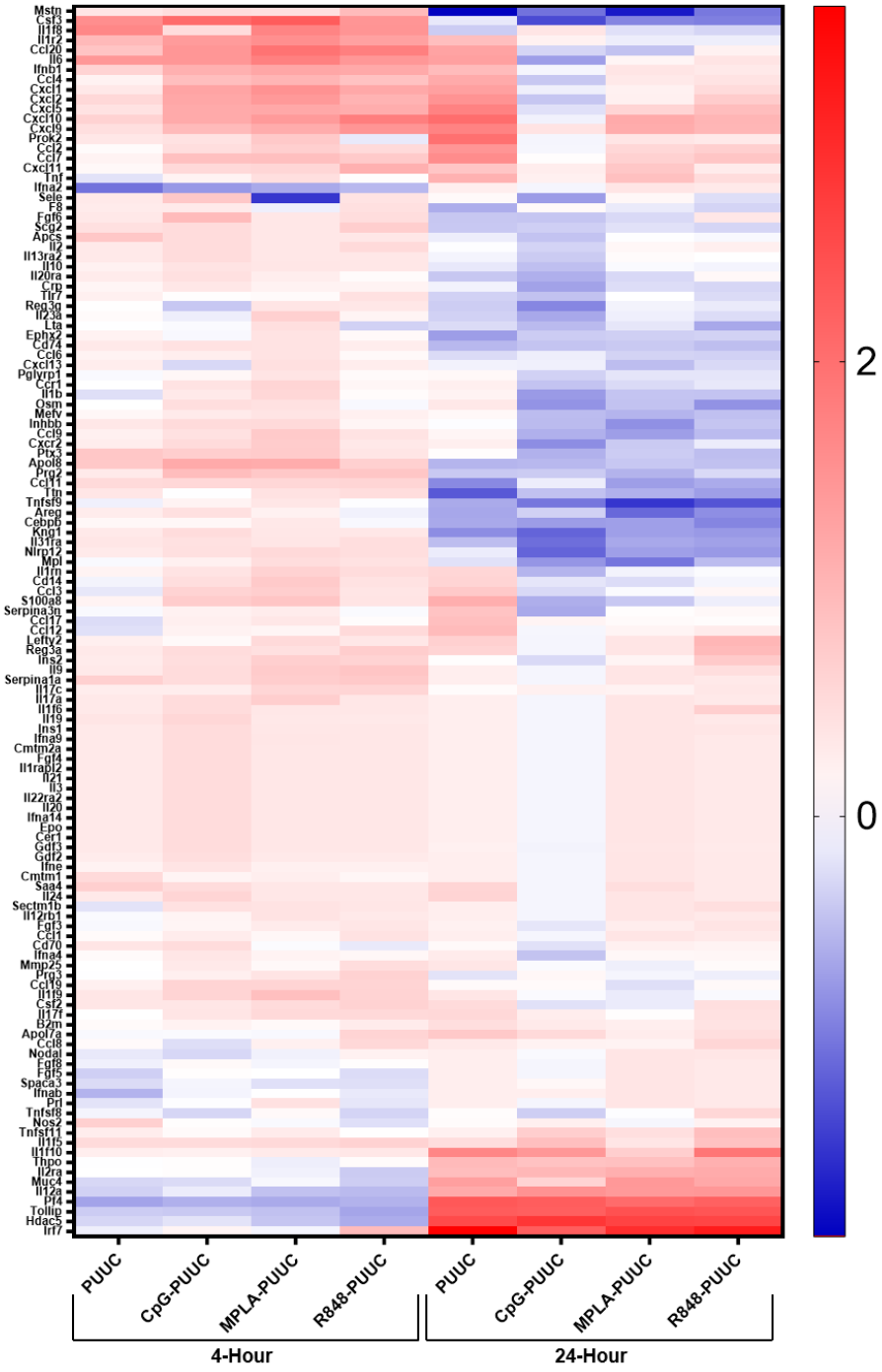

Figure S15: Heatmap depicting fold changes in expression of inflammatory and autoimmunity-related genes 4 and 24 hours after intranasal delivery of PLPs to mouse lungs. Fold change is on the log10 scale.

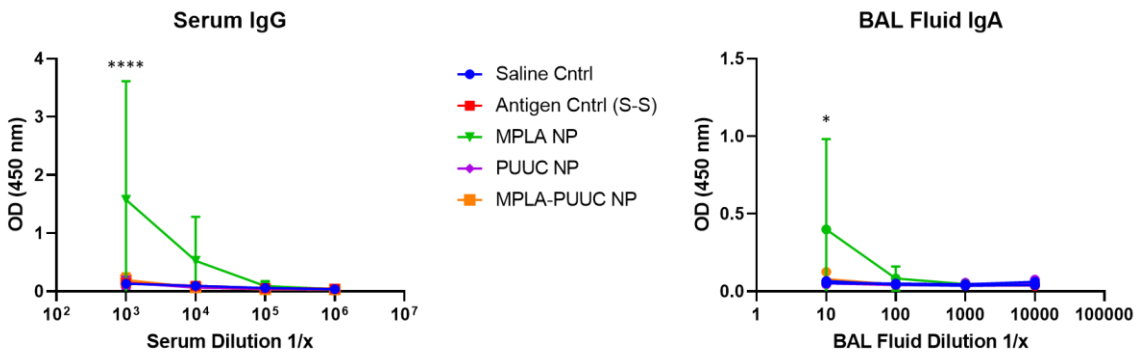

Figure S16: Serum IgG and BAL fluid IgA levels in mouse sera post-booster intranasal vaccination with PLPs.

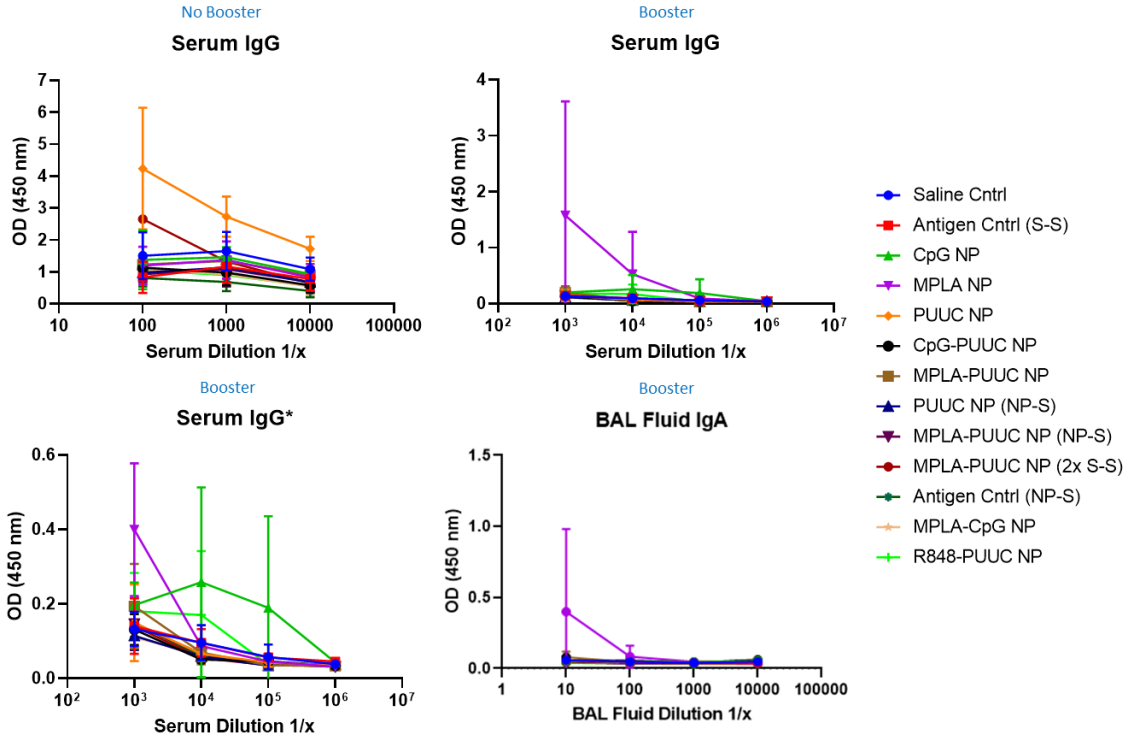

Figure S17: Serological assays measuring mouse serum IgG and BAL fluid IgA before and after booster shots with all PLP treatment groups.

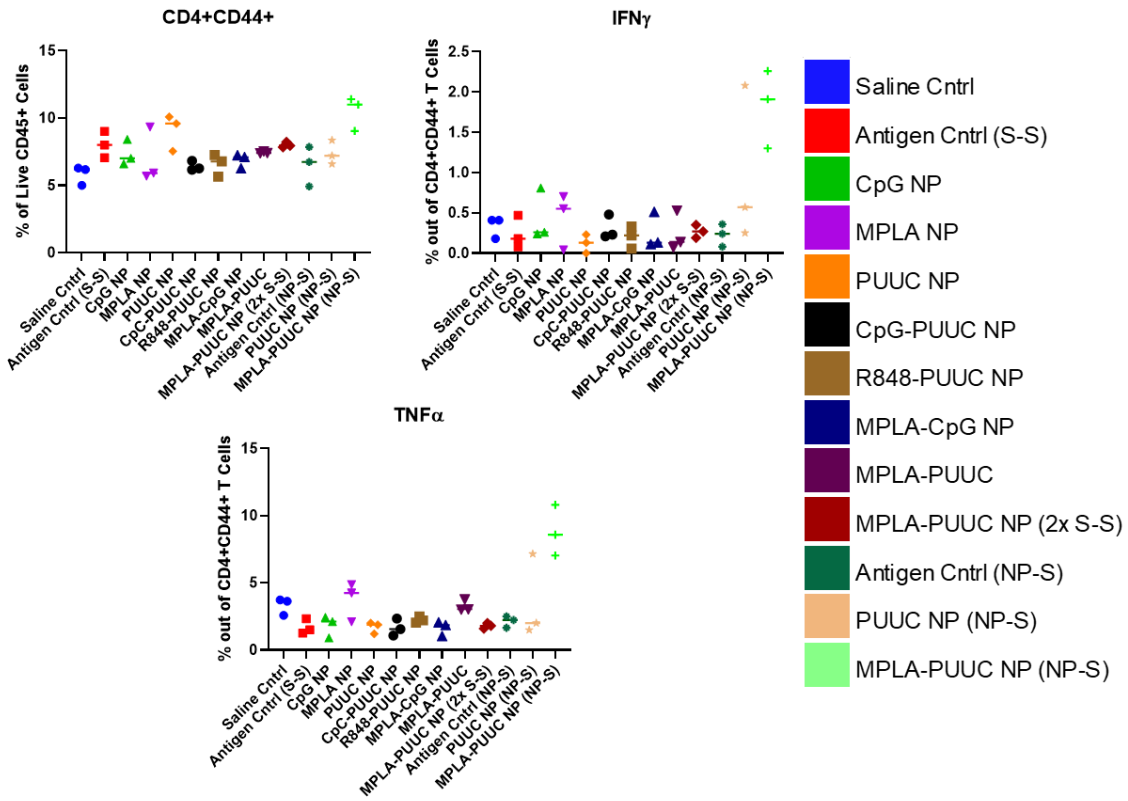

Figure S18: CD4$^+$ T cell populations and cytokine secretion in mouse lung cell culture after restimulation with SARS-CoV-2 spike peptide pool. All PLP treatment groups included.

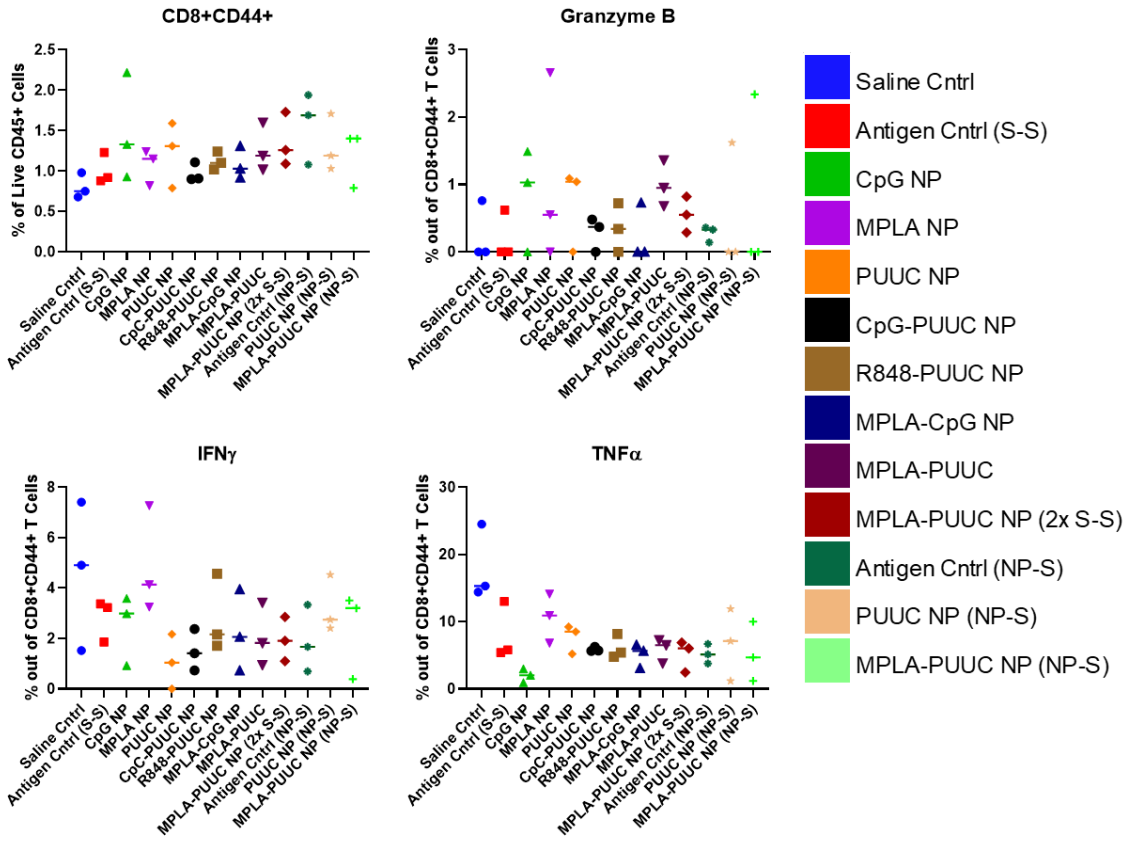

Figure S19: CD8$^+$ T cell populations and cytokine secretion in mouse lung cell culture after restimulation with SARS-CoV-2 spike peptide pool. All PLP treatment groups included.

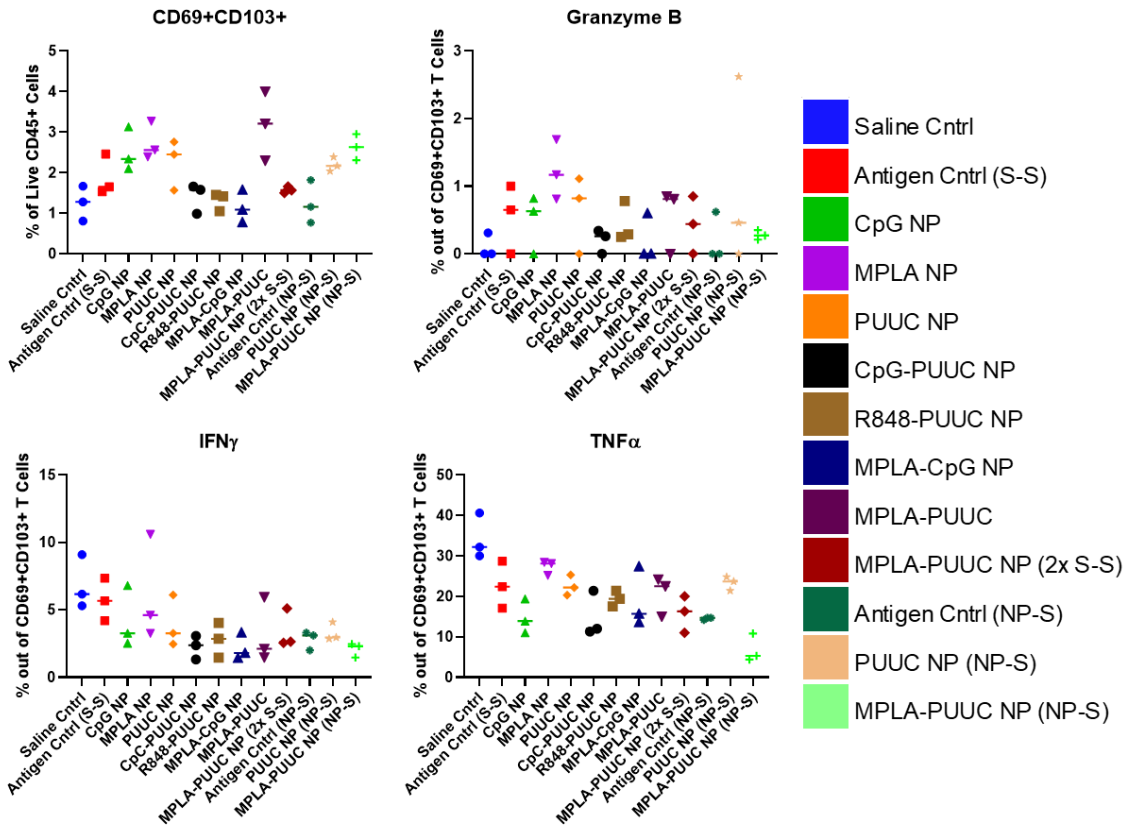

Figure S20: CD103^{+}CD69^{+} T cell populations and cytokine secretion in mouse lung cell culture after restimulation with SARS-CoV-2 spike peptide pool. All PLP treatment groups included.

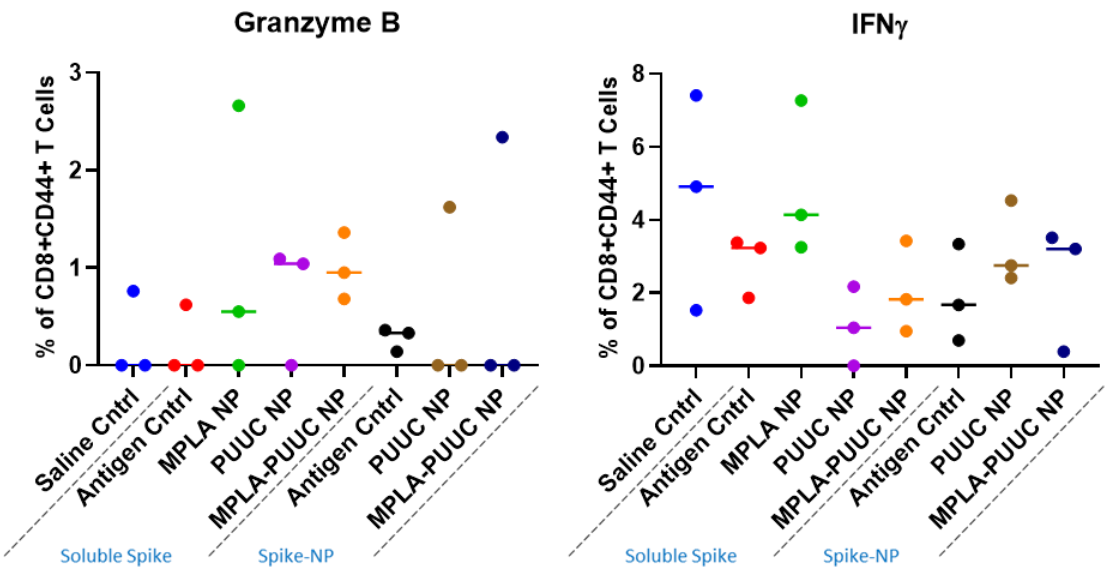

Figure S21: CD8^{+} T cell populations and cytokine secretion in mouse lung cell culture after restimulation with SARS-CoV-2 spike peptide pool. MPLA-PUUC and PUUC NP groups.

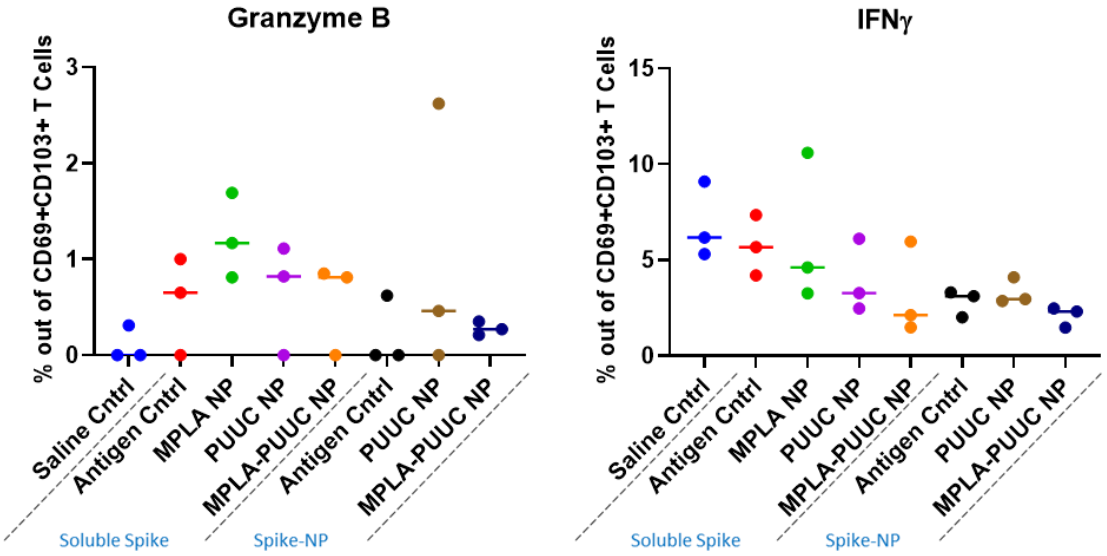

Figure S22: CD103^{+}CD69^{+} T cell populations and cytokine secretion in mouse lung cell culture after restimulation with SARS-CoV-2 spike peptide pool. MPLA-PUUC and PUUC NP groups.

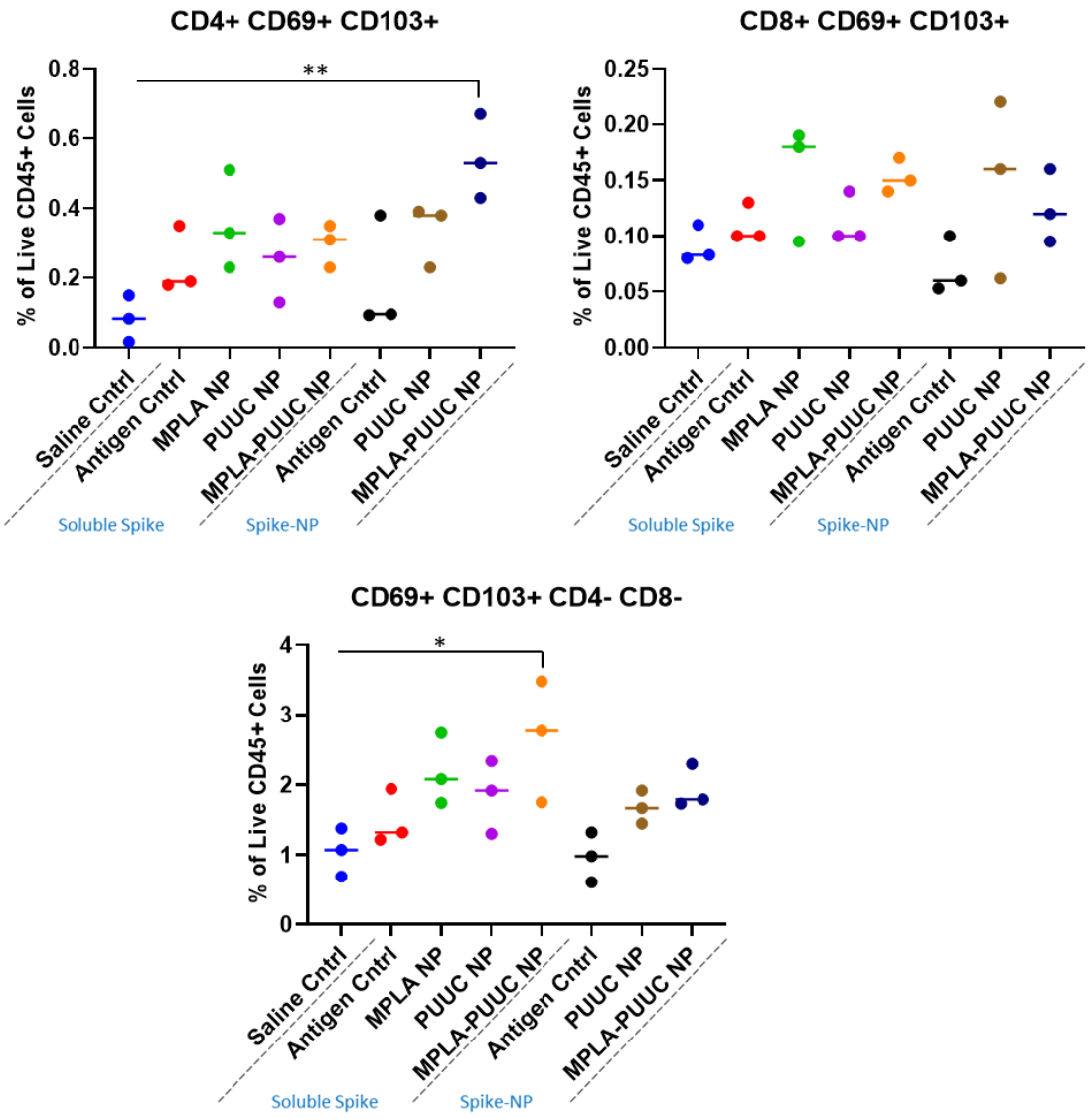

Figure S23: CD103^{+}CD69^{+} T cell populations and cytokine secretion in mouse lung cell culture after restimulation with SARS-CoV-2 spike peptide pool. MPLA-PUUC and PUUC NP groups.

REFERENCES

1. World Health Organization. Vaccines and immunization. https://www.who.int/health-topics/vaccines-and-immunization#tab=tab_1.

2. World Health Organization. *Draft landscape and tracker of COVID-19 candidate vaccines*. https://www.who.int/publications/m/item/draft-landscape-of-covid-19-candidate-vaccines (2021).

3. HogenEsch, H., O'Hagan, D. T. & Fox, C. B. Optimizing the utilization of aluminum adjuvants in vaccines: you might just get what you want. *npj Vaccines* vol. 3 51 (2018).

4. Marrack, P., McKee, A. S. & Munks, M. W. Towards an understanding of the adjuvant action of aluminium. *Nature Reviews Immunology* vol. 9 287–293 (2009).

5. Shardlow, E., Mold, M. & Exley, C. Unraveling the enigma: Elucidating the relationship between the physicochemical properties of aluminium-based adjuvants and their immunological mechanisms of action. *Allergy, Asthma and Clinical Immunology* vol. 14 80 (2018).

6. Trinchieri, G. & Sher, A. Cooperation of Toll-like receptor signals in innate immune defence. *Nature Reviews Immunology* vol. 7 179–190 (2007).

7. Brubaker, S. W., Bonham, K. S., Zanoni, I. & Kagan, J. C. Innate Immune Pattern Recognition: A Cell Biological Perspective. *Annu. Rev. Immunol.* **33**, 257–290 (2015).

8. Saito, T., Owen, D. M., Jiang, F., Marcotrigiano, J. & Gale, M. Innate immunity induced by composition-dependent RIG-I recognition of hepatitis C virus RNA. *Nature* **454**, 523–527 (2008).

9. Zanoni, I. *et al.* CD14 controls the LPS-induced endocytosis of toll-like receptor 4. *Cell* **147**, 868–880 (2011).

10. Didierlaurent, A. M. *et al.* AS04, an Aluminum Salt- and TLR4 Agonist-Based Adjuvant System, Induces a Transient Localized Innate Immune Response Leading to Enhanced Adaptive Immunity. *J. Immunol.* **183**, 6186–6197 (2009).

11. Champion, C. R. Heplisav-B: A Hepatitis B Vaccine With a Novel Adjuvant. *Ann. Pharmacother.* 106002802096205 (2020) doi:10.1177/1060028020962050.

12. Querec, T. *et al.* Yellow fever vaccine YF-17D activates multiple dendritic cell subsets via TLR2, 7, 8, and 9 to stimulate polyvalent immunity. *J. Exp. Med.* **203**, 413–424 (2006).

13. Napolitani, G., Rinaldi, A., Bertoni, F., Sallusto, F. & Lanzavecchia, A. Selected Toll-like receptor agonist combinations synergistically trigger a T helper type 1 - polarizing program in dendritic cells. *Nat. Immunol.* **6**, 769–776 (2005).

14. Whitmore, M. M. *et al.* Synergistic activation of innate immunity by double-stranded RNA and CpG DNA promotes eahanced antitumor activity. *Cancer Res.* **64**, 5850–5860 (2004).

15. Goff, P. H. *et al.* Synthetic Toll-Like Receptor 4 (TLR4) and TLR7 Ligands as

Influenza Virus Vaccine Adjuvants Induce Rapid, Sustained, and Broadly Protective Responses. *J. Virol.* **89**, 3221–3235 (2015).

16. Moody, M. A. *et al.* Toll-Like Receptor 7/8 (TLR7/8) and TLR9 Agonists Cooperate To Enhance HIV-1 Envelope Antibody Responses in Rhesus Macaques. *J. Virol.* **88**, 3329–3339 (2014).

17. Warger, T. *et al.* Synergistic activation of dendritic cells by combined Toll-like receptor ligation induces superior CTL responses in vivo. *Blood* **108**, 544–550 (2006).

18. McCartney, S. *et al.* Distinct and complementary functions of MDA5 and TLR3 in poly(I:C)-mediated activation of mouse NK cells. *J. Exp. Med.* **206**, 2967–2976 (2009).

19. Novak, T. *et al.* RIG-I and TLR4 responses and adverse outcomes in pediatric influenza-related critical illness. *J. Allergy Clin. Immunol.* **145**, 1673-1680.e11 (2020).

20. Szabo, A. *et al.* TLR ligands upregulate RIG-I expression in human plasmacytoid dendritic cells in a type I IFN-independent manner. *Immunol. Cell Biol.* **92**, 671–678 (2014).

21. World Health Organization. The top 10 causes of death. https://www.who.int/news-room/fact-sheets/detail/the-top-10-causes-of-death.

22. Murphy, K. M. *Janeway's Immunobiology*. (W.W. Norton & Company, 2016).

23. Hughes, C. E., Benson, R. A., Bedaj, M. & Maffia, P. Antigen-presenting cells and antigen presentation in tertiary lymphoid organs. *Frontiers in Immunology* vol. 7 481 (2016).

24. Blander, J. M. Regulation of the Cell Biology of Antigen Cross-Presentation. *Annu. Rev. Immunol.* **36**, 717–753 (2018).

25. Brocker, C., Thompson, D., Matsumoto, A., Nebert, D. W. & Vasiliou, V. Evolutionary divergence and functions of the human interleukin (IL) gene family. *Hum. Genomics* **5**, 30–55 (2010).

26. Botos, I., Segal, D. M. & Davies, D. R. The structural biology of Toll-like receptors. *Structure* vol. 19 447–459 (2011).

27. Jin, M. S. *et al.* Crystal Structure of the TLR1-TLR2 Heterodimer Induced by Binding of a Tri-Acylated Lipopeptide. *Cell* **130**, 1071–1082 (2007).

28. Netea, M. G. *et al.* Immune sensing of Candida albicans requires cooperative recognition of mannans and glucans by lectin and Toll-like receptors. *J. Clin. Invest.* **116**, 1642–1650 (2006).

29. Oliveira, A.-C. *et al.* Expression of Functional TLR4 Confers Proinflammatory Responsiveness to Trypanosoma cruzi Glycoinositolphospholipids and Higher Resistance to Infection with T. cruzi . *J. Immunol.* **173**, 5688–5696 (2004).

30. Kurt-Jones, E. A. *et al.* Pattern recognition receptors TLR4 and CD14 mediate response to respiratory syncytial virus. *Nat. Immunol.* **1**, 398–401 (2000).

31. Zhang, X. & Mosser, D. M. Macrophage activation by endogenous danger signals. *Journal of Pathology* vol. 214 161–178 (2008).

32. Tzeng, Y. L., Datta, A., Kumar Kolli, V., Carlson, R. W. & Stephens, D. S. Endotoxin of Neisseria meningitidis composed only of intact lipid A: Inactivation of the meningococcal 3-deoxy-D-manno-octulosonic acid transferase. *J. Bacteriol.* **184**, 2379–2388 (2002).

33. Maeshima, N. & Fernandez, R. C. Recognition of lipid A variants by the TLR4-MD-2 receptor complex. *Frontiers in Cellular and Infection Microbiology* vol. 4 3 (2013).

34. Steinhagen, F., Kinjo, T., Bode, C. & Klinman, D. M. TLR-based immune adjuvants. *Vaccine* vol. 29 3341–3355 (2011).

35. Monie, T. P. Integrated Innate Immunity—Combining Activation and Effector Functions. in *The Innate Immune System* 121–169 (Elsevier, 2017). doi:10.1016/b978-0-12-804464-3.00004-1.

36. Shimizu, T., Kida, Y. & Kuwano, K. Triacylated lipoproteins derived from Mycoplasma pneumoniae activate nuclear factor-κB through toll-like receptors 1 and 2. *Immunology* **121**, 473–483 (2007).

37. Su, L. *et al.* Structural Basis of TLR2/TLR1 Activation by the Synthetic Agonist Diprovocim. *J. Med. Chem.* **62**, 2938–2949 (2019).

38. Da Silva, T. A. *et al.* CD14 is critical for TLR2-mediated M1 macrophage activation

triggered by N-glycan recognition. *Sci. Rep.* **7**, 1–14 (2017).

39. Reed-Geaghan, E. G., Savage, J. C., Hise, A. G. & Landreth, G. E. CD14 and toll-like receptors 2 and 4 are required for fibrillar Aβ-stimulated microglial activation. *J. Neurosci.* **29**, 11982–11992 (2009).

40. Yang, J. & Yan, H. TLR5: Beyond the recognition of flagellin. *Cellular and Molecular Immunology* vol. 14 1017–1019 (2017).

41. Jiang, S., Li, X., Hess, N. J., Guan, Y. & Tapping, R. I. TLR10 Is a Negative Regulator of Both MyD88-Dependent and -Independent TLR Signaling. *J. Immunol.* **196**, 3834–3841 (2016).

42. Yarovinsky, F. *et al.* Immunology: TLR11 activation of dendritic cells by a protozoan profilin-like protein. *Science (80-.).* **308**, 1626–1629 (2005).

43. Oldenburg, M. *et al.* TLR13 recognizes bacterial 23S rRNA devoid of erythromycin resistance - Forming modification. *Science (80-.).* **337**, 1111–1115 (2012).

44. Karikó, K., Ni, H., Capodici, J., Lamphier, M. & Weissman, D. mRNA Is an Endogenous Ligand for Toll-like Receptor 3. *J. Biol. Chem.* **279**, 12542–12550 (2004).

45. Eckmann, L. Innate Immunity. in *Physiology of the Gastrointestinal Tract* vol. 2 1033–1066 (Elsevier Inc., 2006).

46. Triantafilou, K. *et al.* TLR8 and TLR7 are involved in the host's immune response to human parechovirus 1. *Eur. J. Immunol.* **35**, 2416–2423 (2005).

47. Haas, T. *et al.* The DNA Sugar Backbone 2′ Deoxyribose Determines Toll-like Receptor 9 Activation. *Immunity* **28**, 315–323 (2008).

48. Wagner, H. The immunobiology of the TLR9 subfamily. *Trends in Immunology* vol. 25 381–386 (2004).

49. Lee, B. L. *et al.* UNC93B1 mediates differential trafficking of endosomal TLRs. *Elife* **2013**, (2013).

50. Lee, B. L. & Barton, G. M. Trafficking of endosomal Toll-like receptors. *Trends in Cell Biology* vol. 24 360–369 (2014).

51. Chen, H. C., Sun, B., Tran, K. K. & Shen, H. Effects of particle size on toll-like receptor 9-mediated cytokine profiles. *Biomaterials* **32**, 1731–1737 (2011).

52. Brisse, M. & Ly, H. Comparative structure and function analysis of the RIG-I-like receptors: RIG-I and MDA5. *Frontiers in Immunology* vol. 10 1586 (2019).

53. Schnell, G., Loo, Y. M., Marcotrigiano, J. & Gale, M. Uridine Composition of the Poly-U/UC Tract of HCV RNA Defines Non-Self Recognition by RIG-I. *PLoS Pathog.* **8**, (2012).

54. Palchetti, S. *et al.* Transfected poly(I:C) activates different dsRNA receptors, leading to apoptosis or immunoadjuvant response in androgen-independent prostate cancer cells. *J. Biol. Chem.* **290**, 5470–5483 (2015).

55. Yong, H. Y. & Luo, D. RIG-I-like receptors as novel targets for pan-antivirals and vaccine adjuvants against emerging and re-emerging viral infections. *Frontiers in*

Immunology vol. 9 1379 (2018).

56. Sharma, S. & Fitzgerald, K. A. Viral Defense: It Takes Two MAVS to Tango. *Cell* vol. 141 570–572 (2010).

57. Hopfensperger, K. & Sautera, D. Decreased, deformed, defective-how HIV-1 vpu targets peroxisomes. *MBio* **11**, (2020).

58. Fransen, M., Lismont, C. & Walton, P. The peroxisome-mitochondria connection: How and why? *International Journal of Molecular Sciences* vol. 18 (2017).

59. Poeck, H. *et al.* Recognition of RNA virus by RIG-I results in activation of CARD9 and inflammasome signaling for interleukin 1B production. *Nat. Immunol.* **11**, 63–69 (2010).

60. Guilliams, M. *et al.* Dendritic cells, monocytes and macrophages: A unified nomenclature based on ontogeny. *Nature Reviews Immunology* vol. 14 571–578 (2014).

61. van Spriel, A. B. & de Jong, E. C. Dendritic cell science: more than 40 years of history. *J. Leukoc. Biol.* **93**, 33–38 (2013).

62. Kondo, M. *et al.* BIOLOGY OF HEMATOPOIETIC STEM CELLS AND PROGENITORS: Implications for Clinical Application. *Annu. Rev. Immunol* **21**, 759–806 (2003).

63. Merad, M., Sathe, P., Helft, J., Miller, J. & Mortha, A. The Dendritic Cell Lineage: Ontogeny and Function of Dendritic Cells and Their Subsets in the Steady State and

the Inflamed Setting. *Annu. Rev. Immunol.* **31**, 563–604 (2013).

64. Sichien, D., Lambrecht, B. N., Guilliams, M. & Scott, C. L. Development of conventional dendritic cells: From common bone marrow progenitors to multiple subsets in peripheral tissues. *Mucosal Immunology* vol. 10 831–844 (2017).

65. Schlitzer, A. *et al.* Identification of cDC1- and cDC2-committed DC progenitors reveals early lineage priming at the common DC progenitor stage in the bone marrow. *Nat. Immunol.* **16**, 718–728 (2015).

66. Diao, J. *et al.* In Situ Replication of Immediate Dendritic Cell (DC) Precursors Contributes to Conventional DC Homeostasis in Lymphoid Tissue. *J. Immunol.* **176**, 7196–7206 (2006).

67. Naik, S. H. *et al.* Intrasplenic steady-state dendritic cell precursors that are distinct from monocytes. *Nat. Immunol.* **7**, 663–671 (2006).

68. Kashem, S. W. *et al.* Candida albicans morphology and dendritic cell subsets determine T helper cell differentiation. *Immunity* **42**, 356–366 (2015).

69. Mashayekhi, M. *et al.* CD8α+ Dendritic Cells Are the Critical Source of Interleukin-12 that Controls Acute Infection by Toxoplasma gondii Tachyzoites. *Immunity* **35**, 249–259 (2011).

70. Seillet, C. *et al.* CD8α+ DCs can be induced in the absence of transcription factors Id2, Nfil3, and Batf3. *Blood* **121**, 1574–1583 (2013).

71. Puhr, S., Lee, J., Zvezdova, E., Zhou, Y. J. & Liu, K. Dendritic cell development-

History, advances, and open questions. *Seminars in Immunology* vol. 27 388–396 (2015).

72. Waithman, J. *et al.* Resident CD8+ and Migratory CD103+ Dendritic Cells Control CD8 T Cell Immunity during Acute Influenza Infection. *PLoS One* **8**, (2013).

73. Hildner, K. *et al.* Batf3 deficiency reveals a critical role for CD8α+ dendritic cells in cytotoxic T cell immunity. *Science (80-.).* **322**, 1097–1100 (2008).

74. Garcias López, A. *et al.* Migration of murine intestinal dendritic cell subsets upon intrinsic and extrinsic TLR3 stimulation. *Eur. J. Immunol.* **50**, 1525–1536 (2020).

75. Qiu, C.-H. *et al.* Novel Subset of CD8α + Dendritic Cells Localized in the Marginal Zone Is Responsible for Tolerance to Cell-Associated Antigens . *J. Immunol.* **182**, 4127–4136 (2009).

76. Cerovic, V. *et al.* Intestinal CD103- dendritic cells migrate in lymph and prime effector T cells. *Mucosal Immunol.* **6**, 104–113 (2013).

77. Fujimoto, K. *et al.* A New Subset of CD103 + CD8α + Dendritic Cells in the Small Intestine Expresses TLR3, TLR7, and TLR9 and Induces Th1 Response and CTL Activity . *J. Immunol.* **186**, 6287–6295 (2011).

78. Cerovic, V. *et al.* Lymph-borne CD8α+ dendritic cells are uniquely able to cross-prime CD8+ T cells with antigen acquired from intestinal epithelial cells. *Mucosal Immunol.* **8**, 38–48 (2015).

79. Leleux, J., Atalis, A. & Roy, K. Engineering immunity: Modulating dendritic cell

subsets and lymph node response to direct immune-polarization and vaccine efficacy. *J. Control. Release* **219**, 610–621 (2015).

80. Dudziak, D. *et al.* Differential antigen processing by dendritic cell subsets in vivo. *Science (80-.).* **315**, 107–111 (2007).

81. Tussiwand, R. *et al.* Klf4 Expression in Conventional Dendritic Cells Is Required for T Helper 2 Cell Responses. *Immunity* **42**, 916–928 (2015).

82. Plantinga, M. *et al.* Conventional and Monocyte-Derived CD11b+ Dendritic Cells Initiate and Maintain T Helper 2 Cell-Mediated Immunity to House Dust Mite Allergen. *Immunity* **38**, 322–335 (2013).

83. Schlitzer, A. *et al.* IRF4 Transcription Factor-Dependent CD11b+ Dendritic Cells in Human and Mouse Control Mucosal IL-17 Cytokine Responses. *Immunity* **38**, 970–983 (2013).

84. Guilliams, M. *et al.* Skin-draining lymph nodes contain dermis-derived CD103- dendritic cells that constitutively produce retinoic acid and induce Foxp3 + regulatory T cells. *Blood* **115**, 1958–1968 (2010).

85. Doxsee, C. L. *et al.* The Immune Response Modifier and Toll-Like Receptor 7 Agonist S-27609 Selectively Induces IL-12 and TNF-α Production in CD11c + CD11b + CD8 − Dendritic Cells . *J. Immunol.* **171**, 1156–1163 (2003).

86. Neubert, K. *et al.* Antigen Delivery to CD11c + CD8 − Dendritic Cells Induces Protective Immune Responses against Experimental Melanoma in Mice In Vivo . *J.*

Immunol. **192**, 5830–5838 (2014).

87. Tamoutounour, S. *et al.* Origins and functional specialization of macrophages and of conventional and monocyte-derived dendritic cells in mouse skin. *Immunity* **39**, 925–938 (2013).

88. Bajaña, S., Roach, K., Turner, S., Paul, J. & Kovats, S. IRF4 promotes cutaneous dendritic cell migration to lymph nodes during homeostasis and inflammation. *J. Immunol.* **189**, 3368–77 (2012).

89. Kumamoto, Y. *et al.* CD301b+ dermal dendritic cells drive T helper 2 cell-mediated immunity. *Immunity* **39**, 733–743 (2013).

90. Kumamoto, Y., Hirai, T., Wong, P. W., Kaplan, D. H. & Iwasaki, A. CD301B+ dendritic cells suppress T follicular helper cells and antibody responses to protein antigens. *Elife* **5**, (2016).

91. Min, J. *et al.* Inflammation induces two types of inflammatory dendritic cells in inflamed lymph nodes. *Exp. Mol. Med.* 458 (2018) doi:10.1038/emm.2017.292.

92. Wakim, L. M., Waithman, J., Van Rooijen, N., Heath, W. R. & Carbone, F. R. Dendritic cell-induced memory T cell activation in nonlymphoid tissues. *Science (80-.).* **319**, 198–202 (2008).

93. Ersland, K., Wüthrich, M. & Klein, B. S. Dynamic interplay among monocyte-derived, dermal, and resident lymph node dendritic cells during the generation of vaccine immunity to fungi. *Cell Host Microbe* **7**, 474–487 (2010).

94. Serbina, N. V., Salazar-Mather, T. P., Biron, C. A., Kuziel, W. A. & Pamer, E. G. TNF/iNOS-producing dendritic cells mediate innate immune defense against bacterial infection. *Immunity* **19**, 59–70 (2003).

95. Jakubzick, C. *et al.* Minimal differentiation of classical monocytes as they survey steady-state tissues and transport antigen to lymph nodes. *Immunity* **39**, 599–610 (2013).

96. Italiani, P. & Boraschi, D. From monocytes to M1/M2 macrophages: Phenotypical vs. functional differentiation. *Frontiers in Immunology* vol. 5 514 (2014).

97. Hashimoto, D., Miller, J. & Merad, M. Dendritic Cell and Macrophage Heterogeneity In Vivo. *Immunity* **35**, 323–335 (2011).

98. Delamarre, L., Pack, M., Chang, H., Mellman, I. & Trombetta, E. S. Differential lysosomal proteolysis in antigen-presenting cells determines antigen fate. *Science (80-.).* **307**, 1630–1634 (2005).

99. Junt, T. *et al.* Subcapsular sinus macrophages in lymph nodes clear lymph-borne viruses and present them to antiviral B cells. *Nature* **450**, 110–114 (2007).

100. Kirby, A. C., Coles, M. C. & Kaye, P. M. Alveolar Macrophages Transport Pathogens to Lung Draining Lymph Nodes. *J. Immunol.* **183**, 1983–1989 (2009).

101. Suzuki, K., Grigorova, I., Phan, T. G., Kelly, L. M. & Cyster, J. G. Visualizing B cell capture of cognate antigen from follicular dendritic cells. *J. Exp. Med.* **206**, 1485–1493 (2009).

102. Inaba, K. *et al.* Generation of large numbers of dendritic cells from mouse bone marrow cultures supplemented with granulocyte/macrophage colony-stimulating factor. *J. Exp. Med.* **176**, 1693–1702 (1992).

103. Sallusto, F. & Lanzavecchi, A. Efficient presentation of soluble antigen by cultured human dendritic cells is maintained by granulocyte/macrophage colony-stimulating factor plus interleukin 4 and downregulated by tumor necrosis factor α. *J. Exp. Med.* **179**, 1109–1118 (1994).

104. Lutz, M. B. *et al.* Differential Functions of IL-4 Receptor Types I and II for Dendritic Cell Maturation and IL-12 Production and Their Dependency on GM-CSF. *J. Immunol.* **169**, 3574–3580 (2002).

105. Jin, D. & Sprent, J. GM-CSF Culture Revisited: Preparation of Bulk Populations of Highly Pure Dendritic Cells from Mouse Bone Marrow. *J. Immunol.* **201**, 3129–3139 (2018).

106. Helft, J., Bö, J., Schraml, B. U. & Goubau, D. GM-CSF Mouse Bone Marrow Cultures Comprise a Heterogeneous Population of CD11c + MHCII + Macrophages and Dendritic Cells. *Immunity* **42**, 1197–1211 (2015).

107. Brasel, K., De Smedt, T., Smith, J. L. & Maliszewski, C. R. Generation of murine dendritic cells from flt3-ligand–supplemented bone marrow cultures. *Blood* **96**, 3029–3039 (2000).

108. Cunningham, A. L. *et al.* Vaccine development: From concept to early clinical testing. *Vaccine* **34**, 6655–6664 (2016).

109. Eisenbarth, S. C., Colegio, O. R., O'Connor, W., Sutterwala, F. S. & Flavell, R. A. Crucial role for the Nalp3 inflammasome in the immunostimulatory properties of aluminium adjuvants. *Nature* **453**, 1122–1126 (2008).

110. Hollingsworth, R. E. & Jansen, K. Turning the corner on therapeutic cancer vaccines. *npj Vaccines* vol. 4 1–10 (2019).

111. Pitisuttithum, P. & Marovich, M. A. Prophylactic HIV vaccine: vaccine regimens in clinical trials and potential challenges. *Expert Rev. Vaccines* **19**, 133–142 (2020).

112. Pinheiro-Michelsen, J. R. *et al.* Anti-dengue Vaccines: From Development to Clinical Trials. *Frontiers in Immunology* vol. 11 1252 (2020).

113. Didierlaurent, A. M. *et al.* Adjuvant system AS01: helping to overcome the challenges of modern vaccines. *Expert Rev. Vaccines* **16**, 55–63 (2017).

114. Mitchell, T. C. & Casella, C. R. No pain no gain? Adjuvant effects of alum and monophosphoryl lipid A in pertussis and HPV vaccines. *Current Opinion in Immunology* vol. 47 17–25 (2017).

115. Sasaki, S. *et al.* Monophosphoryl lipid A enhances both humoral and cell- mediated immune responses to DNA vaccination against human immunodeficiency virus type 1. *Infect. Immun.* **65**, 3520–3528 (1997).

116. Wheeler, C. M. *et al.* Cross-protective efficacy of HPV-16/18 AS04-adjuvanted vaccine against cervical infection and precancer caused by non-vaccine oncogenic HPV types: 4-year end-of-study analysis of the randomised, double-blind

PATRICIA trial. *Lancet Oncol.* **13**, 100–110 (2012).

117. Cluff, C. W. Monophosphoryl Lipid A (MPL) as an Adjuvant for Anti-Cancer Vaccines: Clinical Results. (2013).

118. Wagstaff, A. J. & Perry, C. M. Topical imiquimod: A review of its use in the management of anogenital warts, actinic keratoses, basal cell carcinoma and other skin lesions. *Drugs* vol. 67 2187–2210 (2007).

119. Marleau, A. M., Lipton, J. H., Riordan, N. H. & Ichim, T. E. Therapeutic use of Aldara™ in chronic myeloid leukemia. *Journal of Translational Medicine* vol. 5 4 (2007).

120. Kim, J. M. *et al.* Efficacy of 5% imiquimod cream on vulvar intraepithelial Neoplasia in Korea: Pilot study. *Ann. Dermatol.* **27**, 66–70 (2015).

121. Han, J. H. *et al.* In vitro and in vivo growth inhibition of prostate cancer by the small molecule imiquimod. *Int. J. Oncol.* **42**, 2087–2093 (2013).

122. Adams, S. *et al.* Immunization of Malignant Melanoma Patients with Full-Length NY-ESO-1 Protein Using TLR7 Agonist Imiquimod as Vaccine Adjuvant. *J. Immunol.* **181**, 776–784 (2008).

123. Sabado, R. L. *et al.* Resiquimod as an immunologic adjuvant for NY-ESO-1 protein vaccination in patients with high-risk melanoma. *Cancer Immunol. Res.* **3**, 278–287 (2015).

124. Pockros, P. J. *et al.* Oral resiquimod in chronic HCV infection: Safety and efficacy

in 2 placebo-controlled, double-blind phase IIa studies. *J. Hepatol.* **47**, 174–182 (2007).

125. Kashem, S. W., Haniffa, M. & Kaplan, D. H. Antigen-Presenting Cells in the Skin. *Annu. Rev. Immunol.* **35**, 469–499 (2017).

126. Van den Boorn, J. G., Barchet, W. & Hartmann, G. Nucleic Acid Adjuvants. Toward an Educated Vaccine. in *Advances in Immunology* vol. 114 1–32 (Academic Press Inc., 2012).

127. Crompton, P. D. *et al.* The TLR9 Ligand CpG Promotes the Acquisition of Plasmodium falciparum -Specific Memory B Cells in Malaria-Naive Individuals . *J. Immunol.* **182**, 3318–3326 (2009).

128. Ellis, R. D. *et al.* Phase 1 Study in Malaria Naïve Adults of BSAM2/Alhydrogel®+CPG 7909, a Blood Stage Vaccine against P. falciparum Malaria. *PLoS One* **7**, e46094 (2012).

129. Cooper, C. L. *et al.* Safety and immunogenicity of CPG 7909 injection as an adjuvant to Fluarix influenza vaccine. *Vaccine* **22**, 3136–3143 (2004).

130. KLINMAN, D. M., XIE, H. & IVINS, B. E. CpG Oligonucleotides Improve the Protective Immune Response Induced by the Licensed Anthrax Vaccine. *Ann. N. Y. Acad. Sci.* **1082**, 137–150 (2006).

131. Korolowicz, K. E. *et al.* Antiviral Efficacy and Host Innate Immunity Associated with SB 9200 Treatment in the Woodchuck Model of Chronic Hepatitis B. *PLoS*

One **11**, e0161313 (2016).

132. Goulet, M.-L. *et al.* Systems Analysis of a RIG-I Agonist Inducing Broad Spectrum Inhibition of Virus Infectivity. *PLoS Pathog.* **9**, e1003298 (2013).

133. Chiang, C. *et al.* Sequence-Specific Modifications Enhance the Broad-Spectrum Antiviral Response Activated by RIG-I Agonists. *J. Virol.* **89**, 8011–8025 (2015).

134. Beljanski, V. *et al.* Enhanced Influenza Virus-Like Particle Vaccination with a Structurally Optimized RIG-I Agonist as Adjuvant. *J. Virol.* **89**, 10612–10624 (2015).

135. Garçon, N. & Di Pasquale, A. From discovery to licensure, the Adjuvant System story. *Human Vaccines and Immunotherapeutics* vol. 13 19–33 (2017).

136. Hancock, R. E. W., Nijnik, A. & Philpott, D. J. Modulating immunity as a therapy for bacterial infections. *Nature Reviews Microbiology* vol. 10 243–254 (2012).

137. Pandey, R. K., Sodhi, A., Biswas, S. K., Dahiya, Y. & Dhillon, M. K. Mycobacterium indicus pranii mediates macrophage activation through TLR2 and NOD2 in a MyD88 dependent manner. *Vaccine* **30**, 5748–5754 (2012).

138. Bekeredjian-Ding, I. *et al.* T Cell-Independent, TLR-Induced IL-12p70 Production in Primary Human Monocytes. *J. Immunol.* **176**, 7438–7446 (2006).

139. Lim, S. N., Kuhn, S., Hyde, E. & Ronchese, F. Combined TLR Stimulation With Pam3Cys and Poly I. *J. Immunother.* **35**, 670–679 (2012).

140. Grossmann, C. *et al.* Enhancement of the priming efficacy of DNA vaccines

encoding dendritic cell-targeted antigens by synergistic toll-like receptor ligands. *BMC Immunol.* **10**, 1–10 (2009).

141. Zhu, Q. *et al.* Using 3 TLR ligands as a combination adjuvant induces qualitative changes in T cell responses needed for antiviral protection in mice. *J. Clin. Invest.* **120**, 607–616 (2010).

142. Wiley, S. R. *et al.* Targeting TLRs expands the antibody repertoire in response to a malaria vaccine. *Sci. Transl. Med.* **3**, 93ra69-93ra69 (2011).

143. Mueller, S. N., Tian, S. & Desimone, J. M. Rapid and persistent delivery of antigen by lymph node targeting PRINT nanoparticle vaccine carrier to promote humoral immunity. *Mol. Pharm.* **12**, 1356–1365 (2015).

144. Smirnov, D., Schmidt, J. J., Capecchi, J. T. & Wightman, P. D. Vaccine adjuvant activity of 3m-052: An imidazoquinoline designed for local activity without systemic cytokine induction. *Vaccine* **29**, 5434–5442 (2011).

145. Madan-Lala, R., Pradhan, P. & Roy, K. Combinatorial Delivery of Dual and Triple TLR Agonists via Polymeric Pathogen-like Particles Synergistically Enhances Innate and Adaptive Immune Responses. *Sci. Rep.* **7**, (2017).

146. Moyer, T. J., Zmolek, A. C. & Irvine, D. J. Beyond antigens and adjuvants: Formulating future vaccines. *Journal of Clinical Investigation* vol. 126 799–808 (2016).

147. Leleux, J. A., Pradhan, P. & Roy, K. Biophysical Attributes of CpG Presentation

Control TLR9 Signaling to Differentially Polarize Systemic Immune Responses. *Cell Rep.* **18**, 700–710 (2017).

148. Gerner, M. Y., Torabi-Parizi, P. & Germain, R. N. Strategically Localized Dendritic Cells Promote Rapid T Cell Responses to Lymph-Borne Particulate Antigens. *Immunity* **42**, 172–185 (2015).

149. Reddy, S. T., Rehor, A., Schmoekel, H. G., Hubbell, J. A. & Swartz, M. A. In vivo targeting of dendritic cells in lymph nodes with poly(propylene sulfide) nanoparticles. *J. Control. Release* **112**, 26–34 (2006).

150. Swartz, M. A., Hubbell, J. A. & Reddy, S. T. Lymphatic drainage function and its immunological implications: From dendritic cell homing to vaccine design. *Seminars in Immunology* vol. 20 147–156 (2008).

151. Griffith, L. G. & Swartz, M. A. Capturing complex 3D tissue physiology in vitro. *Nature Reviews Molecular Cell Biology* vol. 7 211–224 (2006).

152. Takamura, K. *et al.* Regulatory Role of Lymphoid Chemokine CCL19 and CCL21 in the Control of Allergic Rhinitis. *J. Immunol.* **179**, 5897–5906 (2007).

153. Kaiser, A., Donnadieu, E., Abastado, J.-P., Trautmann, A. & Nardin, A. CC Chemokine Ligand 19 Secreted by Mature Dendritic Cells Increases Naive T Cell Scanning Behavior and Their Response to Rare Cognate Antigen. *J. Immunol.* **175**, 2349–2356 (2005).

154. Raju, R. *et al.* Differential ligand-signaling network of CCL19/CCL21-CCR7

system. *Database* **2015**, (2015).

155. Raju, R. *et al.* Differential ligand-signaling network of CCL19/CCL21-CCR7 system. *Database* **2015**, 106 (2015).

156. Johnson, L. A. & Jackson, D. G. Inflammation-induced secretion of CCL21 in lymphatic endothelium is a key regulator of integrin-mediated dendritic cell transmigration. *Int. Immunol.* **22**, 839–49 (2010).

157. Vaahtomeri, K. *et al.* Locally Triggered Release of the Chemokine CCL21 Promotes Dendritic Cell Transmigration across Lymphatic Endothelia. *Cell Rep.* **19**, 902–909 (2017).

158. Hu, B., Guo, H., Zhou, P. & Shi, Z. L. Characteristics of SARS-CoV-2 and COVID-19. *Nature Reviews Microbiology* vol. 19 141–154 (2020).

159. Huang, Y., Yang, C., Xu, X. feng, Xu, W. & Liu, S. wen. Structural and functional properties of SARS-CoV-2 spike protein: potential antivirus drug development for COVID-19. *Acta Pharmacologica Sinica* vol. 41 1141–1149 (2020).

160. Yasui, F. *et al.* Prior Immunization with Severe Acute Respiratory Syndrome (SARS)-Associated Coronavirus (SARS-CoV) Nucleocapsid Protein Causes Severe Pneumonia in Mice Infected with SARS-CoV. *J. Immunol.* **181**, 6337–6348 (2008).

161. Liang, Z. *et al.* Adjuvants for Coronavirus Vaccines. *Frontiers in Immunology* vol. 11 2896 (2020).

162. Gao, Q. *et al.* Development of an inactivated vaccine candidate for SARS-CoV-2.

Science (80-.). **369**, 77–81 (2020).

163. Wang, H. *et al.* Development of an Inactivated Vaccine Candidate, BBIBP-CorV, with Potent Protection against SARS-CoV-2. *Cell* **182**, 713-721.e9 (2020).

164. Zhou, Z. *et al.* A recombinant baculovirus-expressed S glycoprotein vaccine elicits high titers of SARS-associated coronavirus (SARS-CoV) neutralizing antibodies in mice. *Vaccine* **24**, 3624–3631 (2006).

165. Agrawal, A. S. *et al.* Immunization with inactivated Middle East Respiratory Syndrome coronavirus vaccine leads to lung immunopathology on challenge with live virus. *Hum. Vaccines Immunother.* **12**, 2351–2356 (2016).

166. Zhang, N. *et al.* Identification of an ideal adjuvant for receptor-binding domain-based subunit vaccines against Middle East respiratory syndrome coronavirus. *Cell. Mol. Immunol.* **13**, 180–190 (2016).

167. Lund, J. M. *et al.* Recognition of single-stranded RNA viruses by Toll-like receptor 7. *Proc. Natl. Acad. Sci. U. S. A.* **101**, 5598–5603 (2004).

168. Weber, F., Wagner, V., Rasmussen, S. B., Hartmann, R. & Paludan, S. R. Double-Stranded RNA Is Produced by Positive-Strand RNA Viruses and DNA Viruses but Not in Detectable Amounts by Negative-Strand RNA Viruses. *J. Virol.* **80**, 5059–5064 (2006).

169. Kell, A. M. & Gale, M. RIG-I in RNA virus recognition. *Virology* vols 479–480 110–121 (2015).

170. Jensen, S. & Thomsen, A. R. Sensing of RNA Viruses: a Review of Innate Immune Receptors Involved in Recognizing RNA Virus Invasion. *J. Virol.* **86**, 2900–2910 (2012).

171. Shirato, K. & Kizaki, T. SARS-CoV-2 spike protein S1 subunit induces pro-inflammatory responses via toll-like receptor 4 signaling in murine and human macrophages. *Heliyon* **7**, e06187 (2021).

172. Choudhury, A. & Mukherjee, S. In silico studies on the comparative characterization of the interactions of SARS-CoV-2 spike glycoprotein with ACE-2 receptor homologs and human TLRs. *J. Med. Virol.* **92**, 2105–2113 (2020).

173. Zhao, Y. *et al.* SARS-CoV-2 spike protein interacts with and activates TLR4. *bioRxiv* 2020.12.18.423427 (2020) doi:10.1101/2020.12.18.423427.

174. Zhao, K., Wang, H. & Wu, C. The immune responses of HLA-A*0201 restricted SARS-CoV S peptide-specific CD8 + T cells are augmented in varying degrees by CpG ODN, PolyI:C and R848. *Vaccine* **29**, 6670–6678 (2011).

175. Gai, W. *et al.* Effects of different immunization protocols and adjuvant on antibody responses to inactivated SARS-CoV vaccine. *Viral Immunol.* **21**, 27–37 (2008).

176. Langellotto, F. *et al.* A rapidly adaptable biomaterial vaccine for SARS-CoV-2. *bioRxiv* 2020.07.07.192203 (2020) doi:10.1101/2020.07.07.192203.

177. Liu, L. *et al.* Subunit Nanovaccine with Potent Cellular and Mucosal Immunity for COVID-19. *ACS Appl. Bio Mater.* **3**, 5633–5638 (2020).

178. Sokol, C. L., Camire, R. B., Jones, M. C. & Luster, A. D. The Chemokine Receptor CCR8 Promotes the Migration of Dendritic Cells into the Lymph Node Parenchyma to Initiate the Allergic Immune Response. *Immunity* **49**, 449-463.e6 (2018).

179. Kumamoto, Y. *et al.* CD301b+ dermal dendritic cells drive T helper 2 cell-mediated immunity. *Immunity* **39**, 733–743 (2013).

180. Pradhan, P. *et al.* TRAF6-IRF5 kinetics, TRIF, and biophysical factors drive synergistic innate responses to particle-mediated MPLA-CpG co-presentation. *Sci. Adv.* **7**, eabd4235 (2021).

181. Ko, E. J. *et al.* MPL and CpG combination adjuvants promote homologous and heterosubtypic cross protection of inactivated split influenza virus vaccine. *Antiviral Res.* **156**, 107–115 (2018).

182. Pradhan, P. *et al.* The effect of combined IL10 siRNA and CpG ODN as pathogen-mimicking microparticles on Th1/Th2 cytokine balance in dendritic cells and protective immunity against B cell lymphoma. *Biomaterials* **35**, 5491–504 (2014).

183. Kasturi, S. P., Sachaphibulkij, K. & Roy, K. Covalent conjugation of polyethyleneimine on biodegradable microparticles for delivery of plasmid DNA vaccines. *Biomaterials* **26**, 6375–85 (2005).

184. Pai Kasturi, S. *et al.* Prophylactic anti-tumor effects in a B cell lymphoma model with DNA vaccines delivered on polyethylenimine (PEI) functionalized PLGA microparticles. *J. Control. Release* **113**, 261–270 (2006).

185. Abràmoff, M. D., Magalhães, P. J. & Ram, S. J. Image Processing with ImageJ Second Edition. *Biophotonics Int.* **11**, 36–42 (2004).

186. Tseng, Q. *et al.* A new micropatterning method of soft substrates reveals that different tumorigenic signals can promote or reduce cell contraction levels. *Lab Chip* **11**, 2231–2240 (2011).

187. Hoffman, H. Violin Plot. *MATLAB Central File Exchange* https://www.mathworks.com/matlabcentral/fileexchange/45134-violin-plot (2020).

188. Mardia, K. & Jupp, P. *Directional Statistics*. (John Wiley & Sons Ltd, 2000).

189. Best, D. & Fisher, N. Efficient Simulation of the von Mises Distribution. *Appl. Stat.* **28**, 152–157 (1979).

190. Cox, D. Discussion following Mardia, KV. *J. R. Stat. Soc. Ser. B* **37**, 380–381 (1975).

191. Tasdan, F. & Yeniay, O. A comparative simulation of multiple testing procedures in circular data problems. *J. Appl. Stat.* **45**, 255–269 (2018).

192. Robbins, C. S. & Swirski, F. K. The multiple roles of monocyte subsets in steady state and inflammation. *Cellular and Molecular Life Sciences* vol. 67 2685–2693 (2010).

193. Dunay, I. R. *et al.* Gr1+ Inflammatory Monocytes Are Required for Mucosal Resistance to the Pathogen Toxoplasma gondii. *Immunity* **29**, 306–317 (2008).

194. Geissmann, F., Jung, S. & Littman, D. R. Blood monocytes consist of two principal

subsets with distinct migratory properties. *Immunity* **19**, 71–82 (2003).

195. Braza, M. S. *et al.* Inhibiting Inflammation with Myeloid Cell-Specific Nanobiologics Promotes Organ Transplant Acceptance. *Immunity* **49**, 819-828.e6 (2018).

196. Erlich, Z. *et al.* Macrophages, rather than DCs, are responsible for inflammasome activity in the GM-CSF BMDC model. *Nature Immunology* vol. 20 397–406 (2019).

197. Rivollier, A., He, J., Kole, A., Valatas, V. & Kelsall, B. L. Inflammation switches the differentiation program of Ly6chi monocytes from antiinflammatory macrophages to inflammatory dendritic cells in the colon. *J. Exp. Med.* **209**, 139–155 (2012).

198. Baratin, M. *et al.* Homeostatic NF-κB Signaling in Steady-State Migratory Dendritic Cells Regulates Immune Homeostasis and Tolerance. *Immunity* **42**, 627–639 (2015).

199. Aerbajinai, W., Lee, K., Chin, K. & Rodgers, G. P. Glia Maturation Factor-γ Negatively Modulates TLR4 Signaling by Facilitating TLR4 Endocytic Trafficking in Macrophages. *J. Immunol.* **190**, 6093–6103 (2013).

200. Takeuchi, O. & Akira, S. Pattern Recognition Receptors and Inflammation. *Cell* vol. 140 805–820 (2010).

201. Shen, H., Tesar, B. M., Walker, W. E. & Goldstein, D. R. Dual Signaling of MyD88 and TRIF Is Critical for Maximal TLR4-Induced Dendritic Cell Maturation. *J. Immunol.* **181**, 1849–1858 (2008).

202. Latz, E. *et al.* TLR9 signals after translocating from the ER to CpG DNA in the lysosome. *Nat. Immunol.* **5**, 190–198 (2004).

203. Latz, E., Visintin, A., Espevik, T. & Golenbock, D. T. Mechanisms of TLR9 activation. *J. Endotoxin Res.* **10**, 406–412 (2004).

204. Leifer, C. A. *et al.* TLR9 Is Localized in the Endoplasmic Reticulum Prior to Stimulation. *J. Immunol.* **173**, 1179–1183 (2004).

205. Hägerbrand, K., Westlund, J., Yrlid, U., Agace, W. & Johansson-Lindbom, B. MyD88 Signaling Regulates Steady-State Migration of Intestinal CD103 + Dendritic Cells Independently of TNF-α and the Gut Microbiota . *J. Immunol.* **195**, 2888–2899 (2015).

206. Bollampalli, V. P. *et al.* BCG Skin Infection Triggers IL-1R-MyD88-Dependent Migration of EpCAMlow CD11bhigh Skin Dendritic cells to Draining Lymph Node During CD4+ T-Cell Priming. *PLoS Pathog.* **11**, (2015).

207. Pang, I. K., Ichinohe, T. & Iwasaki, A. IL-1R signaling in dendritic cells replaces pattern-recognition receptors in promoting CD8 + T cell responses to influenza A virus. *Nat. Immunol.* **14**, 246–253 (2013).

208. Short, K. K. *et al.* Co-encapsulation of synthetic lipidated TLR4 and TLR7/8 agonists in the liposomal bilayer results in a rapid, synergistic enhancement of vaccine-mediated humoral immunity. *J. Control. Release* **315**, 186–196 (2019).

209. Llufrio, E. M., Wang, L., Naser, F. J. & Patti, G. J. Sorting cells alters their redox

state and cellular metabolome. *Redox Biol.* **16**, 381–387 (2018).

210. Andrä, I. *et al.* An Evaluation of T-Cell Functionality After Flow Cytometry Sorting Revealed p38 MAPK Activation. *Cytom. Part A* **97**, 171–183 (2020).

211. Riol-Blanco, L. *et al.* The Chemokine Receptor CCR7 Activates in Dendritic Cells Two Signaling Modules That Independently Regulate Chemotaxis and Migratory Speed. *J. Immunol.* **174**, 4070–4080 (2005).

212. Liao, X., Makris, M. & Luo, X. M. Fluorescence-activated cell sorting for purification of plasmacytoid dendritic cells from the mouse bone marrow. *J. Vis. Exp.* **2016**, (2016).

213. Blasius, A. *et al.* A cell-surface molecule selectively expressed on murine natural interferon-producing cells that blocks secretion of interferon-alpha. *Blood* **103**, 4201–4206 (2004).

214. Rezzonico, R., Imbert, V., Chicheportiche, R. & Dayer, J. M. Ligation of CD11b and CD11c β2 integrins by antibodies or soluble CD23 induces macrophage inflammatory protein 1α (MIP-1α) and MIP-1β production in primary human monocytes through a pathway dependent on nuclear factor-κB. *Blood* **97**, 2932–2940 (2001).

215. Craig, D. H., Schaubert, K. L., Shiratsuchi, H., Kan-Mitchell, J. & Basson, M. D. Increased pressure stimulates aberrant dendritic cell maturation. *Cell. Mol. Biol. Lett.* **13**, 260–270 (2008).

216. Poon, G. F. T. *et al.* Hyaluronan Binding Identifies a Functionally Distinct Alveolar Macrophage–like Population in Bone Marrow–Derived Dendritic Cell Cultures. *J. Immunol.* **195**, 632–642 (2015).

217. Ricart, B. G., John, B., Lee, D., Hunter, C. A. & Hammer, D. A. Dendritic Cells Distinguish Individual Chemokine Signals through CCR7 and CXCR4. *J. Immunol.* **186**, 53–61 (2011).

218. Dieu, M. C. *et al.* Selective recruitment of immature and mature dendritic cells by distinct chemokines expressed in different anatomic sites. *J. Exp. Med.* **188**, 373–386 (1998).

219. Bachelerie, F. *et al.* International union of pharmacology. LXXXIX. Update on the extended family of chemokine receptors and introducing a new nomenclature for atypical chemokine receptors. *Pharmacological Reviews* vol. 66 1–79 (2014).

220. Mazzotti, C. *et al.* The atypical receptor CCRL2 (C-C Chemokine Receptor-Like 2) does not act as a decoy receptor in endothelial cells. *Front. Immunol.* **8**, 1233 (2017).

221. Scandella, E., Men, Y., Gillessen, S., Förster, R. & Groettrup, M. Prostaglandin E2 is a key factor for CCR7 surface expression and migration of monocyte-derived dendritic cells. *Blood* **100**, 1354–1361 (2002).

222. Robbiani, D. F. *et al.* The leukotriene C4 transporter MRP1 regulates CCL19 (MIP-3β, ELC)-dependent mobilization of dendritic cells to lymph nodes. *Cell* **103**, 757–768 (2000).

223. Partida-Sánchez, S. *et al.* Regulation of dendritic cell trafficking by the ADP-ribosyl cyclase CD38: Impact on the development of humoral immunity. *Immunity* **20**, 279–291 (2004).

224. Tayalia, P., Mazur, E. & Mooney, D. J. Controlled architectural and chemotactic studies of 3D cell migration. *Biomaterials* **32**, 2634–2641 (2011).

225. Sapudom, J. *et al.* Dendritic cell immune potency on 2D and in 3D collagen matrices. *Biomater. Sci.* **8**, 5106–5120 (2020).

226. Mennens, S. F. B. *et al.* Substrate stiffness influences phenotype and function of human antigen-presenting dendritic cells. *Sci. Rep.* **7**, 1–14 (2017).

227. Shen, C. *et al.* Reduced Expression of CD27 by Collagenase Treatment: Implications for Interpreting B Cell Data in Tissues. *PLoS One* **10**, e0116667 (2015).

228. Ulrike Haessler, Marco Pisano, Mingming Wu & Swartz, M. A. Dendritic cell chemotaxis in 3D under defined chemokine gradients reveals differential response to ligands CCL21 and CCL19. *Proc. Natl. Acad. Sci. U. S. A.* **108**, 5614–5619 (2011).

229. Lu, H., Mcdowell, L. M., Studelska, D. R. & Zhang, L. Glycosaminoglycans in Human and Bovine Serum: Detection of Twenty-Four Heparan Sulfate and Chondroitin Sulfate Motifs Including a Novel Sialic Acid-Modified Chondroitin Sulfate Linkage Hexasaccharide. *Glycobiol. Insights* **2**, 13–28 (2010).

230. Sweeney, S. M., Guy, C. A., Fields, G. B. & San Antonio, J. D. Defining the domains

of type I collagen involved in heparin-binding and endothelial tube formation. *Proc. Natl. Acad. Sci. U. S. A.* **95**, 7275–7280 (1998).

231. Murphy, P. M. Double duty for CCL21 in dendritic cell trafficking. *Immunity* vol. 32 590–592 (2010).

232. Schumann, K. *et al.* Immobilized chemokine fields and soluble chemokine gradients cooperatively shape migration patterns of dendritic cells. *Immunity* **32**, 703–713 (2010).

233. Toy, R. *et al.* TLR7 and RIG-I dual-adjuvant loaded nanoparticles drive broadened and synergistic responses in dendritic cells in vitro and generate unique cellular immune responses in influenza vaccination. *J. Control. Release* (2020) doi:10.1016/j.jconrel.2020.10.060.

234. Xiang, S. D. *et al.* Pathogen recognition and development of particulate vaccines: Does size matter? *Methods* **40**, 1–9 (2006).

235. Russo, E. *et al.* Intralymphatic CCL21 Promotes Tissue Egress of Dendritic Cells through Afferent Lymphatic Vessels. *Cell Rep.* 1–12 (2016) doi:10.1016/j.celrep.2016.01.048.

236. Hons, M. *et al.* Chemokines and integrins independently tune actin flow and substrate friction during intranodal migration of T cells. *Nat. Immunol.* **19**, 606–616 (2018).

237. Nicholls, S. E., Winter, S., Mottram, R., Miyan, J. A. & Whetton, A. D. Flt3 ligand

can promote survival and macrophage development without proliferation in myeloid progenitor cells. *Exp. Hematol.* **27**, 663–672 (1999).

238. Hamilton, J. A. GM-CSF in inflammation and autoimmunity. *Trends Immunol.* **23**, 403–408 (2002).

239. Valenzi, E. *et al.* Single-cell analysis reveals fibroblast heterogeneity and myofibroblasts in systemic sclerosis-associated interstitial lung disease. *Ann. Rheum. Dis.* **78**, 1379–1387 (2019).

240. Butler, A., Hoffman, P., Smibert, P., Papalexi, E. & Satija, R. Integrating single-cell transcriptomic data across different conditions, technologies, and species. *Nat. Biotechnol.* **36**, 411–420 (2018).

241. Kowalski, E. J. A. & Li, L. Toll-interacting protein in resolving and non-resolving inflammation. *Frontiers in Immunology* vol. 8 511 (2017).

242. Xi, Y., Day, S. L., Jackson, R. J. & Ranasinghe, C. Role of novel type i interferon epsilon in viral infection and mucosal immunity. *Mucosal Immunol.* **5**, 610–622 (2012).

243. Marks, Z. R. C. *et al.* PROPERTIES AND FUNCTIONS OF THE NOVEL TYPE I INTERFERON EPSILON. *Seminars in Immunology* vol. 43 101328 (2019).

244. Haque, N. S., Tuteja, A. & Haque, N. CC chemokine CCL1 receptor CCR8 mediates conversion of mesenchymal stem cells to embryoid bodies expressing FOXP3+CCR8+ regulatory T cells. *PLoS One* **14**, (2019).

245. Metzemaekers, M., Vanheule, V., Janssens, R., Struyf, S. & Proost, P. Overview of the mechanisms that may contribute to the non-redundant activities of interferon-inducible CXC chemokine receptor 3 ligands. *Frontiers in Immunology* vol. 8 1970 (2018).

246. Angkasekwinai, P. & Dong, C. IL-9-producing T cells: potential players in allergy and cancer. *Nature Reviews Immunology* vol. 21 37–48 (2021).

247. Dooms, H., Kahn, E., Knoechel, B. & Abbas, A. K. IL-2 Induces a Competitive Survival Advantage in T Lymphocytes. *J. Immunol.* **172**, 5973–5979 (2004).

248. Soria-Valles, C. *et al.* MMP-25 Metalloprotease Regulates Innate Immune Response through NF-κB Signaling. *J. Immunol.* **197**, 296–302 (2016).

249. Lai, Y. *et al.* The Antimicrobial Protein REG3A Regulates Keratinocyte Proliferation and Differentiation after Skin Injury. *Immunity* **37**, 74–84 (2012).

250. Olajuyin, A. M., Zhang, X. & Ji, H. L. Alveolar type 2 progenitor cells for lung injury repair. *Cell Death Discovery* vol. 5 1234567890 (2019).

251. Platt, C. D. *et al.* Mature dendritic cells use endocytic receptors to capture and present antigens. *Proc. Natl. Acad. Sci. U. S. A.* **107**, 4287–4292 (2010).

252. Kasturi, S. P. *et al.* Programming the magnitude and persistence of antibody responses with innate immunity. *Nature* **470**, 543–550 (2011).

253. Kazzaz, J. *et al.* Encapsulation of the immune potentiators MPL and RC529 in PLG microparticles enhances their potency. *J. Control. Release* **110**, 566–573 (2006).

254. Henao-Tamayo, M. I. *et al.* Phenotypic definition of effector and memory T-lymphocyte subsets in mice chronically infected with mycobacterium tuberculosis. *Clin. Vaccine Immunol.* **17**, 618–625 (2010).

255. Lawand, M., Déchanet-Merville, J. & Dieu-Nosjean, M. C. Key features of gamma-delta T-cell subsets in human diseases and their immunotherapeutic implications. *Frontiers in Immunology* vol. 8 761 (2017).

256. Son, Y. I. *et al.* A novel bulk-culture method for generating mature dendritic cells from mouse bone marrow cells. *J. Immunol. Methods* **262**, 145–157 (2002).

257. Noubade, R., Majri-Morrison, S. & Tarbell, K. V. Beyond CDC1: Emerging roles of DC crosstalk in cancer immunity. *Frontiers in Immunology* vol. 10 1014 (2019).

258. Blank, C. U. *et al.* Defining 'T cell exhaustion'. *Nat. Rev. Immunol.* **19**, 665–674 (2019).

259. Friedrich, C. *et al.* MyD88 signaling in dendritic cells and the intestinal epithelium controls immunity against intestinal infection with C. rodentium. *PLoS Pathog.* **13**, e1006357 (2017).

260. Moratal, C. *et al.* IL-1β- and IL-4-polarized macrophages have opposite effects on adipogenesis of intramuscular fibro-adipogenic progenitors in humans. *Sci. Rep.* **8**, 1–13 (2018).

261. Atri, C., Guerfali, F. Z. & Laouini, D. Role of human macrophage polarization in inflammation during infectious diseases. *International Journal of Molecular*

Sciences vol. 19 (2018).

262. Born, W. K., Reardon, C. L. & O'Brien, R. L. The function of γδ T cells in innate immunity. *Current Opinion in Immunology* vol. 18 31–38 (2006).

263. Wang, J., Jiang, M., Chen, X. & Montaner, L. J. Cytokine storm and leukocyte changes in mild versus severe SARS-CoV-2 infection: Review of 3939 COVID-19 patients in China and emerging pathogenesis and therapy concepts. *J. Leukoc. Biol.* **108**, 17–41 (2020).

264. Singh, K. *et al.* A meta-analysis of SARS-CoV-2 patients identifies the combinatorial significance of D-dimer, C-reactive protein, lymphocyte, and neutrophil values as a predictor of disease severity. *Int. J. Lab. Hematol.* ijlh.13354 (2020) doi:10.1111/ijlh.13354.

265. Brostjan, C. & Oehler, R. The role of neutrophil death in chronic inflammation and cancer. *Cell Death Discovery* vol. 6 26 (2020).

266. Jasper, A. E., McIver, W. J., Sapey, E. & Walton, G. M. Understanding the role of neutrophils in chronic inflammatory airway disease. *F1000Research* vol. 8 (2019).

267. Pradhan, P. *et al.* TRAF6-IRF5 kinetics, TRIF, and biophysical factors drive synergistic innate responses to particle-mediated MPLA-CpG co-presentation. *bioRxiv* 2020.07.17.207209 (2020) doi:10.1101/2020.07.17.207209.

268. Hadjadj, J. *et al.* Impaired type I interferon activity and inflammatory responses in severe COVID-19 patients. *Science (80-.).* **369**, 718–724 (2020).

269. Hung, I. F. N. *et al.* Triple combination of interferon beta-1b, lopinavir–ritonavir, and ribavirin in the treatment of patients admitted to hospital with COVID-19: an open-label, randomised, phase 2 trial. *Lancet* **395**, 1695–1704 (2020).

270. Jalkanen, J., Hollmén, M. & Jalkanen, S. Interferon beta-1a for COVID-19: Critical importance of the administration route. *Critical Care* vol. 24 1–3 (2020).

271. Shalhoub, S. Interferon beta-1b for COVID-19. *The Lancet* vol. 395 1670–1671 (2020).

272. Al-Tawfiq, J. A., Al-Homoud, A. H. & Memish, Z. A. Remdesivir as a possible therapeutic option for the COVID-19. *Travel Medicine and Infectious Disease* vol. 34 101615 (2020).

273. Grajales-Reyes, G. E. & Colonna, M. Interferon responses in viral pneumonias. *Science (80-.).* **369**, 626–627 (2020).

274. Planet, P. J. *et al.* Lambda interferon restructures the nasal microbiome and increases susceptibility to Staphylococcus aureus superinfection. *MBio* **7**, (2016).

275. Broggi, A. *et al.* Type III interferons disrupt the lung epithelial barrier upon viral recognition. *Science (80-.).* **369**, 706–712 (2020).

276. Major, J. *et al.* Type I and III interferons disrupt lung epithelial repair during recovery from viral infection. *Science (80-.).* **369**, 712–717 (2020).

277. Takamura, S. *et al.* The route of priming influences the ability of respiratory virus-specific memory CD8+ T cells to be activated by residual antigen. *J. Exp. Med.* **207**,

1153–1160 (2010).

278. Harrell, M. I., Iritani, B. M. & Ruddell, A. Lymph node mapping in the mouse. *J. Immunol. Methods* **332**, 170–174 (2008).

279. Esterházy, D. *et al.* Compartmentalized gut lymph node drainage dictates adaptive immune responses. *Nature* **569**, 126–130 (2019).

280. Ma, Q. *et al.* Lymphatic outflow of cerebrospinal fluid is reduced in glioma. *Sci. Rep.* **9**, 1–10 (2019).

281. Han, F. Y., Thurecht, K. J., Whittaker, A. K. & Smith, M. T. Bioerodable PLGA-based microparticles for producing sustained-release drug formulations and strategies for improving drug loading. *Frontiers in Pharmacology* vol. 7 185 (2016).

282. Leleux, J. & Roy, K. Micro and Nanoparticle-Based Delivery Systems for Vaccine Immunotherapy: An Immunological and Materials Perspective. *Adv. Healthc. Mater.* **2**, 72–94 (2013).

283. Zhao, L. *et al.* Nanoparticle vaccines. *Vaccine* vol. 32 327–337 (2014).

284. Polack, F. P. *et al.* Safety and Efficacy of the BNT162b2 mRNA Covid-19 Vaccine. *N. Engl. J. Med.* **383**, 2603–2615 (2020).

285. Dong, Y. *et al.* A systematic review of SARS-CoV-2 vaccine candidates. *Signal Transduction and Targeted Therapy* vol. 5 1–14 (2020).

286. Mayer, C. T. *et al.* Selective and efficient generation of functional Batf3-dependent CD1031 dendritic cells from mouse bone marrow. *Blood* **124**, 3081–3091 (2014).

287. Tomura, M. *et al.* Tracking and quantification of dendritic cell migration and antigen trafficking between the skin and lymph nodes. *Sci. Rep.* **4**, 6030 (2014).

288. Fisher, N. I. *Statistical analysis of circular data*. (Cambridge University Press, 1993). doi:10.1017/cbo9780511564345.

289. Piegorsch, W. W. *Tables of P-values for t- and chi-square reference distributions*. (2002).

290. Watts, A. O. *et al.* β-Arrestin recruitment and G protein signaling by the atypical human chemokine decoy receptor CCX-CKR. *J. Biol. Chem.* **288**, 7169–7181 (2013).

291. Randolph, G. J., Angeli, V. & Swartz, M. A. Dendritic-cell trafficking to lymph nodes through lymphatic vessels. *Nat. Rev. Immunol.* **5**, 617–628 (2005).

292. Scandella, E. *et al.* CCL19/CCL21-triggered signal transduction and migration of dendritic cells requires prostaglandin E2. *Blood* **103**, 1595–1601 (2004).

293. Fainaru, O., Shseyov, D., Hantisteanu, S. & Groner, Y. Accelerated chemokine receptor 7-mediated dendritic cell migration in RunxB knockout mice and the spontaneous development of asthma-like disease. *Proc. Natl. Acad. Sci. U. S. A.* **102**, 10598–10603 (2005).